Synthesis of Carbon Nanotubes on Carbon Fibre for Hierarchical Composites

Inauguraldissertation
zur
Erlangung der Würde eines Doktors der Philosophie
vorgelegt der
Philosophisch-Naturwissenschaftlichen Fakultät
der Universität Basel

von

Wojciech Bożydar Szmyt

aus Polen

2020

Genehmigt von der Philosophisch-Naturwissenschaftlichen Fakultät

auf Antrag von

Fakultätsverantwortlicher: Prof. Dr. Christian Schönenberger
Dissertationsleiter: Prof. Clemens Dransfeld
Korreferent: Prof. Dr.-Ing. habil. Bodo Fiedler

Basel, 13.10.2020

Dekan: Prof. Dr. Martin Spiess

In the memory of my father Ryszard, a sculpture artist and a teacher,
who inspired me to notice, admire and explore the beauty of this world.

Abstract

Carbon fibre (CF) reinforced polymer (CFRP) composites are surpassing steel greatly in terms of strength and stiffness per weight. This makes them particularly attractive when the weight of a part has a major influence on the performance and environmental impact, such as in automotive or airspace applications, wind turbines or sporting goods. The superior mechanical properties of the CFRPs are mostly pronounced along the fibre orientation. However, in load modes such as compression or shear, the CFRP performance is much lower, dominated by the properties of the polymer matrix and the fibre-matrix interface. Therefore, it is critical to enhance the performance of the fibre-matrix interface and of the matrix in order to push the limits of the lightweight CFRP materials. This thesis explores the concept of *hierarchical composites* based on CFs grafted with carbon nanotubes (CNTs) by chemical vapour deposition (CVD) for an additional reinforcement of the CF-matrix interphase region at the nanoscale, harnessing the extraordinary mechanical properties of CNTs. CNT growth on CFs poses a challenge, particularly due to the CF degradation in the CVD process, which occurs due to migration of iron (the common catalyst of CNT growth by CVD) into the CF. This issue leads to trade-offs between the quality of the grown CNTs and the strength of CF. In this work, we utilised an alumina barrier layer, synthesised on the CF by atomic layer deposition (ALD) for protection of the fibre in the harsh CVD conditions as well as for an effective support of CNT growth. In Chapter 2, we demonstrated that a 12 nm alumina film indeed allows to block the migration of iron into the CF, which results in retained CF tensile properties. Moreover, the mechanisms of the detrimental iron migration into CFs are identified and quantified by means of ptychographic X-ray computed tomography and scanning transmission electron microscopy (STEM). In Chapter 3, we addressed the issue of delamination of the alumina film from the CF upon exposure to high temperatures used for CNT growth. A modified ALD process was proposed, including an ozone treatment for enhancement of covalent bonding between the fibre and the alumina film. The preservation of the CF-alumina interface shear strength was evidenced by single fibre pull-out testing. The findings were supported by fracture analysis of the pull-out surfaces by scanning electron microscopy and energy-dispersive X-ray spectroscopic elemental analysis. In Chapter 4, we reported a method of coating of alumina-buffered surfaces with iron catalyst nanoparticles, which allows for a homogeneous CNT growth over substrates of complex geometries, such as CF fabrics. A dip-coating method was applied to deposit the iron catalyst precursor on the substrates. We examined the influence of the iron nitrate solution concentration and ageing time on the resultant catalyst iron nanoparticle coating quality in terms of nanoparticle sizes, coating density and dispersion. Moreover, we proposed an aminosilane treatment of the alumina surface, which we showed to enhance the coating quality. The catalyst nanoparticle coating quality was quantified by SEM image analysis. We showed a correlation between the improvements in the catalyst coating quality with the enhanced CNT growth uniformity, density and alignment. The excellent CNT growth morphology was demonstrated on flat substrates, as well as on complex surfaces of CF fabrics. We have identified, that the theory of gas transport in fibrous structures was lacking in the literature. In Chapter 5 we derived an analytical model of gas transport in fibrous media from basic physical principles. The model is applicable both at low pressures, when the gas transport occurs in the Knudsen regime, as well as at higher pressures, while an analytical continuous transition towards the viscous gas transport regime was delivered. The applicability of the model presented reaches far beyond the processing of the fibres for composites. The theoretical framework provided in Chapter 5 was validated at nanoscale in Chapter 6, where it was applied in a kinetic model of ALD on CNT mats. The modelling allowed to predict a coating thickness profile of CNTs in a multicycle diffusion-limited ALD experiment. The predicted profile was compared with an experimentally obtained one, giving an excellent agreement. Moreover, the chapter provides numerous new physical insights into the kinetics of ALD coating of porous structures in general. Accounting for all the above, we believe that the work presented in this thesis constitutes a major progress in understanding and development of the CF-CNT hierarchical composites.

Acknowledgements

"Friendship is the hardest thing in the world to explain.
It's not something you learn in school.
But if you haven't learned the meaning of friendship,
you really haven't learned anything."

Muhammad Ali

First of all, I would like to thank Clemens Dransfeld, my thesis advisor, who believed in me and gave me the opportunity to be a part of this exciting project. Collaboration with him has been friendly and fruitful. With his precious guidance, the learning curve appeared much less steep, both in engineering and scientific aspects of this work. Also, I cannot thank him enough for his support throughout the whole duration of my PhD project and beyond, despite all the challenging circumstances, such as him moving to The Netherlands for his new professorship position at TU Delft and the novel coronavirus pandemic. Here, I also thank Markus Grob, for taking over the position of the head of IKT after Clemens left and for being a great and friendly boss.

I thank the SNI for providing the resources for making this project possible, as well as for all winter schools, annual meetings and other events, which brought the SNI members together and offered a great platform both for scientific and private exchange, which made me feel that SNI is not just a scientific institute, but family as well.

I would also like to thank Samuel Vogel, who worked on this project before me, for giving me the introduction, which allowed me to use his findings as a wonderful starting point to carry the knowledge further. I hope I was able to do justice to his prior work by expanding on it, publishing it in a prominent journal and proudly including it in this thesis. I cordially thank Celestino Padeste for supervision of my activities in PSI, his invaluable support in writing the thesis and for many discussions which helped me keeping on track. He shared with me his point of view as an experienced chemist, which was really eye-opening for me and constituted a rich contribution to this thesis. I thank Michel Calame for his support, particularly in the administrative aspects of the PhD thesis, as well as for providing his enlightening view on the overall structure and content of the thesis. Owing to his remarks, I learned to take a step back and notice the importance of the broader picture, instead of staying focused on the details, for which I am grateful. I would like to thank Jens Gobrecht for his support of my work at PSI. I thank Ivo Utke and Carlos Guerra-Nuñez for their kind support of the work on the theory and experiments of gas diffusion in fibrous structures, which I proudly report in this thesis.

I give my thanks to Magnus Kristiansen for his help in organisation of getting the chemical vapour deposition infrastructure at PSI to work, and to Michael Grob for the designing and installation of the infrastructure, without whom a massive portion of my work for this thesis would not have been possible. I also thank Thomas Neiger and Eugen Deckardt for their technical assistance in the installations. I am grateful to Michael Spälti and to Malvína Voclová for helping me in the chemistry lab, making the impossible happen. I thank Fabian Schadt and Christian Brauner for their efforts in obtaining the micromechanical testing device, which facilitated carrying out a very important portion of my work for this thesis. I would like to express my gratitude to Agnieszka Karpik, who has been helping me with 3D-printing and 3D imaging of my samples. My special thanks go to Sabine Vogt, the secretary, who helped me out of my administrative trouble many times. I thank Dennis Brütsch and Daniel Zürcher for their kind support at the workshop.

I would like to thank all the people I had a great pleasure to be colleagues with at the FHNW: Jonathan Schmidli, Igor Zhilyaev, Elias Rehmann, Sebastian Wollmann, Jan Hess, Jerome Werder, Leo Walker, Christian Rytka, Lyaysan Amirova, Julia Studer, Panagiota Tsotra, Lucian Zweifel, Sonja Neuhaus, and all others, who made my time at FHNW a wonderful experience.

Table of Contents

Chapter 1

Introduction

"The whole is greater
than the sum of its parts."

Aristotle

This chapter contains literature background regarding carbon fibre-carbon nanotube hierarchical composites and formulates the motivation of this thesis.

1.1. Background

Discovery and development of new materials often lead to major leaps in technology. Material-driven technologies tend to be initially used in high-end applications, gradually paving their way to common use, ultimately impacting or even fundamentally changing our everyday lives. Such was the story of advances in semiconductor materials, for instance, which led to the development of integrated electronic circuits (ICs). The first ICs were used mainly in space exploration programs and by the military, whereas, in modern days, the ICs have become such an integral part of our lives, that we almost do not realise their existence. Iron metallurgy is another example, albeit of much longer history – the developments in the technology of iron metallurgy defined the Iron Age. Iron and steel are thought to have presumably first been used for tools and weapons, which were initially expensive. The material is still with us, well and widespread, present in applications from large-scale constructions to smaller objects of everyday use. We believe that composite materials – carbon fibre-reinforced polymers (CFRP) in particular – share a similar destiny.

As a result of developments in material science and engineering, humanity learned that assembling several materials in specific ways may give new composite materials with better- or entirely new properties, compared to any of the individual constituents. CFRPs are a type of a high-performance composite material, which are nowadays very well-established throughout the industry, as well as in the consumer market, encompassing applications in wind turbines, aerospace and automotive components and sporting goods, to name a few [1]. CFRPs became competitive particularly to metal in structural applications owing to the impressive mechanical properties of the fibres along the fibre direction, which allow saving on the weight of the part to be manufactured, without compromises on its mechanical performance [2]. The substantial reduction of the weight of a land vehicle or an aircraft results in a major decrease in fuel consumption and, consequently, in CO_2 emissions. This is why pushing the mechanical performance of the CFRPs beyond the current limitations if of great importance, both from an economic and an environmental standpoint.

While the technology of CFRPs was continuing its rapid growth and development, new carbon materials such as graphene and carbon nanotubes (CNTs) were discovered. Ideal graphene is a monoatomic sheet of sp^2-hybridised carbon atoms bound together covalently in a honeycomb arrangement, which is essentially an atomic 2D sheet of graphite, see: Figure 1.1a,b. Numerous routes of graphene production have been developed, including mechanical and chemical cleavage and exfoliation of graphite, epitaxial growth, chemical vapour deposition (CVD) and bottom-up synthesis of graphene nanoribbons [3]. CNTs are hollow cylinders of graphene; they can be multi-wall (MWCNTs) or single-wall (SWCNTs), see: Figure 1.1c. Occasionally double-wall CNTs are mentioned as a distinct type. Like graphene, CNTs have been synthesised by various techniques as well, including arc-discharge, laser ablation, CVD, and template synthesis by pyrolysis [4,5].

One can say, that graphene is a basic building block of the carbon materials considered in this work, as the carbon fibres (CFs) as well consist of multilayer graphene grains, i.e. graphitic domains, see: Figure 1.1d. High-performance CFs are typically produced by pyrolysis of polyacrylonitrile (PAN). They owe their high tensile (on-axis) properties – tensile strength and modulus – to the internal structure. The CF tensile performance is dominated by its outer shell, which is highly graphitised with the graphitic planes oriented in line with the fibre axis [6,7]. This characteristic of CFs offers an opportunity of aligning the fibres in the CFRP composite in load direction for harnessing the fibres mechanical properties to the greatest extend possible.

Both graphene and CNTs have generated great interest in numerous potential applications, owing to their extraordinary physical properties [8]. The use of CNTs and graphene in composites for structural applications is motivated mainly by their strength (CNTs: 11-63 GPa; graphene: 130 GPa) and modulus (CNTs: 270-950 GPa; graphene: 1000 GPa) [9,10], which are among the highest

of materials known to man, surpassing steel significantly. However, CNTs and graphene may exhibit lower strength and modulus, depending on the defect density. Although in this work we are focusing on the mechanical aspects of the composites, it is important to keep other potential benefits of incorporating CNTs and graphene in composites in mind, which may reach far beyond the mechanical improvements. Introduced functionalities include shape memory effects [11], enhanced heat dissipation [11–13], or large increases in electrical conductivity [11–16] approaching values required for lightning strike protection of aircraft [16]. The impressive improvements in electrical conductivity of CNT composites are owed to two factors: high electrical conductivity of CNTs reaching values up to 10^7 S/m [17], which is in on par with the most conductive metals (silver, copper and gold) and the extremely low percolation threshold, when embedded in a polymer matrix, achieved at CNT loadings as low as 0.0025 wt% [18]. The percolation is achievable at such low loadings thanks to the ultrahigh aspect ratio and specific area of the CNTs. Furthermore, thermoelectric functionality of CNT-polymer composites tailored by p- and n-type doping of CNTs was reported [15], as well as health monitoring function under cyclic loads and impact damage [19,20].

The incorporation of CNTs or graphene in the CFRP composites, on top of mechanical improvements, may add the above-mentioned functionalities to the material, which can lead to further savings in weight. For instance, in the context of lightning strike resistance of an aircraft, if the electrical conductivity of the CFRP panel gets high enough due to the addition of CNTs, it might eliminate the need to install heavy protective copper meshes in the parts [21]. Another example is energy storage – if a certain capacity to store electrical energy is added to the composite part by the addition of CNTs, the weight of the energy storage-specific components can be reduced [22]. Materials incorporating reinforcements at several length of scales are referred to as *hierarchical composites*, with microscale and nanoscale fillers working in a composite synergistically. In nature, the concept of a hierarchical composite is nothing new. Taking a closer look at wood, for instance, we notice its distinct hierarchical structure, from microscale high-aspect-ratio wood cells, down to nanoscale cellulose fibrils and hemicellulose-lignin matrix [23,24]. The particular combination and geometric arrangement of its multiscale constituents give wood its mechanical properties: toughness, elasticity and strength, at the same time fulfilling the function of transport of nutrients and water. Other examples of hierarchical structures in nature include bone, seashells or glass sponges [23,25], to name a few. Seemingly, nature is pointing us to the direction of hierarchical, multifunctional composites.

The hierarchical composites considered in this work are based on dense, aligned arrays of nanoscale CNTs grown directly on the microscale CFs, see Figure 1.1e (schematic illustration, not to scale). With this hierarchical arrangement of carbon-based materials, we aim to enhance the off-axial performance of the CFRPs, dominated by properties of CF-epoxy interface and the matrix. Notably, commonly in the industry, the CF-matrix interface adhesion is promoted by application of polymeric sizing [26]. The approach to enhance the interface with CNTs constitutes a promising alternative, offering multiple additional benefits on top of the mechanical enhancement, as discussed in the further part of this chapter. In section 1.2, we give a more detailed introduction to CNT- and graphene nanocomposites. In section 1.3 we review the effects of incorporating CNTs together with CFs in composites, outline the challenges in the direct growth of CNTs on CF and describe various approaches to tackle them. Further on, in section 1.4, we motivate the content of the subsequent chapters, the knowledge gaps identified and the way they are addressed.

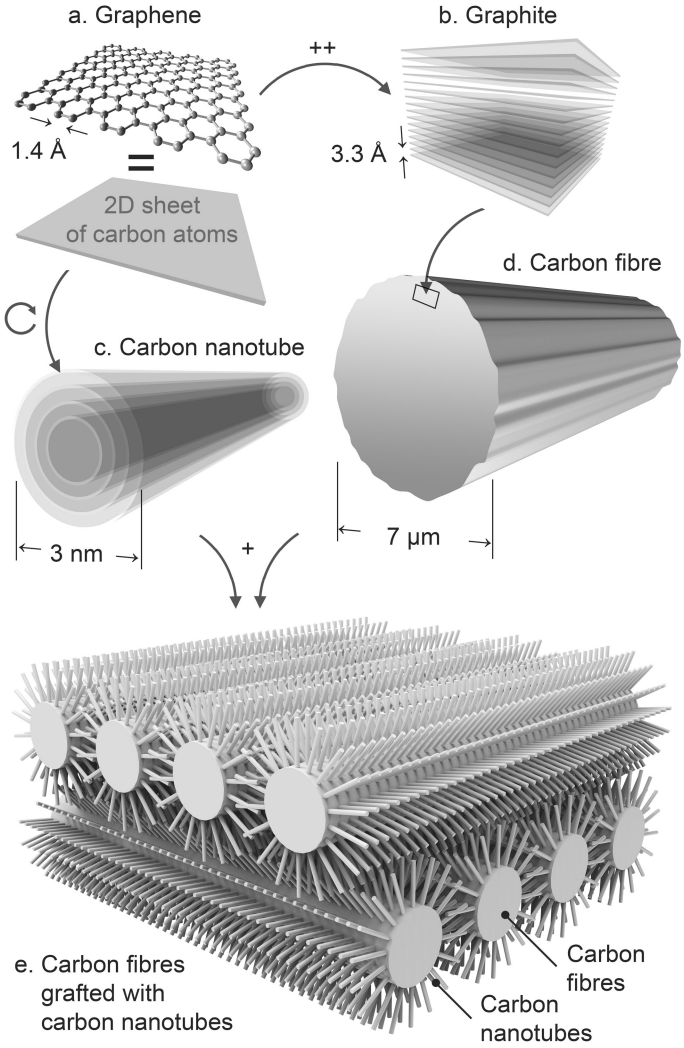

Figure 1.1. Hierarchy of different forms of carbon leading to carbon fibres grafted with carbon nanotubes; a. Graphene – a 2D sheet of sp^2-hybridised carbon atoms arranged in a honeycomb lattice (illustrated additionally as a grey solid for clarity); b. Graphite – a bulk crystalline solid consisting of multiple graphene sheets bound together with van der Waals bonds; c. Carbon nanotube – a cylinder of one- or multiple graphene sheets of nanometre diameters, referred to as a single- or multi-wall carbon nanotube, respectively (the multiwall variety is illustrated); d. Carbon fibre – a solid cylinder of microscopic diameter, highly graphitised. The graphitic planes are preferentially oriented in line with the fibre axis, which improves the fibre mechanical properties; e. Carbon fibres grafted with radially aligned carbon nanotubes – a concept illustration of the multiscale arrangement of the carbon constituents of the hierarchical composites targeted in this work (not to scale).

1.2. Graphene and carbon nanotubes in nanocomposites

1.2.1. Nanocarbons dispersed in polymers

There have been large efforts in science and engineering to produce polymer composites with CNT and graphene nanofillers that would harness their mechanical advantages. In a simple approach, CNTs are dispersed and mixed in the polymer. The filler load is however strongly limited by a rapid increase in polymer viscosity with addition of CNTs [27], hindering the processability. Moreover, as pointed out by Fiedler *et al*., [28] the extremely high surface area of CNTs leads to the tendency to agglomeration. Therefore, the dispersion of the nanofiller needs to be ensured, for instance by stirring, sonication or calendering. Nonetheless, even at low nano-filler loads, significant mechanical improvements were observed [28]. For instance, an increase of fracture energy of epoxy with 1 wt.% filler content of CNTs by 25% in mode I (tensile mode) and by 170% mode II (shearing mode) was reported, compared to the neat epoxy [29]. Graphene-epoxy nanocomposites show improvements in fracture energy

in mode I by ca. 200% [30], 40% in mode II [31] and up to ca. 400%-1600% increase in fatigue life, depending on the load applied [32]. Synergistic toughening effects of incorporating both CNTs and graphene in epoxy for was also observed [11,33]. Meeuw *et al.* [34] examined a broad range of carbon nanofillers in epoxy resin, including, but not limited to, single- and multiwall CNTs and graphene and studied their effects on the rheological, electrical and mechanical properties. They observed, that single-wall CNTs gave the greatest increase in electrical conductivity, while providing improvement both in mode I and mode II fracture toughness, at the same time keeping the epoxy viscosity at levels allowing for effective processing. Notably, all the carbon nanofillers resulted in significant increases in mode I fracture toughness, however, contrarily to other studies cited here above, decreases in mode II fracture toughness were mostly observed with increased filler loading. The latter were attributed to carbon nanofiller particles promoting crack initiation.

Because the strength of the nanofillers considered is so high, breakage of CNT or of graphene planes is far from being the primary failure mode of a nanocomposite. The toughening mechanisms are dominated by crack deflection, increased fracture surface area, creation of shear bands, crack pinning and bridging [33], all of which become apparent even at small filler content. For graphene, additionally graphene layer shearing and separation has been observed as an energy dissipating mechanism [35]. At higher weight percentages of nanocarbon in polymers, the mechanical benefits are lost due to agglomeration [36,37], leading to voids in the material, which poses a challenge on the way to harness the mechanical properties of CNTs and graphene in composites. Nonetheless, the toughness improvements of polymers at small filler weight fractions of CNTs dispersed and mixed in matrices attracted the applications of CNT fillers in hierarchical composites, exploring synergistic effects of the well-established microscale reinforcement by CF and nanoscale reinforcement and toughening by CNTs to improve matrix-dominated composite properties. Enhancements in impact and post-impact performance were reported [38], 200% increase in impact energy absorption [39], and mode I interlaminar fracture toughness of a unidirectional composite (44% improvement at 0.043 wt.% of CNTs) [40]; 32% improvement in flexural strength and 33% in interlaminar shear strength was observed at 0.025 wt.% of CNTs in woven fabric CF-epoxy composites [36]. In another example, at much higher nanocarbon filler loadings (3 wt.%) in woven fabric CF-epoxy composites, increases of 80% and 115% in mode I and mode II fracture toughness, respectively, were measured, as an effect of CNT addition, whereas incorporation of the graphene nanoplatelets resulted in 153% and 42% improvements in mode I and mode II fracture toughness, respectively [41]. At such high filler loadings dispersed in epoxy, care needs to be taken to maintain the filler suspension throughout the impregnation process, e.g. via frequent sonication and/or mixing [41,42], which limits the applicability at larger scales.

1.2.2. Aligned CNTs – an increase of wettability and filler loading

High CNT loadings in epoxies are achievable by impregnation of aligned forests of CNTs (A-CNTs) [43–46]. A-CNTs are arrays of CNTs aligned parallel to each other, typically achieved by direct growth of CNTs on surfaces by catalytic CVD. The alignment arises from a *crowding effect* during the growth when the distances between the tubes are small enough to allow the self-assembly of CNTs into A-CNTs by steric inter-tube interactions [47]. García *et al*. [44] demonstrated, that A-CNTs (as-grown volume fraction ~1%) are readily wetted by epoxy, leading to void-free composite structures. This effect is attributed to the capillary action in A-CNTs. Moreover, even at 20-fold densification of A-CNTs up to 20 vol.% prior to epoxy infiltration, no voids in the nanocomposite were observed, even though the impregnation was driven solely by capillary forces [48]. This approach allowed for impregnation of even millimetre-thick A-CNTs. Hence, A-CNTs are shown to form effective composites with thermosets. Capillary force-driven wetting with polymer matrices allows for forming nanocomposites at high filler fractions, overcoming the re-agglomeration issues. In a follow-up study, García *et al*. [45] carried out micropillar compression testing of A-CNT-epoxy composites along

the CNT alignment axis, obtaining a 220% increase in stiffness at 2 vol.% CNT loads, compared to neat epoxy. Notably, A-CNT composites at 2 vol.% of CNTs exhibited a clear stiffness advantage over the results for analogous tests on randomly-aligned CNT composites across weight fractions of CNTs from 0.1 to 14.3 wt.% (maximum 100% improvement in stiffness), reported by Coleman *et al*. [49]. Bradford *et al*. reported the tensile strength and modulus of A-CNT-epoxy composites of 400 MPa and 25 MPa, respectively, at 27 vol.% of CNTs [50], which are intermediate values between the ones characteristic to a typical neat epoxy and CF. Wicks *et al*. studied the fracture mechanics of A-CNT-polymer composites. No significant improvement of mode I fracture toughness at crack initiation with respect to neat epoxies was observed [51,52], however, a potential for toughening by CNT pull-out and increase of fracture surface area was shown. Therefore, one needs to keep in mind, that sparse, randomly-aligned CNTs are generally more effective for matrix toughening, whereas A-CNTs enhance the stiffness and tensile/compression strength of the composite.

1.3. Carbon nanotubes in hierarchical fibre-reinforced composites

1.3.1. Advantages of direct carbon nanotube growth on carbon fibre

The findings described above demonstrate the potential of CNTs for application in hierarchical composites as a nanoscale reinforcement working in synergy with the microscale fibre reinforcement. The A-CNTs can be used for enhancement of the CF-epoxy interface by forming a nanocomposite interphase region between the fibres and the matrix. Numerical studies have revealed, that A-CNTs at CF in a composite result in a reduction of radial and shear stresses in the CF-epoxy interphase region [53]. Accounting for the fact, that the fibre-matrix interface is the typical failure point of fibre-reinforced plastics upon load modes such as shear, compression or bending, reduction of stresses in the CF-matrix region is expected to be beneficial to composite mechanical performance [54]. Lv *et al*. studied the effect of CNT alignment on the composite performance at a single fibre level [55]. The A-CNT-grafted CFs showed significantly higher improvement of interfacial shear strength (IFSS) between CF and epoxy (175% greater than unsized CFs), with respect to the improvement observed with tangled CNTs (28%). Moreover, the wettability with epoxy was shown to be strictly positively correlated with the IFSS improvement and the wetting behaviour was attributed to the alignment of CNTs as well as to the increase of surface area by several orders of magnitude due to the presence of CNTs. Lv *et al*. also discuss, that the alignment of the CNTs arises from the steric interactions between the growing tubes – they correlate the growth density with CNT alignment. This phenomenon may also be referred to as a crowding effect [47,56]. The enhancements in IFSS due to direct growth of CNTs on CF fabrics correlated with the increased surface area and improved wetting behaviour have been broadly reported in the literature, for instance by Qian *et al*. for PMMA polymer matrix [13] or by An *et al*. further for epoxy matrices [57]. Increases in tensile strength measured due to the direct growth of CNTs on fibres have been reported for unidirectional CF composites in the axial direction [58,59] as well as for isotropic short CF composites [60]. Rahmanian *et al*. [37] studied low filler content composites (1 wt.% of short CF and 1 wt.% of CNTs in epoxy), and examined the effect of CNTs grown directly on CF, CNTs dispersed in epoxy and both of the above. The tensile strength, stiffness and impact resistance of the composites improved in all cases. Moreover, CNTs grown on CF and dispersed in epoxy showed a synergistic reinforcement effect.

1.3.2. Challenges in direct carbon nanotube growth on carbon fibre with chemical vapour deposition

As the reader may have noticed, the above-described mechanical advantages brought into CFRPs by CNTs grown on CFs are related mainly to the matrix-dominated properties or properties dominated by the fibre-matrix interface. However, it has been reported broadly, that the synthesis process of CNTs on CF by CVD is detrimental to fibre mechanical properties. The usually observed drop of the fibre tensile strength and modulus have been attributed to dissolution of the iron catalyst used for CNT

growth into the CFs [13] or to the embedding of catalyst nanoparticles in the CF [55]. The latter has an advantage of strong anchorage of the CNTs in the CFs; however, it comes at a price of impaired axial fibre properties. Aiming at the high-performance composites, it is not acceptable to compromise on the main CFRP advantage, which is their performance in axial direction. The solubility of carbon in iron, being the very effect which makes iron such an effective CNT synthesis catalyst, seems to render its use detrimental to the CF substrate in direct CNT growth. This leads to the effect of etching of the fibre topmost layer, which – as mentioned earlier – carries most of the fibre load. Moreover, this mechanism often leads to the deactivation of the iron catalyst nanoparticles, which results in a sparse CNT growth [13] and, as a consequence, lack of CNT alignment, while at lower growth densities the steric interactions between the tubes no longer provide preferential normal growth direction.

1.3.3. Alternative approaches to carbon nanotube-enhanced hierarchical composites

To circumvent the issues discussed in the previous section and to demonstrate the benefits of the direct growth of CNTs on fibres, the process was carried out on other types of fibres, such as on alumina fibres [61,62] or silicon carbide fibres [12], which are not susceptible to damage by the iron catalyst in the CVD process. The choice of alumina fibres was motivated by the fact, that alumina has been shown to be a very effective support for CNT synthesis due to the specifics of the substrate-catalyst interactions, which will be discussed in section 1.3.5 of this chapter. Importantly, the works on alumina fibres further substantiated the impact of CNT alignment on the impregnation of the fabrics with the polymer matrices. While the extraordinarily strong wetting of A-CNTs grown on flat substrates is intuitively understandable, impregnation of fabrics with CNTs may raise questions about whether the CNTs between the fibres constitute an obstacle to the resin flow, rather than aid it. However, it has been demonstrated, that the A-CNTs on the fibres indeed help the impregnation, leading to void-free composites [61,62]. Moreover, essentially electrically insulating alumina fibre-epoxy composites were rendered conductive by the CNTs [62]. Improvements of mode I interlaminar fracture toughness were also observed both for alumina and silicon carbide fibre composites, due to nano-stitching effect of CNTs by bridging, CNT pull-out and enhanced surface area of the crack [63].

Other attempts to circumvent the issues of CF degradation in the fabrication of CNT-CF hierarchical composites avoid direct growth altogether. The simple approach uses CNT-toughened matrices with CFs, as discussed in section 1.2.1. Otherwise, A-CNT forests, separately grown on flat substrates, were transplanted into the interplay region of the CFRP, leading to an impressive improvement in interlaminar fracture toughness: two-fold in mode I and three-fold in mode II [61,64]. Solvent-spraying of CNTs onto CF fabrics resulted in modest tensile strength and modulus benefits [65] and an increase in mode II interlaminar fracture toughness [66]. Dispersing CNTs in the fibre sizing led to ~70% increase in the fibre-matrix interface shear strength [67].

Recently, Herceg *et al*. [16,68] presented a novel worth-mentioning approach to CNT-CF-epoxy hierarchical composites, which is based on the wet powder impregnation. In short, the process relies on preparing a CNT nanocomposite at high CNT loads (up to 20 wt.%) according to the previously reported recipe [69], grinding it into a microscale powder, mixing the nanocomposite powder with the epoxy matrix and impregnating the CF fabrics. In this approach, one obtains fibre-reinforced composites with a matrix inhomogeneously reinforced with CNTs– i.e. regions of high CNT concentration corresponding to the nanocomposite powder are present, with neat epoxy in between. This unique geometry results in significant enhancement of fracture toughness via multiple crack deflection by the CNT-rich regions. This effect was demonstrated by comparing the mode I fracture toughness of these hierarchical composites with the ones obtained by a homogeneous dispersion of CNTs in the matrix at the same weight fraction, resulting in the 26% advantage of the new approach [68].

Another alternative approach, grafting of CNTs onto CF by electrophoretic deposition (EPD) has been pursued as well. Its scalability to a continuous process on fibre tows has been demonstrated, which makes this approach industrially attractive [70]. CNT EPD on unidirectional CF yielded 100% increase in fibre-matrix interface shear strength [71], up to 70% increases in composite shear strength, 90% increases in mode I fracture toughness [14,72]. Due to the specifics of the method however, the CNTs are deposited flat or in random orientations onto the CF, but still, the mechanical improvements achieved by EPD are significant. In this work we are pursuing the goal of exploiting the reinforcement potential of CNTs in composites in the off-axis direction to its maximum, as well as the CNT-driven wetting enhancement, for both of which the CNT alignment is critical, as discussed for the A-CNT-epoxy nanocomposites in section 1.2.2.

1.3.4. Mitigation of carbon fibre damage in carbon nanotube growth

As discussed in the previous section, we aim at aligned CNTs on carbon fibre surfaces. Radial CNT alignment on CF is achievable exclusively through direct growth; therefore, ways to mitigate the destructive effect of CNT growth on CF were pursued. Various studies attempted lowering the CNT synthesis temperature, hypothesizing that it will reduce the damage, choosing alternative catalysts, which might be less harmful to the fibres, or both of the above. The examined catalysts included nickel [58,73–76], cobalt [76], palladium [77,78], or alloys of iron with nickel [76], cobalt [76] and copper [79], to name a few. The results were encouraging – the synthesis temperature was reduced significantly, the fibre tensile properties were largely preserved and moderate mechanical improvements of hierarchical composites due to the CNTs grown were noted. However, the CNT growth morphology in terms of growth density, alignment and the quality of the grown CNTs generally suffered. Clearly, to effectively exploit the potential of the CNTs in hierarchical composites, another approach was needed.

The application of a barrier layer on the carbon fibre appeared as one solution to this problem. The target function of the barrier layer was to constitute a barrier against penetration of metal catalyst into the fibres and to serve as an effective support to CNT growth. The layer materials examined included aluminium [80], aluminium oxide (alumina) [6,57] and silicon oxide (silica) [55,58].

In the study of Boroujeni *et al*., 75 nm of silica and 2 nm of nickel catalyst were sputtered onto the fabrics for CVD of CNTs for reinforcement of the interply regions [58]. The silica thickness was referred to as a "thermal barrier coating" (TBC), and it was shown to be effective in preserving the on-axis properties of the composite upon the CNT growth. However, the off-axis properties were shown to worsen with the TBC included, which hints that the adhesion between in the new interfaces introduced by TBC - the new composite component – might be an issue (interfaces: CF-TBC, TBC-epoxy or TBC-CNTs). No effect of the silica TBC on the CNT morphology was observed. Contrarily, Lv *et al*. [55] did observe an improvement in grown CNT morphology obtained with the silica coating on CF. The silica film was obtained by dip-coating of the fibres in toluene-based solutions of tetraethoxysilane and silicon tetrachloride (5 vol.% each), followed by hydrolysis and pyrolysis. The barrier coatings were however not conformal and the deterioration of the fibre outer shell with metal catalyst nanoparticles was not avoided. Moreover, the thickness of the silica films obtained with this method was less than 10 nm. The findings of Lv *et al*. indicate the importance of the control of the barrier layer conformality and thickness at nanoscale level.

Steiner *et al*. [6] and An *et al*. [57] applied an alumina coating of CF fabrics by dip-coating in aluminium nitrate salt solution followed by calcination. The fabrics were subsequently dip-coated with the iron catalyst by another dip coating in an iron nitrate solution. The results showed, that the alumina coating serves well as a barrier against the etching of the CF with the metal catalyst. Moreover, it was confirmed, that the alumina film strongly promotes a dense and aligned CNT growth [6,57]. Importantly, Steiner *et al*. [6] also established, that another factor important for preserving the tensile properties of the fibres

during the CNT synthesis is keeping the fibres under tension (≥12% of fibre tensile strength). They hypothesised, that the tension prevents the thermally-induced mechanochemical restructuring of the graphitic CF material, which would otherwise change the proportions of the load-bearing, highly-ordered graphitic phase within the fibres' outer shell and the disordered fibre cores.

1.3.5. Role of the alumina support in the carbon nanotube synthesis

The functions of the alumina coating of CF as effective support of CNT growth by CVD and as a barrier against the destructive penetration of the catalyst into the CF have not been specifically investigated from the fundamental point of view, to the best of our knowledge. This section is dedicated to the description of the role of the catalyst-support interaction in the context of CNT growth by CVD to clarify the motivation of the choice of the system of the alumina layer and iron catalyst. For this purpose, let us follow a route from the metal catalyst or catalyst precursor film on the support to the growth of aligned CNTs.

Initially, a film of metal catalyst or catalyst precursor is present on the support. The film may be in a form of a continuous coating or in form of particles. At high temperature, under a reducing atmosphere, the film gets calcinated under evaporation of gaseous decomposition products and what remains gets reduced to a metallic state [81]. For instance, in case of coating with iron nitrate, the calcination step leads to formation of iron oxide, which is subsequently reduced to metallic iron under reducing, high temperature conditions.

Due to the size effect, the few nanometre thin film melts even hundreds of degrees below the melting temperature of the bulk metal, following the phenomenon referred to as *melting point depression* [82]. The further geometrical evolution of the catalyst is dictated by the wetting behaviour [83], which is determined by the surface energies of the support γ_S, molten metal γ_M and the metal-support interface γ_I. The contact angle θ_C of the droplets on the support is evaluated based on the Young's equation [84]

$$\cos\theta_C = \frac{\gamma_S - \gamma_I}{\gamma_M}. \tag{1.1}$$

If the metal-support interface energy γ_I was too low, the metal would remain in the form of a continuous film (θ_C determined as less than 0 based on equation (1.1)), which is undesirable for CNT growth, as the growth requires nanosized droplets or nanoparticles. Therefore, the interface surface energy needs to be higher, to allow for the droplet formation. This is indeed the case for iron droplets on alumina surfaces [83]. The droplets have a certain mobility on the surface, which causes the *Ostwald ripening* [83,85] – the phenomenon, where mobile particles collide and coalesce, favouring the survival of larger particles over the small ones and narrowing down the particle size distribution. While for CNT growth ideally ~10-20 nm diameter particles are required, the ripening must not proceed towards further coalescence of the particles when this size range is reached. A mechanism hindering the surface mobility of the particles is therefore desired.

There have been conflicting reports regarding the interaction of alumina and iron in the context of CNT growth. Weak interaction and, consequently, high mobility of droplets has been reported to lead to coalescence of iron into large particles ~100 nm in size, unsuitable for CNT growth [86]. Contrarily, iron catalyst particles of desired sizes anchored in alumina surfaces have been reported as well [56]. As it turns out, the type and morphology of the supporting alumina play a critical role in the process. Amama *et al*. [83] examined various types of the alumina supports, here listed from the lowest to the highest catalytic activity resulting: c-cut sapphire, alumina films that were e-beam deposited and annealed, deposited by atomic layer deposition (ALD), electron-beam deposited without annealing and sputter-deposited. Their results showed, that more amorphous and porous the film is, higher

the catalytic activity of deposited iron towards the CNT growth. The imperfections in the alumina film, such as grain boundaries and nanopores, absorb the catalyst, leading to the subsurface diffusion of iron. This effect causes a localised rapid decrease in the interfacial energy γ_I and, consequently, immobilisation of the catalyst droplets, preventing the undesired continuation of the Ostwald ripening [56,83,85,87–89]. Moreover, iron remains strongly bonded with alumina after the solidification [88], which is highly relevant for the mechanical anchorage of the CNTs in the support for the application in hierarchical composites.

While according to results of Amama *et al*. [83], the best catalytic activity is observed for the most amorphous and porous alumina films, for which also the degree of subsurface diffusion was second largest, we need to keep in mind the other target function of the alumina film critical in our application, which is to provide a diffusion barrier against penetration of iron into the underlying CF. ALD alumina shows intermediate catalytic activity. The films synthesised with this method are typically amorphous, but pinhole-free, which may limit the subsurface diffusion of iron mostly to the grain boundaries, with the decreased component of the influence of the nanopores. The porosity of the ALD alumina is 15%, i.e. between the sapphire (0%) and the sputtered alumina (36%) [83]. Moreover, ALD allows for an atomic-level control over the layer thickness on complex geometries, such as of CFs in the form of fabrics or tows, considered in our case. Therefore, alumina synthesised using ALD is our choice as the barrier layer for CNT synthesis on CF. The depth of the subsurface diffusion of iron into the amorphous alumina has been roughly estimated to ~3 nm under CNT growth conditions by CVD [83,85], which dictates the order of magnitude of the thickness of the alumina barrier layer for achieving the protective effect.

1.4. Approach to hierarchical composites in this work

In light of the findings reviewed in section 1.3, the approach to hierarchical composites based on alumina-coated CFs and direct growth of aligned CNTs on the CF by CVD was adopted in this work, specifically motivated by the following:

- The aim is to enhance the CF-matrix interface with radially-aligned CNTs. The CNT alignment is expected to help the impregnation with epoxy by capillary action.
- The above is achievable by direct growth of CNTs by CVD.
- CF tensile properties deteriorate at CVD conditions without the protection layer due to damage of the CF surfaces by the iron catalyst.
- The approaches attempting to mitigate the fibre damage without any protection layer by modifying the CVD process (e.g. lower synthesis temperatures, alternative catalysts) lead to inferior CNT quality, growth density and alignment.
- An alumina support film promotes the desired CNT growth morphology.
- ALD-synthesised alumina is expected to serve both as catalyst support and a diffusion barrier against the etching of CF in contact the catalyst during CNT synthesis.
- The application of ALD as the coating technique allows for an extremely uniform coating and an atomically-precise control over the coating thickness.

The previous efforts of our group reported by Vogel *et al*. [90] have demonstrated the effectiveness of the ALD-synthesised alumina film in the preservation of the CF tensile strength upon exposure to the CNT growth conditions by CVD. The effect of maintaining the fibre under tension throughout the process, suggested previously by Steiner *et al*. [6], has been confirmed as well. The alumina layer thickness sufficient for the CF protection has been established at 12 nm. The following paragraphs specify the motivation, knowledge gaps identified and the way they are addressed in subsequent chapters.

Chapter 2 Protection of carbon fibre with a thin alumina film

In this chapter answers, we explore the mechanisms governing the protection of the CF by the alumina film in the CNT growth process by CVD. Moreover, we investigate mechanisms of migration of the iron catalyst into the CF and what morphological changes this process causes in the fibres.

The morphological changes that occur in the CF shell during the direct growth of CNTs without the protective layer have been largely understudied and remained subject to speculation. Moreover, the function of the alumina film as a barrier against the diffusion of iron into the CF required a direct confirmation. These issues are addressed in a ptychographic X-ray computed tomographic (PXCT) study of CFs with- and without the protective alumina film. The PXCT is a nanoscale 3D imaging method (in our case, 50 nm resolution was achieved), carried out at a synchrotron beamline. The results are additionally confirmed by a complementary scanning transmission electron microscopy (STEM) examination of thin CF slices (~100 nm thick) prepared by focused ion beam milling.

Chapter 3 Mechanical improvement of the alumina – CF interface

This chapter tackles the question whether an ozone treatment provides sufficient adhesion between CF and the alumina protective layer, which does not deteriorate upon exposure to the high temperature conditions of CNT growth by CVD.

The study of Vogel *et al*. [90] has shown, that while the protective effect of the alumina film is achieved, another challenge arises - the interface shear strength between the CF and the alumina drops at the CNT growth conditions. The study of Boroujeni *et al*. [58] indicated that failure at the additional interfaces, which created with the barrier coating, might be an issue. This is clearly unacceptable for application in hierarchical composites, therefore means to mitigate this effect needed to be devised. Here, we present the enhancement of the CF-alumina interface achieved by modifying the ALD process with an ozone treatment, which is expected to promote covalent bonding between the alumina film and the CF substrate. The interface shear strength is examined employing single fibre pull-out testing. Furthermore, the interface failure surfaces are analysed by scanning electron microscopy (SEM) and nanoscale elemental mapping is carried out using energy-dispersive X-ray spectroscopy (EDX) to elucidate the failure mechanisms and confirm the interface strength enhancement.

Chapter 4 Optimisation of carbon nanotube growth morphology on carbon fibre fabrics

In this chapter, we explore the influence of concentration and ageing time of the iron catalyst precursor solution on the surface dispersion quality of the catalyst nanoparticle coating. Moreover, we investigate whether an aminosilane treatment enhances the coating quality and how the catalyst dispersion quality translates to the CNT growth morphology. Ultimately, the question whether the developed catalyst coating process apply well to dense, aligned and homogeneous growth of CNTs on surfaces of complex geometry, such as carbon fibre fabrics is addressed.

We aim at a dense, aligned and uniform CNT growth on the CF to harness the reinforcement potential of the CNTs to the greatest extend. CNT growth is strictly determined by the catalyst nanoparticles; therefore, an appropriate method of coating with the catalyst needs to be considered. For stitching of the interply region of the composites with CNTs, a straightforward sputtering of a thin iron film onto the alumina-coated CF fabric would be the right choice, as the shadowing effect would result in a coating of only the top surfaces of the CF fabrics with the catalyst. In this work, however, the nanoscale reinforcement of CF-epoxy interfaces with CNTs within the fibre tows or fabrics is targeted; therefore, a recipe for a uniform coating of structures as complex as CFs with the iron catalyst needed to be developed. Moreover, the control of the CNT length and alignment in the CVD process had to be achieved, so that the CNTs do not occupy too much space between the fibres, allowing

to retain the fibre volume fractions typical for industrial composites. We demonstrate a novel method of coating with the catalyst precursor by precipitation from iron nitrate solution in isopropanol promoted by an aminosilane treatment of alumina-coated surfaces. The temporal evolution of the precipitation within the solutions is studied by dynamic light scattering. The iron catalyst nanoparticle coatings are examined and quantitatively analysed in terms of surface dispersion quality, areal density and nanoparticle size distributions by scanning electron microscopy image analysis. The effectiveness of the novel recipe for dense, aligned and homogeneous growth of CNTs on the complex surfaces of woven CF fabrics is demonstrated.

Chapter 5 Theory of gas transport in random fibrous structures

This chapter presents an analytical description of the diffusion of gas in random fibrous structures in the Knudsen regime derived from basic principles. This description gives the background to explore the effect of the fibre mat density (fibre length per volume) and average fibre diameter on the gas transport. Furthermore, a generalised model to the transition to the viscous gas transport regime at higher pressures is presented.

The growth of CNTs on substrates of as complex geometries as CF fabrics or tows is not a trivial process from the perspective of gas transport. It has been shown, that the CNT growth, even on flat substrates, is limited by gas diffusion, while the carbon feedstock molecules need to find their way to the catalyst nanoparticle located at the CNT base in the base-growth mode [91]. The longer the CNTs, the stronger the diffusion limitation effect. We expect it to be even more pronounced when the tortuosity of an inter-fibre confined space is considered. We believe that the deep understanding of the gas transport will allow for optimisation of the CVD process for a uniform CNT growth throughout the CF fibres or tows. Alternatively, an accurate model may allow for tailoring the CNT growth rates spatially; for instance aiming at longer CNTs on the outer part of the tows with respect to the tow core. The mean free path of gas molecules within a CNT forest can potentially be significantly shorter than the mean free path in the bulk gas considering the intermolecular collisions only, due to geometrical confinement of the flight paths by the walls of CNTs. In cases, when the mean free path within a given confined space or structure (usually a pipe or a porous material) is much shorter the mean free path in the bulk gas, the gas transport occurs in a *Knudsen regime* [92]. The Knudsen diffusion is very well described in regular porous structures, such as cylindrical pores or trenches. On the other hand, the Knudsen diffusivity in the *inverse porous structures* such as dense CNT forests or arrays of fibres has been described mostly by phenomenological, probabilistic or otherwise approximate models. The analytical description of the phenomenon from the physical principles, and thus, its fundamental understanding, have remained elusive. Here, the Knudsen diffusivity within fibrous structures is analytically described from basic physical principles for the first time, along with numerous other gas transport parameters specific to this type of structures. A continuous transition from the Knudsen diffusion to the viscous gas transport regime is also provided, which becomes important at higher gas pressures, i.e. when the mean free paths in the bulk and in the space confined by CNT walls are comparable. The findings are relevant in other contexts as well, such as gas-phase functionalisation of the CNTs for enhanced binding with the matrix [93], densification of hairy fibres by chemical vapour infiltration [94] and many other applications, which are impacted by gas transport in fibrous membranes in general.

Chapter 6 Atomic layer deposition on porous substrates: from general formulation to fibrous substrates and scaling laws

In this chapter we present a fundamental description of the ALD coating kinetics of arbitrary porous structures. From the model, we derive the main physical parameters that influence the single- and multicycle ALD coating thickness, and we show how to fundamentally distinguish the reaction- and diffusion-limited ALD coating regime. Ultimately, we demonstrate that the gas transport theory

in fibrous structures, developed in Chapter 5, allows to accurately predict the ALD coating profile on CNT mats.

The introduced theoretical framework of gas transport in fibrous structures required an experimental validation. Naturally, in the context of hierarchical composites and CNT growth on CF tows or fabrics, one would consider a multiscale model accounting for macroscale diffusion of carbon precursor between the CF tows, microscale diffusion through the tows, nanoscale diffusion between the growing CNTs and depletion of the carbon precursor concentration as it feeds the CNT growth. This kind of model would be characterised however by a large number of unknown parameters. Given the novelty of the theory of gas diffusion developed in Chapter 5, for its validation, a simpler model system needed to be considered, to pave the way towards application of the diffusion theory in more complex systems. We present a continuum diffusion-reaction model of ALD on forests of CNTs grown on flat substrates, which accounts for the diffusion of precursor gas in the fibrous medium of the CNT forests and the self-limiting surface reaction of the precursors on the CNT surfaces. The model predicts the profile of the coating thickness in a multi-cycle ALD experiment. At each cycle, the coated CNT diameter grows, which decreases the diffusivity and increases the surface area to coat, both of which have an impact on the depth into the fibrous structure which gets coated in a single ALD cycle. The diameter profile of the ALD-coated CNT forest is examined by SEM, whereas the surface area – by a Brunauer–Emmett–Teller (BET) krypton surface adsorption. The experimental results are compared with model predictions. The modelling presented in this chapter not only validates the diffusion theory described in Chapter 5, but also provides new insights into ALD on porous structures in general with the new scaling laws describing the process.

Chapter 2

Protection of carbon fibre with a thin alumina film

"Each one has to find his peace from within. And peace to be real must be unaffected by outside circumstances."

Mahatma Gandhi

This chapter is based on the published work W. Szmyt, S. Vogel, A. Diaz, M. Holler, J. Gobrecht, M. Calame, C. Dransfeld, *Carbon*. 115 (2017) 347–362.

Wojciech Szmyt contributed to this work with conceptualisation, methodology and software for formal data analysis, experimental investigations, writing of the original draft and visualisation of the data. **Samuel Vogel** took part in conceptualisation, investigation, writing the original draft, project administration and funding acquisition. **Ana Diaz** assisted with the tomography measurements, processed the data for tomographic reconstruction, assisted with the development and use of software for formal data analysis, investigation, writing the original draft as well as with manuscript review. **Mirko Holler** performed the tomography measurements, assisted with the processing of the data for ptychographic reconstruction, assisted with manuscript review and investigation supervision. **Jens Gobrecht** provided the facilities for CNT growth and he and **Michel Calame** supported the work by reviewing the manuscript and project supervision. **Clemens Dransfeld** participated in conceptualisation, manuscript review, carried out project supervision, administration and funding acquisition.

Abstract

Composite materials based on carbon fibre (CF) are prone to failure at the fibre-matrix interface upon compression or stress transverse to the fibre axis. The direct growth of carbon nanotubes on CF constitutes a novel approach to enhance the mechanical properties of the interface. However, the challenge is that, during the growth, tensile properties of the fibre are altered due to the diffusion effect of iron nanoparticles used in the process, leading to CF surface defect formation. In this work, we deliver and discuss an analysis methodology on ptychographic X-ray computed tomography (PXCT) images in order to assess the iron nanoparticle abundance within CFs. PXCT provides 50 nm - resolved 3D electron density maps of the CFs. We evidence the protective effect of an ultrathin alumina film against iron infiltration into CF during the CNT growth. This method potentially allows to evaluate the efficiency of other diffusion-minimizing approaches. The conclusions of the PXCT examination are validated by energy-dispersive X-ray spectroscopy and scanning transmission electron microscopy carried out on thin sample slices cut with a focused ion beam. The results provide a new insight into the mechanical performance of CFs and therefore constitute valuable knowledge for the development of hierarchical composites.

2.1. Introduction

Carbon fibre reinforced polymers (CFRP) easily overcome the traditional metal solutions in terms of strength- and stiffness-to-mass ratio owing to their extraordinary tensile mechanical properties in the fibre direction. The failure of CFRP occurs typically at the fibre-matrix interface upon stress in the direction transverse to the CF or compression. Hierarchical composites constitute a novel approach to enhance the mechanical properties of the CF-based composites utilizing the direct growth of nanoscale carbon nanotubes (CNT) on the surface of the microscale CF with chemical vapour deposition (CVD) before the impregnation with the polymer [95]. The CNT CVD growth process is typically catalyzed by iron nanoparticles (NPs). The direct CNT growth on the CF is challenged by surface defect formation induced by the iron catalyst, leading to strongly altered tensile properties of the CF, because the tensile failure of the fibre often originates at a defect [96]. Qian *et al.* [97] have observed homogeneously distributed pits in the surface of a CF after CNT growth and subsequent chemical removal of iron. They related this effect directly to the defect-induced strength decrease. They have also come to a conclusion that dissolution of iron in CF along with the resulting defect formation occurs in the same CVD parameter window, as the efficient CNT growth, which has appeared as a challenge. In a later study, Qian *et al.* [13] have experimentally verified that the strength of CF decreases significantly in the process, which supported the previous observations. Zhu *et al*. [98] have attributed the roughening of CF to recrystallisation of CF surface and etching with hydrogen at CNT growth temperatures up to 750°C, however they also state a hypothesis that at higher temperatures iron NPs diffuse into the CF body and thus get disabled as CNT growth catalyst. Sonoyama *et al.* [99] have tackled the challenge of iron dissolution in CFs and NP deactivation by introducing a novel two-step CVD process based on ferrocene, xylene and H_2S vapours, hypothesizing that the sulphur absorbed by iron minimises the unwanted effects. However, the mechanical properties of such prepared hairy fibres have not been examined. Zhang *et al.* [100] have reported, that at the CVD processing temperature of 750°C the tensile properties of the fibres do not change significantly, however this reasoning was based on results with unusually large error bars. The preservation of the tensile properties in the process is crucial for the hierarchical composites to supersede the classical CFRP, which has been recently addressed in ways such as the alternative choice of the catalyst system [76,79], different CVD growth reaction mechanism [76], non-covalent fibre functionalisation with polymeric coating [6,75] or application of a protective alumina film prior to coating with the catalyst [6,90]. The latter was the subject of our recent study where we have shown that the application of a 12 nm thick alumina layer as a first processing step preserves the mechanical strength of the fibre during CNT growth [90]. For the convenience of the reader, the results are described briefly in Appendix A.1. Degradation of high tensile strength carbon fibre coated with 0.1-0.5 µm thick nickel films upon CVD processing

conditions has been studied by Warren *et al.* [101], where the diffusion-controlled carbon dissolution in metal and precipitation have been pointed out as the main mechanisms governing the process. The diffusion of iron particles into CFs at CVD processing temperatures is not well understood yet. In a previous work we presented 3D electron density maps of CF sections with and without alumina protective layer with a resolution of about 50 nm [102]. Measurements were done using ptychographic X-ray computed tomography (PXCT) [103,104] with a high-resolution instrument [105]. Here, we introduce a methodology of quantitative assessment of iron NP abundance below the surface of the CF that overcomes the challenge that the NPs are not resolved in the PXCT measurements. The results of this novel method of 3D imaging and the unprecedented data analysis approach are confirmed by means of energy-dispersive X-ray spectroscopy (EDX), scanning electron microscopy (SEM) and scanning transmission electron microscopy (STEM) carried out on thin transverse slices of CFs cut with a focused ion beam (FIB). The results prove the protective effect of the thin alumina film against iron diffusion into CFs.

2.2. Experimental

The CFs that were used in the experiments were the commercially unsized and oxidative treated type of AS4 produced by Hexcel, USA, as used by Steiner *et al.* [6]. The CFs have been coated with alumina of two different thicknesses using the atomic layer deposition (ALD) technique [90,106]. The iron catalyst has been deposited with a metal sputtering method on such prepared CFs as well as on a neat CF. Afterwards, the CNT growth has been carried out using a CVD technique based on hydrocarbon thermal decomposition. The sample preparation was equivalent to the one discussed in our previous work [102] and is described in detail in the following section 2.2.1. The EDX elemental characterisation and STEM imaging have been performed as a validation of the PXCT results. CF slices of ~100 nm thickness were cut using FIB in order to enable a clear identification of the positions of iron NPs by STEM for the subsequent analysis. A pristine CF was taken as a control sample. Subsequently, the PXCT imaging of the samples has been performed in order to assess the abundance of iron NPs within the fibres and thus evaluate the protective effect of the alumina film. Afterwards, EDX elemental characterisation and STEM imaging has been performed as a validation of the PXCT results. CF slices of ~100 nm thickness were cut using FIB in order to enable a clear identification of the positions of iron NPs by STEM for the subsequent analysis.

2.2.1. Sample preparation

Initially, the CFs were coated with alumina films using ALD, which is a thin film fabrication technique that allows for extremely uniform coating of outer surfaces of samples of virtually any geometric complexity while guaranteeing an atomic precision in layer thickness control. This feature of the method makes it ideal for a uniform and conformal coating of a CF with a barrier film. Alumina has been chosen as the coating material as it is a typical support for CNT growth [107]. The samples have undergone a 10-minute ultra violet / ozone treatment before the ALD coating. The coating has been carried out using a commercial ALD system Savannah 100 (Cambridge NanoTech, UK). The precursors for alumina ALD process were trimethyl aluminium (TMA) and deionised water. The process temperature has been set to 225°C. In our previous study the ALD growth rate of alumina film has been calibrated by means of ellipsometry of a silicon wafer coated simultaneously alongside the CF in the ALD reactor. In the present study we are investigating the protective effect of the 12 nm-thick alumina film against the iron NP diffusion. Additionally, a film of 500 nm thickness is examined being well above the 50 nm resolution of the images obtained in this study.

The CVD growth of CNTs on a solid substrate requires delivery of a metal catalyst on the surface, typically iron. In this study, the surfaces of fibres have been coated with iron catalyst thin film using magnetron sputtering. In this method, metal is physically vaporised from a target using an electron beam in vacuum. The surface of the sample in the reactor is coated with the metal. The reactor chamber

pressure during depositions was 1.2×10^{-5} mbar. The reactor was kept at room temperature. The deposition rate was measured by a quartz balance and was set to 0.5 Å·s^{-1}. The deposition rate was controlled by adjusting the acceleration voltage of the electron beam prior to opening the shutter. The deposition was terminated at 5 nm film thickness by closing the shutter. The fibres were coated from two opposite sides in separate processes in order to partially overcome the shadowing effect of the technique.

After the sputtering of the catalyst, the CNT growth was carried out. The CNTs were grown on the samples in a custom atmospheric pressure CVD reactor. The samples of carbon fibre were put into a 136 mm diameter quartz tube of the CVD oven. The process time was 15 minutes. The growth has been carried out at a 750°C temperature. The gases used in the process were ethylene and hydrogen. The volumetric flow rate of each gas was 1 L·min^{-1}. At this stage of the process, the sputtered iron film gets reduced by hydrogen and undergoes transformation into metallic NPs, such that the CNT growth can be initiated and continued.

Ultimately, four different samples were prepared for the further examination. One pristine CF without any further treatment was taken as a control. The second sample was sputtered with an iron catalyst film of 5 nm nominal thickness and CNT growth was carried out on it. Another two CFs were prepared with a protective alumina layer of 12 nm and 500 nm thickness, respectively, prior to catalyst sputtering and subsequent CNT growth. The set of the prepared samples is summarised in Table 2.1.

Table 2.1. Summary of carbon fibre samples.

Sample name	**alumina ALD**	**iron sputtering**	**CNT growth**
Pristine	None	None	None
Unprotected	None	5 nm	Done
12 nm protected	12 nm	5 nm	Done
500 nm protected	500 nm	5 nm	Done

2.2.2. Single fibre imaging using ptychographic X-ray computed tomography

X-ray ptychography is a coherent diffraction imaging technique in which the specimen is scanned across a coherent finite illumination in such a way that adjacent illumination areas partially overlap [108]. At each scanning position, coherent diffraction patterns are recorded in the far field and used in phase retrieval algorithms to reconstruct the complex-valued transmissivity of the specimen, providing an image with both absorption and phase contrast [109]. Many such phase images acquired at different incidence angles of the specimen with respect to the incoming beam can be then combined tomographically to yield the 3D electron density distribution within the sample [103].

PXCT measurements were carried out at the cSAXS beamline of the Swiss Light Source at the Paul Scherrer Institut in Villigen, Switzerland, with a photon energy of 7 keV. We used a recently developed instrument that makes use of laser interferometry for high-accuracy positioning of the specimen with respect to the illuminating optics [105]. Details of the experimental setup and data acquisition can

be found in Ref. [102], but for the reader's convenience we describe them briefly in the following paragraph.

The coherent X-ray illumination onto the sample was defined by a Fresnel zone plate made of Au [110] with 150 μm diameter and 60 nm outer-most zone width, resulting in a focal length of 52.82 mm at the X-ray photon energy of 7.00 keV which was used in the experiment. We estimate that a flux of about 6.4×10^8 photons/s was delivered by the Fresnel zone plate. The sample was placed 1 mm downstream the focus in such a way that the size of the beam on the sample was about 3 μm. Coherent diffraction patterns were recorded from the specimen in transmission geometry at different positions of the sample following the pattern of a Fermat spiral [111] with an average spacing between scanning points of about 0.8 μm. Diffraction patterns were recorded with a Pilatus 2M detector with 172 mm pixel size [112] placed at 7.355 m from the sample with an acquisition time of 0.1 s for each diffraction pattern. We thus estimate a flux density of 1.2×10^8 photons/μm^2 incident on the specimen for each ptychographic scan. Ptychographic scans were acquired at different angles of the specimen with respect to the incoming beam in equal angular steps between 0 and 180°. Due to the inactive areas of the detector in the gaps between modules, the detector was translated in both directions perpendicular to the beam propagation direction alternating between two positions at consecutive angular steps. In the ptychographic reconstructions, each pair of consecutive scans were reconstructed together, such that two images were obtained while sharing the same illumination probe, as explained in [113] and introduced for tomographic acquisitions in Ref. [105].

All samples were measured as described in Ref. [102], except that for the pristine CF 250 projections were recorded instead of 375, as the absence of CNTs around the pristine CF yielded a lateral size significantly smaller compared to the other samples. We estimate that a dose of 3.4×10^7 Gy was imparted on the pristine specimen and 5.1×10^7 Gy on all other specimens. This difference in dose has basically no effect in the measurements in terms of resolution or radiation damage, as we do not expect radiation damage for these specimens. Ptychographic reconstructions were performed using a difference map algorithm [114] followed by a maximum likelihood optimisation as a refinement step [115]. For the reconstructions we first used an area of 800×800 pixels of the recorded diffraction patterns for the pristine CF, obtaining a pixel size of 9.47 nm in the reconstructed images. As it became apparent that the resolution of the images was significantly worse, about 50 nm, for the other samples we used 600×600 pixels of the diffraction patterns, obtaining a pixel size of 12.62 nm. The phase images were further corrected for zero and first order terms and registered in the vertical direction as described in Ref. [116], and registered in the horizontal direction by tomographic consistency [117] to obtain 3D electron density maps. The 3D resolution was estimated to be about 50 nm comparing the Fourier shell correlation of two subtomograms with half the number of projections with the half-bit threshold [118].

2.2.3. Microscopic and elemental examination of thin carbon fibre slices

PXCT examination gives a vast amount of spatial information about the sample, being a non-destructive imaging method. Additionally, the unprecedented 3D image analysis approach introduced and discussed in the further part of the work allows overcoming the challenge that the sizes of iron NPs are below the resolution of the imaging method. Considering the magnitude of novelty in using PXCT for this purpose, it was decided to validate the results by another method that is well-established. Moreover, due to the fact that PXCT gives no information about the elemental composition, this aspect needed to be verified as well. The method of our choice for validation is FIB/STEM/EDX examination of thin fibre slices, which has been carried out in a Helios NanoLab™ 650 DualBeam™ microscope produced by FEI Company, equipped with a gallium ion gun, field-emission electron gun, nanomanipulator Omniprobe 200 produced by Oxford Instruments, EDAX X-ray detector produced by Oxford Instruments and gas injection system for focused-ion-beam-induced deposition (FIBID)

of platinum for precise welding at nanoscale. Two samples were examined: the unprotected one and the one protected with the 12 nm alumina film.

Initially, fibres were mounted horizontally on SEM stubs by a conductive carbon tape and additionally welded with a silver paint for increased conductivity and stability. Care was taken to keep the ends of fibres loose for convenient further nanomanipulation. The stage was moved to a eucentric position in which is the sample plane perpendicular to the ion beam and in an optimum working distance with respect to the electron beam being ~4 nm. In such a configuration, ion beam milling is performed perpendicularly to the fibre axis and the process can be monitored in-situ by sequential SEM imaging.

The procedure began with cutting off the loose part of the fibre, see Figure 2.1a. After that, a nanomanipulator needle approached the fibre end from a side and was welded to it by platinum FIBID, see Figure 2.1b. Subsequently, fibre was cut above the welded point resulting in ~500 nm thick CF slice, see Figure 2.1c. The cutting was performed with 30 kV ion acceleration voltage and relatively high current in the range of 0.79-2.5 nA. The rectangle scan was chosen as the scanning strategy for cutting. Final polishing of the sample was then performed from both sides of each slice in order to obtain the desired thickness and to get rid of the most of gallium redeposition that could obscure the results, see Figure 2.1d. The polishing was performed at the same acceleration voltage of 30 kV, but at a smaller current within the range of 70-200 pA in order to obtain a smooth well-defined surface of limited gallium contamination. The scanning strategy for polishing was a sequential line scan gradually proceeding towards the desired slice surface. It was ensured, that the scan line proceeded to a new position after it had already successfully milled away its target.

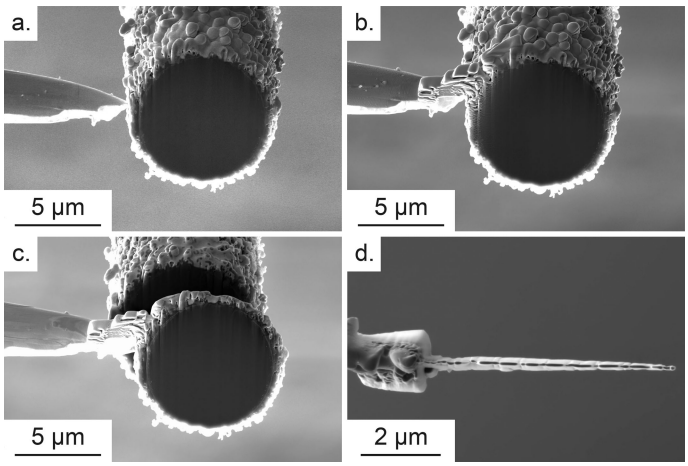

Figure 2.1. SEM images of subsequent steps of FIB cutting procedure of CF slices; (a) loose-end of the fibre cut off; (b) nanomanipulator needle welded to CF using focused-ion-beam-deposited platinum; c. relatively thick CF slice cut off; (d) thin CF slice after polishing (top view).

2.3. Results and discussion

2.3.1. Examination of CNT growth effect by means of scanning electron microscopy

Scanning electron microscopy (SEM) has been carried out in order to examine the result of CNT growth and to observe the iron NPs on the CF surface using Zeiss Supra VP55 high resolution field emission scanning electron microscope. It has been estimated from the SEM image that the iron NP diameters fall between 20 and 40 nm, whereas the areal density of the NPs is approximately equal to 6×10^{10} cm^{-2}, see Figure 2.2. Moreover, the CNT morphology exhibits bamboo-shaped structures.

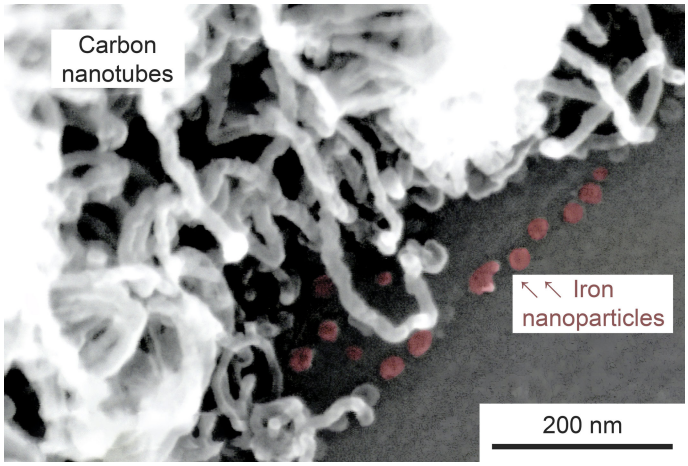

Figure 2.2. SEM image of iron NPs (coloured in red for visibility) and CNTs grown on the surface of a CF.

2.3.2. Assessment of the electron density of the materials present in the samples for the purpose of PXCT data analysis

The theoretical electron density of a material can be calculated using the equation

$$\varrho = \frac{\Delta N_e}{\Delta V} = \frac{N_\mathrm{A} d}{\mu} \sum_i N_i Z_i, \tag{2.1}$$

where ϱ is the electron density, d is the mass density of the material, N_A is the Avogadro number, μ is the molar mass of a stoichiometric unit of the material, i is the index of an element present in the material, N_i is the number of atoms of the i-th element in a stoichiometric unit of the material and Z_i is the atomic number of the element. The materials to consider in our case are the bulk of carbon fibre, iron in NPs assumed to be in a ferrite phase at room temperature, and alumina in the barrier layer. The CNTs and iron within CNTs are not considered because these nanostructures are not resolved in enough detail in the PXCT electron density maps. Besides, iron within CNTs or CNT morphology do not influence fibre strength, contrarily to iron NPs within the CF body, therefore their analysis is beyond the scope of this work. Table 2.2 is partially reproduced from our previous work [102] and summarises the parameters of the considered materials. Cementite (Fe_3C) is added to the table of materials as it has been reported in literature that it can at least partially participate as intermediate species in the process of iron-catalysed graphitisation of amorphous carbon [119,120].

Table 2.2. Properties of the materials considered within this work. The body of the CF is predominantly composed of C and N, its stoichiometry is taken as fractional. Densities are given at room temperature.

Material	**Density[a] / g cm^{-3}**	**Stoichiometry**	**Molar mass / g mol^{-1}**	**Atomic numbers**	**Electron density[b] / Å^{-3}**
alumina	3.00[c]	Al_2O_3	101.96	$_{13}$Al, $_{8}$O	0.89
CF	1.79[d]	$C_{0.95}N_{0.05}$[d]	12.11	$_{6}$C, $_{7}$N	0.54
ferrite	7.88[e]	Fe	55.85	$_{26}$Fe	2.21
cementite	7.70[f]	Fe_3C	179.55	$_{26}$Fe, $_{6}$C	2.17

[a] given at room temperature
[b] calculated using equation (2.1).
[c] density of alumina ALD film obtained at 177°C by Groner *et al.* [121]

[d] atomic fractions of the respective elements in the CF composition, calculated using the data from the Hexcel©, HexTow® AS4 Carbon Fibre Product Data Sheet [122]
[e] calculated using crystallographic data obtained by von Batchelder *et al.* [123]
[f] calculated using crystallographic data obtained by Wood *et al.* [124]

For the sake of simplicity, in this work we assume that the NPs are composed of pure iron. This assumption does not alter the results significantly, as the difference between the electron densities of ferrite and cementite is smaller than 2%. Figure 2.3 presents representative tomographic cross sections of the four samples obtained by PXCT. The values in Table 2.2 show that the electron density of iron is more than four times greater than that of CF. Therefore it is reasonable to attribute the voxel groups of elevated electron density in Figure 2.3b to iron NPs within the unprotected CF. This effect is not visible in the other three electron density maps. The 12 nm alumina film is not clearly visible in Figure 2.3c, because the thickness of the film is smaller than the PXCT resolution and the electron density of the alumina is not more than twice the one of the CF. Instead, only a slightly elevated electron density on the CF surface is observed. It is non-trivial to determine how much it is influenced by the presence of the alumina or by the iron NPs condensed on the surface. Nonetheless, the high-density voxels are always on the surface of a CF and never underneath it, which is in agreement with the hypothesis of the diffusion-blocking effect of the 12 nm alumina film. A detailed analysis of iron NP abundance is carried out in the further part of this work. The 500 nm alumina film is easily resolved in the images and such prepared samples exhibit no presence of iron below the CF surface, as shown in Figure 2.3d. The electron density of the alumina has been measured to be 0.82 $Å^{-3}$ which is in a good agreement with the corresponding value 0.89 $Å^{-3}$ form the Table 2.2.

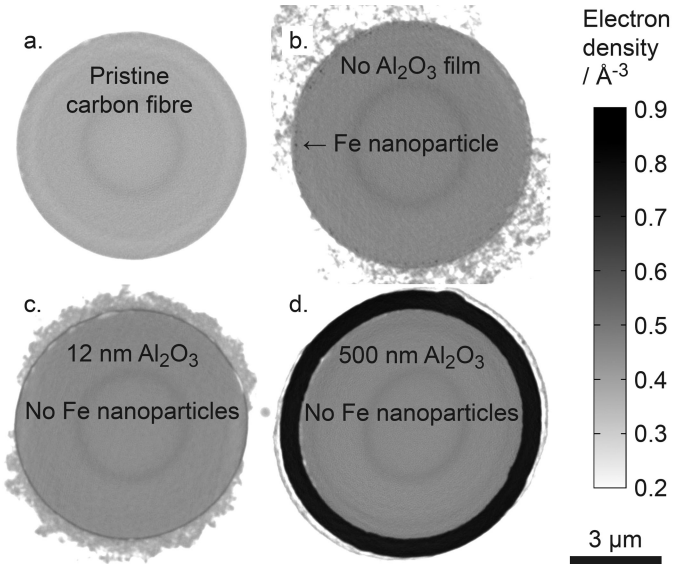

Figure 2.3. Representative averages over 25 subsequent slices of electron density maps of CFs with a total thickness of about 328 nm; (a) pristine carbon fibre control sample; (b) unprotected CF grafted with CNTs exhibiting presence of iron NPs below its surface; (c) CF with 12 nm alumina film showing no iron NPs below the surface; (d) CF with 500 nm thick alumina film showing no presence of iron below the fibre surface

2.3.3. Fitting of cylindrical mask to CF for spatial data analysis of 3D PXCT images

The 3D electron density maps of each sample consist of stacks of equally-spaced 2D slices approximately perpendicular to the fibre axis, which is almost parallel to the rotation axis, z. For the sake of generality and greater accuracy, the CFs are assumed to have an elliptical cross section. To analyse the data we fit an elliptic cylinder to the CF section with an automated algorithm. This is performed the following way:

- The largest ellipse which fits inside the CF is sought for each slice. The ellipse is defined by

$$\vec{r}(\vartheta) = \vec{r}_0 + \begin{pmatrix} \cos\vartheta_0 & \sin\vartheta_0 \\ -\sin\vartheta_0 & \cos\vartheta_0 \end{pmatrix} \begin{pmatrix} a\sin\vartheta \\ b\cos\vartheta \end{pmatrix}, \qquad \vartheta \in [0,2\pi), \tag{2.2}$$

  where ϑ is the angular argument, $\vec{r}$ is the position vector of the ellipse point for the given ϑ, $\vec{r}_0$ is the position vector of the geometric centre of the ellipse, ϑ_0 is the angle of rotation of the ellipse, a and b are the ellipse axes, as shown in Figure 2.4. The size parameter of the ellipse is defined as $a^2 + b^2$. The ellipse is considered to be inside the CF if all the voxels intersected by the ellipse have an electron density not lower than the threshold 0.4 Å^{-3}. This value was chosen arbitrarily as smaller than the CF electron density giving the best fitting results and it can be adjusted to the needs of a specific case. As a result, the algorithm returns a set of parameters for each slice: a, b, ϑ_0, $\vec{r}_0$.

- The lengths of the axes and the ellipse rotation angle are calculated as mean values of a, b and ϑ_0 from all 2D slices. The centre position is calibrated using a linear fit of $\vec{r}_0$ as a function of the z coordinate of each slice.
- The distance from the ellipse edge is assigned to each voxel for the purposes of further spatial image analysis, which constitutes a so-called distance map.

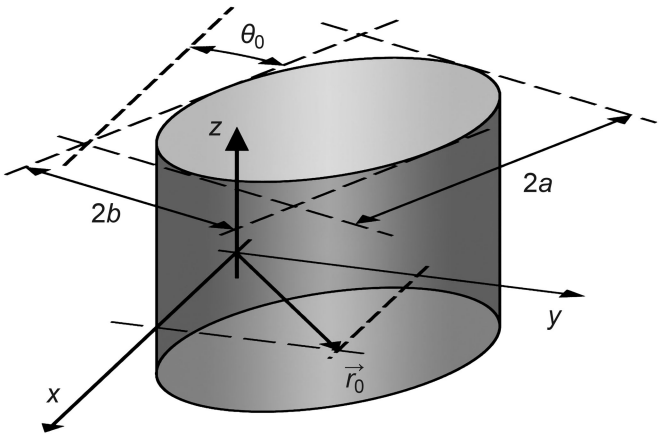

Figure 2.4. Illustration of the geometric parameters of the fibre orientation and dimensions discussed in section 2.3.3. The cylinder represents the fibre surface. The xy plane is the plane of tomography slices, whereas the z axis is the axis of rotation. The fibre axis is deviated from z by not more than 1°.

If the CF axis was significantly deviated from the perpendicular to the map axis z, it would be necessary to account for this deviation in the analysis. However, in practice this angle never deviated from the parallel by more than 1°, therefore it was convenient to assume that the fibre axis is perpendicular to the slices. Such an approximation introduced a maximum relative systematic error in the x, y coordinates within each slice of $1/\cos(1°)-1 \approx 2\times10^{-4}$. The corresponding spatial error is estimated by multiplication of the nominal radius of the CF of 3.5 μm by the relative error, giving 0.7 nm. This value is much smaller than the spatial resolution of about 50 nm, therefore we claim that the approximation does not yield a significant error of voxel positions within each slice. However, because the distance between the extreme tomography slices is as large as 8.2 μm, the subtle tilt of the fibre axis leads to a maximum shift between the CF cross sections of 8.2 μm·tan1°≈140 nm, which is already significant. Therefore, for the purposes of the analysis, the only necessary transformation was the calibration of the centre of the elliptical CF cross sections. Effectively, the distances of each voxel from the ellipse edges can be considered as the distances from the cylinder wall and a 3D distance map is obtained.

2.3.4. Histograms of electron density

To investigate the presence of iron within the carbon fibre with and without the alumina protection film, it is necessary to analyse the electron density distributions. The histograms of voxels from 650 tomographic slices corresponding to 8.2 µm long fragments of CFs with and without the thin alumina film have been prepared as a function of electron density and distance from the CF edge, namely depth into the CF, and are shown in Figure 2.5.

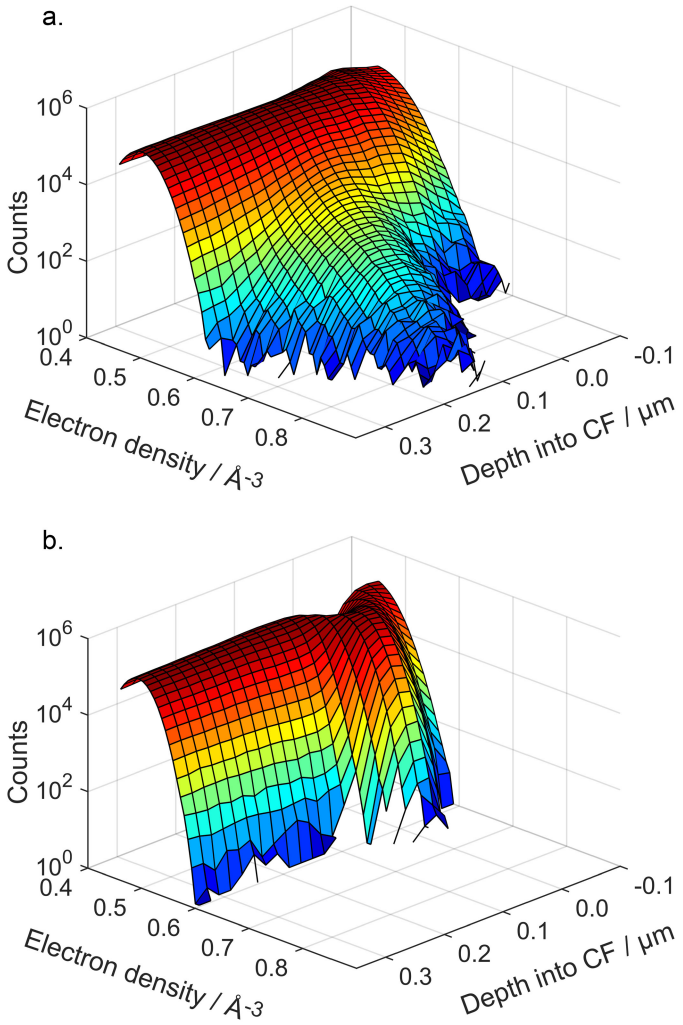

Figure 2.5. Sample without (a) and with (b) a 12 nm thick protective alumina film - surface plots of histograms of voxels versus depth into CF and electron density. A high electron density shoulder is visible only for the unprotected CF, which is related to presence of iron below its surface.

Although iron has a nominal electron density of 2.21 $Å^{-3}$, in the histograms we cannot explicitly resolve any high electron density peak that would correspond to such a high value. This is due to the fact that the size of the NPs is below the resolution of the 3D image. Physically, iron NP constitutes a highly localised spot of elevated electron density with respect to the surrounding body of a CF. Due to the resolution limitation, the image of the original physical object is smoothened with a so-called point spread function (PSF). Effectively, if the PSF width is comparable to- or greater than the NP diameter, the high electron density values are not even present in the images. Instead, in the histogram of the unprotected carbon fibre one can notice an effect of a long shoulder reaching elevated electron densities up to about 0.9 $Å^{-3}$ at depths around 0.1 µm. Such an effect was not observed for the protected CF or at depths greater than 0.3 µm for the unprotected CF, therefore we reason that it represents the abundance of iron NPs. In the following we introduce a methodology that allows investigating

the size distribution of NPs as a function of the depth into the CF, despite the fact that they are unresolved in the measurement.

2.3.5. Assessment of the resolution blur from PXCT data

Although the voxel size is 12.62 nm, the effective resolution of the 3D images acquired by PXCT is about 50 nm, limited by the density contrast of the features within the sample and by the dose, which limits the maximum angle of the X-rays scattered and measured with sufficient signal-to-noise ratio. Besides the voxel size and electron density noise, we include the effect of a PSF which accounts for this resolution limit. All three mentioned factors result in the resolution of 50 nm estimated using the Fourier shell correlation of two subtomograms with a half-bit threshold as described in [118]. Even though the measurement resolution is defined, an explicit form of the point spread function that blurs the image in our measurements remains unknown and its estimate is crucial for the further analysis of the abundance of the unresolved iron NPs.

In order to investigate the behaviour of the point spread function in the plane perpendicular to the rotation axis, we examined the electron density profile at a well-defined interface between the carbon fibre and the 500 nm alumina film. We have evaluated a mean cross section along 650 slices and extracted an electron density profile as a function of the depth into the CF. Assuming that the interface is locally flat and sharp, one can extract the profile of one-dimensional PSF

$$p(x) = \int_{-\infty}^{\infty} h(x-\tau)\mathrm{PSF}(\tau)\mathrm{d}\tau = \int_{-\infty}^{x} \mathrm{PSF}(\tau)\mathrm{d}\tau \Rightarrow \mathrm{PSF}(x) = \frac{\mathrm{d}}{\mathrm{d}x}p(x), \qquad (2.3)$$

where $p(x)$ is the measured edge profile and $h(x)$ is the Heaviside step function. It needs to be pointed out that because the PSF is a three-dimensional function, such a way of extracting the PSF does not produce an explicit curve, but is rather useful to qualitatively examine the general behaviour of the function in the radial direction. The results are shown in Figure 2.6. The profile in the figure has been obtained as mean values of electron density of all the voxels of the 3D map that fall spatially within the range of depths into the CF between x_i-Δ/4 and x_i+Δ/4, where i indexes the points of the graph and Δ is the PXCT cubic voxel size equal 12.61 nm. The derivative has been calculated using a five-point numerical differentiation. The result shows that, although there are ripples visible in the PSF, it might be well described with a Gaussian of standard deviation equal to 31.04±0.34 nm. The ripples may be neglected since in the case of the barely resolved iron NPs, they generate deviations in electron density well below the noise level.

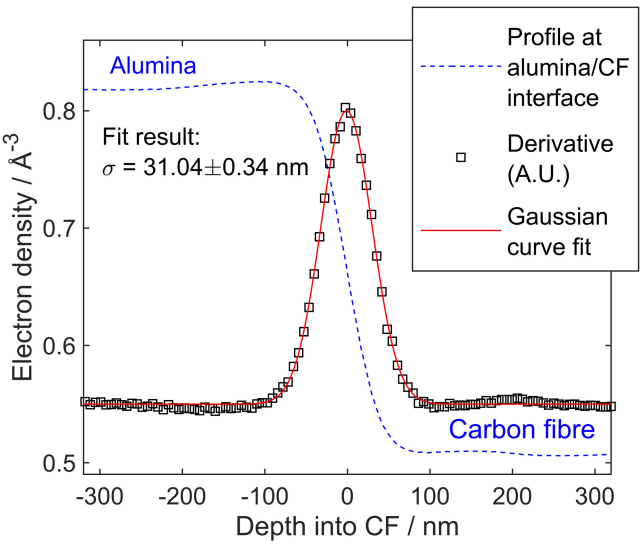

Figure 2.6. Electron density profile of the interface between CF and alumina on the sample coated with 500 nm alumina (blue dashed line) and its derivative representing the rough estimate of the point spread function in lateral direction (black squares) along with the Gaussian curve fit (red solid line). The derivative is scaled in arbitrary units and translated to fit in the graph.

Because of the rotational character of the measurement and tomographic reconstruction procedure, an anisotropy of resolution between the radial and the axial direction might appear. In order to estimate the axial blur and crosscheck the value of the radial blur, we introduce an approach that relies on analysis of features significantly larger than the experimental resolution. In the tomograms of the hairy fibres one can notice several ball-shaped structures of diameter ~500 nm of a uniform electron density slightly lower than the one of the CF, see Figure 2.7. We have used such features to assess the blur in three dimensions assuming that the PSF is estimated by a 3D radial-symmetric Gaussian kernel defined as

$$G(r,z) = \frac{1}{(2\pi)^{3/2}\sigma_r^2\sigma_z}\exp\left(-\frac{r^2}{2\sigma_r^2}-\frac{z^2}{2\sigma_z^2}\right), \tag{2.4}$$

where σ_r and σ_z are the standard deviations of the Gaussian kernel in radial and axial directions, respectively. Effectively, an anisotropy in PSF between the radial and the axial direction of the blur is assumed.

The method relies on finding a closest reproduction of the experimental map of a given feature using an optimisation algorithm finding a minimum of the mean square deviation of a reproduced map from the experimental map. The mean square deviation is calculated in the following way:

i. Thresholding of the experimental map using an electron density threshold ϱ_T resulting in a 3D binary matrix.
ii. Multiplication of the binary matrix by a defined electron density ϱ.
iii. Convolution of the matrix with a 3D Gaussian with given σ_r and σ_z, resulting in a simulated map.
iv. Calculation of the mean square deviation of the simulated map from the experimental map.

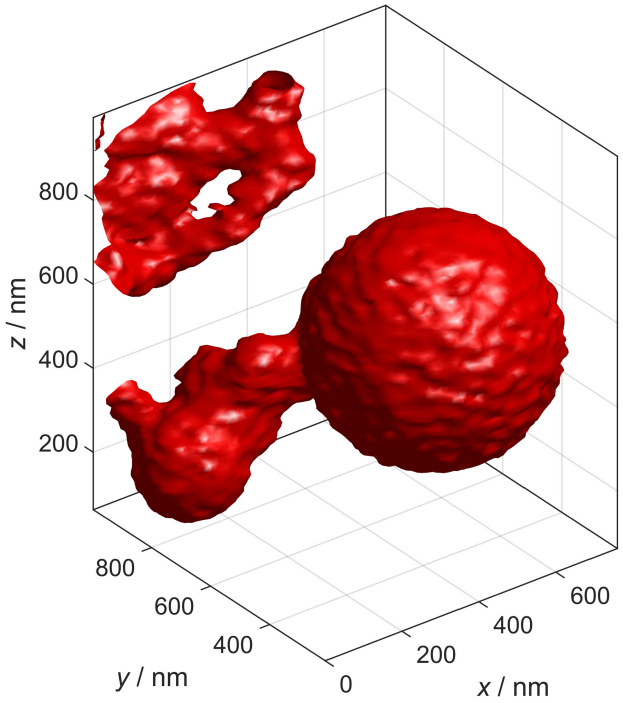

Figure 2.7. One of the spherical-shaped features found in an unprotected carbon fibre tomogram used for resolution assessment. An isosurface render is shown at an electron density of 0.2 Å^{-3}.

Effectively, the mean square deviation is a function of ϱ_T, ϱ, σ_r and σ_z and a minimum of this function is found using the `fminsearch()` function implemented in MATLAB and Optimization Toolbox Release 2016b, The MathWorks, Inc., Natick, Massachusetts, United States, relying on the simplex search method with 10^{-4} tolerance of the function value and arguments [125]. Effectively, ϱ_T, ϱ, σ_r and σ_z constitute a set of the fit parameters. Their initial values were set to 0.2 Å^{-3}, 0.4 Å^{-3}, 30 nm, 25 nm, respectively. The procedure was repeated for 11 extracted features resulting in a set of 11 corresponding σ_r and σ_z values. Effectively, σ_r=31.7±3.5 nm and σ_z=26.9±3.2 nm have been obtained, which represent mean values ± double standard deviation of the obtained value set. One slice of a representative feature image and its simulation using the parameters fitted to this particular feature is shown in Figure 2.8.

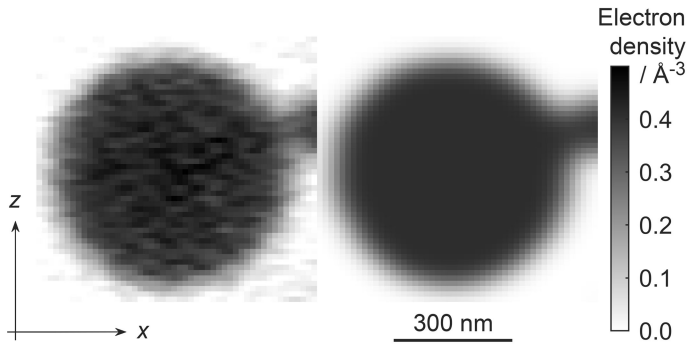

Figure 2.8. A representative slice of an example reproduction result; (a) the experimental map, (b) the map simulated using the resulting parameters after the fit to this particular feature: σ_r=30.9 nm, σ_z=27.3 nm, ϱ_T=0.19 Å^{-3}, ϱ=0.41 Å^{-3}.

There is a good agreement between the estimate of radial component of the blur obtained with this method and with the sharp interface profile analysis, which constitutes an ensuring cross-check of the blur value. A two-sample Kolmogorov-Smirnov test was carried out in order to verify

the hypothesis that σ_r and σ_z come from the same distribution. The hypothesis was rejected at a 5% significance level (p-value equal 6.6×10^{-6}), therefore we can say that the axial-radial anisotropy of the blur is significant and an anisotropic Gaussian blur needs to be applied for the following analysis.

2.3.6. Methodology of assessment of abundance of iron nanoparticles from PXCT 3D images

In order to assess the amount of iron infused into the CF we have developed a self-consistent algorithm that reproduces the experimental electron density distributions in a simulation. We assume that the resolution exhibits a Gaussian behaviour, which means that sharp physical features in the images are Gaussian-blurred with the radial σ_r and axial σ_z values estimated in section 2.3.5. The measurement noise is assumed to be Gaussian as well and it is added to the electron density of the voxels after the blur.

Initially, a set of maps of NPs of volumes v ranging from 0 to 15×10^4 nm^3 with a Δv=5×10^3 nm^3 increment is prepared. The NPs are assumed to be spherical and are defined by a step function with values ranging from 0, meaning lack of iron in a given voxel, to 1 meaning 100% of iron in the voxel. Each NP is defined on a Cartesian 3D grid with δ=3.155 nm voxel size being 4 times smaller than the experimental voxel size Δ. Each electron density map is a cube of volume V=252.4^3 nm^3 corresponding to the side equal $8\times\sigma_r$ of the radial component of the blur. The cubic map with a NP of v=0 corresponds to a cube of pure carbon fibre material. The electron density maps are numerically convolved with a three dimensional Gaussian kernel of radial σ_r=31.7 nm and axial σ_z=26.9 nm.

Having generated the set of maps of NPs of different sizes blurred with a given Gaussian function, we have defined a self-consistent algorithm that finds a distribution of iron NP volumes in the given volume of the experimental electron density map by reproducing the experimental electron density histogram in the simulation. The algorithm utilizes a random walk of the simulation parameters, namely the electron density of the CF ϱ_{CF}, the rms of the electron density noise and $f(x,v)$, which is the function that constitutes a distribution of NPs with respect to their volume v and depth into the CF x that need to be taken in order to produce the simulated electron density histogram resembling the experimental one presented in Figure 2.5a. The function is defined as

$$\mathrm{d}n(x,v) = f(x,v)\mathrm{d}x\mathrm{d}v, \tag{2.5}$$

where $\mathrm{d}n(x,v)$ is equal to the areal density of NPs of volumes $(v, v+\mathrm{d}v)$ within a slice of volume in a range of depths $(x, x+\mathrm{d}x)$. The distribution is related to the number of voxels being drawn randomly from a NP map

$$N_{\mathrm{drawn}}(x_i, v_j) = \left[VN_{\mathrm{H}}(x_i)\cdot f(x_i, v_j)\Delta v\right], \tag{2.6}$$

where the square bracket represents rounding, $N_{\mathrm{H}}(x_i)$ is the number of voxels of the experimental map taken to produce the histogram for a given x_i. The random draw is done in such a way that all the draws are independent. In other words the voxels drawn are allowed to repeat. The distribution f is kept normalised at all times so that the total number of voxels being randomly drawn is equal to $N_{\mathrm{H}}(x_i)$ at each depth x_i individually. When f is found, it can be used to determine the atomic concentration of iron with respect to the depth into the CF,

$$c(x) = \frac{d_{\mathrm{Fe}}N_{\mathrm{A}}}{\mu_{\mathrm{Fe}}}\int_0^{v_{\max}} vf(x,v)\mathrm{d}v, \tag{2.7}$$

where d_{Fe} is the mass density of iron, N_{A} is the Avogadro number, μ_{Fe} is the molar mass of iron, $v_{\max}$ is the maximum of the discrete mesh of NP volumes. Furthermore, to check how much of iron has infused into the CF during the process compared to the sputtered 5 nm iron film, one can calculate an equivalent film thickness

$$t \approx \int_0^{x_{\max}} \int_0^{v_{\max}} v f(x,v)\,\mathrm{d}x\mathrm{d}v, \tag{2.8}$$

where t is the equivalent film thickness, $x_{\max}$ is the maximum depth into the CF taken into consideration. The approximation in equation (2.8) holds when $x \ll \inf\{a^2/b, b^2/a\}$ because it has been derived assuming that the radius of curvature of the CF surface is much larger than x.

The initial values of the simulation parameters are arbitrary and they reflect the further convergence efficiency. The initial values of the parameters resulting in relatively fast convergence are listed in Table 2.3. In each random walk step the parameters are randomly altered in an arbitrary way. In the case of our algorithm, the parameters are multiplied by a log-normally distributed random number, $\mathrm{M_p}$, with the location parameter μ=1 and the scale parameter σ_{p}, ensuring that the multiplicator is always positive and close to 1,

$$\mathrm{M_p} \sim \ln\mathcal{N}\left(\mu = 1, \sigma_{\mathrm{p}}\right), \tag{2.9}$$

where p indexes the fitting parameter. The values of σ_{p} for each parameter taken in our algorithm are listed in the Table 2.3.

Table 2.3. Simulation parameters that undergo random walk, their initial values and scale parameters σ_{p} of a log-normally distributed random variable that multiplies the parameters in each iteration.

Parameter p	**Initial value**	**σ_{p} of step**
ϱ_{CF}	0.5 Å^{-3}	2.0×10^{-3}
rms	0.025 Å^{-3}	1.0×10^{-2}
f	$\propto$exp (-v/3)	3.5×10^{-1}

In order to convert the drawn voxels to electron density, we use a scaling function and add noise

$$\varrho_{\mathrm{drawn}} = (\varrho_{\mathrm{Fe}} - \varrho_{\mathrm{CF}}) \cdot I + \varrho_{\mathrm{CF}} + \mathrm{noise}, \qquad \mathrm{noise} \sim \mathcal{N}(\mu = 0, \mathrm{rms}) \tag{2.10}$$

where ϱ_{drawn} is the resulting electron density of a given drawn voxel, ϱ_{Fe}, ϱ_{CF} are the electron density of iron and carbon fibre, respectively, I is the value of a drawn voxel. A histogram of one range of depths $(x - \Delta x/2, x + \Delta x/2)$ is fitted at a time, where Δx=20 nm is the depth bin width. In each step all the simulation parameters are altered. The new set of parameters is accepted if an optimisation function returns a lower value than the previous one. The optimisation function is defined as

$$\mathrm{opt} = \frac{\sum_k \left(\left(H_{\mathrm{e}}(k) - H_{\mathrm{s}}(k)\right)^2 \cdot \left(H_{\mathrm{e}}(k)\right)^{-1}\right)}{\sum_k \left(H_{\mathrm{e}}(k)\right)^{-1}}, \tag{2.11}$$

where $H_e(k)$ and $H_s(k)$ are the experimental and simulated histogram bins, respectively, of the k-th electron density. The optimisation function has a meaning of a weighted average of squares of deviations of a simulated histogram from an experimental histogram, where the weights are equal to the inverse of the number of counts of the k-th bin of the experimental histogram. The weights were chosen in such a way in order to account for the expected dispersion of the number of counts. It is known that if the measurement points are not correlated, the fitting procedure minimfs the uncertainty of the parameter estimators when the weights are defined as inverses of variances of each measurement. It is assumed that the distribution of counts is Poissonian with mean equal to variance and defined as λ. Therefore, since the number of counts $H_e(k)$ is a good estimate of λ, the choice of weight $\lambda^{-1} \approx (H_e(k))^{-1}$ is justified. Only the bins with non-zero number of counts at both histograms are taken into the convergence evaluation to avoid division by zero. The convergence criterion is arbitrary and we have defined it as $opt < 10^{-4}$, which has given a satisfactory convergence of the histograms.

2.3.7. Results and discussion of nanoparticle abundance assessment from PXCT data

Figure 2.9 presents an example of histogram fitting results for the depth range between 110 nm and 130 nm, where the electron density shoulder is the most pronounced.

The fitting procedure has been repeated 50 times in order to get the statistical measure of an error. Figure 2.9a shows an experimental histogram along with the simulated histogram, whereas Figure 2.9b presents the corresponding fitted NP volume distribution f. Both fitted curves represent the geometric mean, whereas the 95% confidence intervals in both cases represent a double geometric standard deviation, namely,

$$U, D = \exp\left(\overline{\log X} \pm 2\sqrt{\overline{\left(\log X - \overline{\log X}\right)^2}}\right), \tag{2.12}$$

where X is the sample element, U and D are the upper and lower bounds of the confidence interval, respectively, whereas the bar represents a mean value. Geometric statistics has been chosen, since it is more representative for the data on logarithmic scale. In Figure 2.9a the lower histogram bins appear to have a greater spread. On a logarithmic scale the magnitude of spread corresponds to the relative error of measurement. It remains in agreement with the assumption of Poissonian-distributed number of bin counts, which has a relative error equal to the inverse of the square root of number of counts. Figure 2.10 shows the full distribution $f(x, v)$ of iron NPs. It can be seen that at large depths there is a sharp peak at volume $v \approx 0$. It is expected, because it corresponds to a vast dominance of pure carbon fibre material and it means that barely any NPs of any size are detected at depths larger than 300 nm. At the range of depths from 75 nm to 125 nm however, there appears an island of iron NPs of volumes $\sim 3.5 \times 10^4$ nm^3, corresponding to a diameter of 40 nm, whereas in other regions NPs of smaller diameter dominate. This result is in good agreement with SEM measurements, one of them shown in Figure 2.2, where the NP size has been determined to fall within a range between 20 nm and 40 nm. This agreement indicates that the methodology applied for the NP distribution assessment is accurate.

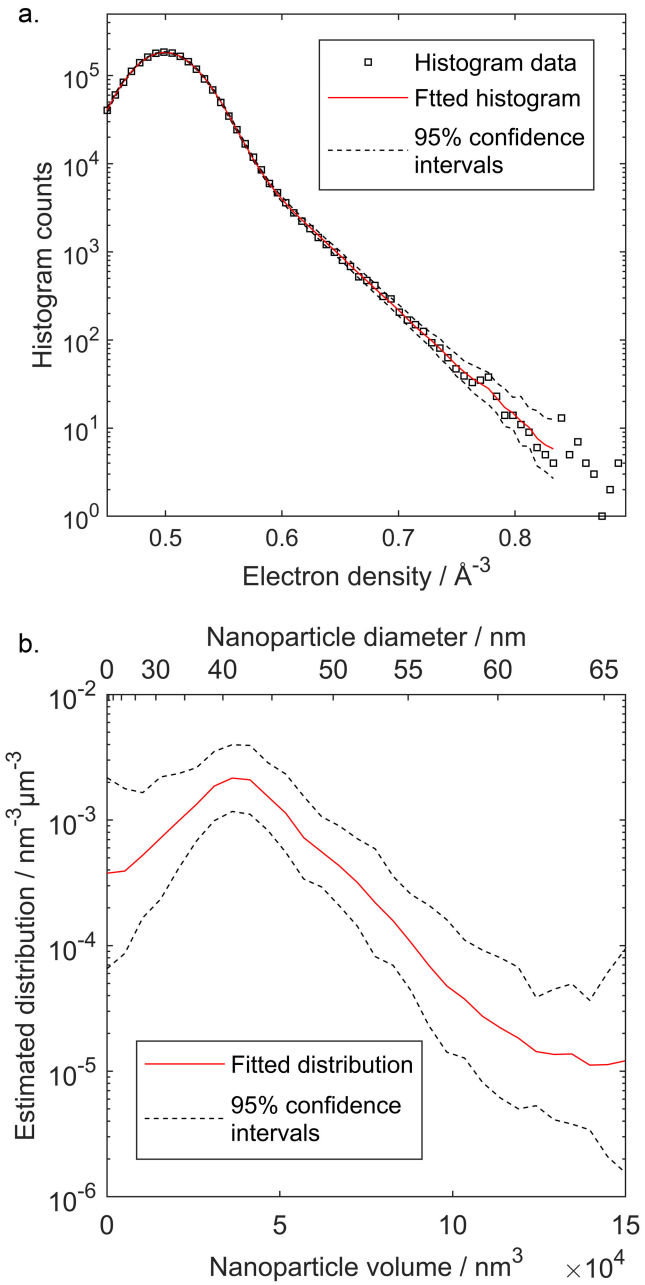

Figure 2.9. The result of the fitting procedure; (a) experimental histogram of electron density voxels in the range between 110 nm and 130 nm (black open squares) and the simulated curve (red solid line); (b) the corresponding NP volume distribution (red solid line). A NP diameter axis corresponding to the volume axis is added at the top of the graph. In both cases, the black dashed lines stand for the 95% confidence intervals.

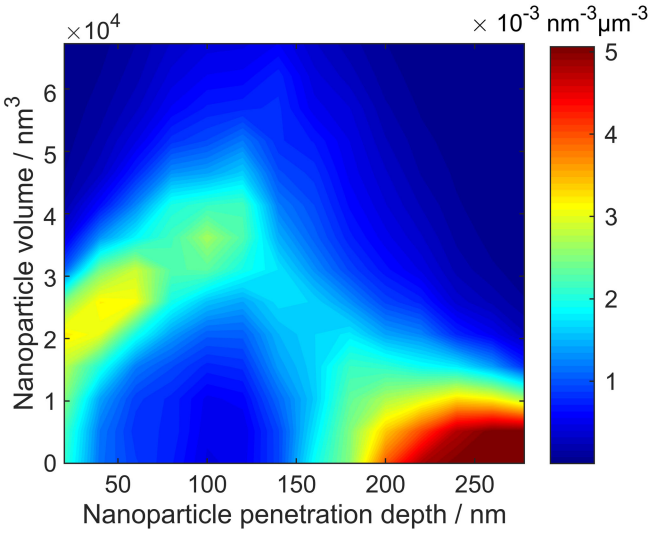

Figure 2.10. Iron NP distribution with respect to NP volume and depth into the CF from PXCT data analysis. The 2D distribution describes number of NPs per nm^3 of NP volume and per μm^3 of the sample volume. The position of the peak of the distribution is visibly elevated at depths around 100 nm, which reflects the presence of NPs of largest size in this region. Colour coding reaches values up to 5×10^{-3} $nm^{-3}\mu m^{-3}$ to emphasise the relevant features.

Figure 2.11 shows a graph of the iron atomic concentration versus depth into the CF calculated using equation (2.7). Error bars represent a double standard deviation. From the graph it is clear that there is a measurable amount of iron below the surface of CF. The concentration curve is a peak curve with the centre at about 100 nm below the CF surface and width of about 150 nm, which is considerably larger than the resolution. Therefore it can be reasoned that the NPs have penetrated the CF significantly during the CNT growth processing. The iron film thickness equivalent to the amount of iron detected within the fibre volume has been evaluated using equation (2.8), obtaining a value t=5.42±0.31 Å. It constitutes a significant fraction of the 5 nm-thick sputtered film (greater than 10%), especially taking into account that the 5 nm is merely a peak value, as the sputtering - being a field-of-view coating technique - has been performed only from two sides of a fibre and the actual sputtered thickness averaged over the CF surface is smaller. It means that not only does the iron cause defects penetrating into the CF, but also the penetration itself depletes the total amount of iron that should have been physically accessible on the surface for CNT growth and, effectively, the growth efficiency may decrease.

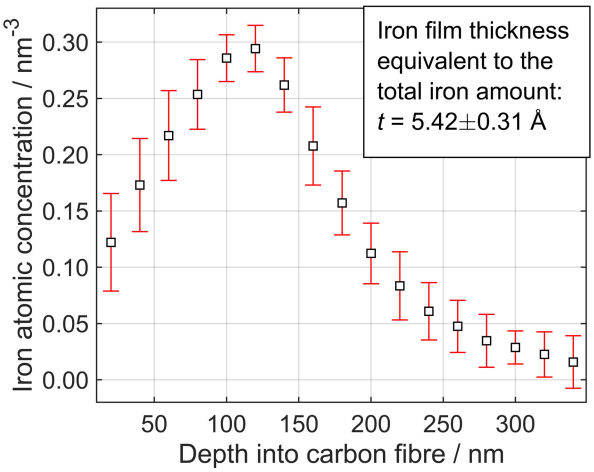

Figure 2.11. Iron atomic concentration versus depth into the CF calculated from the distribution of iron NPs estimated from data extracted from PXCT.

The observation of iron NPs within the fibre indeed proves the hypothesis that the NP volumetric diffusion occurs during a direct growth of CNTs. However, it also raises a question why such a phenomenon occurs. It does not seem to be a typical diffusion of iron within the carbon fibre, because the material of the NPs seems to be localised instead of being diffusively blurred. Therefore we hypothesise that the fundamental mechanism of the phenomenon is the carbon diffusion within iron that drives the NP transport within the carbonaceous body of the fibre. This is supported by the fact that carbon is soluble in iron and volumetric carbon diffusion through a metallic NP is a crucial element of both tip- and root growth of multiwall CNTs [107]. It has been observed that the choice of different catalyst systems such as Fe-Cu [79] or Fe-Ni [76] mixtures instead of pure iron minimises the etching into carbon. We believe that the methodology of data analysis introduced in this work allows for a direct quantitative assessment of the etching in the mentioned systems as well as in the ones that will be developed in the future. It can lead to a better fundamental understanding of the process and provides a new insight into the process optimisation.

2.3.8. Validation of PXCT data analysis results by means of scanning transmission electron microscopy and energy-dispersive X-ray spectroscopy

The results of PXCT imaging data analysis were cross-checked with STEM and EDX. Both have been carried out in the Helios NanoLab™ 650 FIB/SEM. Slices of CF samples of ~100 nm thickness prepared by FIB cutting were examined. The two critical samples were analysed: the unprotected- and 12 nm-alumina-protected CF.

STEM examination has been conducted to confirm the conclusions from PXCT. Bright field (BF) images at 30 kV electron acceleration voltage have revealed the positions and shapes of NPs by reduced intensity, see Figure 2.12. The resolution of STEM was much higher than that of PXCT and the edges of NPs are resolved, therefore a straightforward image analysis can be applied. From the STEM images it is clearly seen, that the iron nanoparticles are indeed localised instead of being diffusively blurred, which supports the hypothesis of diffusion of iron NPs driven by carbon diffusion through a NP. In the case of the unprotected CF, the NPs were present both below and over the CF surface in the CNTs, see Figure 2.12a. As expected, the protected CF sample exhibited no presence of NPs below its surface, only above it within the grown CNTs, which remains in agreement with the PXCT results, see Figure 2.12b.

Furthermore, the two-dimensional volume-penetration depth distribution has been estimated from the STEM data, see Figure 2.13. The particle sizes have been extracted using ImageJ software with a built-in particle analysis tool. Prior to particle analysis, the image has been processed in ImageJ with background subtraction and thresholding. As a result, the algorithm returns particle areas. In the further analysis it is assumed, that the NPs are spherical. Due to a low number of particles available for analysis, the distribution has been estimated using a kernel probability density estimation function `ksdensity()` based on the method described in [126] available in MATLAB and Statistics and Machine Learning Toolbox Release 2016b, The MathWorks, Inc., Natick, Massachusetts, United States. The default smoothing parameter was chosen, being proven to be optimum for normal distributions. Compared to the analogous distribution extracted from PXCT (Figure 2.10), a main difference is the appearance of a high peak at volume ~10^4 nm^3 and depth ~75 nm. This volume corresponds to NP diameter of ~25 nm, which is half of the resolution of PXCT. It can be explained by the fact, that in this region of depths the concentration of small NPs gets very large, as seen in STEM images (Figure 2.12a) and there is a high chance that multiple NPs fall as close together as PXCT resolution. Therefore the NP agglomerates could have been interpreted by the 3D image analysis as a lower quantity of larger NPs. This phenomenon constitutes a limitation of the 3D image analysis

methodology developed in this work, as the algorithm assumes that NPs are well separated from each other, however it does not significantly alter the total amount of iron estimated as a result. This statement is supported by simulations, as discussed in Appendix A.3.

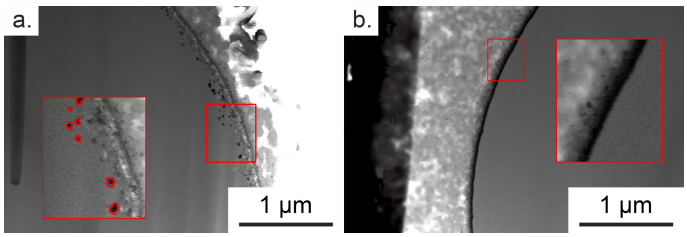

Figure 2.12. Thin BF STEM images performed on thin CF slices; (a) unprotected fibre; (b) 12 nm-alumina protected fibre. We can observe spots of reduced intensity, which correspond to iron NPs. The insets show magnifications of the relevant regions; additionally, edges of NPs are shown as extracted using ImageJ, several NPs were ignored because of ambiguity due to of overlapping or low contrast.

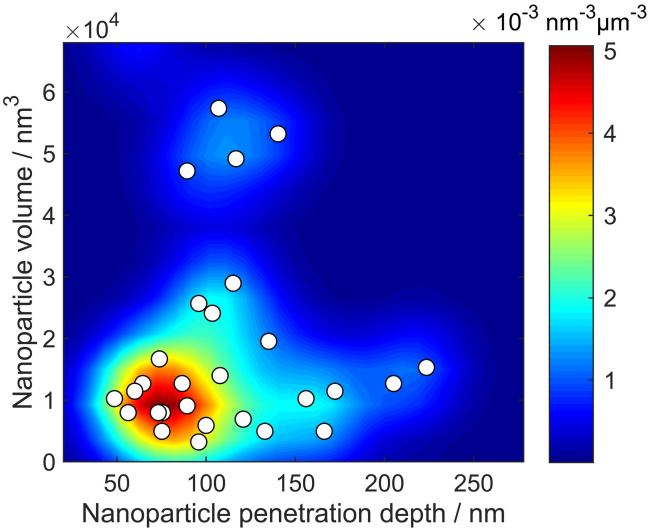

Figure 2.13. Nanoparticle volume-penetration depth measurement points from STEM image analysis for the unprotected CF (white filled circles) and the corresponding distribution approximated using two-dimensional kernel density estimation (colourful contour plot); for comparison with Figure 2.10.

The iron atomic concentration versus depth has been numerically evaluated from the NP volume-position data, see Figure 2.14. Numerical integration assumed spherical shapes of iron NPs and an average CF slice thickness of approximately 100 nm. The data extracted from PXCT is shown for comparison. The agreement is well pronounced. The positions of the peak of iron concentration are very close and the decay with increasing depth behaves similarly. The spread of the distribution from PXCT is noticeably larger, however it can correspond to the NP position uncertainty originating from the 50 nm resolution of PXCT. The differences between the two curves of iron atomic concentration may also arise from a vast discrepancy of statistical sampling between the two methods. The PXCT analysis has been carried out on ~8.2 µm long CF, whereas the STEM only on a ~100 nm thick CF slice. Moreover, the thickness of CF slice for STEM is already of the order of magnitude of the NP size, therefore a substantial number of NPs could have been cut with a FIB effectively exhibiting a smaller diameter than prior to processing.

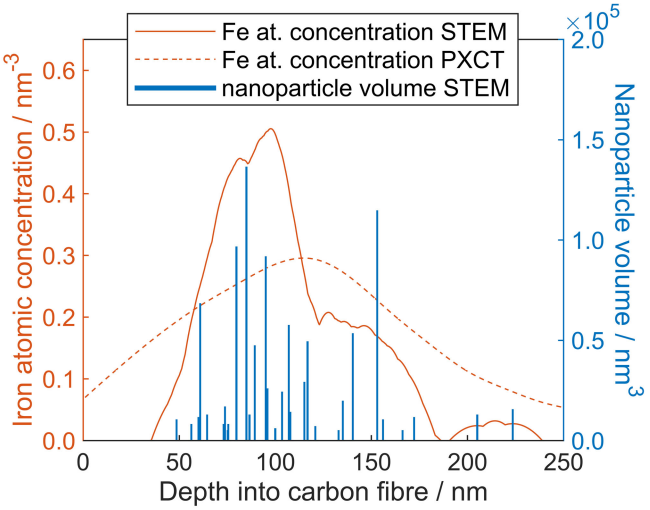

Figure 2.14. NP volume obtained from STEM image analysis (black solid bars), iron atomic concentration evaluated from NP volume from STEM data assuming spherical NPs (red solid line) and iron atomic concentration extracted from PXCT data for the purpose of comparison (blue dashed line). All data are plotted as a function of the depth into the CF

EDX has been conducted to examine the elemental composition of the specific nanoscale features of the samples. The results are treated qualitatively, because quantification is substantially sensitive to a precise knowledge of the geometry that is not available in this study. Nonetheless, the results provide the information critical to confirm the conclusions obtained with the PXCT analysis. In the case of the unprotected CF, EDX has been carried out on three regions of interest (ROIs): the inside of the fibre (control) and on two iron NPs below the surface. The largest NPs found in the SEM image were examined (diameters 53±2 nm and 40±2 nm of nanoparticle 1 and 2, respectively, see: Figure A.2 in Appendix A.2). In the case of the protected CF, two ROIs were examined: the inside of the fibre (control), and alumina film with no NPs. For EDX a 3 kV acceleration voltage was chosen, which allowed to examine all the relevant elements present in the samples. The examination has revealed that the NPs are indeed composed of iron and also partially of oxygen. This is concluded from the increased intensity of the iron and oxygen peaks for the case of ROIs with NPs in reference to the control, see Figure 2.15a. Since the CNT growth has been carried out in a reducing hydrogen atmosphere and the NPs are well-embedded within the CF or CNTs, it is possible that iron got oxidised in the ambient atmosphere after the FIB cut. As expected, the ROI of the CF with a protective alumina film exhibits elevated intensities of aluminium and oxygen peaks, see Figure 2.15b. We note that the EDX measurements on these ROIs caused a change in the appearance of these regions in the SEM image in Figure A.2 in Appendix A.2, which is discussed therein.

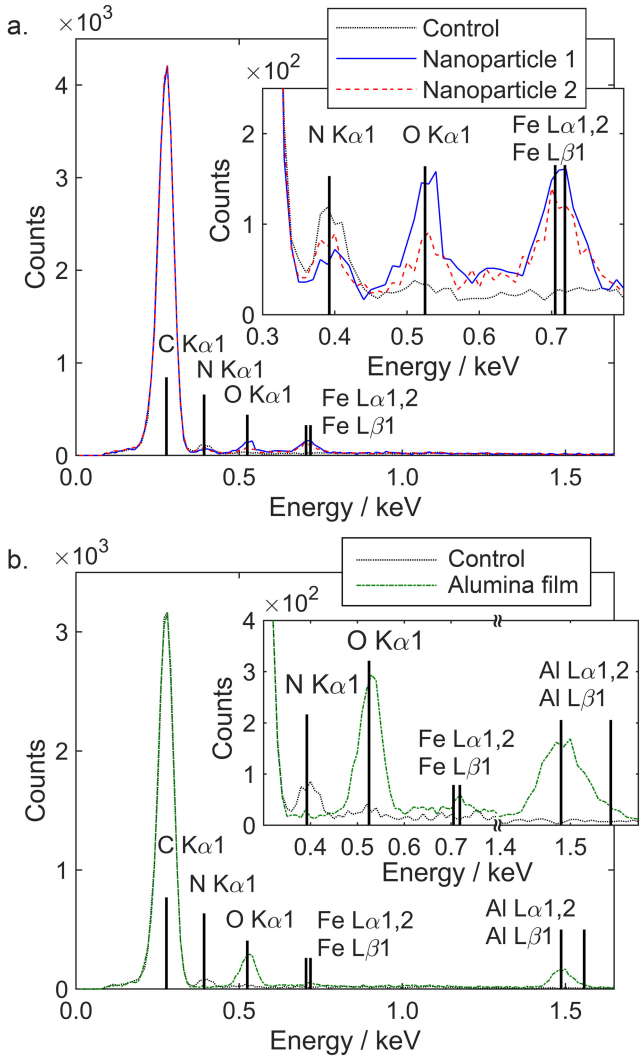

Figure 2.15. EDX spectra of the (a) unprotected and (b) 12 nm alumina protected CF at different ROIs: control (black dotted line), nanoparticle 1 (blue solid line), nanoparticle 2 (red dashed line), alumina layer (green dash-dotted line). The nominal positions of X-ray emission peaks are indicated by vertical solid black lines. The insets show magnifications of the most relevant peaks. The positions of ROIs corresponding to the spectra in the graph (a) are indicated in Figure A.2 in Appendix A.2.

2.3.9. Comparison between the PXCT and the FIB/STEM/EDX approaches

We have successfully verified the results and conclusions of PXCT data analysis by FIB/STEM/EDX investigation. It was only possible thanks to the advantages of the latter approach. The first one is the possibility of direct identification of elements as opposed to PXCT, which identifies only average local electron density. The other advantages are a high resolution down to several nanometres as compared to 50 nm resolution of PXCT and the relatively high availability of the equipment, as PXCT is performed on synchrotrons. On the other hand, using PXCT has enabled us to obtain data of a high statistical content non-destructively, coming from a large uninterrupted volume of CF that is not possible to probe with the other approach. The other reason for us to use PXCT was the simplicity of sample preparation. Furthermore, we have developed an algorithm that is able to overcome the limitations of the resolution of the PXCT method to a great extent.

From our experience, we recommend using PXCT on microfibres when a large volume of the fibre should be analysed, when a destructive method is unacceptable and especially when the interesting features of the samples are at a scale of more than the PXCT resolution. Alternatively, we would

recommend the FIB/STEM/EDX approach in the cases when a low information volume is satisfactory, when elemental analysis is crucial and if the high resolution is required to resolve fine features of the sample.

2.4. Summary and conclusion

In this work we introduce a methodology for the assessment of iron NP size distribution within CFs based on electron density histograms and successfully apply it. The methodology relies on a self-consistent algorithm overcoming the obstacle that the NPs are not resolved in the measurement, which might be useful in other studies of features of size below the measurement resolution. The data analysis shows that, in the case of the unprotected carbon fibre, NPs of diameter around 40 nm are present at a depth of about 100 nm below the fibre surface. In the case of a CF protected with a 12 nm alumina film prior to growth, we do not observe any presence of iron below the fibre surface. We have verified the conclusions of PXCT imaging and data analysis conducting STEM and EDX examination, which provided a substantial reassurance both on the PXCT results and on the novel 3D image analysis methodology. Therefore, in this work we confirm that such an ultrathin film constitutes a sufficient barrier against iron infiltration in the growth process of CNTs on CF, effectively blocking the further defect formation. This explains the preservation of mechanical strength observed in our recent study [90]. The data analysis methodology can be applied to evaluate the efficiency of other etching-preventing solutions such as the ones introduced in Refs. [76,79] or in future methods. We state a hypothesis that the transport of NPs within the bulk of CFs is driven by diffusion of carbon through each NP, which is why the NPs retain the integrity instead of getting diffusively dissolved in the body of CF. The results obtained improve the understanding of the mechanical properties of carbon fibres after processing and constitute a significant step in the development of hierarchical composites.

Acknowledgements

We would like to thank Dr. Manuel Guizar-Sicairos from the Paul Scherrer Institute for discussions and sharing his expertise in the resolution-limiting effects occurring in PXCT imaging. We would also like to thank the crew of Nano Imaging Lab at University of Basel for consultation on the strategy for the verification of the PXCT results, especially Daniel Mathys with whom the FIB/STEM/EDX examination has been carried out. We also acknowledge the Swiss Nanoscience Institute at University of Basel for funding this research (SNI PhD project P1402).

Chapter 3

Mechanical improvement of the alumina – CF interface

"Obstacles cannot crush me;
every obstacle yields to stern resolve."

Leonardo da Vinci

This chapter is based on our published work W. Szmyt, M. Calame, C. Padeste, C. Dransfeld, in: Proc. ICCM22 - 22nd Int. Conf. Compos. Mater., Melbourne, Australia, 2019, © Engineers Australia.

Wojciech Szmyt contributed to this work with conceptualisation, methodology, formal analysis, experimental investigations, writing of the original draft and visualisation of the data. **Michel Calame** provided the resources (access to infrastructure), assisted with manuscript review and study supervision. **Celestino Padeste** took part in conceptualisation, manuscript review and study supervision. **Clemens Dransfeld** participated in conceptualisation, manuscript review, study supervision, carried out project administration and funding acquisition.

Abstract

We aim to synthesise carbon nanotubes (CNTs) on carbon fibre (CF) to obtain a hierarchical composite of improved mechanical performance as compared to classical CF-based composites. A 12 nm thick aluminium oxide film applied by atomic layer deposition (ALD) provides protection of the CF from deterioration during CNT growth in a chemical vapour deposition (CVD) process. However, the adhesion of alumina to CF, grown in a classical water/trimethylaluminium ALD is severely diminishing during CNT growth, as detected by interface shear strength (IFSS) measurements. In our approach to improve the CF-alumina adhesion, we employed a pre-treatment of the CF with ozone and entirely replaced water with ozone in the ALD process, to promote the covalent bonding of the alumina to the CF surface. The current results show a new perspective in achieving the CNT synthesis on the CF while successfully mitigating its detrimental effects on the fibre mechanical properties.

3.1. Introduction

Modern high-performance structural parts are often made of carbon fibre (CF)-reinforced plastics due to their excellent mechanical properties and low weight. Their mechanical advantages are well-pronounced mainly in the fibre direction, dominated by the CF properties. However, in the direction perpendicular to the fibre or upon shear loading, the mechanical performance is significantly weaker, governed by the properties of the polymer matrix and fibre-matrix interface in particular.

We aim to significantly enhance the fibre-matrix interface by synthesizing carbon nanotubes (CNTs) directly on the surface of the CF, thus creating a hierarchical composite (see: Figure 3.1). The CNTs exhibit outstanding mechanical properties, which makes them a great choice for the nanoscale reinforcement. We are synthesizing CNTs directly on the CF in an aligned and dense manner. This approach results in the higher load and alignment of CNTs in the matrix between the fibres as compared to other approaches, e.g. CNT dispersion in the matrix or grafting of CNTs onto CF using electrophoresis [95]. Moreover, owing to the outstanding heat- and electrical conductivity of the CNTs, the incorporation of CNTs in the matrix results in a significant increase in the conductivities of the composite [95] desirable in many applications.

There are many challenges in the development of the hierarchical composite. It has been shown, that in the chemical vapour deposition (CVD) process of CNT synthesis, the CF mechanical properties are severely deteriorated [100]. We have identified that the migration of the iron catalyst nanoparticles into CF in is a phenomenon significantly contributing to this process. We have also established that a 12 nm thick aluminium oxide film provides a sufficient diffusion barrier, ensuring the protection of the CF in the harsh CVD conditions [90,127]. We have however found that the adhesion of the alumina to the CF, measured as interfacial shear strength (IFSS), diminishes substantially at the high-temperature CNT synthesis conditions [90]. This issue is addressed in this study.

To ensure a good adhesion of the protective alumina film to the CF, we developed a process that results in covalent bonding between the film and the fibre. For this purpose, we modified the atomic layer deposition (ALD) process used to coat the CF with alumina. In the classical ALD alumina film synthesis, one alternately exposes the substrates to vapours of water and trimethylaluminium (TMA), forming an extremely uniform layer of aluminium oxide with atomic precision control of thickness. This process is referred to as "TMA+H_2O" in this work. In the new approach, we employed a pre-treatment of CF with ozone and we entirely replaced water with ozone in the ALD process in order to promote the covalent bonding not only at defect sites of the graphitic CF surface, but also uniformly over its entire surface. In this work, we are referring to this ALD configuration as "TMA+O_3".

So far, we have been testing the IFSS between alumina and CFs by means of single fibre fragmentation tests as described earlier [90]. In this study, we employed a different micromechanical testing approach - the single fibre pull-out test. We found it to be vastly more efficient with large sample sets when an automated embedding and testing system is employed (FIMATEST by Textechno Herbert Stein GmbH & Co. KG, Germany [128]). In order to elucidate the particular mechanisms of failure, the pulled-out fibre tips were analysed by means of scanning electron microscopy (SEM) and energy-dispersive X-ray spectroscopy (EDX).

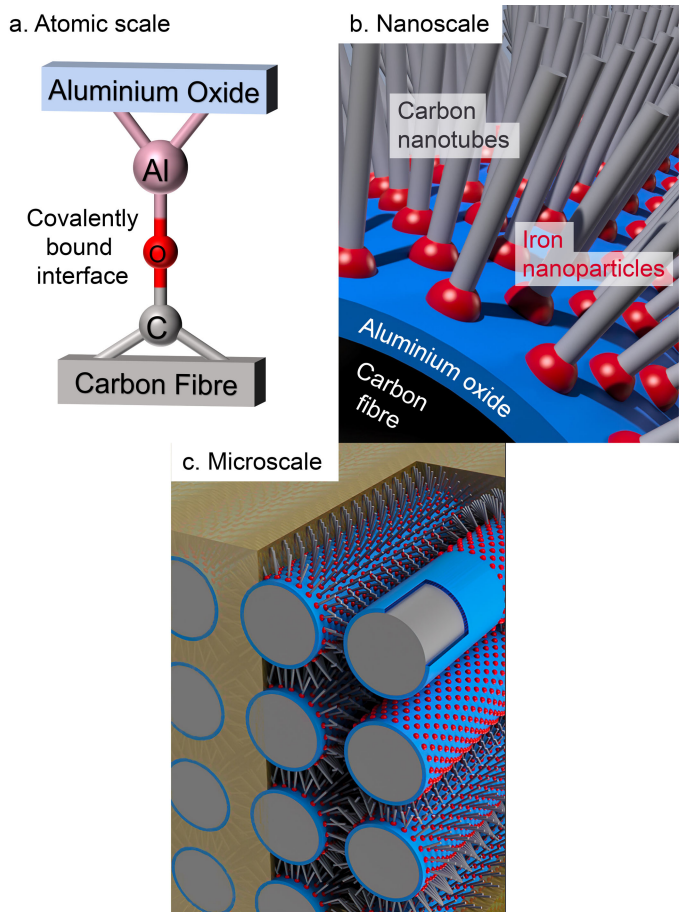

Figure 3.1. Schematic illustration of the scales of the hierarchical composite; a. atomic scale, where the chemical bonds between the constituents are considered – the CF-alumina interface is illustrated; b. nanoscale, where the formation of catalyst nanoparticles and, subsequently, CNTs takes place; c. microscale, where impregnation of the CNT-grafted CFs with epoxy occurs.

3.2. Experimental

3.2.1. Sample preparation and processing

Single PAN-based unsized CFs (HexTow® 12k AS4 by Hexcel®) of ca. 110 cm length and of 7.1 μm diameter were carefully separated from the continuous tow and wound around 65 mm × 65 mm quartz frames for further processing (see: Figure 3.2a). During the winding, the fibres were kept under tension of 0.9 GPa (20% of the ultimate fibre tensile strength) provided by a 3.6 g weight attached to the free fibre end while winding. The CFs were stabilised on the quartz frames with a ceramic adhesive that sustains temperatures up to 1400 °C. The fibres were afterwards heat-treated in air for 2 h at 400 °C in order to burn off any possible residues of sizing or other impurities and underwent 10 min room-temperature UV-ozone cleaning in air. Subsequently, ALD coating with alumina was done at two different configurations (TMA+H_2O and TMA+O_3). Alumina-coated CFs were afterwards heat-treated at various temperatures in a CVD furnace under inert atmosphere of argon to mimic the high

temperature conditions of CNT growth, but omitting the exposure to reactive gases. Such prepared single CFs were then subjected to pull-out testing in order to mechanically examine the CF-alumina interface. The failures of CF interfaces were ultimately examined by SEM. An analogous treatment was applied to the substrates used for the subsequent CNT growth, which were ca. 15 mm × 20 mm pieces of PAN-based 0°-90° CF woven fabric and to 10 mm × 10 mm silicon wafer pieces with 100 nm thermal oxide, see: Figure 3.2b. Table 3.1 summarises the sample processing.

Table 3.1. Summary of the sample processing.

Purpose	Examination of CF-alumina interface	Demonstration of CNT growth on alumina-coated silicon wafer and on alumina-coated CF fabric	
Sample type	PAN-based single continuous CF wound on a quartz frame	Si wafer with ~100 nm thermal oxide	PAN-based 0°-90° CF woven fabric
Processing steps	2 h at 400 °C in air	Isopropanol rinsing in ultrasound	2 h at 400 °C in air
	10 min UV-ozone cleaning	10 min UV-ozone cleaning	
	Alumina ALD, 2 variants: TMA+H_2O, TMA+O_3	Alumina ALD, 1 variant: TMA+O_3	
	15 min at temperatures in range 400 °C-750 °C in Ar	CNT growth catalyst coating, CNT CVD at 725 °C	
Examination	Pull-out test, SEM, EDX	SEM	

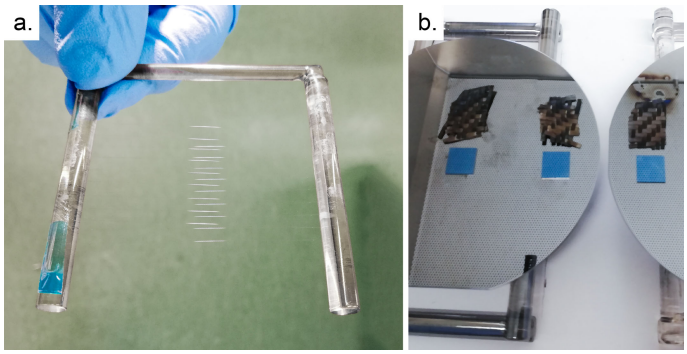

Figure 3.2. Three types of samples analysed in this study: a) continuous CF wound around a quartz frame under tension, stabilised by adhesive tape. The fibre is barely visible with naked due to its small diameter of 7.1 µm, however a bright reflection of light from its surface allows to distinguish its position; b) silicon pieces and CF woven pieces coated with CNT growth catalyst – such samples were placed on a silicon wafer supports during CVD.

3.2.2. Atomic layer deposition

The alumina ALD was carried out in a commercial Cambridge NanoTech Inc. Savannah 100 reactor. All gases used in the system were of purity class 6.0, all liquid precursors were ALD-grade (Sigma Aldrich). The aluminium precursor was TMA. The oxidants were either ultrapure water or ozone delivered by an ozone generator OL80F (OzoneLab™ Instruments) that used a feed of oxygen. Nitrogen was used as a carrier gas, which was constantly fed at 20 sccm throughout the synthesis. The reactor temperature was 225 °C, at base pressure of 48 Pa. In each deposition, the ALD consisted of 100 coating cycles resulting in a 12 nm thick alumina film [90]. In the TMA+O_3 ALD process, the ozone exposure

was carried out as a first processing step in the ALD reactor. The TMA+H_2O and TMA+O_3 ALD programs are summarised in Table 3.2.

Table 3.2. Summary of ALD programs for alumina synthesis.

ALD variant	TMA+H_2O	TMA+O_3
Ozone exposure	-	(0.1 s O_3 pulse, 1 s wait)×30
Nitrogen purging	-	40 s wait
Alumina synthesis	(0.15 s TMA pulse, 40 s wait, 0.1 s H_2O pulse, 40 s wait)×100	(0.15 s TMA pulse, 40 s wait, 0.1 s O_3 pulse, 40 s wait)×100

3.2.3. Heat treatment under inert atmosphere

The heat treatment process was performed in a CVD reactor custom-made for the purpose of CNT synthesis. The reactor chamber is a quartz tube of 13.6 cm inner diameter. Argon (Ar, purity class 6.0) is delivered at one end of the quartz tube.

The continuous single fibre samples wound on quartz frames (Figure 3.2a) were put on quartz stands and inserted into the reactor chamber. The system was then purged with 3 L/min of Ar for 10 min. Afterwards the heating from the room temperature to the set temperature was started, which takes ~10 min. The samples were kept at these conditions for 20 min. The oven cooldown to 200 °C takes about 2h, followed by sample extraction.

3.2.4. Single fibre pull-out test

The fibre-matrix IFSS was examined on the single fibre level using the single fibre pull-out test by means of the semi-automatic FIMATEST system by Textechno H. Stein GmbH & Co. KG, Germany. The system is comprised of the FIMABOND embedding station and the FAVIMAT testing station equipped with the specialised fibre pull-out device. More detailed information on the system itself can be found in the literature [128,129], while here we focus on describing our specific procedure parameters.

For embedding, the fibre is inserted into a nozzle under air suction, which stabilises the fibre in the nozzle and keeps it straight, see Figure 3.3a. The fibre is trimmed to stick out by few millimetres. A crucible is placed on a heater in the embedding chamber and a droplet of epoxy matrix. We used a low viscosity, hot-curing epoxy system composed of Araldite® LY 564 epoxy (85 wt.% of Bisphenol A diglycidyl ether and 15 wt.% 1,4-Butanediol diglycidyl ether, which acts as a reactive diluent) and Aradur® 2954 hardener, (cycloaliphatic polyamine), both form, Huntsman, US. A droplet of the resin mix is delivered into the crucible (Figure 3.3b), which is heated up to 70 °C in 1 min to decrease the mix viscosity. The fibre is then positioned over the middle of the droplet lowered to contact the matrix (Figure 3.3d). The positioning process takes ~2 min. The embedding proceeds at 200 µm/min down to the set depth of 60 µm. Afterwards, the temperature is increased to 120 °C in 1 min and held constant for 10 min, which is enough to reach the gelation point of the matrix. Afterwards, the system is cooled down to 30 °C, the sample is extracted, put on a hot plate at 130 °C for 2 h for post-curing and cooled down to room temperature. According to a cure kinetic model established for this particular epoxy system [130], the degree of cure of the epoxy is over 95% after this treatment. Such prepared samples are ready for the pull-out test. We prepared 6-10 samples for each IFSS data point, which provided enough statistics for conclusive results.

The pull-out testing has been carried out at the following configuration: the load cell of maximum force of 210 cN was installed, the pull-out speed was set to 100 µm/min. The software provided by Textechno evaluates the following quantities describing the mechanical performance of the interface: critical interfacial energy release rate, apparent IFSS, local IFSS, interfacial frictional stress, debonding work and pull-out work. The quantities mentioned above were evaluated based on the parameters extracted from the pull-out force-displacement curves, as shown in Figure 3.4, and analysed using the theoretical framework described and discussed in literature [131–133]. While we were focusing on the stress-controlled debonding, the comparison of the mechanical performance of our samples is based on the value of the local IFSS. This way, we avoided the influence of the friction and scale effects on the measured IFSS value (no averaging or apparent behaviour) [131]. The exact procedure of evaluation of the local IFSS is explained in literature [131,133]; in short, the value of the local IFSS is determined to the largest extend by the debonding force F_d, indicated in Figure 3.4. F_d is the force at which a major change of slope of the force-displacement curve is observed, which reflects the initiation of the interface crack.

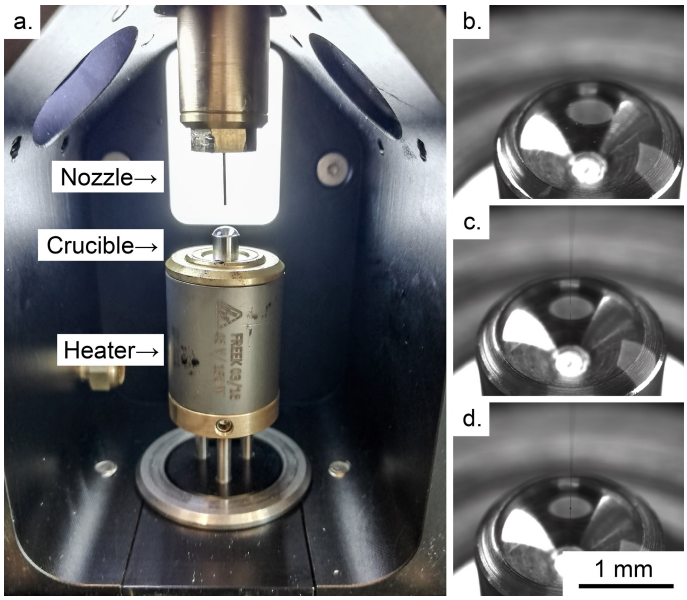

Figure 3.3. Single fibre pull-out test sample preparation in FIMABOND system – embedding phase; a – picture of the embedding chamber, b – epoxy droplet in a crucible heating up, c – fibre approaching the middle of the droplet, d – fibre-matrix contact, embedding at a desired length.

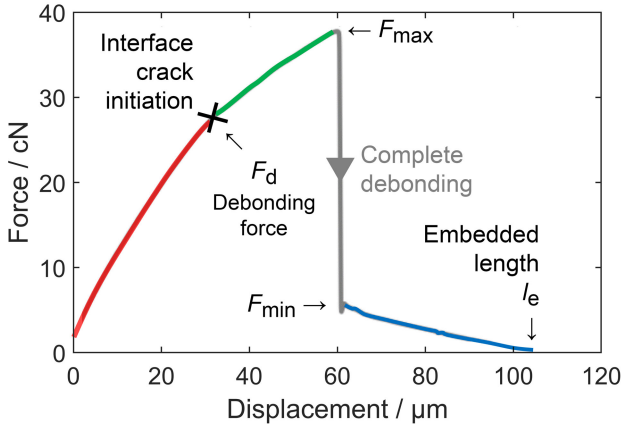

Figure 3.4. Typical force-displacement curve recorded during a single fibre pull-out test. The parameters extracted from the curve are indicated. Graph redrawn based on a figure in the work of Mäder *et al*. [129].

3.2.5. Scanning electron microscopy and Energy-Dispersive X-ray spectroscopy

The topographic qualitative imaging of the pull-out failure surfaces was carried out in a Hitachi S-4800 high-resolution SEM equipped with a cold field emission gun. The working distance was kept at ~5 mm, acceleration voltage was set to 5 kV. In the imaging, a secondary electron detector was used. The further elemental characterisation was done using the Hitachi Regulus 8230 SEM at 5 kV acceleration voltage, equipped with a cold field emission gun and a large area (100 mm^2) Ultim® Extreme silicon drift windowless EDX detector by Oxford Instruments.

3.3. Results and discussion

3.3.1. Interface shear strength

The results of the mechanical testing of the fibre-matrix interface are summarised in Figure 3.5. It is of note that the error bars represent the 95% confidence intervals of the mean value obtained by a bootstrap method described in more detail in [134]. This method is advised for an accurate evaluation of distributions of statistical estimators given small number of samples [135], like in the case of this study.

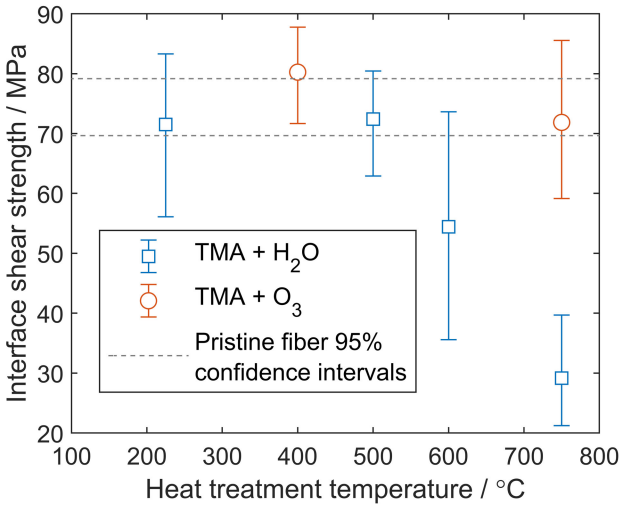

Figure 3.5. IFSS measured by pull-out tests of alumina-coated CF in two different ALD configurations: classical TMA+H_2O and TMA+O_3, after heat treatment under inert atmosphere of Ar in the CVD furnace. The dashed line represents the 95% confidence interval of the IFSS between pristine fibre and the matrix. Error bars represent 95% confidence intervals obtained by a bootstrap method.

The available data indicates that there is a declining trend of the IFSS at increasing heat treatment temperatures for the CFs coated with aluminium oxide with the classical TMA + H_2O ALD (blue open squares in Figure 3.5). This observation is in agreement with our previous findings from single fibre fragmentation testing [90], which constitutes a confirmation, that the alumina-CF interface degrades upon exposure to thermal treatment equivalent to the CNT growth conditions by CVD. The sample corresponding to the datapoint at 225 °C did not undergo heat treatment other than during the ALD process, which itself is carried out at 225 °C.

Our new approach of pre-treatment of the CF with ozone and replacing water with ozone entirely in the ALD process (TMA + O_3) was hypothesised to i) improve on the thermomechanical stability of the interface as compared to TMA+H_2O and ii) to retain the IFSS at the level of interface between the matrix and pristine fibre. The experimental data is clearly confirming that the both hypotheses. Hence, we conclude, that with the TMA+O_3 ALD approach, the CF is protected by the alumina film

against the harsh CVD conditions, while the mechanical properties of alumina-CF interface are preserved and will not constitute a weak spot of the hierarchical composite ultimately aimed for.

3.3.2. CF-epoxy interface failure analysis

The CF tips after pull-out tests were examined with SEM, see Figure 3.6. The secondary electron contrast in the SEM images is indicating that the sample TMA+H_2O heat treated at 600 °C has two distinct types of surfaces. Because of the fact, that alumina is an insulator, it tends to give higher secondary electron contrast due to charging effects. Apparently, parts of the alumina film were peeled off in the course of the pull-out test. This means, that the alumina-CF interface failed on a large fraction of the embedded surface. The sample TMA+O_3 heat treated at 750 °C however does not exhibit this kind of feature; i.e. the alumina film remained on the CF surface and the failure had occurred at the alumina-resin interface.

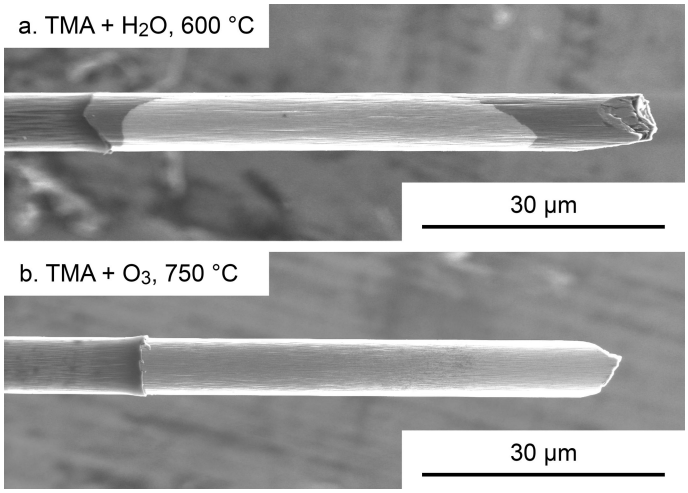

Figure 3.6. Interface failure analysis by SEM imaging of the typical fibre tips after pull-out test ALD configuration and heat treatment temperatures are noted on the in the figure.

In order to confirm the findings from the secondary electron imaging, we carried out elemental analysis of the interface fracture features. Spot EDX spectra collected for relevant points of the samples are presented in Figure 3.7, where the emission lines of relevant elements are denoted. The small-intensity peaks around 1 keV might correspond to impurities and secondary excitations in the SEM chamber, therefore they remain unattributed[1]. For the TMA+H_2O CF sample heat treated at 600 °C, spot spectra were collected on the bright- and dark contrast surface areas, shown in Figure 3.7a. Aluminium is indeed identified on the bright contrast spot, and a complete lack thereof on the dark contrast spot, judging primarily from the Al K$\alpha_{1,2}$ X-ray emission line intensity. Although the Al Kβ_1 is technically present in the spectrum, it is less intense than the Al K$\alpha_{1,2}$ double line and it is not resolvable from it in this measurement. The oxygen signal, O Kα_1, is also stronger for the bright patch, which remains in agreement with the presence of the surface oxide. Expectedly, the signals originating from the underlying CF do not show significant difference (the C Kα_1 from carbon and the N Kα_1 from the nitrogen, the primary impurity in the PAN CF). The sample TMA+O_3 heat treated at 750 °C expectedly shows consistent presence of aluminium across the pull-out interface as well as above the embedding line (see: Figure 3.7b), which further confirms the fact, that the aluminium oxide coating indeed remains firmly adhered on the fibre after the pull-out.

[1] One peak may correspond to sodium, which is a typical trace impurity in the CF [136] with the Kα_{12} and Kβ_1 lines at 1.04 and 1.07 keV, respectively. The other peak corresponds well to copper with Lα_{12} and Lβ_1 at 0.93 and 0.95 keV, respectively, which might originate from secondary excitations within the SEM chamber.

To further show, that the bright patches of the CF correspond to the alumina film, an EDX line scan and mapping and were performed. The line scan was carried out across the edge of the apparently peeled alumina film, and the results do expectedly show a clear drop in both the aluminium and the oxygen signal, see Figure 3.8. In the EDX maps, the colour intensity corresponds to the intensity of the emission line considered, normalised to the maximum detected value, see: Figure 3.9. We considered the relevant emission lines which are present in the sample: C Kα_1, N Kα_1, O Kα_1, and Al K$\alpha_{1,2}$. The Si lines were ignored, as they originated from the silicon substrates on which the CFs were placed for imaging. The EDX maps show consistently high aluminium and oxygen signal on the bright patches of CF, both in overview maps and detail maps, Figure 3.9a and b, respectively. Notably, the slight decrease of carbon signal can also be noticed on the same regions, which is attributed to attenuation of the impinging electrons and of the induced X-rays in the thin aluminium oxide film.

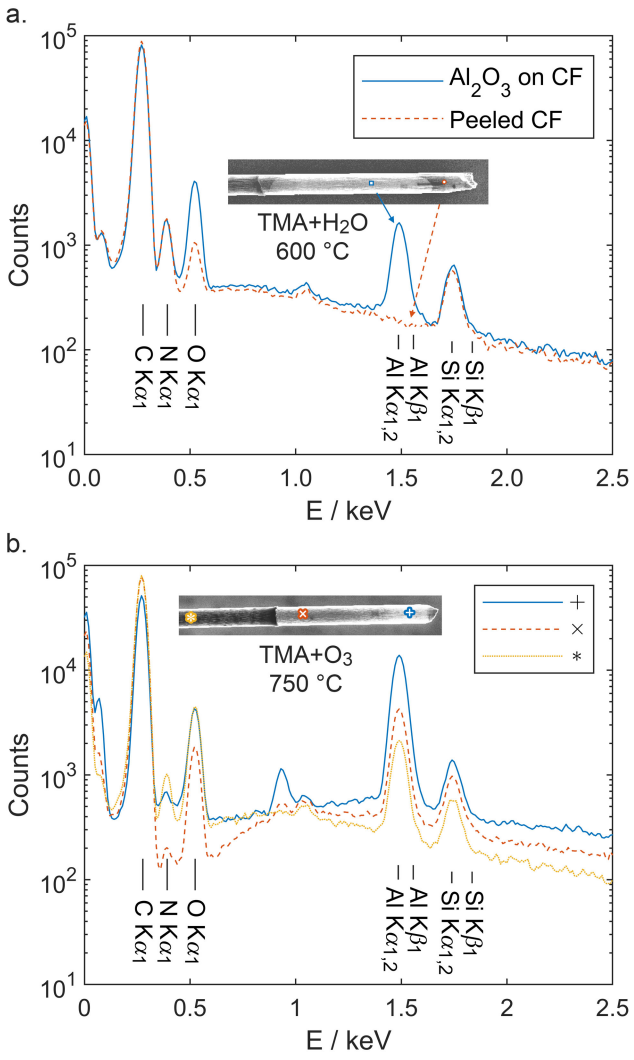

Figure 3.7. Spot X-ray fluorescence spectra collected by EDX; a) spots on the bright and dark areas of the pulled-out surface of the TMA+H_2O CF sample heat treated at 600 °C, b) spectra along the fibre TMA+O_3 heat treated at 750 °C. Spot analysis locations are indicated in the inset SEM images.

An interesting observation can be made from the EDX elemental mapping shown in Figure 3.9. The X-ray contrast of the carbon, nitrogen and oxygen lines shows a topography shadowing effect, whereas the aluminium signal does not – the latter even exhibits an enhancement on both the CF edges. This effect is attributed to two factors. First, the geometrical factor is that the alumina is present only on the surface, whereas the underlying CF constitutes the bulk, which affects the X-ray information depth. The other factor is that the Al K lines are more energetic than the C, N and O K lines, and as such

they have a higher penetration depth in the material of CF, practically to the level of transparency, whereas the C, N and O lines get more attenuated in the CF. The enhancement of the aluminium signal on the CF edges comes from the fact, that for these sample points the films are inclined with respect to the impinging electron beam, and, consequently, a larger number of aluminium atoms falls within the excitation range and emit the characteristic X-rays.

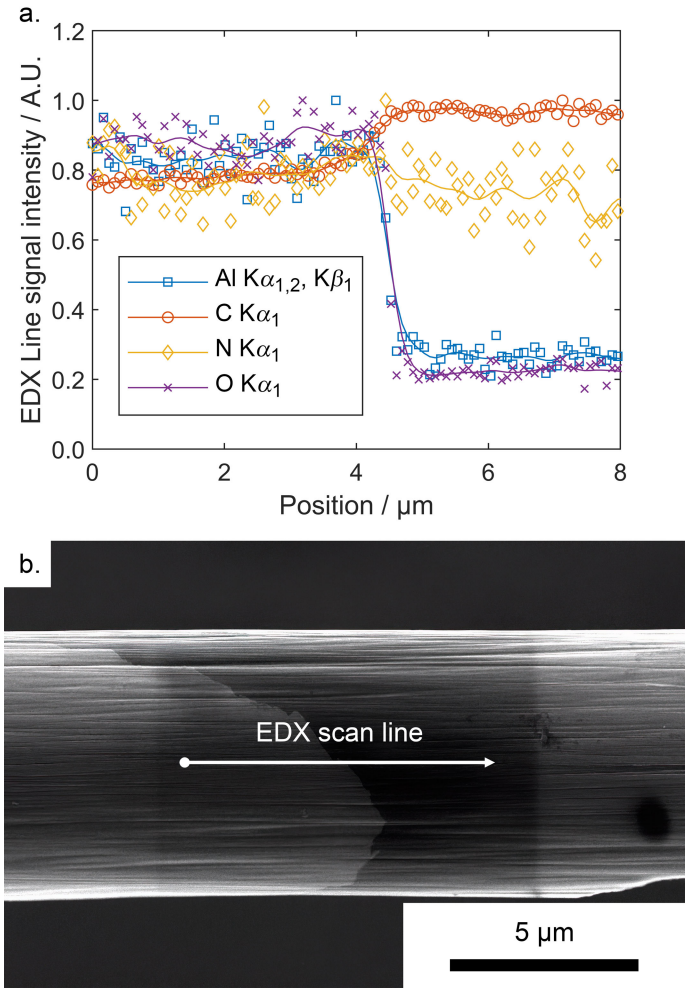

Figure 3.8. EDX line scan over the edge of film partially peeled off from the CF; a) normalised relative intensities. The continuous lines are gaussian-smoothing of the data, prepared to guide the eye (the standard deviation of the gaussian equals 170 nm); b) the location of the line scan indicated in the corresponding SEM image. The central region in the image appears darker because of the carbon contamination due from the prior imaging.

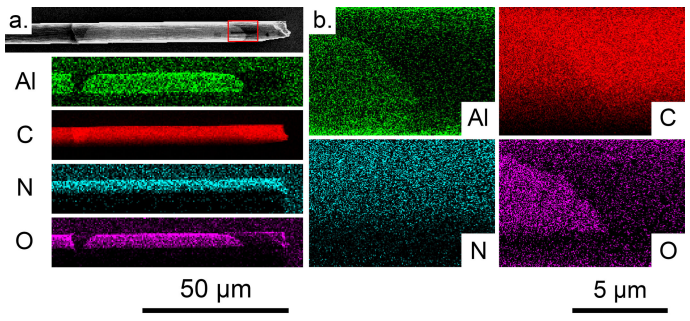

Figure 3.9. EDX mapping of the elements found in the sample based on the C Kα_1, N Kα_1, O Kα_1, and Al K$\alpha_{1,2}$ X-ray emission line intensities. SEM image and EDX maps of the entire fibre pull-out surface overview are shown in a). The red box in the SEM image indicates the location of the maps collected at higher magnification, shown in b).

3.4. CNT growth

Having established a thermomechanically stable alumina interface we were aiming for a CF-CNT-epoxy based hierarchical composite. Here, we are showing the example results of CNT syntheses that we found to be reproducible and applicable to alumina-coated surfaces. The substrates may be flat, like Si wafers, or complex, like CF woven fabrics. For a homogeneous CNT growth, it is critical to coat the surface uniformly with a thin film of catalyst. Prior to the catalyst coating, the samples were coated with Al_2O_3 using the TMA+O_3 process. We developed a method of catalyst coating that relies on surface functionalisation with amine groups, which subsequently facilitates the uniform precipitation of catalyst precursor from an iron salt solution, as described in detail in Chapter 4 of this work. The CVD of CNTs was performed at 725 °C in a similar way as described in our previous work [127]. The SEM images of the preliminary growth results are given in Figure 3.10. Figure 3.10a shows an overview image of a grown CNT forest, part of which was scratched off with a razor blade in order to expose the cross section. The growth is remarkably homogeneous. The higher magnification images Figure 3.10b,c qualitatively indicate a high apparent degree of CNT alignment and high areal density of the CNT forests on the Si substrate. The images in Figure 3.10d-f demonstrate the homogeneous CNT growth obtained on the CF woven. A high areal density and alignment of CNTs is preserved when the technique is applied to as complex substrates as CF at growth length extending over several micrometres.

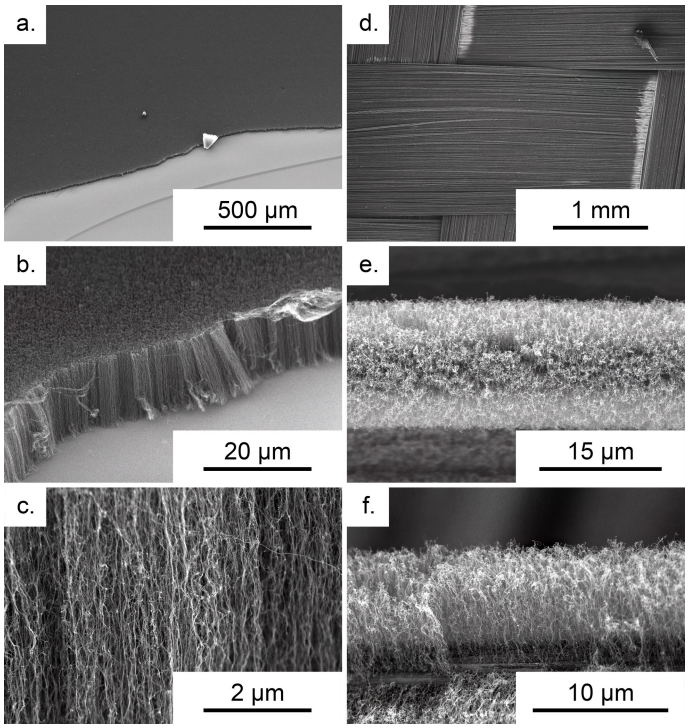

Figure 3.10. SEM imaging of preliminary CNT growth results on a flat substrate of Si wafer (images a-c) and on complex surface of CF (images d-f) at increasing magnifications (top to bottom).

3.5. Conclusions and outlook

The presented results show a new perspective on achieving the CNT synthesis on CFs while successfully mitigating the detrimental effects on the fibre mechanical properties in the process. The 12 nm thick alumina film protects the fibre under the CVD conditions and we have developed a method that allows to preserve the CF-alumina IFSS. As a consequence, the CF-alumina interface shear strength will no longer constitute a weak spot of the composite after the CNT growth at elevated temperatures. Moreover, we have presented the CNT growth of high degree of apparent alignment and density. The CVD parameters still need to be optimised for the desired length of the CNTs and the influence of CNTs on the fibre-matrix IFSS remains yet to be tested. The findings of this study

constitute a significant step in the close investigation and development of hierarchical fibre architectures in polymer matrices.

Acknowledgements

We would like to thank the SNI, Basel, Switzerland for the funding of this project (SNI PhD project P1402), Claudia Poitzsch from Textechno Herbert Stein GmbH & Co. KG, Germany for the kind support in the fibre-matrix adhesion testing, to Michael Grob from FHNW, Windisch, Switzerland, Thomas Neiger and Eugen Deckardt form PSI, Villigen, Switzerland for the installation of the chemical vapour deposition reactor and to Dimitrios Kazazis from PSI, Villigen Switzerland for assistance in elemental characterisation and for invaluable insights into EDX data interpretation.

Chapter 4

Optimisation of carbon nanotube growth morphology on carbon fibre fabrics

"We cannot live better than
in seeking to become better."

Socrates

This chapter presents unpublished work, to be submitted as a manuscript for publication.

Wojciech Szmyt contributed to this work with conceptualisation, methodology, development of software for formal data analysis, experimental investigations, writing of the original draft and visualisation of the data. **Celestino Padeste** took part in conceptualisation, experimental investigations, manuscript review and study supervision. **Clemens Dransfeld** participated with conceptualisation, manuscript review, study supervision, carried out project administration and funding acquisition.

Abstract

Carbon nanotubes (CNTs) are commonly synthesised by various methods, including arc discharge, laser ablation, plasma torch and chemical vapour deposition (CVD). The CVD technique allows for growth of CNTs attached with one end to the substrate in dense arrays. When the process is carried out on the carbon fibre (CF) substrates, one obtains so-called fuzzy fibres. This type of geometry results in enhancements of fibre-matrix interface mechanical properties by CNTs in fibre-reinforced polymer composites. High CNT growth density, alignment and homogeneity are desired for maximising the benefits to the mechanical properties, wetting of the fabrics with epoxy matrices and thermal- and electrical conductivity, particularly in the off-plane direction. However, obtaining such a morphology of CNT arrays on CFs has been posing a challenge. CNTs synthesised directly on CF are often sparse, tangled and grown inhomogeneously. The morphology of CNT arrays synthesised by chemical vapour deposition (CVD) is strictly determined by the dispersion of the catalyst nanoparticles (typically iron) on the substrate surface. The difficulties in CNT growth on CFs for fuzzy-fibre composites arise to a large extend due to adverse catalyst-CF interactions, leading to catalyst deactivation, agglomeration or catalyst-induced fibre damage. In this work, we present a new strategy of coating with iron catalyst for a homogeneous, dense and aligned CNT growth on substrates as complex as CF fabrics. The substrates are initially coated with a 12 nm thin alumina film by atomic layer deposition (ALD), which we showed previously to serve well as a protection of the CF in the harsh CVD conditions (Chapter 2) and to adhere well to the CF (Chapter 3). Subsequently, the substrates are treated with a (3-aminopropyl)trimethoxysilane solution in ethanol (aminosilane treatment), followed by an immersion in iron nitrate solution in isopropanol, controlled for ageing time. Lastly, the substrates undergo a high-temperature treatment in hydrogen for formation of nanoparticles on the surface. By SEM image analysis, we demonstrate that the aminosilane treatment promotes a homogeneous coating with the iron nitrate, leading to well-dispersed, dense and homogeneous catalyst nanoparticle coatings. The dispersion quality is assessed by Delaunay Triangulation Area Disorder. Moreover, time-resolved dynamic light scattering experiments reveal the importance of the ageing of the iron nitrate solutions – considerable nanoparticle formation is shown to occur in the solutions upon ca. 30 min solution ageing time, which we have found to be beneficial to the catalyst coating quality. Ultimately, we demonstrate excellent CNT growth results, both on flat silicon test substrates and on CF fabrics, in terms of growth density, alignment and homogeneity, corresponding to the catalyst coating. The methodology presented in this chapter constitutes a significant step in development of hierarchical composites, as well as in other potential applications, which require CNTs grown in a dense, homogeneous and aligned fashion on complex substrates.

4.1. Introduction

Carbon fibre reinforced polymer (CFRP) composites are widely applied materials in structural applications, which require high mechanical performance at low weight, such as in aerospace and automotive industry [137,138], high-end sporting goods [139], energy sector [1] and more. The excellent mechanical properties of CFRP are however mostly pronounced in the direction of the carbon fibre (CF). The typical failure of such composites occurs at the fibre-matrix interface in presence of transverse tensile, shear or compression stresses. There have been numerous approaches to overcome these issues. Macroscale modifications to the composite structure, improving the composite integrity in out-of-plane direction, include for instance through-plane stitching [140] or three-dimensional weaving [141,142]. At the nanoscale, attempts to improve the CF-matrix interface included surface functionalisation of CF using nitrenes [143], carboxyl functionalisation of the CF surface [144], grafting of CF with polyhedral oligomeric silsesquioxane [145], grafting with vinyl monomers [146], with graphene oxide [147] or with carbon nanotubes (CNTs) [148]. The latter approach, particularly promising due to extraordinary mechanical properties of the CNTs, resulted in a new type of composites, often referred to in literature as CF-CNT hybrid composites, hierarchical composites or fuzzy-fibre composites. The CFs have been grafted with CNTs by solvent-based

chemistry [149–151] or electrophoresis [72,152,153]. Chemical vapour deposition techniques (CVD) were applied to grow the CNTs on the CF directly [13,75,76,97,154–156]. The CNT growth by CVD relies on coating of the substrates with metal catalyst nanoparticles and a subsequent thermal decomposition of molecules of a gaseous carbon source [157,158]. With the CVD, contrarily to the other approaches of obtaining CNTs on CF, a radial alignment of CNTs is achievable. Such an architecture is expected to be optimal for transverse reinforcement and to inhibit fibre microbuckling, being a critical failure mode of a composite upon compression loads [97]. The CNT growth by CVD is however known to be harmful to the CF mechanical properties, due to dissolution of the catalyst particles in the fibre, inducing defects [97]. Our solution to this issue is the application of an ultrathin protective layer of alumina on the fibres, which has been discussed in our previous works [90,127,159]. In short, we showed, that the alumina film allows to retain the strength of the fibres upon the CNT growth [90], which is directly related to the film blocking the diffusion of the iron catalyst nanoparticles into the fibres [127], as discussed in Chapter 2. Moreover, the issue of the shear strength of the alumina-CF interface has been addressed in Chapter 3 [159].

The main goals of this work was to obtain CNT growth on alumina-coated CFs in a way applicable in composites, focusing on the growth morphology. For this application it is important that the CNTs are grown uniformly over the surface of the fibres and that their length does not hinder the ultimate fibre volume fraction in the composite, allowing to reach the levels typical for the industry (usually 0.5-0.65 [160]). Moreover, a priority was given to the radial alignment of the CNTs, aiming at improvements in mechanical properties of hierarchical composites preferentially in the direction perpendicular to the fibre axis.

The issue of the CNT length certainly hindering the fibre volume fraction is shown in Figure 4.1a, where the carbon fibre underneath a CNT forest of about 70 μm in thickness is outlined with green dashed lines. For the used HexTow® AS4 (Hexcel Corporation, [122]), which is a typical PAN-based CF, of 7.1 μm diameter and for a fibre volume fraction of 0.5-0.65, we estimate of an optimum CNT forest thickness of 0.8-1.2 μm, only. The length of the synthesised CNTs is influenced by a multitude of process parameters, such as reaction time, temperature, choice of the catalyst material and the type of carbon precursor and gas flow [161]. In this study, we are focusing on optimising the CNT growth length and uniformity catalysed by iron catalyst nanoparticles in an atmospheric pressure CVD reactor using ethylene as the carbon source.

The uniformity of the CNT growth on surfaces by catalytic CVD is primarily determined by the surface distribution of metal catalyst nanoparticles, while each catalyst nanoparticle may constitute an origin point of an individual CNT [162]. A severe case of a non-uniform growth is presented in Figure 4.1b, where the catalyst coating had not reached the areas visible on the left hand side, resulting in a negligible growth on parts of the fibres. The case of Figure 4.1b represents a large-scale inhomogeneity in the catalyst coating. The nanoscale homogeneity of the catalyst particle coating, i.e. its dispersion, is an important factor for the CNT growth morphology as well. According to the established mechanism of the formation of vertically-aligned CNT forests [158,163], the alignment of the CNTs stems from the contact steric interactions between the neighbouring tubes during the growth, which constricts the growth to the direction normal to the surface. In case of bad dispersion, i.e. if the catalyst tends to agglomerate and leaves considerable areas of the substrate sparsely covered with nanoparticles, the growth orientation orthogonal to the substrate surface is no longer favoured.

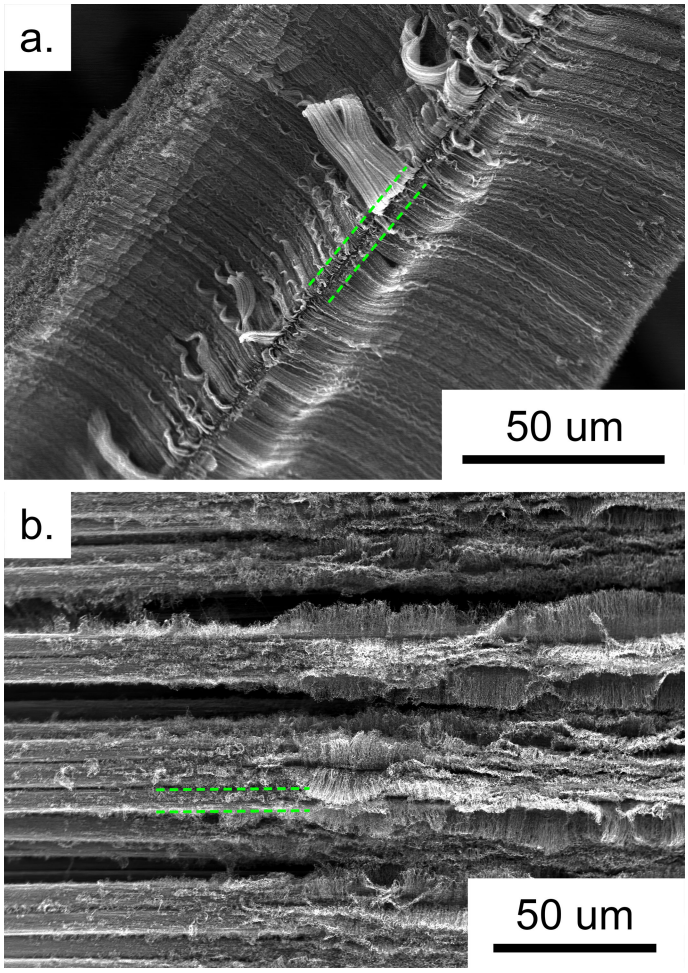

Figure 4.1. SEM images of the typical issues with morphology of the CNTs grown on CF; a) too long CNTs occupying too much space, due to too high growth rate and/or too long reaction time, b) a non-uniform CNT growth resulting from inhomogeneities in catalyst coating. The green dashed lines outline the CFs. The images originate from our own studies.

Radio-frequency magnetron sputtering and thermal evaporation are typically used methods of coating of substrate surfaces with metal catalyst films. They are well-suited for flat substrates, but – being directional methods – they suffer from shadowing effects, which renders them mostly unusable in our application. Utilisation of so-called floating catalyst CVD is a promising alternative [100,164], which does not require any catalyst coating. However, with this method, the levels of the achieved growth density, homogeneity and alignment have to date been rather limited. We have therefore directed our efforts towards catalyst deposition methods based on liquid treatments. Such methods include dip-coating of fibres in catalyst precursor solutions [57,59,75,98,156,165], mostly using iron, nickel or cobalt as catalyst. Early studies involving dip-coating have shown its potential in growing CNTs on CF [98], indicating however that further research is needed in order to achieve the desired morphology. Further improvements were achieved by oxidation of fibre surface before the coating [165], non-covalent surface functionalisation using poly(styrene-alt-[dipotassium maleate]) [75] or by application of buffer layers [57], to name a few examples. Several groups have focused on alternative catalyst systems such as iron alloys, in order to lower the synthesis temperature and mitigate the impact of the process on the CF mechanical performance [76,79,154]. In our work, we employ a thin alumina film as a CF protection [90,127], (see also: Chapter 2 of this work) and develop a strategy for the catalyst coating specific for the alumina surfaces and the subsequent CNT growth.

Inspired by a the study of McGregor and Swinburne [166], showing that amines form complexes with Fe^{2+} and Fe^{3+} ions, we aimed at amine functionalisation of the alumina-coated surfaces to promote the precipitation of the catalyst precursor from the solutions onto the substrate surfaces. For the functionalisation agent, we have chosen (3-aminopropyl)trimethoxysilane (APTMS), due to its reported use for amine surface functionalisation of alumina [167,168]. The functionalisation is carried out by an immersion of the substrates in ethanol solutions of APTMS. This step is referred to as *amino-silane treatment*. We used iron nitrate nonahydrate dissolved in isopropanol as the catalyst film precursor, taking care of the fact that ageing of the solution is a crucial factor for precipitation of the catalyst from the solution, as noticed by Li *et al*. [75]. In this work we expanded on the aspect of the precipitation of iron catalyst from the solution and investigated the phenomenon by means of dynamic light scattering (DLS) experiments. Furthermore, we evaluated the influence of the amino-silane treatment, iron nitrate solution concentration, its ageing time and the time of immersion of substrates in the iron nitrate solution on the morphology of the catalyst coating by means of SEM image analysis of the catalyst coating results. From the images we extracted information about the distributions of nanoparticle areal number density, size and an equivalent iron oxide coating thickness, which we use as metrics for the catalyst coating quality. Furthermore, we present the CNT growth conducted on silicon substrates and on carbon fibres by means of atmospheric pressure CVD with our novel recipe and the analysis of its morphology by scanning electron microscopy (SEM) and confocal laser scanning microscopy (CLSM).

4.2. Experimental and analytical methods

4.2.1. Sample preparation

Two types of samples were used in this study. One was a twill-type biaxial weave carbon fibre fabric of 3000 fibres in a yarn, 245 g/m^2 consisting of polyacrylonitrile-based fibres of high tensile strength and ~7.1 µm individual fibre diameter, (HP-T240CE, HP-Textiles GmbH, Germany). The other type were pieces of standard silicon wafers with native oxide. The fibre weaves were initially heat treated in air at 400 °C for 2 h in order to burn off organic residues, such as the fibre sizing and binders. Figure 4.2 illustrates the further preparation steps, which were the same for both types of samples. After 10 min UV-ozone cleaning in air (UVO 144A, Jelight Company Inc., US) the samples were ALD-coated with 12 nm aluminium oxide in a commercial reactor Savannah 100 (Cambridge Nanotech Inc.), using trimethylaluminum as an aluminium precursor (vapour deposition system grade, Sigma Aldrich) and ozone as the oxidiser (generated from 99.9999% purity oxygen using OL80F oxygen generator, OzoneLab™, Canada). Details of the ALD process are given in section 3.2.2 of this work

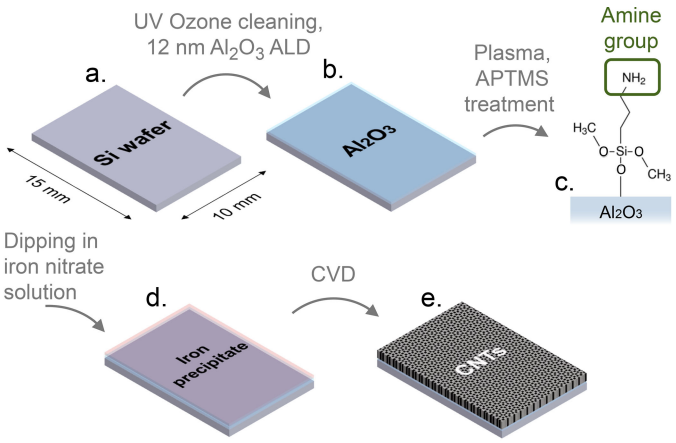

Figure 4.2. Subsequent steps of the sample preparation towards the CNT synthesis, illustrated for the case of the silicon substrate. The carbon fibres undergo the same treatment. Explanation of the processing stages: a) pristine substrate, b) alumina-coating, c) amine surface functionalisation, d) precipitation of the catalyst precursor film onto the substrate surface, e) catalyst calcination, reduction and restructuring followed by CNT growth by CVD.

Subsequently, the ALD-coated samples were treated in RF oxygen plasma for 2 min at 80 % power (Femto Low-Pressure Plasma System, Diener electronic GmbH, Germany) and immediately afterwards immersed for 20 min in a freshly prepared 1 vol% solution of (3-aminopropyl)trimethoxysilane, (>96.0 %, Tokyo Chemical Industry Co., Ltd) in ethanol (reagent-grade, VWR Chemicals). For specific samples this step was omitted for comparison. Afterwards, the samples were gently rinsed with ethanol, followed by blow-drying with pressurised nitrogen. For coating with iron precipitate, the samples were immersed in 2-20 mM solutions of iron(III) nitrate nonahydrate (>99.0 %, supplied by Fluka AG) in isopropanol (reagent-grade, VWR Chemicals). The treatment time, molar concentration and ageing time of the iron nitrate solutions were controlled for each sample. Afterwards, the samples were gently rinsed in isopropanol and blow-dried. For specified samples, the rinsing was omitted for comparison. In these cases, the liquid layer of iron nitrate solution was blown off and the surface was blow-dried immediately with the pressurised nitrogen.

Subsequently, the CVD process of CNT growth was carried out in a custom made, ambient pressure, CVD reactor with a single heating zone. The chamber is a quartz tube of 13.6 cm inner diameter and 90 cm in length. The middle of the tube is heated by a thermostat-controlled joule-heating element covering ca. 30 cm of the middle part of the reactor. The characterisation of the temperature profile within the reactor along the tube axis with a thermocouple probe revealed a constant temperature zone in the middle of the reactor and a temperature gradient on the sides. This allowed to perform several syntheses at a range of temperatures in one experiment. The feed of the carrier- and reactive gases is supplied from one end of the tube. The reactor schematic along with the temperature profile characterised along the reactor axis at the 750 °C setting is shown in Figure 4.3.

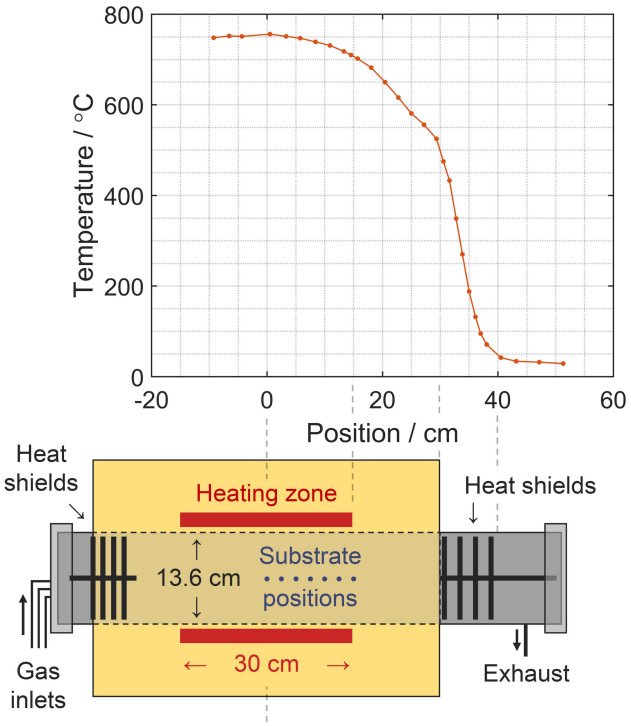

Figure 4.3. Temperature profile measured at the temperature setting of 750 °C with respect to the position along the reactor axis and the schematic illustration of the CVD reactor, drawn in line- and to scale with the horizontal axis of the graph. Example locations of sample placement along the reactor axis are indicated.

For the CVD process, we placed the samples in the reactor at ambient conditions, within a few centimetres of the tube axis at the position along the axis corresponding to the desired synthesis temperature. Subsequently, the reactor was purged with 2 L/min of argon (purity 99.9999 %) for at least

15 min. The heating was switched on together with addition of 0.6 L/min of hydrogen (purity 99.9999%) to the gas supply. The set temperature was reached within ca. 10 min in each synthesis. Due to the considerable volume of the reactor chamber (ca. 50 L), the hydrogen concentration does not instantly saturate in the reactor upon switching on, instead it gradually reaches the stable level during the time of the heating. The hydrogen supply was kept at the constant rate for the next 10 min in order to achieve a complete reduction of the iron coating and its coalescence into well-defined catalyst nanoparticles. Ultimately, the dosing of 0.4 L/min of the carbon precursor ethylene (99.9999 % purity) took place for a controlled time. Subsequently, the system was kept at the set synthesis temperature for 15 min under 2 L/min argon flow and 0.6 L/min hydrogen flow. Afterwards, the heating was switched off. The hydrogen flow was switched off at 500 °C and the further cooldown continued under 2 L/min of argon flow. The samples were extracted from the reactor at a temperature below 200 °C. The gas flows and temperatures are plotted in Figure 4.4a, taking an example ethylene dosing time of 10 min and the temperature setting of 725 °C. Additionally, we evaluated the respective gas concentrations and molar fractions, shown in Figure 4.4b,c, respectively. The methodology of the gas concentration evaluation is explained in Appendix B.1.2.

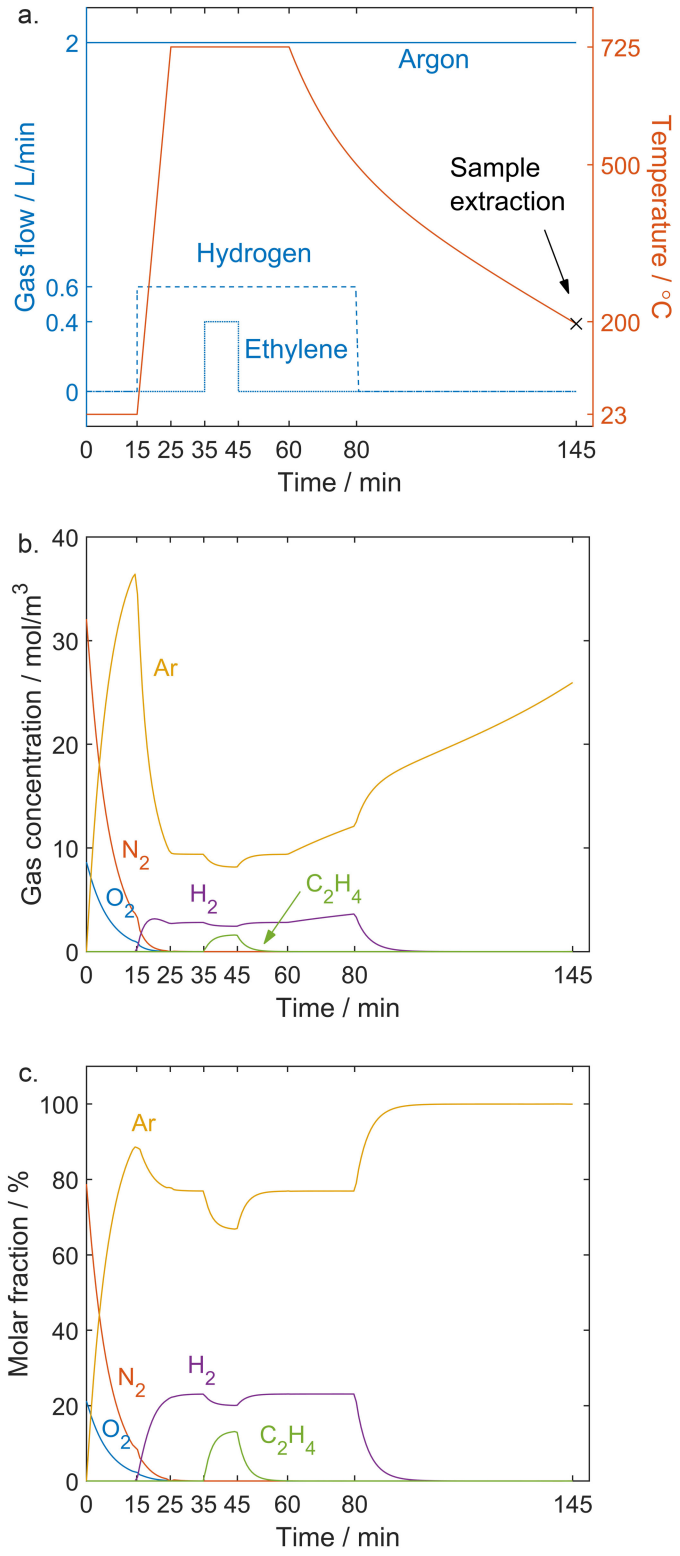

Figure 4.4. Graphs of gas flows and temperature (a), gas concentrations in the middle of the reactor (b) and molar fractions of the respective gases (c) for the temperature setting of 725 °C and the ethylene dosing time of 10 min. The gas concentrations and molar fractions are calculated using the methodology explained in Appendix B.1.2. The molar fraction of the gases correspond to the respective partial pressure as a percentage of 1 atm.

4.2.2. Nanoparticle precipitation analysis by DLS

The sample preparation for the DLS analysis was carried out at room temperature. Initially, 20 mL of 20 mM solution of iron nitrate nonahydrate in isopropanol was prepared. Subsequently, after a defined ageing time, 10 µL of the solution was sampled and into a measurement cuvette filled with 1.5 mL of isopropanol. The cuvette was immediately sealed and put into the DLS measurement device (Zetasizer Nano ZS, Malvern Instruments Ltd., UK) for the measurement to be carried out. Higher concentrations were causing oversaturation of the DLS signal, hence the 10 µL diluted to 1.5 mL was found to be optimal. The DLS spectra were recorded between 6 min and 46 min after the initial solution preparation in order to elucidate the temporal evolution of nanoparticle sizes in the solutions.

4.2.3. Imaging of the nanoparticle coatings and CNTs

Samples with nanoparticle coatings and with synthesised CNTs were inspected using a Hitachi S-4800 SEM with a cold-field emission gun, run in a secondary electron mode at 5 kV acceleration voltage. Additionally, CLSM (VK-X1000, Keyence) was employed to characterise the topography of the most uniform CNT forests obtained, as found by SEM.

4.2.4. Nanoparticle coating image analysis

The quality of the catalyst nanoparticle coatings was assessed by SEM image analysis. The coating morphology, density and uniformity were quantified based on the following information extracted from the SEM images: nanoparticle areal densities, nanoparticle size distributions and an equivalent iron oxide coating thickness. The quantities were extracted from the images using and algorithm discussed further in this section.

Moreover, the quality of the dispersion was assessed based on the *area disorder of Delaunay triangulation* ($\mathrm{AD_{Del}}$), described in detail in the work of Bray *et al*. [169], where the Delaunay triangulation was shown to be an effective tool in quantitative assessment of the nanoparticle dispersion. In short, the method relies on the measure of the relative standard deviation of the areas of triangles formed by the centroids of the nanoparticles (their geometric centres of mass) as triangle vertices. The triangles are obtained specifically by the so-called Delaunay triangulation algorithm, described for instance in the work of Lee and Schachter [170], which returns a net of connections between the given vertices, composed preferentially of triangles of larger internal angles and avoiding tight-wedge triangles. Essentially, such a set of triangles is found, for which no triangle vertex is within a circumcircle of any other triangle. It is crucial to apply periodic boundary conditions in the triangulation, so that locally ordered, but clustered NPs are not misclassified as well-dispersed [169,171]. The $\mathrm{AD_{Del}}$ is expressed as

$$\mathrm{AD_{Del}} = 1 - \frac{1}{1 + \mathrm{S}_{A_\mathrm{D}}/\bar{A}_\mathrm{D}}, \tag{4.1}$$

where A_D is the area of the Delaunay triangle (in principle, a random variable), $\bar{A}_\mathrm{D}$ is its mean, whereas $\mathrm{S}_{A_\mathrm{D}}$ represents its standard deviation. The values of $\mathrm{AD_{Del}}$ can be interpreted quantitatively. The $\mathrm{AD_{Del}}$ takes values in the range between 0 and 1. For perfectly homogeneously dispersed systems, all Delaunay triangles are the same shape, therefore the relative standard deviation of the triangle areas is 0, which brings the value of $\mathrm{AD_{Del}}$ to 0. For extremely clustered systems, the relative standard deviation of the areas can be arbitrarily large, in which case the $\mathrm{AD_{Del}}$ converges to 1. For the uniformly randomly distributed point-like particles on the surface, as obtained in a homogeneous Poisson process (HPP), the $\mathrm{AD_{Del}}$ equals 0.468 [169]. Realistically however, the finite size of particles constraints the complete randomness of the particle positions. In this case, a hard-core model (HM) needs to be considered

as a benchmark. The HM can be achieved by sequential random addition of disks onto surface with the constraint of no overlap of the disk faces. In the work of Bray *et al*. [169], expected values of AD_{Del} were obtained with respect to the surface coverage with disks in the HM model. In this work, we obtain the benchmark AD_{Del} values by interpolating using a piecewise polynomial between the values of Bray *et al*. with respect to the evaluated surface coverage from the images, see: Figure 4.5. In such a way, we can assess how the quality of dispersion compares to the randomly distributed, non-overlapping particles, as given in the HM model.

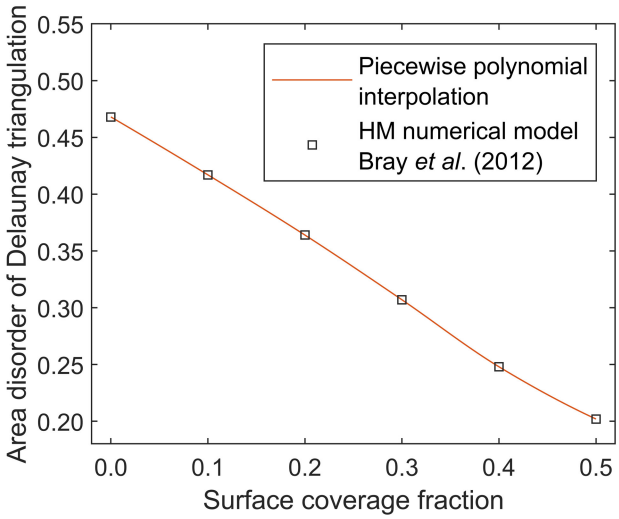

Figure 4.5. The values of the area disorder of Delaunay triangulation obtained for the model of randomly distributed, non-overlapping disks (HM model) by Bray *et al*. [169], interpolated for a sample-specific benchmark depending on the surface coverage with particles.

For the purpose of an automated, reliable and repeatable analysis, an image analysis algorithm was developed in MATLAB™ R2019b (The MathWorks, Inc, US), aided by the Image Processing Toolbox™. For a detailed description of the functions of the toolbox used in the presented algorithm, we refer to its documentation [172]. The crucial goal for the algorithm was to achieve an automatic segmentation of the nanoparticles in the images, corresponding as close as possible to the actual outlines of the particles and the subsequent triangulation for quantification of the NP dispersion. The effects of the subsequent steps of the image processing are presented in Figure 4.6. The algorithm was the following. Initially, the images (Figure 4.6a) were automatically contrast adjusted, scaling the pixel brightness values linearly over the entire 8-bit greyscale range, so that the darkest pixel has a value of 0 and the brightest one - 255. The median filter within the region of 3 by 3 pixels (the function `medfilt2()` at default settings), was additionally applied in order to minimise the image noise, thus obtaining the result as shown in Figure 4.6b. Subsequently, the brightness values were adaptively scaled in a way, that both the dark background and the bright nanoparticles lay on their respective uniform brightness levels, close to black and close to white, respectively, This step was carried out in order to subtract the image background and to negate the differences between the brightest- and darkest-appearing nanoparticles in the images, which could be inaccurately segmented otherwise. The effect was achieved by addition a top-hat filtered image to the original and subtraction of its bottom-hat filtered version, obtained by the `imtophat()` and `imbothat()` functions, respectively. Both functions take a structuring element as a parameter. In our processing, a structuring element shaped as a disk of radius of 8 pixels generated by the function `strel()` was found to yield the best results. The effect of this step is presented in Figure 4.6c. For samples 3 and 4 this step was however ineffective due to very low number of particles in the images, therefore only a background subtraction with a rolling-ball algorithm (ball radius 20 pixels, implemented in ImageJ) and a subsequent brightness adjustment was carried out for these images instead. Therefore the results from samples 3 and 4 have

to be considered as less accurate as compared to the rest of the samples. Ultimately, thresholding was carried out, yielding a binary image of the nanoparticles (Figure 4.6d). The threshold of 60% brightness was found to give the best segmentation accurately outlining the particles.

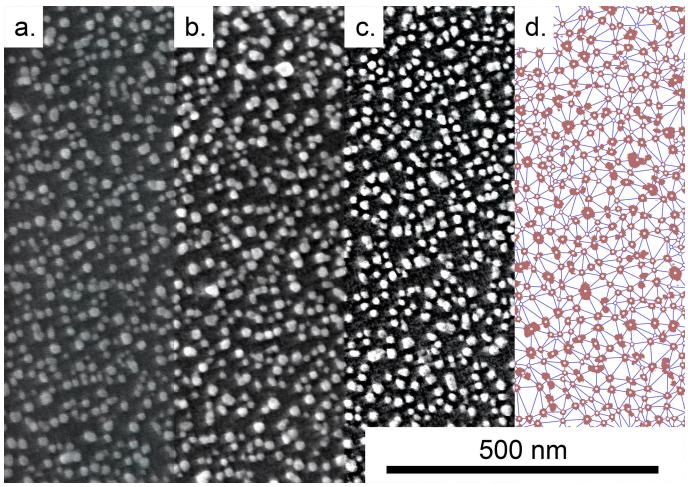

Figure 4.6. Subsequent steps towards the accurate and reproducible segmentation and triangulation of nanoparticles in SEM images; a) original image; b) linear normalisation of the image brightness and median filtering; c) local contrast enhancement; d) thresholding and Delaunay triangulation. In d), the red patches represent the NPs segmented from the image, the white dots correspond to the centroids of the NPs, whereas the blue lines show the Delaunay triangulation result.

Collection of nanoparticle areas and centroids was performed on such prepared images using the function `regionprops()`.The nanoparticle areal densities ρ_{A} were evaluated as the number of detected particles N_{p} divided by the area of the image A_{img},

$$\rho_{\mathrm{A}} = \frac{N_{\mathrm{p}}}{A_{\mathrm{img}}}. \tag{4.2}$$

The particle diameters were estimated assuming approximately circular shapes of the particles, i.e.,

$$d_i = 2\sqrt{\frac{A_i^2}{\pi}}, \tag{4.3}$$

where d_i is the diameter of the i-th particle in the image, whereas A_i is its area found from the image analysis. Detected nanoparticles of diameters less than 4 nm were neglected from the analysis as originating mainly from noise. The equivalent iron oxide thickness h_{eq} was evaluated as the total volume of particles in the image divided by the area of the image, assuming a hemispherical shape of particles, taking the diameters as estimated with equation (4.2). It gives

$$h_{\mathrm{eq}} = \frac{1}{S_{\mathrm{img}}}\sum_i V_i = \frac{\pi}{12 \cdot S_{\mathrm{img}}}\sum_i d_i^3. \tag{4.4}$$

The further image analysis was carried out in order to assess the quality of the nanoparticle surface dispersion based on the area disorder of Delaunay triangulation. The centroids of the detected nanoparticles were further used as vertices for the Delaunay triangulation using the `delaunay()`

function. The periodic boundary conditions were obtained the following way: the vertices (x_i, y_i) were cloned 9 times and shifted by $\Delta x \in \{\pm L_x, 0\}$, $\Delta y \in \{\pm L_y, 0\}$, the L_x and L_y being the width and the height of the image, so that together they formed a lattice of 3 by 3 adjacent sets of vertices. The triangulation was carried out on the sum of all 9 sets, giving N triangles (x_{ij}, y_{ij}), where $i \in \{1, \dots, N\}$ enumerates the triangles and $j \in \{1,2,3\}$ is the number of the given triangle vertex. To select the unique triangles, the following criterion was applied:

$$U_i = \forall_j(x_{ij} > 0) \wedge \exists_j(x_{ij} \leq L_x) \wedge \forall_j(y_{ij} > 0) \wedge \exists_j(y_{ij} \leq L_y), \tag{4.5}$$

where U_i is a Boolean logical variable, true if the given triangle is unique in the periodic domain and false if it is not. Such unique triangles were selected and their areas were further analysed as described above in this paragraph. A synthetic example of the triangulation is shown in Figure 4.7,where the 30 particles were generated with an HM model within a domain of L_x=3, L_y=2. The minimum distance between particles was set as 0.3. A set of cloned triangulations are plotted, shifted by $\Delta x \in \{\pm 1.05 \cdot L_x, 0\}$, $\Delta y \in \{\pm 1.05 \cdot L_y, 0\}$, in order to illustrate the effectiveness of the selection of the unique triangles fulfilling the periodic boundary condition with the criterion (4.5). Clearly, the cloned triangulations fit together forming a periodic structure, which was the goal of the algorithm.

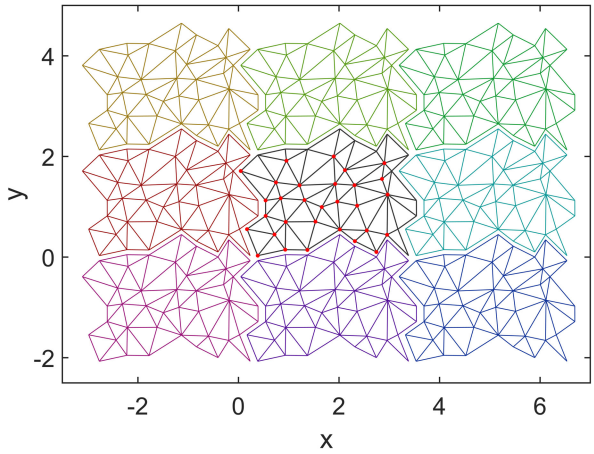

Figure 4.7. Delaunay triangulation of 30 particles generated with an HM model within a domain of width and height equal 3 and 2, respectively, with a minimum distance between particles set as 0.3. The centroids of the particles are indicated by red dots, whereas the solid lines represent the result of triangulation. A lattice of cloned triangulations shifted by ±1.05 times the domain height and/or width is shown to illustrate that the periodic boundary condition for the triangulation is fulfilled.

4.3. Results and discussion

4.3.1. DLS analysis of nanoparticle precipitation in solution

To analyse the nanoparticle formation in iron nitrate solution in isopropanol, two types of measurement series were gathered. In the first series, referred to as *sampled*, the ageing was performed in three 20 mM solutions of iron nitrate nonahydrate in isopropanol. Identical solutions were prepared in time intervals of 12 min, and then 10 µL of each was sampled into 1.5 mL of isopropanol in a DLS cuvette to be measured 2-3 times. In the second series, referred to as *continuous*, one 20 mM solution of iron nitrate nonahydrate in isopropanol was prepared, 10 µL of which was diluted in 1.5 mL of isopropanol in a cuvette and aged directly in the DLS throughout the duration of the measurements.

Notably, the role of the solvent needs to be emphasised. The solutions in isopropanol appeared gradually more and more cloudy over time, which indicated a precipitation of particles in the solution, which we found beneficial to the coating process. We have not observed such an effect in acetone, ethanol or methanol for instance, nor did we successfully obtain catalyst coatings with these other solvents.

The nanoparticle size distributions were evaluated with aid of the software provided by Malvern Instruments. For the purpose of the evaluation, the shape of the nanoparticles was approximated as spherical and the refractivity was set as 2.9, which is a higher limit for amorphous iron(III) oxide [173]. Because of these necessary approximations, the results need to be considered as a rough estimate in terms of evaluated nanoparticle sizes. The results of the DLS are gathered in Figure 4.8.

Clearly, both the sampled and the *continuous* measurement series follow the same trend, rising from very small detected nanoparticle sizes to around 12 nm within about 30 minutes after the initial mixing. Lack of any significant difference between the trends at times up to 30 min indicates, that the nanoparticle precipitation kinetics in the solution does not depend significantly on the concentration within the given concentration range. It constitutes a strong indication, that the process is surface-limited rather than concentration-limited. It is likely, that the trend for the *sampled* series, aged in the more concentrated 20 mM solutions, could continue towards higher particle sizes, instead of following the saturating behaviour as the *continuous* series, which is aged much more diluted in a cuvette. The divergent trends are indicated in Figure 4.8. Within the timeframe of the ageing relevant in our experiments, which is 30 minutes, both series exhibit the same behaviour, which is precipitation of nanoparticles of sizes in the range very well-suited as catalyst for synthesis of multiwall CNTs by CVD [161].

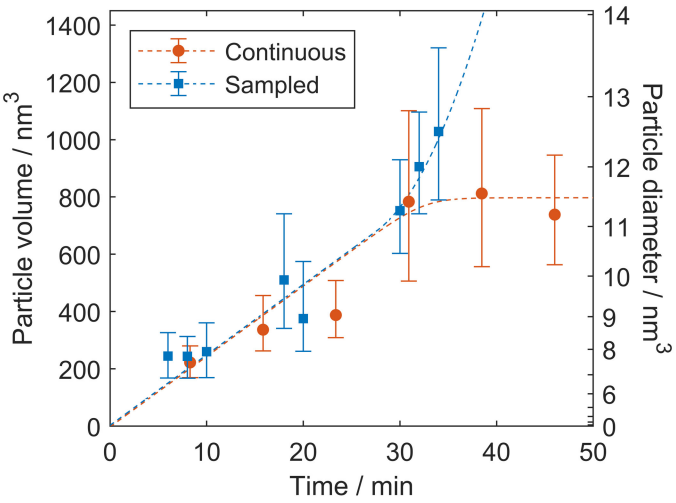

Figure 4.8. The nanoparticle size distributions measured by DLS with respect to the time elapsed from the initial mixing of the solution. The right auxiliary axis is scaled nonlinearly, reflecting the nanoparticle diameter. The error bars represent the 25th and the 75th percentile of the respective distribution. The dashed lines show the trend lines, graphed to guide the eye.

4.3.2. SEM analysis of iron oxide nanoparticle coating

In order to evaluate the developed strategy for uniform surface coating with CNT synthesis catalyst, a range of diced silicon substrates was prepared, varying the fluid treatment parameters, as summarised in the Table 4.1. All samples had been plasma treated, ALD-coated and plasma-treated again right before the fluid treatment, according to the description given in the paragraph 4.2.1. Subsequently, the full CVD process was carried out exactly as for the purpose of CNT growth, omitting however the carbon precursor dosing. In such a way we were able to achieve iron catalyst precipitate calcination,

reduction and formation of nanoparticles, which could be subsequently quantitatively studied by SEM. It is of note, that the coated samples were examined by SEM before the CVD processing as well, and no nanoparticles were observed, which constitutes a confirmation, that the transformation of the iron precursor coating into catalyst nanoparticles indeed occurs during the reduction step of the CVD process. The restructuring of the catalyst precursor film is known to be driven by minimising the surface energy, favouring its nanodroplet-like morphology [174–176].

Table 4.1. Varied parameters of the catalyst coating process

Sample number	Amino-silane treatment time	$Fe(NO_3)_3$ solution concentration	$Fe(NO_3)_3$ solution ageing time	$Fe(NO_3)_3$ solution immersion duration	Post-immersion rinsing with isopropanol
1	none	20 mM	10 min	3 s	no
2	none	20 mM	20 min	3 s	no
3	none	2 mM	10 min	3 s	no
4	none	2 mM	20 min	3 s	no
5	20 min	20 mM	20 min	10 min	yes
6	none	20 mM	20 min	10 min	yes

Samples 1-4 were prepared using a common strategy of short (in this case: 3 s) dipping of the substrates in the iron precursor solution – referred to as dip-coating – without any subsequent rinsing. For these samples, the solution concentration and ageing time was varied. Samples 5 and 6 on the other hand, were prepared to elucidate the effect of a longer immersion time in the catalyst precursor solution and the amino-silane treatment. The pixel size at the chosen SEM magnification of 10^5 was 0.99 nm and the collected images were of size 1280 px by 896 px. The images were taken at 4 to 8 different spots across the 10×15 mm^2 samples to assess the macroscale coting homogeneity. For sample 4, images from only 2 spots were analysed, as in most images no nanoparticle coating could be found. The image analysis followed the procedure explained in section 4.2.4. Moreover, the surface dispersion of nanoparticles was quantified based on the area disorder of Delaunay triangulation, AD_{Del}. We refer to Appendix B.2, all the images, triangulations, the respective histograms and parameters extracted from each image are shown. The resulting statistics is gathered and visualised in the form of box plots in Figure 4.9. The upper and lower bounds of the boxes represent q_1 and q_3, the first and third quartile, respectively, whereas the red bar across the box represents q_2, the median. The whiskers denote the entire range of data, excluding the ignored nanoparticles of diameters less than 4 nm.

The following observations can be made from the data. Samples 1 and 2 show high areal densities (Figure 4.9a); however. the scatter in the data is relatively high. Sample 2 shows higher densities than sample 1, which may indicate the benefit of the 20 min ageing time as compared to the shorter 10 min. However, the large spread of the values reveal considerable inhomogeneity of the coating on the sample scale. Samples 3 and 4 show very low densities of nanoparticle coatings, revealing that the 2 mM concentration of the iron nitrate solution is too low to obtain considerable nanoparticle coatings in these conditions. Moreover, much less nanoparticles were found on sample 4 as compared to sample 3, which indicates that at such low concentration of iron nitrate solution, the increased ageing time is no longer beneficial. Sample 5 on the other hand, which has been prepared according to our new recipe, indeed shows a high nanoparticle areal density at minimal spread (see: Figure 4.9a). This is crucial for dense, uniform and aligned CNT synthesis across the surfaces [177]. Sample 6, although exhibiting higher densities than sample 5, shows higher scatter in the data.

In terms of the amount of the deposited iron catalyst (Figure 4.9b), the observations are largely in line with the ones from the nanoparticle areal density. Samples 1-2 show a high amount of deposited iron, however with a large scatter in the data. Despite the higher areal density of particles of sample 2 compared to sample 1, the amount of deposited iron is lower, which is explained by slight differences in the nanoparticle size distributions (Figure 4.9c). Samples 3 and 4 both show very low amounts of deposited iron, for sample 4 almost negligible, which is in line with the particle areal densities discussed above. Sample 5 exhibits the best uniformity, reflected by the low scatter in the data, while maintaining the high value of the density. Sample 6 is similar to sample 5 in terms of consistency, however the amount of the deposited catalyst for this sample is lower. All the samples yielded relatively consistent diameter distributions, as seen in Figure 4.9c; most of the detected particles being in the range of 10-16 nm (25^{th} and 75^{th} percentiles of the overall diameter data), which is well-suited as a catalyst for the CNT growth [161].

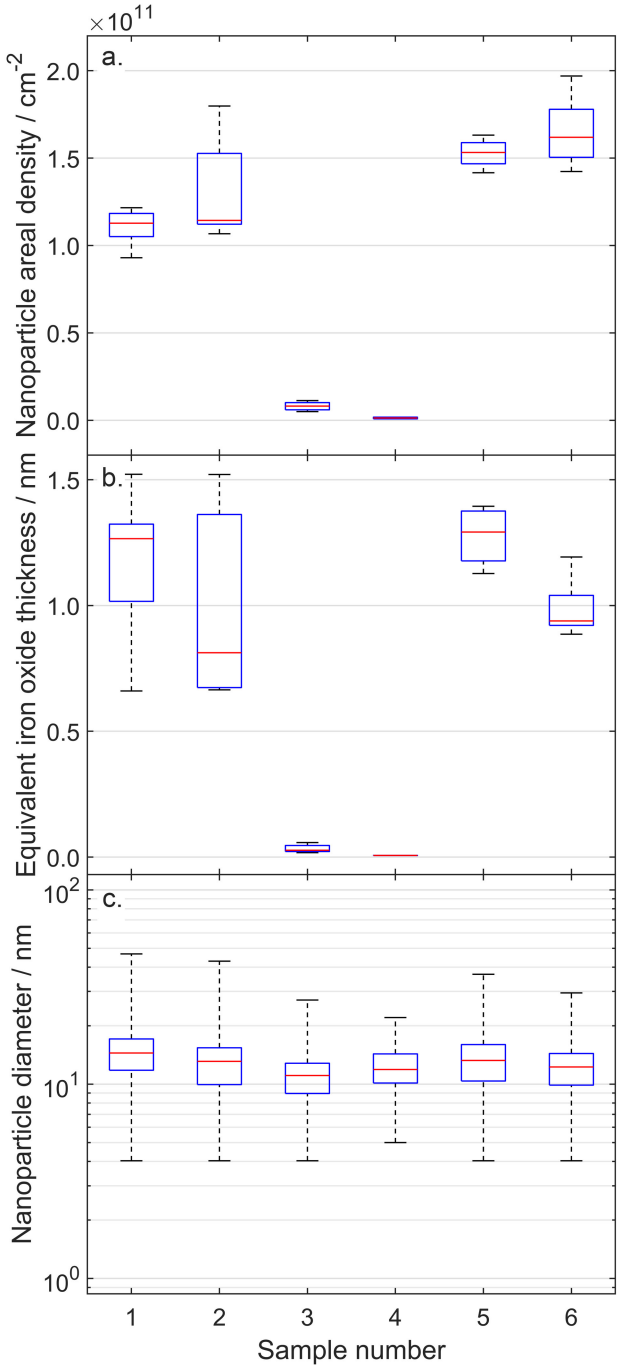

Figure 4.9. Statistics of the nanoparticle data as collected from SEM image analysis. The box blot limits represent the 25th and 75th percentile, the bar in the middle is the median, whereas the whiskers denote the maximum and minimum values. For sample assignments, see Table 4.1.

The area disorder of Delaunay triangulation AD_{Del} as a measure of the nanoparticle dispersion is shown in Figure 4.10, together with the benchmark of hard disks randomly-distributed on the surface (HM model). These values were evaluated based on interpolation of the numerical results of Bray *et al*. [169] with respect to the surface coverage with particles as obtained from the image analysis. Sample 1 shows a significantly lower level of disorder, with respect to the benchmark, which indicates a good quality of the dispersion. Sample 2, on the other hand, shows no significant difference between the obtained values and a random particle arrangement. This means that the particle coating cannot be considered well-dispersed, because an overlap with the random arrangement indicates a tendency to agglomeration. This finding is consistent with the large variability in nanoparticle areal density and the amount

of deposited catalyst for this sample (Figure 4.9a,b), which means that the coating inhomogeneities for this sample are present both on the macroscale across the sample, as well as locally in the nanoparticle dispersion. The results for samples 1 and 2 show, that within the strategy of 3 s dipping without the subsequent rinsing, increasing the iron nitrate solution ageing time from 10 min to 20 min is not beneficial for the particle coating dispersion. For samples 3 and 4 the surface coverage was so small (~1 % or lower for sample 3 and even less for sample 4, see Appendix B.2, Figure B.9 and Figure B.11), that the expected values of AD_{Del} in HM model converge to the solution for the uniformly-distributed point-like particles, as in HPP model. Hence, for these samples the benchmark is shown as horizontal bars instead of box plots. For sample 3, the AD_{Del} are very high, as well as their spread. This is expected, when a low number of particles is detected per image. The values of AD_{Del} greatly exceeding the benchmark in a large fraction of images indicate a strong tendency to agglomeration, which is evident from visual inspection of the SEM images as well (see Figure B.9 in Appendix B.2). The AD_{Del} of sample 4, on the other hand, indicates a better dispersion of particles compared to the random model. However, this result may be a false positive, attributed to a selection bias: due to the very low particle areal density, the SEM images were taken in locations where at least several nanoparticles could be found, therefore it cannot be assumed that the individual images are representative to for entire sample in terms of nanoparticle dispersion. Sample 5 shows the lowest average level of disorder of all samples, significantly lower than its benchmark as well. Moreover, the spread in the data is very small as well, indicating a high degree of coating homogeneity on a macro scale across the sample. Clearly, the recipe including the amino-silane treatment is beneficial for the catalyst dispersion quality. Sample 6, on the other hand, shows an increased disorder as compared to the one of sample 5. It also does overlap with its benchmark range and the spread in its values is higher with respect to sample 5. The inset in Figure 4.10 shows a magnification of the data from sample 5 and 6 to emphasise the difference between the two. The visual inspection of the images agrees with this finding, while in the images of sample 6 we see regions where the particles are visibly less dense than in the surrounding area, whereas no such effect is observed in the images of sample 5. Representative images of samples 5 and 6 and their triangulations are shown in Figure 4.11, where the relative deviations of the triangle areas from the mean value are color-coded to designate the regions of agglomeration (red) and the regions of sparse coating (blue). All the images with the main subsequent processing steps and triangulation results are available in Appendix B.2. To summarise, the analysis of the AD_{Del} of sample 5 and 6 further confirms the effectiveness of the amino-silane treatment for the catalyst coating dispersion quality.

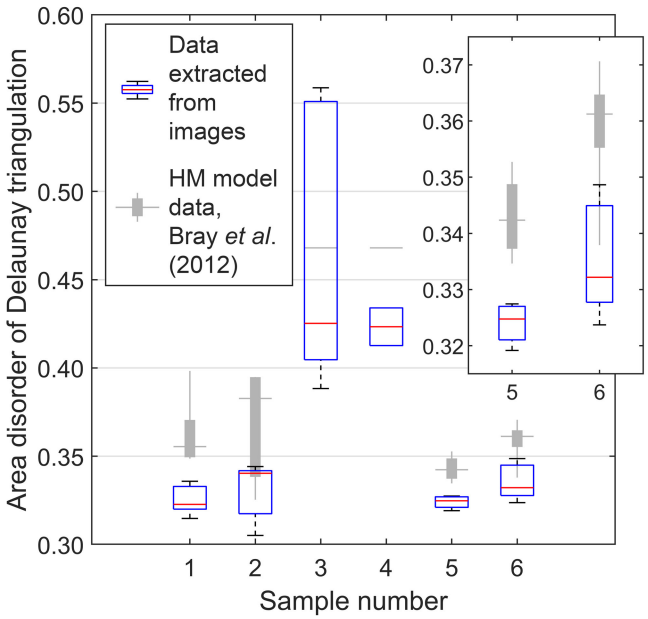

Figure 4.10. Area disorder of Delaunay triangulation as a measure of the nanoparticle dispersion in the form of boxplots based on the distributions of the data extracted from image analysis. The box edges represent the 25th and 75th percentiles; the red bar is the median value, whereas the whiskers indicate the maximum and minimum value in the distribution. Lower values of the area disorder mean better dispersion. The grey filled boxplots constitute a benchmark, which is the area disorder of random distributions of non-overlapping particles of finite diameter (hard-core model, HM), based on the work of Bray *et al*. [169], evaluated for the given surface coverage with nanoparticles. The inset shows magnification of data of samples 5 and 6 to emphasise the difference between the two.

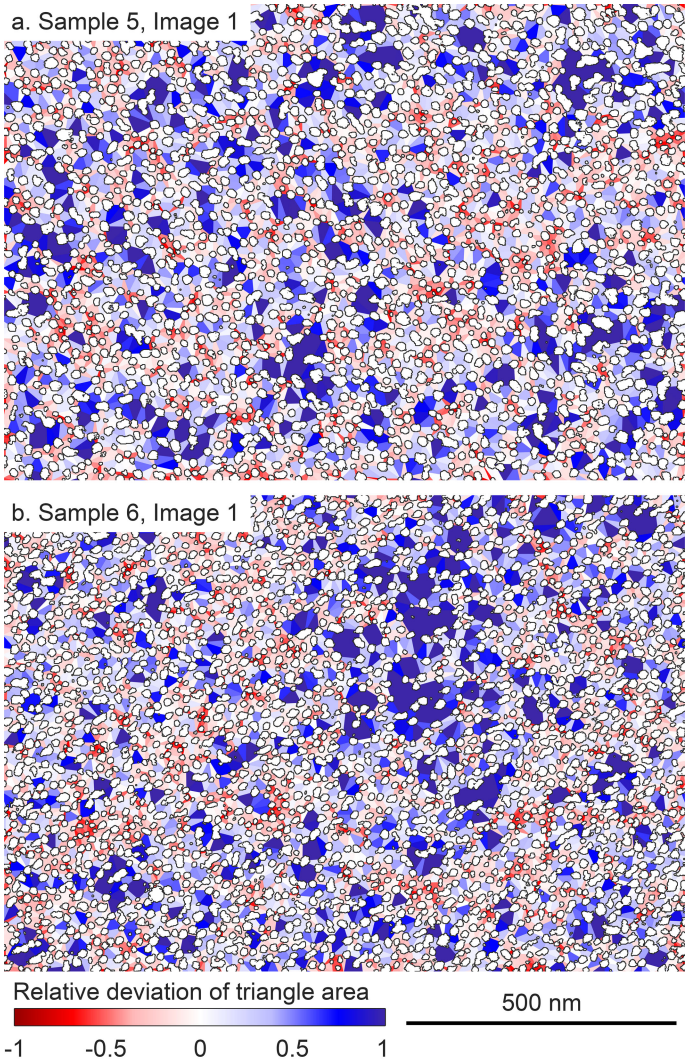

Figure 4.11. Delaunay triangulation result of the nanoparticles detected in representative images of sample 5 (a), and sample 6 (b); i.e. images were selected, for which AD_{Del} was within the 25^{th}-75^{th} percentile range. The colour grading of the triangle faces represents the relative deviation of the triangle area from the mean value. The overlay of white patches with the black outline represents the nanoparticles in the images.

To summarise, the results presented show, that the developed method of iron catalyst coating promoted by an amino-silane treatment and benefitting from the appropriately set iron nitrate solution ageing time indeed leads to uniform, well-dispersed nanoparticle coatings of high areal densities and nanoparticle sizes as desired for the dense, aligned and uniform CNT growth.

4.3.3. Analysis of CNT growth on Si and on CF

One of the first indications of the benefit of the amino-silane treatment on the uniformity and reproducibility of dense CNT growth that we observed was an experiment on Si wafer substrates. In this experiment, the substrates were immersed in 20 mM iron nitrate solutions during the solution ageing, for 20 and 40 minutes, respectively. For this experiment, the carbon precursor dosing time in the CVD process was set to 10 min. A comparison was made between applying and omitting the amino-silane treatment. The growth morphology, examined by SEM, is shown in Figure 4.12.

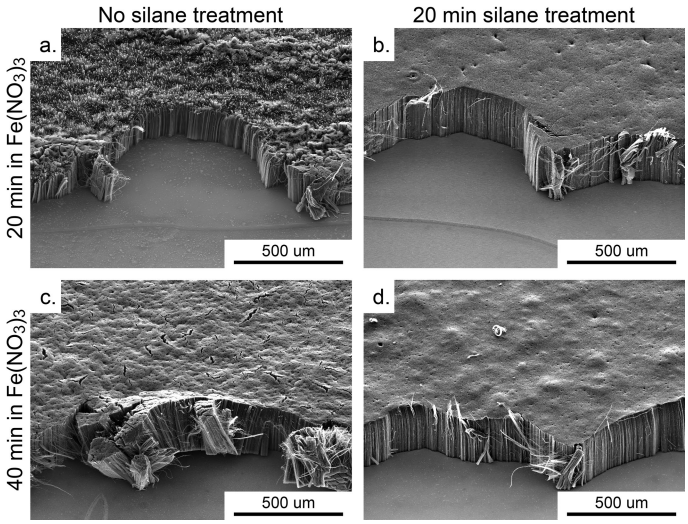

Figure 4.12. Morphology of CNT forests from an experiment on silicon wafer surfaces, showing that amino-silane treatment indeed promotes the uniform CNT growth. It expectedly correlates with the advantage of sample 5 over sample 6 in terms of dispersion quality of catalyst nanoparticle coating (see: Figure 4.9,10 and Table 4.1).

One can clearly see, that the growth is more uniform for both the amino-silane-treated samples (Figure 4.12b,d) in comparison to the other two (Figure 4.12a,c). The cracked top of the CNT forest (Figure 4.12c) indicates large inhomogeneity of the CNT growth rate, which is related to strong imperfections in the catalyst distribution on the surface. A striped growth, as seen in Figure 4.12a, indicates a patchy coating with catalyst.

In order to show how the CNT length can be controlled towards the applicability in hierarchical composites, we carried out a series of experiments, proceeding gradually towards shorter CNT lengths by decreasing the ethylene dosing time and decreasing the synthesis temperature. We were able to decrease the ethylene dosing time down to 1 min while maintaining an accurate control and repeatability of the process. The peak concentration of ethylene reached in the reactor at 725 °C for 10 min- and 1 min dosing times are estimated to be ca. 1.6 mol/m^3 and 0.6 mol/m^3, respectively. The ethylene exposure is estimated as 22 mol/cm^2 and 2.4 mol/cm^2 for 10 min and 1 min ethylene dosing time, respectively. The methodology of the gas flow calculations is presented and discussed in Appendix B.1. The CNT forest thickness on silicon substrates has been evaluated at a range of temperatures from 725 °C down to 645 °C. The CNT forest thickness, directly related to the growth rate, was found to approximately follow the Arrhenius law, as shown in Figure 4.13. The found dependency enables us to control the thickness of the CNT forests grown. We have noted from SEM imaging, that the CNTs grown at 675 °C and lower become crooked and tangled, as presented in Figure 4.14. This effect reflects a deterioration of the CNT quality and, by implication, an expected decrease in their potential mechanical performance. Therefore the temperature of 700 °C is established as the lower limit for the high-quality CNT growth in our system.

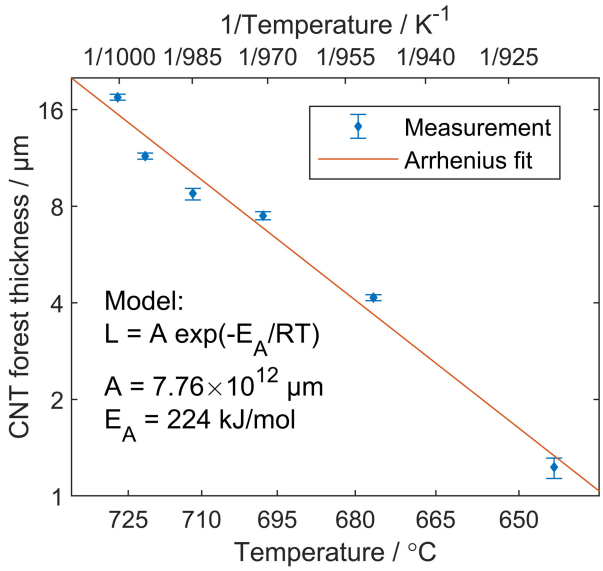

Figure 4.13. CNT forest thickness (logarithmic scale) grown at 1 min ethylene dosing time with respect to the inverse of temperature in K approximately following the Arrhenius law.

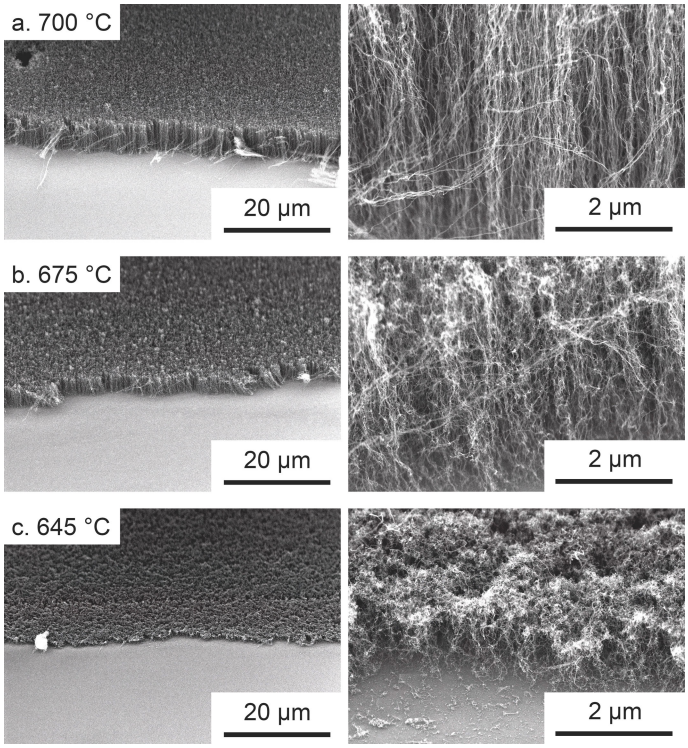

Figure 4.14. SEM images of the CNT forests grown on Si at temperatures of 700 °C and below, illustrating the declining CNT quality towards lower synthesis temperatures. Images on the left- and the right-hand side are taken at two different magnifications, showing the forest overview and detail, respectively.

Figure 4.15 shows SEM of the CNT forests synthesised at temperatures differing by only 5 °C with an ethylene dosing time reduced to 1 min. The CNT forests on the silicon substrates are remarkably uniform, which highlights the beneficial effect of the decrease of the immersion time of the substrate in the iron nitrate solution to 10 min and letting the solution age for 20 min prior to the immersion. High uniformity was also observed on the CFs. The thickness of the CNT forests on the CFs entered the range that we expect to be applicable in composites, being only few micrometre thick, in particular for the 720 °C sample (Figure 4.15c). Notably, the thickness of the CNT forest obtained on the CF is apparently smaller, than the one on the flat silicon substrates in the same conditions. We believe that this

effect is to some extend related to the difference of the surface geometry. The CNTs grown on the flat substrates remain straight due to the physical constraints between the tubes, which is why the CNT tortuosity, areal density and length are intrinsically related to each other [177]. On surfaces of positive curvature, such as the CF, as the CNTs grow radially, at greater distances from the surface there is gradually more space for the CNTs available to occupy. This leads to increased CNT forest tortuosity further from the fibre surface. Therefore, the thickness of the CNT forests can be lower on CF than on the flat silicon at a close actual CNT length.

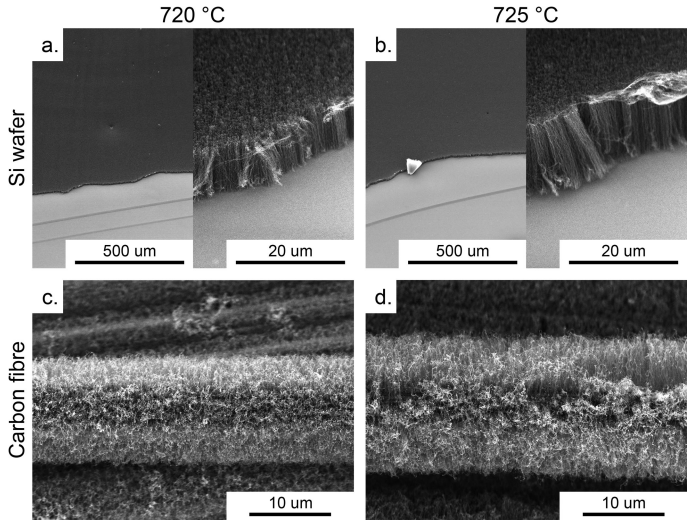

Figure 4.15. CNT growth results on silicon (a,b) and on carbon fibre (c,d) carried out at CVD temperatures of 720 °C (a,c) and 725 °C (b,d) at the ethylene dosing time of 1 min. The samples were coated with the catalyst using the strategy developed in this work, including the amino-silane treatment and ageing of iron nitrate solution. The growth is remarkably uniform, aligned and of the thickness desirable for application in hierarchical composites.

In order to obtain a measure of the uniformity of the CNT growth in the optimised conditions as shown in Figure 4.15a,b., the topography of the CNT forests was evaluated by means of CLSM, a 3D imaging technique. Figure 4.16 shows regions of 1000 µm by 1000 µm of the topography of the CNT forests grown on silicon substrates at 720 °C and 725 °C, respectively, both synthesised with 1 minute of ethylene dosing time. We can see, that the measured height deviates by less than one micrometre within the area of the topography images. The standard deviations of the measured height for the 720 °C and 725 °C synthesis were found to be only 88 nm and 72 nm, which represents only 1.4% and 0.8% of the forest height, respectively.

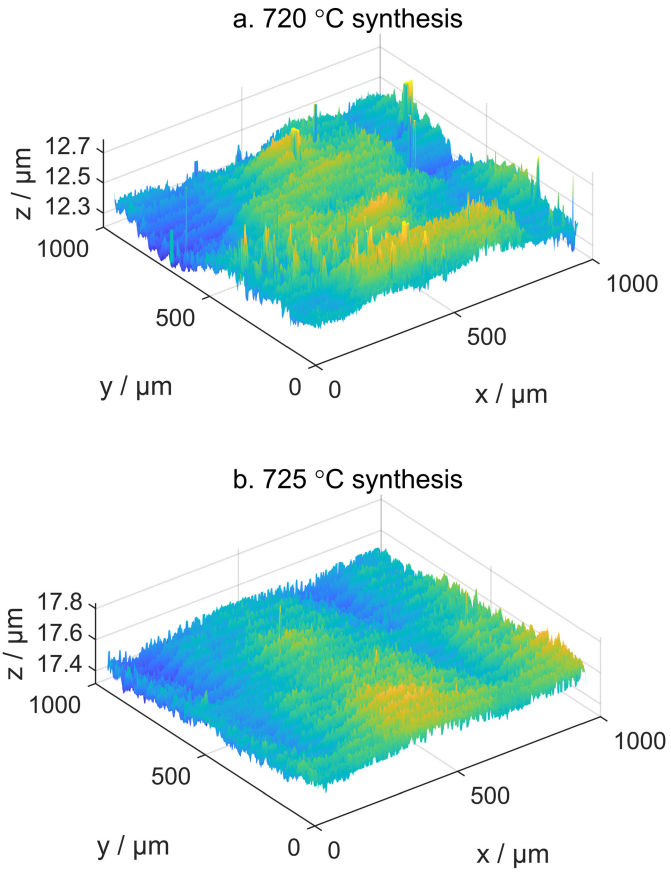

Figure 4.16. Topography of CNT forests synthesised with 1 min ethylene dosing time at the temperatures 720 °C (a) and 725 °C (b). The substrates were coated with the catalyst using the strategy developed in this work, including the amino-silane treatment and ageing of iron nitrate solution. A 5 px × 5 px median was applied to filter out the noise in the images. For better visibility, the scale of the z-axis is enhanced by a factor of 500.

4.4. Conclusions and outlook

In this study, we successfully established a facile route to grow carbon nanotubes in a morphology desired for hierarchical composites, i.e. fulfilling the requirements of high density of CNT forests, radial alignment on carbon fibre, growth uniformity and optimised CNT forest thickness. We confirmed the role of precipitation of iron catalyst precursor from an iron(III) nitrate nonahydrate solution in isopropanol, which is controlled by the ageing time of the solution. We presented a novel strategy for improvements in catalyst coating morphology with application of surface functionalisation with (3-aminopropyl)trimethoxysilane prior to the immersion in an appropriately aged iron nitrate solution. The uniform catalyst coating indeed led to remarkably uniform, dense and aligned CNT forests on CF, and the forest thickness could be controlled by synthesis gas composition and temperature.

Acknowledgements

The authors of the chapter cordially thank Agnese Carino (Bioenergy and Catalysis Laboratory, PSI, Switzerland) for assistance with the DLS experiments, Agnieszka Karpik (Institute of Polymer Engineering, FHNW, Switzerland) for help with the CLSM measurements and Michel Calame (Transport at Nanoscale Interfaces, Empa, Switzerland) for providing access to infrastructure.

Chapter 5

Theory of gas transport in random fibrous structures

"The world as we have created it
is a process of our thinking.
It cannot be changed
without changing our thinking."

Albert Einstein

This chapter presents published work: W. Szmyt, C. Guerra-Nuñez, C. Dransfeld, I. Utke, Solving the inverse Knudsen problem: Gas diffusion in random fibrous media, *J. Membr. Sci.*, 2020

Wojciech Szmyt contributed to this work with conceptualisation, methodology, development of software for formal data analysis, writing of the original draft and visualisation of the data. **Carlos Guerra-Nuñez** assisted with conceptualisation and manuscript review. **Clemens Dransfeld** participated with manuscript review, study supervision, carried out project administration and funding acquisition. **Ivo Utke** took part in conceptualisation, manuscript review, study supervision and project administration.

Abstract

About a century ago, Knudsen derived the ground-breaking theory of gas diffusion through straight pipes and holes, which since then found widespread application in innumerable fields of science and inspired the development of vacuum and related coating technologies, from academic research to numerous industrial sectors. Knudsen's theory can be straightforwardly applied to filter membranes with arrays of extended holes for example, however, for the inverse geometry arrangement, which arises when solid nanowires or fibres are arranged into porous interwoven material (like in carpets or brushes) the derivation of an analytical theory framework was still missing. In this paper, we have identified the specific geometric and thermodynamic parameters that determine the gas diffusion kinetics in arrays of randomly oriented cylinders and provide a set of analytical expressions allowing to comprehensively describe the gas transport in such structures. We confirmed analytical solutions by Monte Carlo simulations. We specify our findings for an atomic layer deposition process, the diffusion of trimethyaluminium molecules into a carbon nanotube array, but highlight the applicability of our derivation for other fields comprising gas diffusion membranes, composite materials, fuel cells and more.

List of symbols

Latin:

d	average fibre diameter
D_b	diffusivity in the bulk gas
D_eff	effective diffusivity
D_K	Knudsen diffusivity
$\widetilde{D}_\mathrm{eff}$	effective diffusivity, reduced
$\widetilde{D}_\mathrm{K}$	Knudsen diffusivity, reduced
$\widetilde{D}_\mathrm{p}$	diffusivity in the viscous flow regime, reduced
d_m	kinetic diameter of a gas molecule
D_p	diffusivity in the viscous flow regime
J	gas flux through the membrane
k	number of spatial dimensions
k_B	Boltzmann's constant
Kn	Knudsen number
l	thickness of the fibrous membrane
L_z	axial length of the simulation volume cylinder
l_0	average fibre length

n	gas concentration
N_A	Avogadro's constant
p	gas pressure
pdf_θ	probability density function of the polar angle
pdf_φ	probability density function of the azimuthal angle
pdf_x	probability distribution of the molecule flight path length
R	universal gas constant
r	distance between fibre axis to the molecule flight trajectory
$\vec{r}_0$	origin point of a generated cylinder
T	Temerature
t_D	diffusion-driven infill time
t_f	mean time of flight of a molecule in the space confined by the fibrous structure
v	mean absolute thermal velocity of gas molecule
x_0	x-coordinate of the origin point of a generated cylinder
y_0	y-coordinate of the origin point of a generated cylinder
z_0	z-coordinate of the origin point of a generated cylinder

Greek:

α	surface area to volume ratio of membrane composed of randomly-oriented cylinders
α_0	surface area to volume ratio of membrane composed of non-intersecting cylinders
Δl	the total length of the fibres within the considered volume element
δl	length of the fibre axis element crossing the molecule flight path collision cylinder
ΔN	number of gas molecules in the volume element considered
$\Delta\vec{r}$	spatial displacement of a single step in the randon walk or orientation vector of a generated cylinder
δs	length of the projection of the fibre axis element crossing the molecule flight path collision cylinder onto the plane perpendicular to the flight path
ΔS	surface area element
Δt	duration of a single step in a random walk

ΔV	element of volume considered
$\Delta\vec{x}$	molecule flight path vector
ε	porosity of a membrane composed of randomly-oriented cylinders
ε_0	porosity of a membrane composed of non-intersecting cylinders
Γ	gas impingement rate
Γ_b	gas impingement rate, classical
λ^2	mean square flight distance of a molecule within the fibrous structure
λ_b	mean free path in the bulk gas
λ_f	mean flight path in the space confined by the fibrous structure
μ	molar mass (subscript indicates the species)
φ	azimuthal angle
σ	fibre axis length per volume
σ_0	areal density of fibres
τ	tortuosity of the random fibrous structure
τ_eff	effective tortuosity
τ_K	Knudsen tortuosity
τ_p	tortuosity of the porous structure
θ	polar angle

5.1. Introduction

A deep understanding of the gas transport in porous media is fundamental in many fields, spanning from the development of fuel cells [178–180], molecular sieving [181], direct contact membrane distillation [182–184], geologic carbon sequestration to management of nuclear waste, and many more [185]. Moreover, knowledge of the gas transport specifics is particularly important in material science, e.g. for a uniform coating of complex porous structures from gas-phase deposition techniques, such as in atomic layer deposition (ALD) [186–192] chemical vapour deposition (CVD) [193] or chemical vapour infiltration (CVI), relevant to numerous sectors in industry [194]. The mechanisms of gas transport in the porous media include viscous flow, surface diffusion, molecular diffusion and Knudsen diffusion [195]. Depending on the physicochemical parameters of a system considered, some of the mentioned mechanisms can be neglected, while other ones prevail and govern the process. Particularly, the Knudsen diffusion becomes significant in the so-called *molecular regime* of gas transport, when the mean free path of gas molecules exceeds the characteristic dimension of the pores. This is why an accurate description of the Knudsen diffusion - and the transition to bulk diffusion - is of great importance for the case of tightly porous media.

Ever since the seminal work of Martin Knudsen [92,196,197], it has been established that modelling the gas transport in the molecular regime requires a detailed analysis of the flight paths of individual molecules. In this regime, the paths are unconstrained by the intermolecular collisions, being hindered only by the solid walls of the medium in which the diffusion occurs. Consequently, the geometry of the porous medium plays a key role in the modelling. Often, the molecular gas transport models for particular geometries are based on probabilistic numerical approaches, such as direct Monte-Carlo methods [198–201] or Markov chains [202]. Analytical expressions are available for relatively simple geometries such as cylindrical pores [92,203], rectangular cross-section trenches [204], tortuous capillaries [205] or randomly packed hard spheres [206], to name a few examples. These expressions are often used as approximations for gas diffusion in more complex media. To the best of our knowledge however, there has been no analytical model for the Knudsen diffusion in randomly-oriented fibrous structures.

In a recent work, Yazdani *et al*. [187] modelled a case that is close to the one considered here, namely, a gas diffusion in vertically-aligned carbon nanotube (CNT) arrays; with the purpose to uniformly coat the nanostructure with ALD. Therein, a cylindrical pore approximation was employed and an expression for an effective pore diameter was proposed. This approach allowed to grasp the general trends of the diffusion coefficient with respect to the average CNT diameter and areal density. In a subsequent work [207], we introduced a diffusion model derived from basic physical principles and obtained an improved expression for the diffusion coefficient in CNT arrays with ideal vertically-aligned geometry. Here, we culminate in deriving a much more general gas diffusion model for real-world fibrous three-dimensional porous structures. It will allow to greatly expand the range of structures for which the close-form equations for gas transport are available, including electrospun fibres [208], curly CNT arrays [91], gas diffusion layers for polymer electrolyte membranes [178] and more. The previous attempts to describe the gas diffusion within random fibrous media [208–211] relied on semi-empirical formulae or probabilistic simulations. Close-form expressions for gas transport parameters in such structures have remained elusive, until now.

The aim of this work was to derive and validate an analytical model for the inverse problem of gas diffusion in random fibrous media. We identify the specific geometrical parameters that determine the gas diffusion kinetics in arrays of randomly oriented cylinders. Expressions for the Knudsen diffusion coefficient and the Knudsen number, which determines the boundary between the Knudsen and bulk diffusion are derived. Moreover, we extend the model to express the effective diffusion coefficient in cases when both Knudsen and bulk diffusion are significant, which is relevant at relatively

higher pressures [212]. Additionally, an expression for a gas impingement rate within such structures is given. We validate the analytical model by means of Monte-Carlo simulations.

5.2. Assumptions of the model

To specify the applicability of the model presented in this work, we list and discuss the model assumptions. The model presented in this work accounts for both the Knudsen diffusion and a transition to the bulk gas diffusion. While the bulk gas diffusion is already well-described and understood, initially we describe the diffusion in the purely molecular regime. The continuous extension to transition- and bulk diffusion regime is described in section 5.3.

In the following derivation, the gas transport within the nanostructure is assumed to occur in a molecular regime, i.e. the mean free path in the bulk gas λ_b at the gas concentrations considered is much longer than the mean flight path of a molecule in the space confined by the walls of the porous structure λ_f. It is established for an ideal gas [213], that the λ_b is expressed as

$$\lambda_\mathrm{b} = \frac{k_\mathrm{B} T}{\sqrt{2} p \pi d_\mathrm{m}^2}, \tag{5.1}$$

where the k_B is the Boltzmann's constant, T – temperature, d_m – gas molecule diameter, p – gas pressure. The λ_f, referred to in the further part of this work as *mean flight path*, needs to be expressed specifically for the given porous structure geometry and in this work we are establishing it for an array of randomly-oriented cylinders.

Effectively, intermolecular collisions are neglected, only the molecule-wall collisions are accounted for. This assumption comes down to ensure that the Knudsen number Kn, as we defined below, is much higher than 1,

$$\mathrm{Kn} \coloneqq \lambda_\mathrm{b}/\lambda_\mathrm{f} \gg 1, \tag{5.2}$$

while the molecular flow component is stated to become apparent at Kn=1 or greater [214,215]. Notably, in literature, a slip-flow regime is sometimes specified for $\mathrm{Kn} \in (0.001, 0.1)$ [178], however in this work we are limiting the division into bulk gas diffusion regime, transition regime and molecular regime, for simplicity and clarity. The Kn is conventionally defined as a ratio of λ_b to the inner diameter of the given pipe. It has been established so, because for the cylindrical pores, the λ_f is in fact equal to the pore diameter. However, in the inverse Knudsen problem that we are considering, there are no pores *per se*. This is why we are proposing the unambiguous definition of the Knudsen number (5.2), which is applicable to all kinds of porous structures, including the curly fibre bushes.

We are treating the subsequent flights of a molecule from one wall collision to another as a random walk process, consisting of the following steps:

- Collision of a molecule with a cylinder wall,
- Release of a molecule from the cylinder surface following the Lambert's law of emission,
- Free flight of a molecule from one cylinder wall to another at a speed corresponding to the mean absolute velocity v from the Maxwell-Boltzmann distribution,
- Collision of a molecule with another cylinder wall.

The mean absolute velocity v is expressed as

$$v = \sqrt{\frac{8RT}{\pi\mu}}, \tag{5.3}$$

where T is temperature, R – universal gas constant, μ – molar mass of the diffusant.

Due to the strictly random orientations and locations of the cylinders, the angle of emission of a molecule is immediately "forgotten" by the molecule upon release – mathematically, it has no bearing on the molecule flight distance. Notably, this is contrary to the anisotropic case of unidirectional cylinders, where the release angle is in fact the key factor determining the path length between subsequent collisions [207].

Following the Einstein-Smoluchowski model [216,217], the diffusion coefficient for a random walk is expressed as

$$D_{\mathrm{K}} = \frac{\langle|\Delta\vec{r}|^2\rangle}{2k\langle\Delta t\rangle}, \tag{5.4}$$

where $|\Delta\vec{r}|$ is a single random walk step distance, Δt - its duration, whereas k – the number of dimensions in which the diffusion is considered. The triangular brackets represent an expected value of the given random quantity. Given the formula (5.4) it becomes clear that in order to fundamentally describe the Knudsen gas transport, it is crucial to accurately capture the statistical nature of the molecule scattering, as done for instance by Colson *et al.* for the case of cylindrical nanopores [218].

In general, if the geometry of the porous structure considered is anisotropic, the diffusion needs to be expressed in each independent dimension. For instance, in our previous work [207] where we considered an anisotropic diffusion within arrays of unidirectional cylinders. Therein, the 1-dimensional (k=1) diffusion along the direction of fibre axis and the transverse 2-dimensional diffusion (k=2) needed to be evaluated separately. In this work however, as the considered geometry of tortuous cylinder arrays is isotropic by nature, the 3-dimentional isotropic diffusion model (k=3) is developed.

We define the t_{f} as the mean time of flight of a molecule in the space confined by the structure

$$t_{\mathrm{f}} \coloneqq \langle\Delta t\rangle \tag{5.5}$$

and λ^2 as the mean square flight distance of the molecule in the confined space, or *mean square displacement*

$$\lambda^2 \coloneqq \langle|\Delta\vec{r}|^2\rangle, \tag{5.6}$$

both of which are determined by the geometry of the specific type of the porous structure.

5.3. Generalisation towards a transition to a viscous regime at high pressures

Although in the derivations in this work a purely molecular regime of gas transport is considered, the results obtained are straightforwardly generalised to account for a continuous transition to a bulk diffusion regime, where Kn takes values of the order of magnitude of unity or smaller. It is important in cases where the gas pressure is relatively high, e.g. in the spatial ALD [212] or CVD [219].

The effective diffusion coefficient D_{eff} can be expressed in terms of the Knudsen diffusivity D_{K} and the diffusivity through the porous medium in a purely viscous regime D_{p},

$$D_{\mathrm{eff}} = \frac{1}{\frac{1}{D_{\mathrm{K}}} + \frac{1}{D_{\mathrm{p}}}}. \tag{5.7}$$

In the work of Poodt *et al*. [212], D_{p} has been simply approximated as the bulk gas diffusivity D_{b}, from the classical gas kinetics [213] being

$$D_{\mathrm{b}} = \frac{\lambda_{\mathrm{b}} v}{3}. \tag{5.8}$$

This approximation however does not account for the fact, that even in a purely viscous gas transport regime the diffusivity of gas through the porous medium is not equivalent to the bulk diffusivity [220]. It is so, because the cross section of gas flow is reduced by the factor of porosity ε and the concentration gradient is applied over a longer path due to tortuosity of the porous structure τ_{p}. Hence, the expression for the diffusion coefficient in porous structures in viscous regime is

$$D_{\mathrm{p}} = \frac{\varepsilon}{\tau_{\mathrm{p}}} D_{\mathrm{b}}. \tag{5.9}$$

The geometrical factors ε and τ_{p} are discussed in more detail in the further part of this work.

5.3.1. Reduced diffusivity

In the context of gas transport in porous media, the diffusivity is often expressed in a reduced form as a ratio between the diffusivity in porous medium to the diffusivity in the bulk gas [221–223]. Particularly, the reduced diffusivity in the viscous regime in becomes

$$\widetilde{D}_{\mathrm{p}} = \frac{D_{\mathrm{p}}}{D_{\mathrm{b}}} = \frac{\varepsilon}{\tau_{\mathrm{p}}}. \tag{5.10}$$

We can express the effective diffusivity accounting for both Knudsen and viscous diffusion in the dimensionless terms analogously,

$$\widetilde{D}_{\mathrm{eff}} = \frac{D_{\mathrm{eff}}}{D_{\mathrm{b}}} = \frac{\varepsilon}{\tau_{\mathrm{eff}}}, \tag{5.11}$$

where the reduced diffusivity is denoted with a $\widetilde{D}_{\mathrm{eff}}$ and an effective tortuosity τ_{eff} is implicitly defined. If we additionally define a *Knudsen tortuosity* τ_{K} analogously as the τ_{p} in equation (5.9), we obtain

$$D_{\mathrm{K}} = \frac{\varepsilon}{\tau_{\mathrm{K}}} D_{\mathrm{b}}, \qquad \widetilde{D}_{\mathrm{K}} = \frac{\varepsilon}{\tau_{\mathrm{K}}}, \tag{5.12}$$

$$D_{\mathrm{eff}} = \frac{\varepsilon}{\tau_{\mathrm{K}} + \tau_{\mathrm{p}}} D_{\mathrm{b}}, \qquad \widetilde{D}_{\mathrm{eff}} = \frac{\varepsilon}{\tau_{\mathrm{K}} + \tau_{\mathrm{p}}}. \tag{5.13}$$

The form of equations (5.11-1313) shows, that the tortuosity contributions originating from different factors add up to an effective tortuosity. The physical meaning of τ_{K} becomes clear with the completed derivation of the D_{K} in section 5.4.5.

5.4. Transport of gas between randomly-oriented fibres

Examples of locally randomly oriented fibres are shown in Figure 5.1. The interwoven CNTs (Figure 5.1a) were synthesised on an alumina-coated Si wafer by catalytic CVD – the synthesis details available elsewhere [127]. Figure 5.1b depicts a nanoscale fibrous structure of cellulose aerogel[2], whereas Figure 5.1c shows mullite microfibres[3]. Similar arrangements can be found in materials like electrospun fibre mats, recycled carbon fibre, *etc*. We are deriving a new set of parameters describing the kinetics of the gas transport within such structures accounting for the specifics of their geometry.

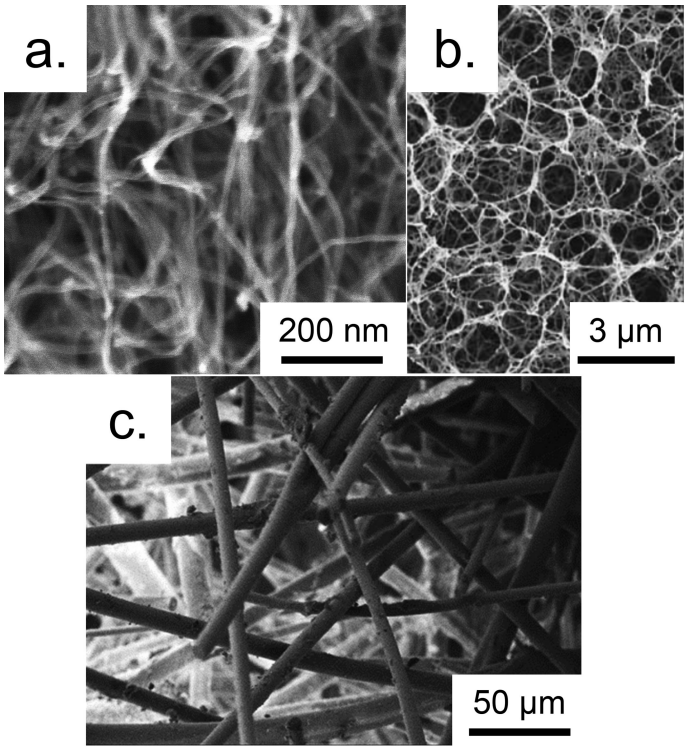

Figure 5.1. Example SEM images of randomly oriented fibrous structures; a) CNTs, b) cellulose aerogel[2], c) mullite fibres[3]

5.4.1. Definition of the structure geometry

Figure 5.2 schematically illustrates the geometry considered, based on the CNTs as grown by means of catalytic CVD on a planar substrate (Figure 5.2a) and straight random fibres (Figure 5.2b). The substrate is shown for illustrative purposes only, while it does not affect the diffusion within the membrane. The fibrous mat is of approximately uniform thickness, l. The constituent

[2] Reprinted from [224] Colloids and Surfaces A: Physicochemical and Engineering Aspects, Vol. 240, Issue 1-3, H. Jin, Y. Nishiyama, M. Wada and S. Kuga, Nanofibrillar cellulose aerogels, Pages 63-67, Copyright 2004, with permission from Elsevier.
[3] Reprinted from [225] Journal of the European Ceramic Society, Vol. 36, Issue 6, J. He, X. Li, D. Su, H. Ji and X. Wang, Ultra-low thermal conductivity and high strength of aerogels/fibrous ceramic composites, Pages 1487-1493, Copyright 2016, with permission from Elsevier.

cylinders are randomly-oriented or tortuous (locally random in orientation), of an average length l_0 and diameter d.

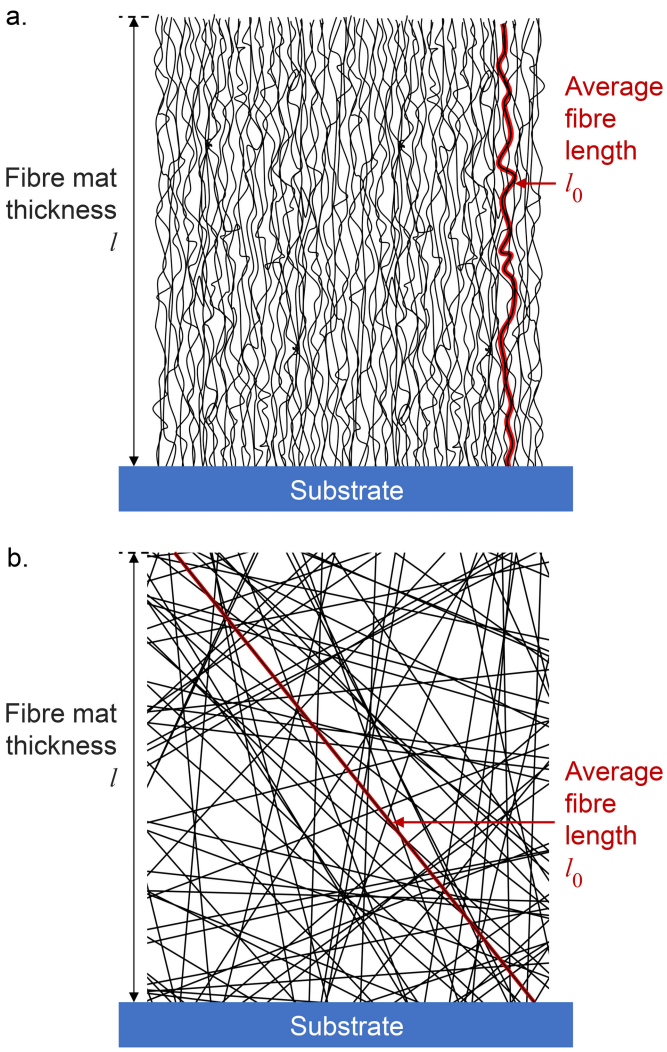

Figure 5.2. Side-view schematic illustration of mats of randomly-oriented fibres: a) tortuous and b) straight. The average fibre length l_0 and fibre mat thickness l are denoted.

In such a case, one can define an *average cylinder axes length per volume* σ

$$\sigma \coloneqq \frac{\Delta l}{\Delta V} = \frac{\Delta S \sigma_0 l_0}{\Delta V} = \frac{l_0}{l}\sigma_0 = \tau\sigma_0, \tag{5.14}$$

where ΔV is the volume considered, ΔS – the substrate surface in the representative volume, Δl is the total length of fibres in this volume, σ_0 is the areal density of the cylinders on the substrate, whereas the $\tau \coloneqq l_0/l$, by one of the common simple definitions, represents *tortuosity* [226]. Consequently, the axes length per volume σ also has a meaning of an *effective areal density* of the cylinders on the substrate. For the perfectly isotropic orientations, the τ equals

$$\tau = 2, \tag{5.15}$$

which is shown in Appendix C.1. Due to the random and isotropic nature of the defined system, it is safe to assume, that the tortuosity of the pores between the fibres is the same as the tortuosity of the fibres themselves, therefore τ from equation (5.15) can be substituted into equation (5.9) as τ_{p}.

The other key parameters describing the structure are the surface-area-to-volume ratio α_0,

$$\alpha_0 = \sigma\pi d \tag{5.16}$$

and the volume fraction of the void or *porosity* ε_0,

$$\varepsilon_0 = 1 - \sigma\frac{\pi d^2}{4}. \tag{5.17}$$

The simplistic expressions (5.16,17) hold under an assumption that the fibres are not intersecting or that the intersections between the fibres can be neglected. There are cases however, when the intersections do occur and need to be accounted for. One of such cases is the coating of dense carbon nanotube arrays with thin films, especially if the film thickness is of the order of magnitude of the nanotube diameter or greater. The intersections alter the contribution of individual fibres to the surface area and to the void volume fraction. It is so, because the intersecting cylinder volumes count only once, whereas the intersecting cylinder surfaces do not count at all. The following expressions for the surface area to volume ratio α and porosity ε do account for the intersecting cylinders:

$$\alpha = \sigma\pi d \exp\left(-\sigma\frac{\pi d^2}{4}\right), \tag{5.18}$$

$$\varepsilon = \exp\left(-\sigma\frac{\pi d^2}{4}\right). \tag{5.19}$$

The derivations of (5.18,19) can be found in Appendix C.2. On note is that, equations (5.18,19) converge asymptotically to equations (5.16,17), respectively, for small $\sigma\pi d^2/4$ as shown in Figure 5.4a,b. Moreover, they are applicable for every fibre orientation distribution, such as vertically aligned cylinders, as considered in our earlier work [207], and tortuous fibres, as herein. The d and σ are experimentally accessible in a relatively straightforward way, for instance by coupling BET surface area measurements and SEM imaging or directly by means of nano- or microtomography.

Although the expressions (5.16-19) are not crucial for the further derivations in this work, we are providing them for the benefit of the scientific community, with a view for the experimental evaluation of the geometrical parameters in the forthcoming studies. Nonetheless, while in the analytical derivations we are assuming perfectly random orientations and positions of the cylinders without any hindrance to cylinders crossing, equations (5.18) and (5.19) reflect the theoretically considered case.

5.4.2. Regular porous structures vs. inverse porous structures

Equation (5.18) reveals at which fibre diameter the geometry turns from an inverse-porous to a regular porous structure, e.g. in cases where a growing film infills a nanowire array, aerogel or fibre fabric to a compact nanocomposite in the CVI process. We notice, that it is characteristic for the inverse porous structures that their surface area to volume ratio α increases as the film thickness increases. Examples of such structures include CNT or nanowire arrays, fibre carpets, fibrous aerogels, *et cetera*. The regular porous structures exhibit a decrease in α with the increasing coating thickness,

as schematically illustrated in Figure 5.3. Examples of such porous structures include anodic alumina porous membranes (and others geometrically alike), cracks in solids, microchannels and opals, to name a few. This finding allows us to establish a clear geometrical distinction between the inverse and regular porous structures.

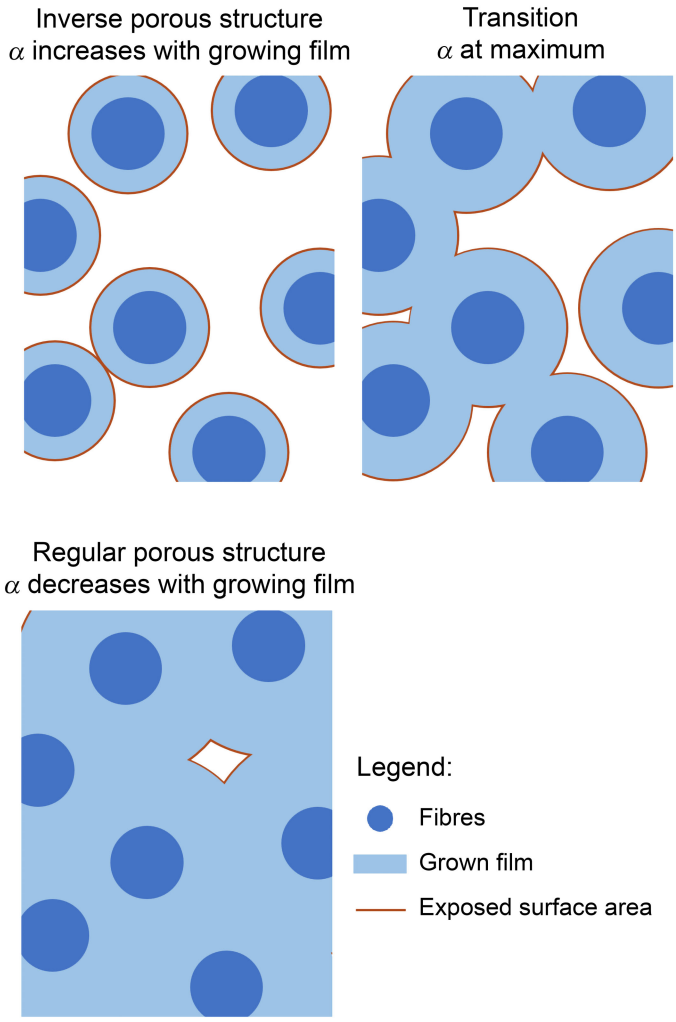

Figure 5.3. Schematic illustration of the variation in the surface area to volume ratio α with increasing thickness of the coating film infilling the fibrous structure – a transition from an inverse to a regular porous structure.

The expression (5.18) reflects both the regular- and inverse behaviours and a transition between them, as seen in Figure 5.4a. The maximum possible value of α for the given σ is equal $\sqrt{2\pi\sigma/e}$ and it is reached at the d=$\sqrt{2/(\pi\sigma)}$. This finding is relevant for the applications in which maximizing the surface area to volume ratio of the porous structure is of interest. Interestingly, the d=$\sqrt{2/(\pi\sigma)}$ is also an inflection point of the ε (5.19), which means that at this critical cylinder diameter the void volume fraction begins to flatten out to converge asymptotically to 0 at high d.

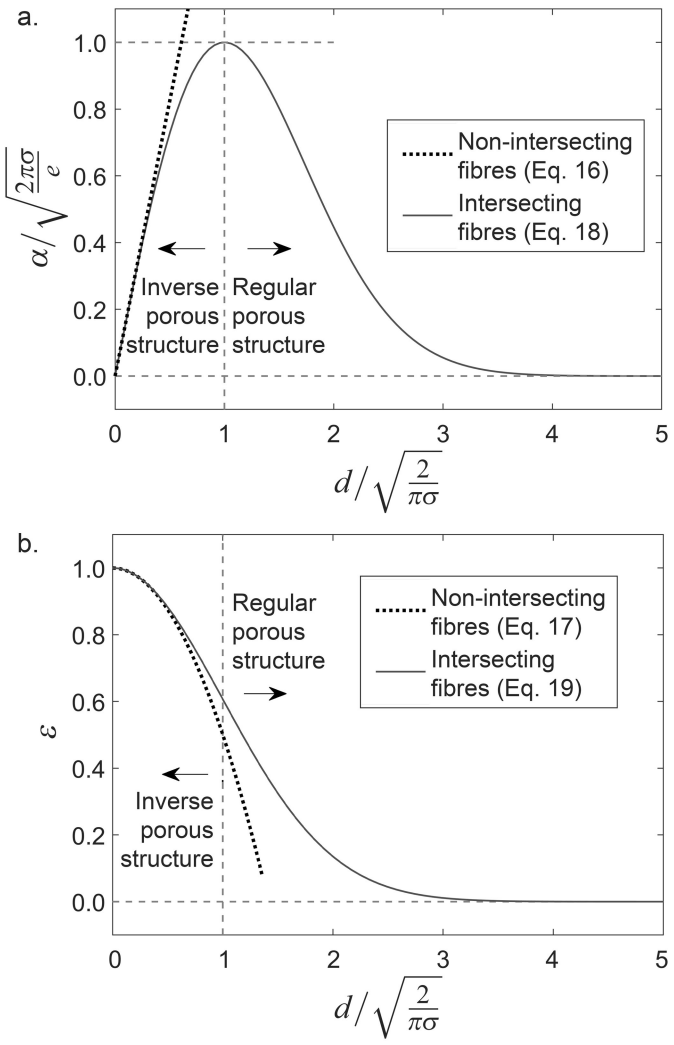

Figure 5.4. The surface area to volume ratio α (a) and void volume fraction ε (b) in arrays of the cylinders of diameter d. The axes are scaled to the characteristic values for generality. Orthogonal dashed lines were added to guide the eye. Inverse and regular porous structure regimes are indicated. The values of ε for non-intersecting fibres are plotted up to the physical limit of close-packing of cylinders.

5.4.3. Isotropic fibre orientations – angular distribution

In the derivations, we are assuming that the cylinders are randomly oriented and locally straight, i.e. the radius of curvature is much larger than the individual cylinder diameter. To describe the orientations of the cylinders, we are using the isotropic angle distribution expressed in the spherical coordinate system:

$$\mathrm{pdf}_{\varphi}(\varphi) = \frac{1}{2\pi}, \qquad \varphi \in [0,2\pi), \tag{5.20}$$

$$\mathrm{pdf}_{\theta}(\theta) = \sin\theta\,, \qquad \theta \in \left[0,\frac{\pi}{2}\right], \tag{5.21}$$

where φ and θ represent the azimuthal and polar angle, respectively, whereas the $\mathrm{pdf_s}$ denotes the probability density function of the quantity given in the subscript s. Due to the isotropy, the orthogonal reference frame can be defined freely at the convenience of particular derivation.

5.4.4. Mean molecule flight path

Analogously, as in our previous work [207], we derive the mean flight path λ_f and a mean flight time τ_f of a molecule in the given porous geometry. For simplicity, we are assuming that the size of the gas molecules is much smaller than the diameter of the cylinders. To account for the finite molecule diameter, one can use the equations obtained here, with the cylinder diameter d increased by $2d_m$, d_m being the molecular diameter.

The molecule on a straight path $\Delta\vec{x}$ can only encounter a fibre wall if the fibre axis crosses a cylindrical space of a diameter equal d axially oriented along the molecule flight path $\Delta\vec{x}$, which is illustrated in Figure 5.5. This cylinder is referred to as *molecule path cylinder*.

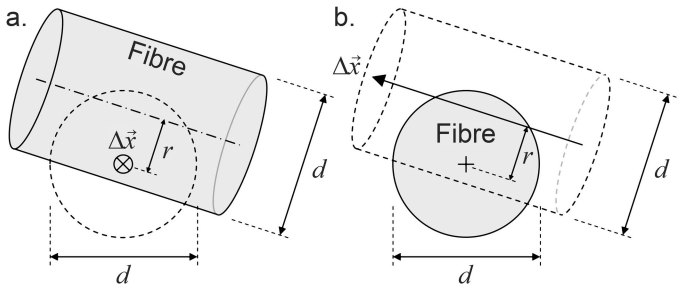

Figure 5.5. Projected views of the molecule flight path $\Delta\vec{x}$ encountering a fibre of a diameter d. The molecule's path cylinder is denoted with dashed lines. Distance r of fibre axis to the axis $\Delta\vec{x}$ needs to be smaller than $d/2$ so that the molecule hits the fibre wall.

The expected length of fibre axes Δl within the volume of molecule path cylinder is expressed following the definition (5.14),

$$\Delta l = \sigma \Delta V = \sigma \frac{\pi d^2}{4} |\Delta\vec{x}|. \tag{5.22}$$

The λ_f can be defined as the $|\Delta\vec{x}|$, for which the expected number of encountered fibres is 1. In other words, the $|\Delta\vec{x}|$ is equal to λ_f when the Δl is equal to the average length of a single fibre axis $\langle\delta l\rangle$ crossing the cylinder, which is expressed mathematically

$$\Delta l = \langle\delta l\rangle \Rightarrow |\Delta\vec{x}| = \lambda_f. \tag{5.23}$$

The geometry that is the basis for the following derivation is illustrated in Figure 5.6. The distance r of the fibre axis to the molecule path cylinder axis is uniformly distributed,

$$\mathrm{pdf}_r(r) = \frac{2}{d}, \qquad d \in \left[0, \frac{d}{2}\right). \tag{5.24}$$

It results from the fact that from the perspective along the molecule flight path axis, the fibre presents itself as a two-dimensional stripe-shaped target of a width d (see: Figure 5.5) and there is no preference

to any particular distance r. The validity of this assumption is further substantiated by a stochastic simulation in the Appendix C.5.

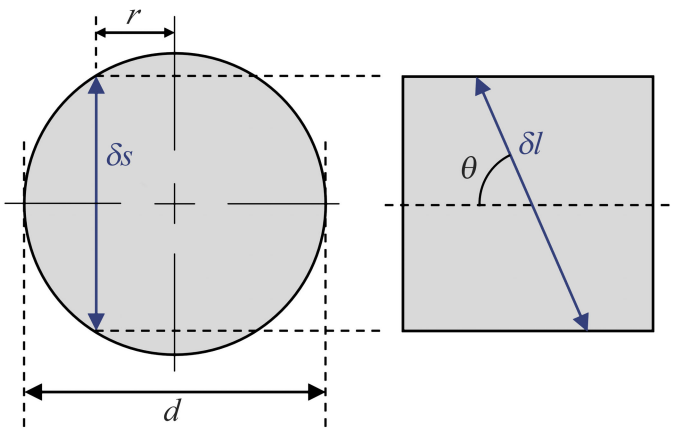

Figure 5.6. Illustration of the geometry of the fibre axis crossing the molecule path cylinder; projected cross-sectional view along and perpendicular to the molecule path cylinder axis. The δs is the length of the element of the fibre axis crossing the molecule flight path cylinder projected onto the plane normal to the flight path. The δl is the actual length of the fibre axis element.

In the derivation of $\langle \delta l \rangle$, it is convenient to initially obtain the projection of δl onto the plane perpendicular to the $\Delta\vec{x}$, denoted as δs. Based on the geometry presented in Figure 5.6, the δs is expressed as

$$\delta s = d\sqrt{1-\left(\frac{2r}{d}\right)^2}. \tag{5.25}$$

Given the δs, the angle θ and the probability distributions (5.21) and (5.24), we obtain the δl,

$$\delta l = \frac{\delta s}{\sin\theta}, \tag{5.26}$$

and its expected value,

$$\langle \delta l \rangle = \int_0^{d/2} \mathrm{pdf}_r(r)\delta s(r)\mathrm{d}r \int_0^{\pi/2} \mathrm{pdf}_\theta(\theta)\frac{1}{\sin\theta}\,\mathrm{d}\theta = \frac{\pi^2 d}{8}. \tag{5.27}$$

Ultimately, taking equation (5.22), condition (5.23), and substituting equation (5.27), we obtain

$$\lambda_\mathrm{f} = \frac{\pi}{2}\frac{1}{\sigma d} = \frac{\pi^2}{2}\frac{\varepsilon}{\alpha}. \tag{5.28}$$

In our previous work [207], section *Probability distribution of the transverse penetration distance*, we justified that the probability distribution function $\mathrm{pdf}_x(x)$ of the molecule flight path length x follows the Beer-Lambert law,

$$\mathrm{pdf}_x(x) = \frac{1}{\lambda_\mathrm{f}} e^{-\frac{x}{\lambda_\mathrm{f}}}. \tag{5.29}$$

The same holds for the case considered in this work.

5.4.5. Mean flight time and diffusion coefficient

Knowing the distribution of the molecule flight path and taking the mean absolute velocity of a molecule v as obtained from Maxwell-Boltzmann distribution, we can define the mean flight time

$$t_\mathrm{f} \coloneqq \langle \Delta t \rangle = \frac{\lambda_\mathrm{f}}{v} = \frac{\pi}{2}\frac{1}{v\sigma d} = \frac{\pi^2}{2}\frac{\varepsilon}{v\alpha}. \tag{5.30}$$

We express the mean square displacement as

$$\lambda^2 = \langle x^2 \rangle = \int_0^\infty x \, \mathrm{pdf}_x(x) = 2\lambda_\mathrm{f}^2 \tag{5.31}$$

set k=3 in equation (5.4), as such isotropic diffusion is 3-dimentional, ultimately obtaining the expression for the Knudsen diffusion coefficient of randomly oriented cylinder arrays,

$$D_\mathrm{K} = \frac{2\lambda_\mathrm{f}^2}{2 \cdot 3t_\mathrm{f}} = \frac{v\lambda_\mathrm{f}}{3} = \frac{\pi}{6}\frac{v}{\sigma d} = \frac{\pi^2}{6}\frac{\varepsilon v}{\alpha}. \tag{5.32}$$

We can define the Knudsen tortuosity τ_K in analogy to the diffusivity in viscous regime expressed with equation (5.9),

$$D_\mathrm{K} = \frac{\varepsilon}{\tau_\mathrm{K}} D_\mathrm{b} \Rightarrow \tau_\mathrm{K} \coloneqq \frac{2}{\pi^2}\lambda_\mathrm{b}\alpha. \tag{5.33}$$

From equation (5.33) we can see, that τ_K is proportional to the surface area enhancement of a membrane per thickness equal to λ_b and $2/\pi^2$ is a proportionality coefficient. This statement is elaborated on in the Appendix C.3.

5.4.6. Knudsen number

Knowing the λ_f, it is straightforward to establish the Knudsen number Kn, following the definition (5.2),

$$\mathrm{Kn} = \frac{\lambda_\mathrm{b}}{\lambda_\mathrm{f}} = \frac{\frac{k_\mathrm{B}T}{\sqrt{2}p\pi d_\mathrm{m}^2}}{\frac{\pi}{2}\frac{1}{\sigma d}} = \frac{\sqrt{2}\sigma d k_\mathrm{B}T}{\pi^2 p d_\mathrm{m}^2} = \frac{\sqrt{2}}{\pi^3}\frac{\alpha}{\varepsilon}\frac{k_\mathrm{B}T}{p d_\mathrm{m}^2}. \tag{5.34}$$

5.4.7. Impingement rate

By definition, the impingement rate Γ is the number of molecules ΔN that hit the surface area ΔS within the time Δt,

$$\Gamma \coloneqq \frac{\Delta N}{\Delta S \Delta t}. \tag{5.35}$$

We set the number of molecules to the average number in the given volume of void within the nanostructure, given the gas concentration n (molecules per unit volume),

$$\Delta N = n\varepsilon\Delta V. \tag{5.36}$$

The surface area is

$$\Delta S = \alpha\Delta V. \tag{5.37}$$

The Δt is effectively the mean time between collisions, while in this time each molecule should hit the surface once on average,

$$\Delta t = t_{\mathrm{f}}. \tag{5.38}$$

Putting together equations (5.35-38), we obtain

$$\Gamma = \frac{n \cdot \varepsilon\Delta V}{\alpha\Delta V \cdot t_{\mathrm{f}}} = \frac{\varepsilon n}{\alpha t_{\mathrm{f}}} = \frac{2nv}{\pi^2} \approx 0.203 \cdot nv, \tag{5.39}$$

which has the same dependency on the gas concentration n and mean absolute velocity v as the bulk gas impingement rate from the classical gas kinetics Γ_{b},

$$\Gamma_{\mathrm{b}} = \frac{nv}{4} = 0.25 \cdot nv, \tag{5.40}$$

differing only slightly by a numerical multiplicative factor – approx. 0.203 vs. 0.25. The impingement rate onto cylinder walls in the molecular regime needs to be described with Eq. (5.39), whereas the impingement rate onto a macroscopic object placed within the fibre bushes (e.g. a substrate or large particles), follows the classical expression for Γ_{b}, as expanded on in the Appendix C.4.

5.5. Comparison of the analytical model with Monte-Carlo simulation results

The key parameter that fundamentally describes the gas transport kinetics is the mean flight path λ_{f}, while the other parameters (diffusion coefficient D, impingement rate Γ and Knudsen number Kn) are intrinsically based on its value. Therefore, we have designed a Monte Carlo (MC) simulation to verify the validity of the derivation of λ_{f} presented in section 5.4.4. The simulation is based on generation of randomly-oriented cylinders within the specifically chosen simulation volume and measuring the distance of flight of a molecule from the release from a given cylinder wall to the collision with another cylinder.

5.5.1. Simulation algorithm

We have established, that we can limit the simulation volume ΔV to the molecule path cylinder (see: Appendix C.5). The geometry for the fibre generation is illustrated in Figure 5.7. We define the cylinder to be of diameter equal to the diameter of the fibres and of length L_z equal to 10× the expected mean

flight path λ_f described with the derived equation (5.28). Subsequently, the fibre axis lines are generated within the cylinder volume the following way. The origin point r_0=(x_0,y_0,z_0) of each line is randomised, so that

$$\begin{cases} x_0 = r\cos\varphi \\ y_0 = r\sin\varphi, \end{cases} \tag{5.41}$$

where r is generated by the distribution (5.24) and φ by (5.20), whereas the z_0 is uniformly distributed within [0, L_z]. The orientation of the fibre axis is defined by a vector $\Delta\vec{r}$=(Δx,Δy,Δz), where

$$\begin{cases} \Delta x = -\sin\varphi\sin\theta \\ \Delta y = \cos\varphi\sin\theta \\ \Delta z = \cos\theta \end{cases}. \tag{5.42}$$

The φ is the same as for generating r_0, and θ is generated by the distribution (5.21). A periodic boundary condition is applied to the bases of the simulation volume cylinder, which means that if the line is found to cross any of the bases of a cylinder, it is continued at the other base with the same orientation and origin shifted by $\pm L_z$, the sign depending which base was crossed. Examples of such random fibre generation are visualised in Figure 5.8, where the cylinders of d=20 nm and σ=10^{11} cm^{-2} were generated within a cylinder of a larger diameter equal 3×d (Figure 5.8a-c) and 11×d (Figure 5.8d) and shown only within the diameter 2×d (Figure 5.8a-c) and 10×d (Figure 5.8d). In the simulation we generate the cylinders in $x\in(0, 10\times\lambda_f)$, however the cylinders in Figure 5.8 are rendered only within $x\in(0, 3\times\lambda_f)$ for illustrative purposes.

The length of the fibre axis segment crossing the molecule flight cylinder δl is evaluated for each generated fibre. The generation of fibres continues until a total length of fibre axes Δl=$\sigma\Delta V$ is reached, as required by equation (5.14).

We define a 1D grid of 0.5 nm pitch along the flight path coincident with the axis z. The evaluation of the flight path length is based on finding the value of z_r, corresponding to the z coordinate of release of a molecule from the fibre surface, and finding the z_c corresponding to the collision of a molecule with the other fibre. The flight path length Δz is evaluated as a difference between z_c and z_r. The exact procedure is described in more detail in the Appendix C.6. The entire process is repeated multiple times for each choice of σ and d in order to obtain enough statistics of the flight path lengths.

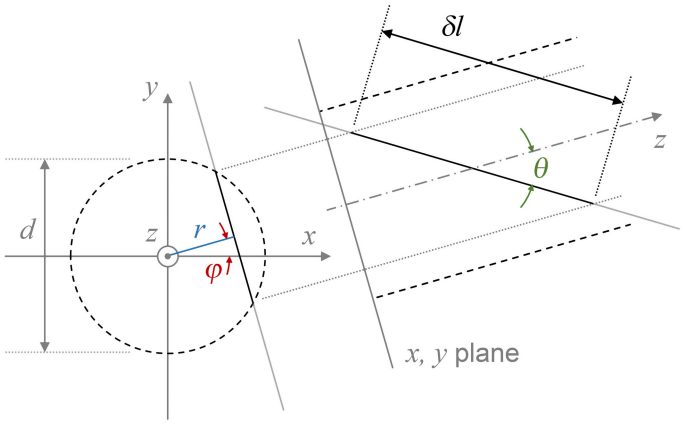

Figure 5.7. Schematic illustration of the geometry used for the generation of the fibres within the molecule path cylinder presented in two projections. The dashed line represents the molecule path cylinder, the dashed-dotted vector is the collision cylinder axis, the solid line is the axis of the fibre crossing the molecule path cylinder.

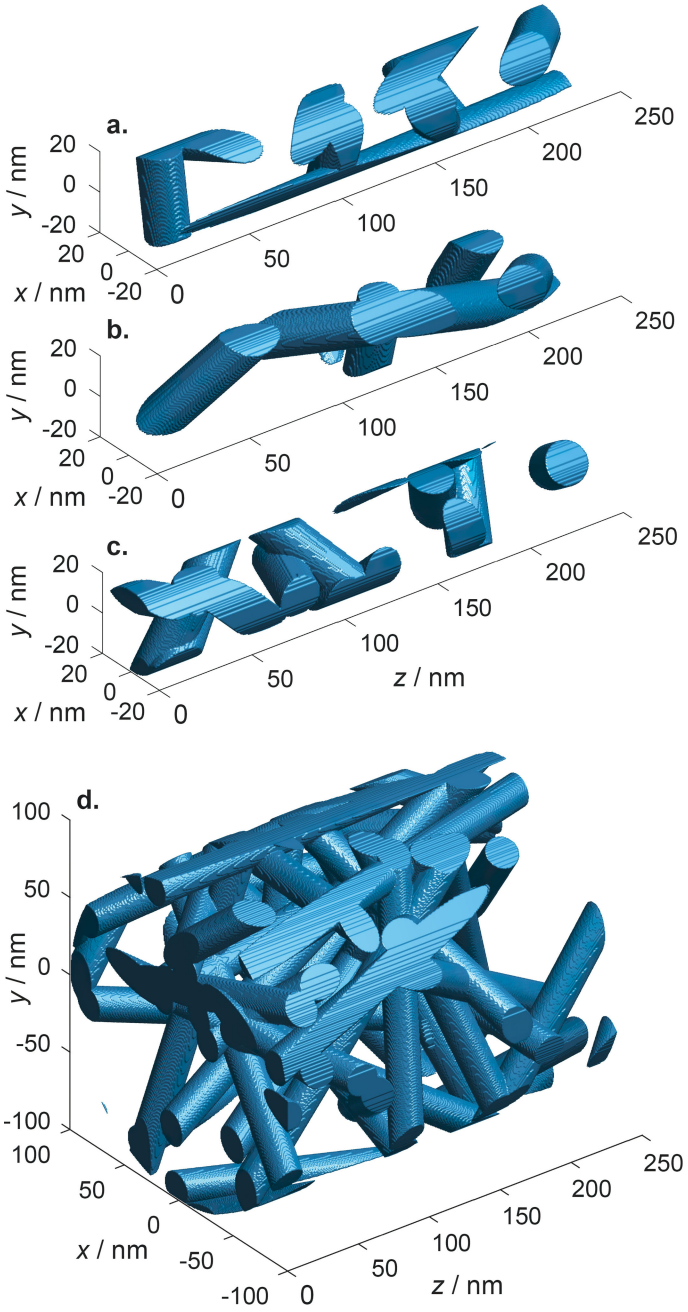

Figure 5.8. Example of 3D visualisations of the random fibre generation for the diameter d=20 nm, axes length per volume σ=10^{11} cm^{-2}; a-c shown within a cylinder of diameter equal 2×d (a-c) and in a cylinder of diameter 10×d (d).

5.5.2. MC Simulation results compared with analytical model

We evaluated 7 different values of d ranging from 20 to 50 nm at a constant σ equal 6×10^{10} cm^{-2} and 5 different values of σ ranging from 2×10^{10} to 10×10^{10} cm^{-2} at a constant d equal 30 nm. The number of repetitions was chosen to be 10^6. Histograms of the set of obtained values of Δz have been evaluated at 20 bins between 0 and 5×λ_f, normalised to the number of counts in the first bin. The histograms were compared to the analytically obtained probability density functions of the mean flight path (5.29), where the values of the function (5.29) were proportionally rescaled in a way for the function to return 1 at the location of the first bin. The results are presented in Figure 5.9.

The agreement between the analytically obtained flight path distribution and the one obtained by the stochastic simulation is excellent, which allows us to confirm that the formula for the mean flight path λ_f derived in section 5.4.4 is correct, as well as the t_f, D, Kn and Γ, all of which depend on the λ_f directly.

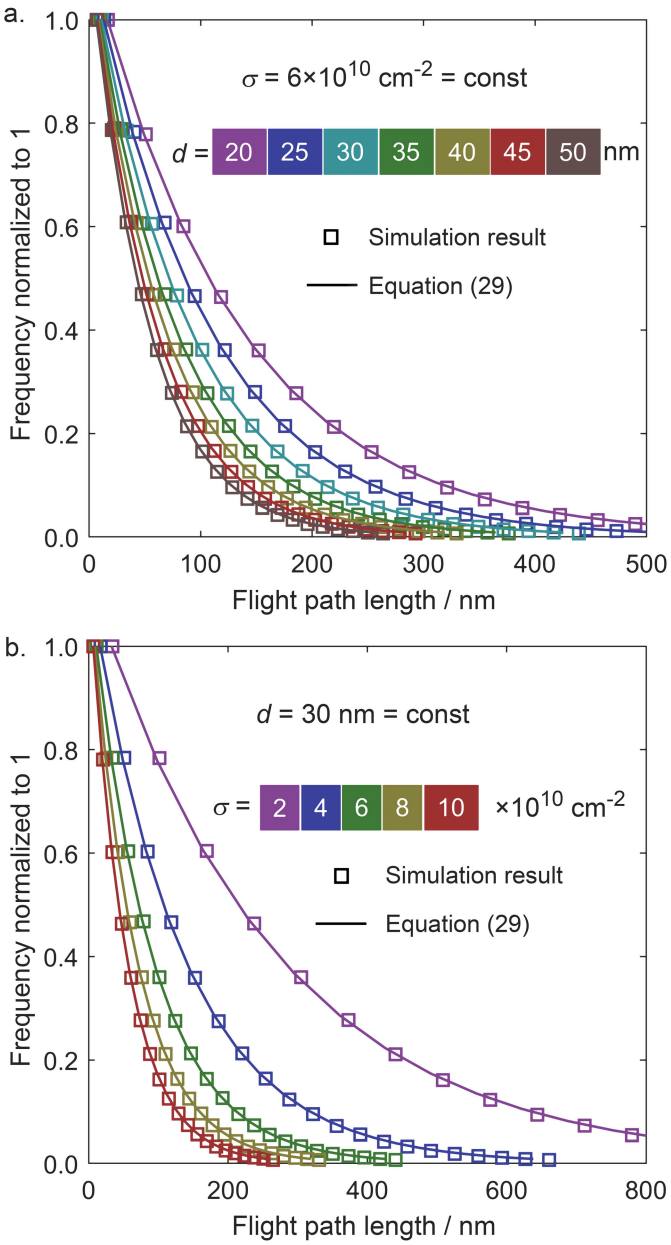

Figure 5.9. The histogram data of the flight path length distribution compared to the analytically evaluated probability distribution; a) varying fibre diameter d at constant fibre axes length per volume σ, b) varying σ at constant d. We are emphasizing, that the solid lines are not a fitting result, but they are directly calculated using equation (5.29) and normalised to the height of the first bin. The number of MC repetitions 10^6 ensures that the relative uncertainties of the bin heights are negligible.

5.6. Practical calculations

5.6.1. Diffusion coefficient for atomic layer deposition on carbon nanotubes

In this section, we are evaluating the diffusion coefficient for a model case of atomic layer deposition of Al_2O_3 on arrays of CNTs. The diffusing species that we consider here is the trimethylaluminium (TMA) gas precursor–used typically for ALD of Al_2O_3 together with H_2O, O_2 or O_3 as the oxygen

precursor [227]. We set the temperature to 225 °C (498.15 K) and pressure equal to 1 mbar. At these conditions the TMA exists primarily in a monomeric form, although a significant amount of a dimer might be present as well [228]. For simplicity, we are considering only the monomer of a molar mass equal μ_{TMA}=72.09 g/mol. The diffusion coefficient has been evaluated for a range of values of σ from 2×10^{10} to 10×10^{10} cm^{-2} and d from 7 to 30 nm, realistic for the ALD-coated CNTs. The mean absolute velocity is calculated from the Maxwell-Boltzmann distribution. The results are shown in Figure 5.10a. The diffusivity exhibits a decreasing behaviour both with respect to the increasing d and σ.

The same conditions were used to calculate the effective diffusivity using equation (5.7) at a range of pressures from 10^0 to 10^4 mbar, corresponding to the transition from the molecular regime to the viscous regime of gas flow. As an example, let us consider the value of d=20 nm. The results of the calculations described previously are shown in Figure 5.10b, where the bulk diffusivity and Knudsen diffusivity top limits are indicated as well. Notably, the Knudsen diffusivity does not depend on the pressure, because in this regime the intermolecular collisions are neglected. However, at an increasing pressure, the bulk diffusivity becomes a limiting factor for the diffusion, which comes from the fact, that at higher gas concentrations the intermolecular interactions begin to play a role.

Additionally, we evaluated the characteristic time of diffusion-driven infill (alternatively: evacuation) of the structure with gas t_D. It is estimated as a time, for which the diffusion length equals the thickness of the membrane. Consider the CNT mat of a thickness l=1 mm. While the diffusion length can be estimated as $(Dt)^{0.5}$, we obtain

$$t_D = \frac{l^2}{D}. \tag{5.43}$$

The estimation is shown in the right axis of the graph in Figure 5.10b. We need to emphasise, that the t_D is not equivalent to the time required for a conformal coating of the CNTs with ALD. For this purpose a scaling law for conformal coating of CNTs needs to be derived accounting for surface reactions, analogously as in the work of Yazdani *et al.* [187]. It is however, a good estimate of the time for which a steady state of diffusion is reached within the membrane.

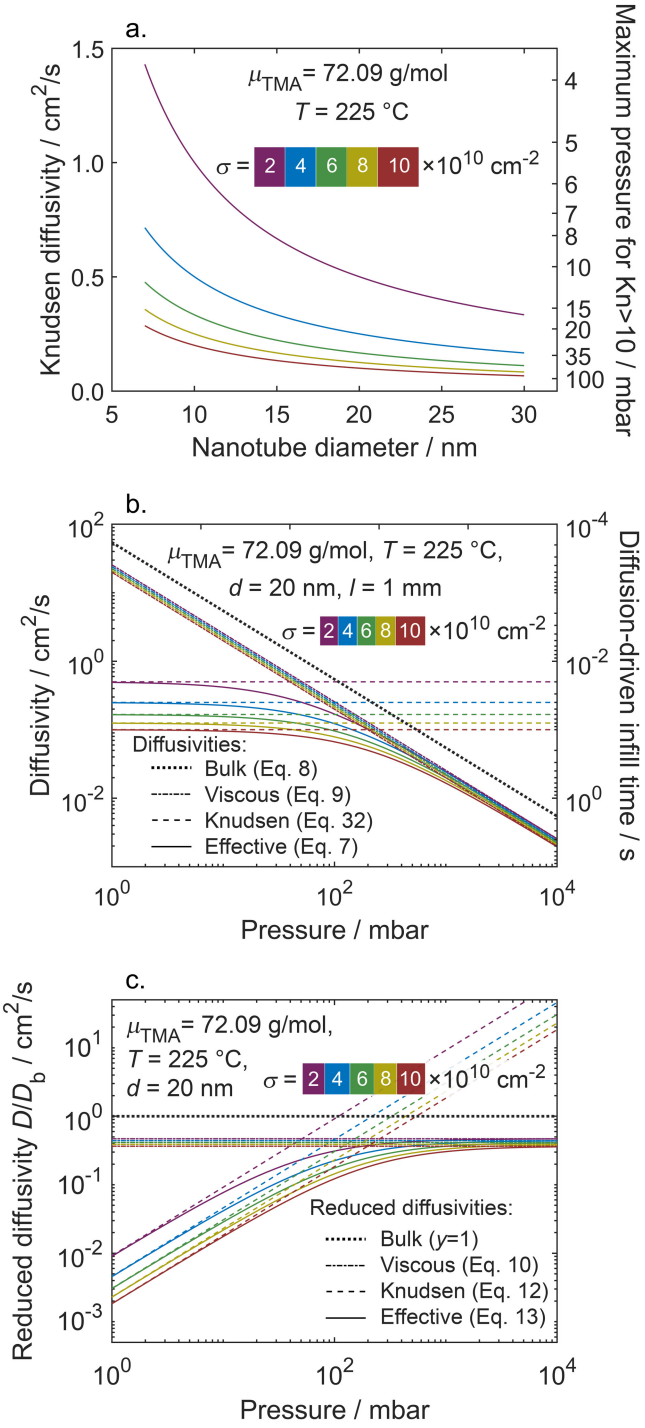

Figure 5.10. Example calculations of the diffusivity of TMA in a molecular regime (a) and in a transition regime (b,c) in arrays of tortuous carbon nanotubes for given values of nanotube diameter d and fiber axes length per volume σ. The diffusivity is presented both directly (b), as well as in a reduced form (c), normalised to the bulk diffusivity. The bulk diffusivity is plotted for reference. Additionally, a maximum pressure for the Knudsen regime (Kn>10) is indicated on the right axis of (a) and a diffusion-driven infill time is indicated on the right axis of (b).

5.6.2. Gas flux through a fibrous membrane in Knudsen regime

In this paragraph, we provide an example implementation of our diffusion theory in estimation of fluxes of different gases through a fibrous membrane, specifically in the Knudsen regime. A flat membrane is

considered as a simple example, however one needs to keep in mind, that the theory is applicable to more complex geometries as well.

The diffusion-driven gas flux within the membrane J is expressed as [229]

$$J = -D_{\mathrm{K}} \frac{\mathrm{d}n}{\mathrm{d}z}, \tag{5.44}$$

where n is the gas concentration in terms of number of molecules per volume, z – position coordinate across the membrane. In this formulation, the flux J refers to the number of molecules crossing the unit surface area of the membrane per unit time. Let us consider the case, when the concentration of the diffusant on one side of the membrane is n_{D}, whereas beyond the membrane it is negligible or equal 0, which is fulfilled either when the membrane is exposed to vacuum or to another gas, without the diffusant under consideration. The system is schematically illustrated in Figure 5.11.

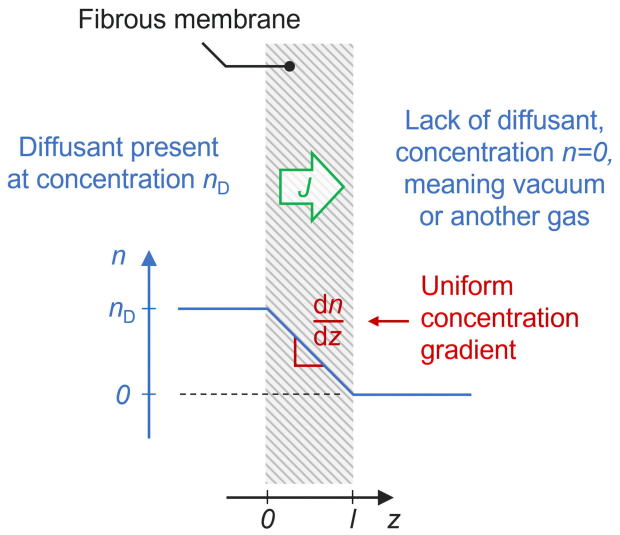

Figure 5.11. Schematic illustration of the considered system of gas flow through a fibrous membrane. Gas concentration and position coordinate are indicated with the respective axes.

Integrating equation (5.44) across the coordinate z, we obtain

$$J = D_{\mathrm{K}} \frac{n_{\mathrm{D}}}{l}. \tag{5.45}$$

Furthermore, we substitute the diffusivity D_{K} from equation (5.32), mean absolute thermal velocity of gas molecules v from (5.3) and express n_{D} in terms of temperature T and pressure p_{D}, utilizing the ideal gas law. Thus, the expression for the gas flux becomes

$$J = \frac{1}{3}\sqrt{\frac{2\pi}{\mu_{\mathrm{D}} RT}}\frac{1}{l\sigma d} N_{\mathrm{A}} p_{\mathrm{D}} = \frac{1}{3}\sqrt{\frac{2\pi}{\mu_{\mathrm{D}} RT}}\frac{\pi\varepsilon}{\alpha l} N_{\mathrm{A}} p_{\mathrm{D}}. \tag{5.46}$$

The form of equation (5.46) reveals that at the given diffusant pressure p_{D}, the flux is inversely proportional both to the square root of temperature T and to the square root of molecular weight of the diffusant μ_{D}. Owing to the theory of gas diffusion in random fibrous media developed

in this work, the dependence of J on the geometric parameters of the membrane is simply captured by the multiplicative term $(l\sigma d)^{-1}$ or $\pi\varepsilon(\alpha l)^{-1}$, equivalently.

We demonstrate the calculations for gases covering a range of molar masses from 4 to 146 g/mol: helium (He), water (H_2O), oxygen (O_2), chlorine (Cl_2) and sulfur hexafluoride (SF_6). The fluxes are estimated for temperatures form 20 to 300 °C (293 to 573 K). We consider a CNT membrane of thickness l=1 mm, axes length per volume σ=6×10^{10} cm^{-2} and CNT diameter d=20 nm. In such a membrane, the mean flight path of the gas molecules is estimated as ca. 130 nm, according to equation (5.28). The diffusant pressure p_D=20 mbar is chosen, so that the Knudsen number Kn is greater than 10 for all the cases, ensuring the Knudsen gas transport regime. According to equation (5.34), the lowest Knudsen number is obtained for the largest kinetic diameter d_m at the lowest temperature T considered. Sulfur hexafluoride has the largest kinetic diameter of all the gases considered d_m=550 pm [56], whereas the lowest temperature considered is T=293 K. Substituting these values to equation (5.34) together with p_D=20 mbar, we obtain Kn≈11.5, which confirms Knudsen flow conditions throughout the parameter range in the calculations. The results are shown in Figure 5.12.

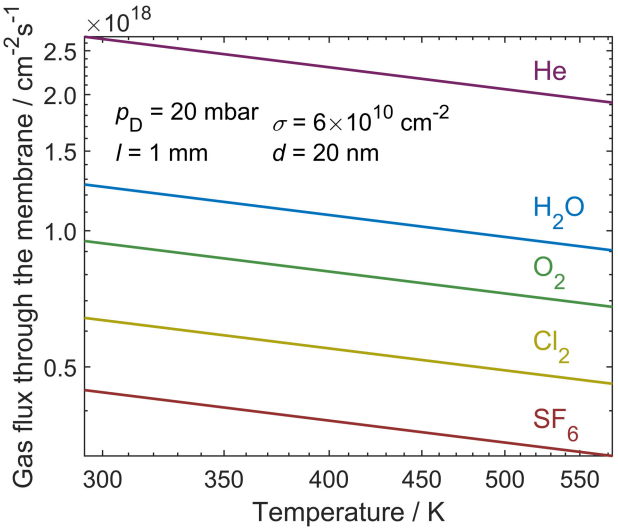

Figure 5.12. Results of example calculations of gas flux through a fibrous membrane, shown on a dual logarithmic scale plot. In the figure, the physical parameters which were kept constant are indicated: gas pressure p_D, membrane thickness l, fibre axes length per volume σ and fibre diameter d. A range of gases has been considered: helium (He), water (H_2O), oxygen (O_2), chlorine (Cl_2) and sulfur hexafluoride (SF_6), covering a range of molar masses from 4 to 146 g/mol.

The graph in Figure 5.12 reveals the dependence of the gas flux on temperature as well as on the molar mass – lighter and cooler gasses diffuse faster at the given pressure, which is characteristic to the Knudsen diffusion and can be utilised for the purpose of gas filtering. The gas fluxes obtained in our calculations are of the order of magnitude of 10^{18} molecules per square centimeter of the membrane per second.

5.7. Conclusions and outlook

We have developed a new theoretical framework for the Knudsen diffusion in randomly oriented fibrous media and a transition to bulk gas diffusion regime. The model is derived from the basic physical principles, which gives an advantage over empirical or probabilistic approaches in terms of generality, simplicity and wide applicability. Moreover, the analytical expressions provided allow for straightforward development of scaling laws for various processes involving numerous gas transport processes in various fibrous media. This includes for instance, the prediction of the gas exposure required for a conformal coating of CNTs with ALD, or for a complete infiltration of fibrous structures

for composites in CVI, estimation of the growth rate of CNTs synthesised by CVD in case of significant diffusion limitation of the growth, or optimizing the properties of fibrous membranes for the desired gas transport performance in given conditions, among other examples. We have provided a comprehensive set of analytical expressions for the gas diffusion parameters: Knudsen number (5.34), Knudsen diffusivity (5.32), effective diffusivity accounting for transition to bulk diffusion (5.7), mean flight path confined by the structure (5.28), mean time between subsequent molecule-wall collisions (5.30) and the impingement rate (5.39). The set of geometrical parameters determining the Knudsen diffusion is narrowed down to the mean fibre diameter and the fibre length per unit volume, both of which are accessible experimentally in a straightforward way, e.g. by tomography or by coupling microscopy and BET surface area measurements. The present model can serve as a base to generalise the description of gas transport within fibres that are quasi-unidirectional, conceptually between ideally straight (as described in our previous work [207]) and isotropically oriented, like herein. We plan to implement the presented theoretical framework into more complex processes involving e.g. pressure differential, thermal gradient, surface- or gas phase chemical reactions, physisorption, surface diffusion and thermal decomposition. These findings have a substantial impact in various fields of science and technology such as membrane science, composite and nanocomposite technologies, gas phase functionalisation, thin film coating by CVD or ALD, CNT synthesis and more.

Acknowledgements

The author cordially thanks the members of the Nanolino group at the Physics Department, University of Basel, Switzerland and members of the Swiss Nanoscience Institute for insightful comments.

Chapter 6

Atomic layer deposition on porous substrates: from general formulation to fibrous substrates and scaling laws

"Have the courage to follow
your heart and intuition.
They somehow already know
what you truly want to become."

Steve Jobs

This chapter presents unpublished work, to be submitted for publication in a journal.

Wojciech Szmyt contributed to this work with conceptualisation, methodology, development of software for formal data analysis, experimental investigation, writing of the original draft and visualisation of the data. **Carlos Guerra-Nuñez** assisted with conceptualisation and manuscript review. **Lukas Huber** took part in experimental investigations and writing the original manuscript. **Clemens Dransfeld** participated with manuscript review, study supervision, carried out project administration and funding acquisition. **Ivo Utke** contributed with conceptualisation, manuscript review, study supervision and project administration.

Abstract

Atomic Layer Deposition (ALD) is a technique of choice for uniform, conformal coating of substrates of complex geometries, owed to its characteristic self-limiting surface reactions upon sequential exposure to precursor vapours. In order to achieve the uniform coating however, a sufficient gas exposure needs to be provided. This requirement becomes particularly relevant for highly porous and high aspect-ratio substrates, where the gas transport into the substrate structure is limited by diffusion (diffusion-limited regime), or for ALD precursor systems exhibiting low surface reaction rate (reaction-limited regime). The sufficient exposure is often determined experimentally, this approach is however highly inefficient, requiring extensive screening for large ranges of system parameters for each distinct type of substrate, precursor system or ALD reactor operating mode. It is therefore beneficial to predict the process regime and employ appropriate scaling laws in the selection of experimental parameters. In this chapter, a kinetic diffusion-reaction continuum model of ALD on high surface area substrates is developed, applicable both for regular and inverse porosity of the substrates. We begin with formulation of the continuum model of a single cycle ALD based on the notation of Yanguas-Gil *et al.* (2017). We introduce a new parametrisation of the system based on its natural system of units, dictated by the scales of the physical phenomena governing the process. We present a range scaling laws valid for a general porous substrate, which scale intuitively with the natural units of the system. The scaling laws describe the coating depth in a diffusion-limited regime with respect to the gas exposure, chemisorption coverage in a reaction-limited regime with respect to the gas exposure, the width of the reaction zone in the diffusion-limited regime. Expressing the ALD continuum model in terms of its natural units facilitated new physical insights. For the first time, the distinction between diffusion- and reaction-limited ALD regimes is directly quantitatively related to the width of the reaction zone and the profile of chemisorption coverage in a single cycle ALD, all of them being determined by the natural length unit of the system. Moreover, we find that the Knudsen number for the given type of a porous structure is uniquely and solely determined by the value of the so-called gas excess number. This means, that if the diffusion occurs in a Knudsen regime, the frozen surface approximation is necessarily justified; i.e. the time for the gas flux to equilibrate within the porous structure is much shorter than the time necessary for the conformal coating. The new insight into the phenomena governing the process is given. Further on, we particularise the model system for the multicycle diffusion-limited coating of random fibrous mats and present experiment of ALD on forest of tortuous carbon nanotubes (CNTs). We specify the general scaling law for coating depth in the diffusion-limited regime for the particular case of CNT substrate, which gives an expression for the diameter profile of the coated CNTs in a multicycle ALD. The surface area of coated CNTs determined by the Brunauer–Emmett–Teller (BET) method for krypton sorption measurements, the gas exposure estimated based on the analysis of the pulsing pressure curve allow to predict the diameter profile and compare it with the diameters measured by SEM, giving an excellent agreement. The results constitute a validation of the modelling carried out in this work. Moreover, the theoretical framework describing gas transport in random fibrous media introduced in the previous chapter is validated as well.

List of symbols

Latin:

A	total surface area of carbon nanotubes coated with ALD
D	Knudsen diffusivity
d	carbon nanotube diameter
d_{aux}	auxiliary variable defined for expression of diameter profile

d_{m}	molecule diameter
d_{max}	maximum diameter of carbon nanotubes coated with ALD
d_{mini}	minimum diameter of carbon nanotubes
$d_{\mathrm{N_2}}$	nitrogen molecule kinetic diameter
d_{TMA}	trimethylaluminium molecule kinetic diamete
h	layer thickness increment in a single ALD cycle,
h_{T}	Thiele number
J	classical gas impingement rate
J_{wall}	gas impingement rate onto walls of porous nanostructure
k	proportionality constant relating d_{aux} and z
k_{B}	Boltzmann's constant
Kn	Knudsen number
l	thickness of the porous structure
$\mu_{\mathrm{Al_2O_3}}$	molar mass of alumina
$\mu_{\mathrm{N_2}}$	molar mass of nitrogen
μ_{TMA}	molar mass of trimethylaluminum
n	precursor gas concentration
$\bar{n}$	precursor gas concentration, dimensionless
n_0	precursor gas concentration unit
N_{A}	Avogadro's constant
N_{cyc}	number of ALD cycles
N_d	number of diameter measurements
n_{R}	precursor concentration in ALD reactor over sample
$\bar{n}_{\mathrm{R}}$	precursor concentration in ALD reactor over sample, dimensionless
p	precursor pressure
P/P_0	relative pressure in Brunauer–Emmett–Teller (BET) surface area measurement
$p_{\mathrm{N_2}}$	partial pressure of nitrogen

p_{TMA}	partial pressure of trimethylaluminium
$\varrho_{\mathrm{Al_2O_3}}$	density of ALD-deposited alumina
S	surface area of silicon wafer support covered by carbon nanotubes
$\bar{s}$	pore wall surface area to pore volume ratio
s_0	surface area of a reactive surface site
t	time
$\bar{t}$	time, dimensionless
T	absolute temperature
v	mean absolute velocity from Maxwell-Boltzmann distribution
w_{II}	width of the reaction zone
z	spatial coordinate of depth into the porous structure
$\bar{z}$	spatial coordinate of depth into the porous structure, dimensionless
z_{c}	depth reached by ALD coating in a given cycle in diffusion-limited regime

Greek:

α	ratio of pore wall surface area to the total volume of membrane
β_0	initial reaction probability upon collision of precursor molecule with available surface site
ε	porosity
λ_{b}	mean free path of precursor molecule in bulk gas
λ_{f}	mean flight path of a molecule confined by the porous structure
Φ_{wall}	gas exposure experienced by walls of the porous structure
σ	fibre axes length per volume
τ_{c}	mean diffusion time until chemisorption (time unit)
τ_{f}	mean flight time of a molecule confined by the porous structure
Θ	ALD surface coverage

6.1. Introduction

6.1.1. Background

Atomic Layer Deposition (ALD) is a thin-film synthesis technique, which allows to achieve an atomic thickness precision, conformal, pinhole-free coating of highly complex substrate geometries, such as high aspect-ratio structures [106,186], porous structures [230,231] and high-surface-area materials [232]. In particular, coating of carbon nanotubes (CNTs) with ALD has been a widely pursued topic, due to the attractive physical properties of CNTs, including their outstanding electrical conductivity and high surface area. ALD coating of CNTs finds applications in synthesis and tailoring the properties of novel functional materials for energy storage [233–235], energy conversion [236], photocatalysis [237–239], biosensing [240,241] and more.

ALD is a variant of chemical vapour deposition, which relies on a sequential exposure of the substrates to the chemical vapours, referred to as *precursors*, which undergo self-limited chemical reactions on the substrate surface, referred to as *chemisorption*. Typically, the ALD process is designed with the aim of obtaining a conformal coating. For this purpose, two main conditions need to be fulfilled. First, the substrate surface needs to have a high density of reactive surface sites, while low densities tend to result in an island-like growth instead of a conformal film [242,243]. This issue is especially important in coating of CNTs, due to their intrinsic chemical inertness [244]. It has been addressed, for instance, by applying a plasma treatment [242,243], exposure to ozone [245], a non-covalently adsorbed nucleation layer of NO_2 [246] or by tailoring the synthesis temperature throughout the process [188,242]. The other condition for the conformal coating is the sufficient exposure to the precursor species [233,246], so that the surface reactive sites are uniformly covered in each cycle. This necessitates both providing the sufficient amount of the precursor (relevant for the ultrahigh surface area materials), as well as letting the precursor exposure time long enough for the diffusion to drive the precursor molecules to the available reactive sites (relevant for tightly porous substrates). The diffusion and precursor supply limitation can be also turned into an advantage in synthesis of intentionally non-conformal coatings, such as fine-tuned pore openings [247] or functional coating of the topmost features of the high aspect-ratio structure [248]. It becomes clear, that for design and optimisation of the ALD on porous media, a rigorous modelling is needed, accounting for the gas transport and reaction kinetics, and the emerging scaling laws.

A thorough review of various approaches to the modelling of ALD on porous nanostructures can be found in the recent work of Cremers *et al*. [249], including ballistic, Monte-Carlo, continuum, analytical and semi-analytical models. In this work, we aim to describe the process behaviour of ALD by a continuum model, analytically distinguish the diffusion-limited and reaction-limited ALD process, establish analytical scaling laws for coating depth in diffusion-limited regime and surface coverage in reaction-limited regime. The continuum model introduced in this work follows the notation of Yanguas-Gil and Elam [250,251]. The model accounts for a langmuirian chemisorption and diffusion of the precursor species within the porous nanostructure. We introduce a novel parametrisation of the model in the natural system of units imposed by the phenomena governing the process. This approach allows for elucidating the physical effect of the process parameters on the system behaviour and for establishing the new scaling laws for a general case of ALD on arbitrary porous substrates. We present a new physical insight into the problem of ALD coating of porous substrates, quantitatively describing the distinction of the ALD coating regimes, the single-cycle coating profile shape and their inherent interdependence. Finally, we particularise the model for the case of ALD coating of random fibrous structures and experimentally validate its performance in predicting the coating profile in a multicycle ALD coating compared to the experiment on a CNT forest substrate. Moreover, the experimental results constitute a validation of the Knudsen diffusion model in fibrous structures, developed in our previous work [252].

6.1.2. The continuum diffusion-reaction model

In the formulation of the continuum model of ALD on porous nanostructures we follow the notation of Yanguas-Gil [251]. The model is used in this work in the context of coating of CNT carpets, we are however emphasizing that the applicability of the model encompasses the entire variety of porous substrates, provided that the specified parameters for the given substrate structure are determined. The model assumes a uniform diffusivity and pore surface area to pore volume ratio within the substrate, and an irreversible Langmuirian adsorption of molecules, referred to as *chemisorption*. In one dimension, the model is expressed with the following set of differential equations:

$$\begin{cases} \dfrac{\partial n}{\partial t} = -J_{\mathrm{wall}}\beta_0\bar{s}(1-\Theta) + D\dfrac{\partial^2 n}{\partial z^2}, \\ \dfrac{\partial \Theta}{\partial t} = J_{\mathrm{wall}}\beta_0 s_0(1-\Theta) \end{cases} \tag{6.1}$$

where n, t, D, z, β_0, $\bar{s}$, J_{wall}, Θ and s_0 represent volumetric gas concentration (number of gas molecules per volume), time, diffusivity, axial coordinate, reaction probability upon collision of a precursor molecule with an available surface site, pore wall surface area to pore volume ratio, gas impinging rate onto pore walls, surface coverage and an average surface area of an adsorption site, respectively.

From the classical kinetic theory of gases, the gas impingement rate is

$$J = \frac{nv}{4}, \tag{6.2}$$

the v being the mean thermal velocity of precursor molecules. Here however, we express the impinging rate in a more general form, specific to porous nanostructures denoted as J_{wall}

$$J_{\mathrm{wall}} = \frac{n}{\tau_{\mathrm{f}}\bar{s}}, \tag{6.3}$$

where τ_{f} is the mean time of flight of a precursor molecule in the space confined by the nanostructure, which is related to the mean flight path length between subsequent molecule-wall collisions λ_{f},

$$\tau_{\mathrm{f}} = \frac{\lambda_{\mathrm{f}}}{v}. \tag{6.4}$$

Although in the cylindrical pores the impinging rate J_{wall} as described with equation (6.3) is equivalent to (6.2), we argue that it is not the case in general, as presented in the previous chapter of this thesis for the case of fibrous membranes [252]. Moreover, D and $\bar{s}$ can be set as position-dependent in 3 dimensions, reflecting the inhomogeneous geometry. In the inhomogeneous formulation of the problem however, the diffusion term in the model (6.1) needs to be generalised as either $\partial/\partial z(D\partial n/\partial z)$ or $\nabla(D\nabla n)$, depending whether the problem is one- or three-dimensional, respectively. The anisotropy of diffusivity can be captured by expressing D as a diffusion tensor instead of a scalar, also possibly position-dependent. In this work however we analyse the simple case of one-dimensional diffusion invariable with in position, therefore D is set as a scalar. The value or expression for D depends on the gas pressure as well [212], because pressure affects the mean free path of molecule in a gas and thus, determines the diffusion regime. The ratio of the mean free path in bulk gas λ_{b} to the mean flight length between subsequent molecule-wall collisions λ_{f} is referred to as *Knudsen number*, Kn,

$$\mathrm{Kn} = \frac{\lambda_\mathrm{b}}{\lambda_\mathrm{f}}. \tag{6.5}$$

For tightly porous structures at low gas pressures Kn is much greater than 1, which determines the Knudsen regime of gas diffusion. In this regime the intermolecular collisions can be neglected and the molecule flight paths are ballistic [92,196]. In the opposite case, when Kn≪1, the diffusion occurs in a viscous regime, whereas the intermediate values of Kn~1 define a transition regime of diffusion. The model discussed here remains valid in any diffusion regime, however when we particularise the model for the case of coating of CNT arrays, a purely Knudsen regime of diffusion is assumed.

Notably, $\bar{s}$ can be expressed as

$$\bar{s} = \frac{\alpha}{\varepsilon}, \tag{6.6}$$

where α and ε represent the surface area to volume ratio and porosity, respectively. We are considering nanostructures fixed on planar substrates on the bottom, whereas the top side is exposed to the precursor gas. Hence, the boundary conditions for the gas phase are

$$n(z = 0, t) = n_\mathrm{R}(t), \tag{6.7}$$

$$D\frac{\partial n}{\partial z}(z = l, t) = 0, \tag{6.8}$$

where n_R is the precursor concentration in the reactor, to which the structure is exposed, whereas l is the total thickness of the structure. The condition (6.7) reflects the continuum requirement, which is that the concentration of gas at the top of the nanostructure must be the same as directly above the nanostructure. Whereas, the condition (6.8) is equivalent to forcing the gas flux to be equal zero at the coordinate of the substrate[4].

As we assume no precursor gas in the pores of the structure initially, the initial condition for n is

$$n(z, t = 0) = 0. \tag{6.9}$$

The chemisorption coverage Θ, not having the flux term in its governing equation, in principle does not require boundary conditions. However, some solvers might require to provide them for running properly in conjunction with the other equation containing the flux term. In such a case, one may accurately set both boundary conditions to zero flux of Θ at both boundaries, analogously to (6.8). As an initial condition for Θ we set

$$\Theta(z, t = 0) = 0, \tag{6.10}$$

[4] Notably, if the porous membrane considered is planar and exposed from both sides, the same set of boundary conditions can be applied - in such a case, l refers to the z coordinate in the middle of the membrane thickness and the solution is given for one exposed side, the other one being symmetrical. The zero-flux boundary condition in the middle arises then from the symmetry of the problem.

while at the beginning of the cycle we are expecting no coverage. The main variables of the model system (6.1) are illustrated in Figure 6.1

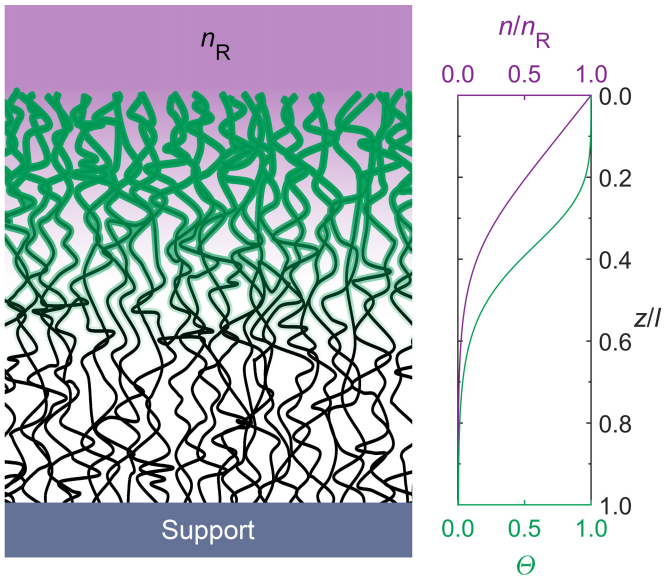

Figure 6.1. The main variables of the model system (6.1) illustrated together with a graph of its typical numerical solution. In the graph the gas concentration in the membrane n is normalised to the gas concentration surrounding the sample n_R, whereas the depth coordinate z – to the membrane thickness l. The single-cycle ALD coverage Θ is dimensionless. Colour-coding: n – purple –, Θ – green.

6.1.3. The dimensionless form of the model

In the work of Yanguas-Gil [251] the model was reduced to a dimensionless form, taking the membrane thickness and gas concentration upon pulsing as a base for the system of units. Here however, a different reduction is presented, where the system of units is dictated strictly by the physical phenomena governing the system behaviour, which leads to a parameterless form of equation system itself. There are several good reasons why it is beneficial to develop such a dimensionless model, expressing the existing physical equations in terms of their natural units. First of all, such a form of the model is simple, straightforward to implement in a simulation. Moreover, it helps to identify the factors effectively influencing the solution and allows to find out how the solution is scaled by inspection of how the units of the system change with the process parameters. Above all else, however, a single solution of the dimensionless model constitutes an entire class of real physical solutions, while the solution domain scales with the units of respective quantities. This approach allows for a straightforward identification and quantification of the scaling laws that govern the behaviour of the system captured by the model.

The time unit τ_c is determined by both the time of flight and the reaction probability,

$$\tau_c = \frac{\tau_f}{\beta_0}. \tag{6.11}$$

It can be interpreted as a mean time until a precursor molecule is chemisorbed when the coverage Θ equals 0. Consequently, the distance unit λ_c is determined by the diffusivity and the time unit,

$$\lambda_c = \sqrt{2D\tau_c}, \tag{6.12}$$

which represents the diffusion length of a molecule (root mean square displacement along the z axis direction due to diffusion) until chemisorption takes place at zero coverage, Θ=0. The unit of gas concentration is set as

$$n_0 = \frac{\bar{s}}{s_0}, \tag{6.13}$$

being the precursor concentration in the porous structure, for which the number of gas molecules contained in the pores equals the number of adsorption sites, i.e. the amount of gas, that would fully saturate the self-limiting chemisorption on the structure surface. The coverage Θ is naturally dimensionless and, as such, it requires no unit. Applying the system of units (6.11-13) to the model (6.1), we obtain the dimensionless and form of the model, with no parameters:

$$\begin{cases} \frac{\partial \bar{n}}{\partial \bar{t}} &= -\bar{n}(1-\Theta) &+\frac{1}{2}\frac{\partial^2 \bar{n}}{\partial \bar{z}^2} \\ \frac{\partial \Theta}{\partial \bar{t}} &= +\bar{n}(1-\Theta) & \end{cases}. \tag{6.14}$$

The dimensionless boundary- and initial conditions become

$$\bar{n}(\bar{z}=0,\bar{t}) = \bar{n}_{\mathrm{R}}(\bar{t}), \tag{6.15}$$

$$\frac{\partial \bar{n}}{\partial \bar{z}}\left(\bar{z}=\bar{l},\bar{t}\right) = 0, \tag{6.16}$$

$$\bar{n}(\bar{x},\bar{t}=0) = 0, \tag{6.17}$$

$$\Theta(\bar{x},\bar{t}=0) = 0. \tag{6.18}$$

Notably, we find a direct relation of the dimensionless gas concentration $\bar{n}_{\mathrm{R}}$ to the Knudsen number, which is discussed in section 6.1.5, exemplified for the specific case of randomly-oriented fibres.

It is also convenient to express the gas impingement rate J_{wall} in the dimensionless terms,

$$J_{\mathrm{wall}} = \frac{1}{\tau_{\mathrm{c}}\beta_0 s_0}\bar{n}. \tag{6.19}$$

Setting $(\tau_{\mathrm{c}}\beta_0 s_0)^{-1}$ as the unit of J_{wall}, we obtain the dimensionless gas impingement rate equivalent to the dimensionless gas concentration. Analogously, the gas exposure onto nanostructure walls Φ_{wall} becomes

$$\Phi_{\mathrm{wall}}(t) = \int_0^t J_{\mathrm{wall}}\mathrm{d}t = \frac{1}{s_0\beta_0}\int_0^{\bar{t}} \bar{n}\,\mathrm{d}\bar{t}. \tag{6.20}$$

Consequently, $(s_0\beta_0)^{-1}$ is set as the natural unit of gas exposure, the physical meaning of which depends on the ALD regime, as discussed in the further part of this work. We define the gas exposure Φ

onto macroscopic surfaces analogously as a time integral of the classical gas impingement rate J, expressed with equation (6.2).

6.1.4. ALD coating regimes and their corresponding scaling laws

The kinetics of ALD on porous nanostructures is defined by the balance between the rates of the two competing mechanisms – diffusion and chemisorption. Depending which one constitutes the kinetically-limiting factor to the process, the ALD occurs in a *reaction-limited regime*, a *diffusion-limited regime* [186,251], or between the two mentioned extremes, in what we refer to as a *transition regime*, in which the reaction rate is closely in line with the diffusion rate. The characteristic behaviour of coating in the three distinguished ALD regimes is schematically illustrated in Figure 6.2, taking an array of vertically aligned nanotubes as an example nanoporous structure. In the reaction limited regime, the reaction probability is relatively low, which leads to multiple collisions of the precursor molecules with the walls that do not lead to chemisorption. Effectively, molecules are able to diffuse through the entire structure and react randomly anywhere on substrate surface, resulting in a uniform and coating. In the diffusion-limited regime on the other hand, the molecules diffuse freely through the already-coated topmost section of the porous structure and react at a high probability on the surface once an available surface site is encountered. It results in what is referred to as a step coverage – a front of a conformal film coating, propagating into the structure gradually with the continuing precursor exposure. The transition regime lies in between of the two mentioned extremes. For both the extreme regimes, analytical solutions of the model (6.1) and the resultant scaling laws are presented in the further part of this work. The transition regime requires solving (6.1) numerically.

The main question remains, what process parameters dictate the ALD regime and the coating profile. It has been qualitatively identified in literature, that the low reactive sticking probability β_0 results in the reaction-limited process, whereas the high Knudsen number results in a diffusion-limited ALD [186]. Many studies have indicated, that lowering the β_0 results in a smoothening of the step-coverage profile dictated by the diffusion-limited regime [186,192,253]. We encompass the quantitative description of both the growth regime and the coverage profile shape with one decisive parameter – the mean diffusion path until chemisorption λ_c.

In the work of Yanguas-Gil [251], so-called Thiele number h_T was defined (otherwise referred to as Thiele modulus), which relates the ratio of the reaction rate to the diffusion rate [254], allowing to determine the ALD regime. The $h_T \ll 1$ defines a diffusion-limited regime, whereas $h_T \gg 1$ – a reaction-limited regime. Expressing h_T in terms of the units defined in the present work,

$$h_T \coloneqq l\sqrt{\frac{\bar{s}J_{wall}\beta_0}{nD}} = \frac{l}{\sqrt{D\tau_c}} = \frac{\sqrt{2}l}{\lambda_c}, \tag{6.21}$$

we find, that h_T is of the order of magnitude of the ratio of the structure thickness l and the mean diffusion path until chemisorption λ_c. Therefore, the value of λ_c compared to the thickness l determines the growth regime. It is also consistent with the dependency of the ALD regime on β_0, while λ_c depends on β_0 as well (see: equation 6.12). Moreover, we find, that λ_c quantitatively corresponds to the width of the spread of the coating profile of a single ALD cycle, as discussed in detail further in this section, which ultimately unites the description of the ALD regime and the coating profile shape.

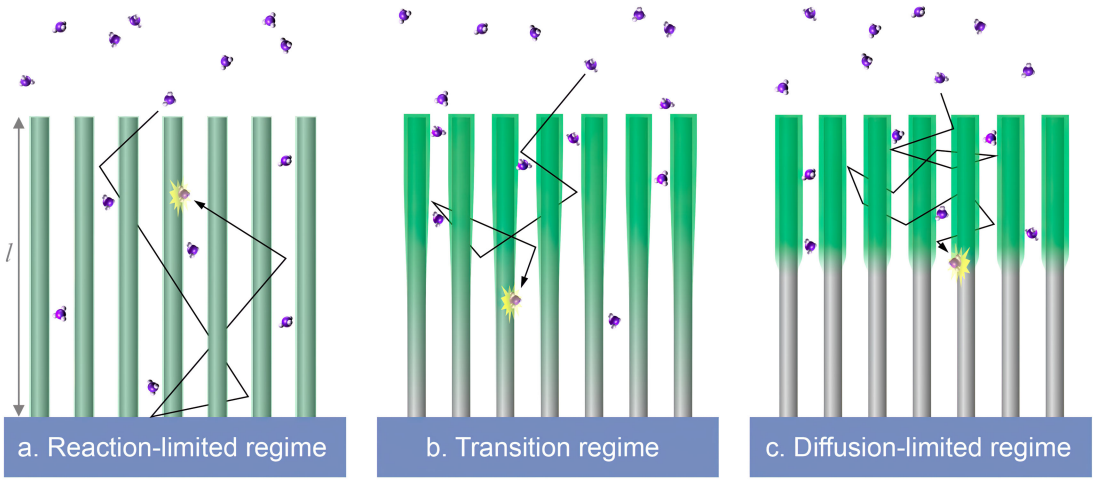

Figure 6.2. Illustration of the three distinct coating regimes of porous nanostructures, exemplified by vertically aligned cylinder array as a substrate; a) reaction-limited regime, b) transition regime, c) diffusion-limited regime. Green colour represents the chemisorption coverage. The thickness of the porous substrate is denoted with l.

Reaction-limited regime criterion and scaling laws

If the molecule is diffuses all the way through the structure, bouncing between structure walls multiple times and still have a low probability that it has chemisorbed on the way, the ALD occurs in the so-called *reaction-limited regime*. This is described by the Thiele number h_T much greater than 1, or the criterion

$$\lambda_\mathrm{c} \gg l. \tag{6.22}$$

In this case, before a significant coverage is reached, the gas concentration n equilibrates throughout the structure, in equilibrium with the gas concentration in the reactor n_R. The chemisorption occurs gradually, uniformly over the whole surface area of the nanostructure. To apply this extreme in the model system (6.1), we set $n{\equiv}n_\mathrm{R}(t)$ throughout the structure, which gives a reduction to one differential equation

$$\frac{\mathrm{d}\Theta}{\mathrm{d}t} = \frac{s_0}{\bar{s}}\frac{n_\mathrm{R}}{\tau_\mathrm{c}}(1-\Theta) \tag{6.23}$$

with the initial condition

$$\Theta(t=0) = 0. \tag{6.24}$$

The solution of this system is

$$\Theta(t) = 1 - \exp\left(-\frac{s_0}{\bar{s}\tau_\mathrm{c}}\int_0^t n_\mathrm{R}(t')\mathrm{d}t'\right) = 1 - e^{-\int_0^{\bar{t}} \bar{n}_\mathrm{R}(\bar{t}')\mathrm{d}\bar{t}'}. \tag{6.25}$$

Using the definition of the gas exposure Φ_wall (6.20) we obtain the solution expressed with respect to the Φ_wall,

$$\Theta(\Phi_{\mathrm{wall}}) = 1 - \exp(-s_0\beta_0\Phi_{\mathrm{wall}}) = 1 - \exp(-\bar{\Phi}_{\mathrm{wall}}). \tag{6.26}$$

Equation (6.26) reveals, that in the context of the reaction-limited regime, the unit of exposure $(s_0\beta_0)^{-1}$ can be understood as the characteristic exposure that provides surface coverage fraction equal $1 - e^{-1}$. If the n_{R} can be assumed constant over the timespan of the precursor exposure, we obtain

$$\Theta(t) = 1 - \exp\left(-\frac{s_0 n_{\mathrm{R}}}{\bar{s}\tau_{\mathrm{c}}}t\right) = 1 - e^{-\bar{n}_{\mathrm{R}}\bar{t}}, \tag{6.27}$$

conveniently expressed in terms of dimensionless quantities.

Transition regime

In the transition regime, the diffusion and reaction rate are of the same order of magnitude. In this case, a significant fraction of the precursor molecules manages to diffuse all the way through the structure and still not chemisorb. Still however, a considerable fraction of the precursor molecules gets chemisorbed on the way. In this case, the regime condition is

$$\lambda_{\mathrm{c}} \sim l, \tag{6.28}$$

or by the Thiele number of the order of unity. Simple analytical approximate solutions of the model system (6.1) are not available for this regime. The solution needs to be evaluated numerically.

Diffusion-limited regime

If the molecule is only able to travel a short path within the porous structure until it chemisorbs, relative to the whole depth of the structure to coat, the diffusion is the limiting factor in the process. Hence, the diffusion-limited ALD process is defined by Thiele number h_{T} much smaller than 1, or by the condition

$$\lambda_{\mathrm{c}} \ll l. \tag{6.29}$$

The following derivation is based on the considerations of Gordon *et al*. [191], which focused on ALD in narrow holes and trenches. Here, however, we are expressing the coating kinetics for the case of a general nanoporous material, at the same time pinpointing the geometrical and physical parameters that are determining the coating behaviour.

Solving the model (6.1) for selected diffusion-limited regime conditions (l=100 λ_{c} and l=1000 λ_{c}, n_{R}=0.01 $\bar{s}/s_0$ in both cases), we obtain solutions for the gas concentration and chemisorption as shown in Figure 6.3.

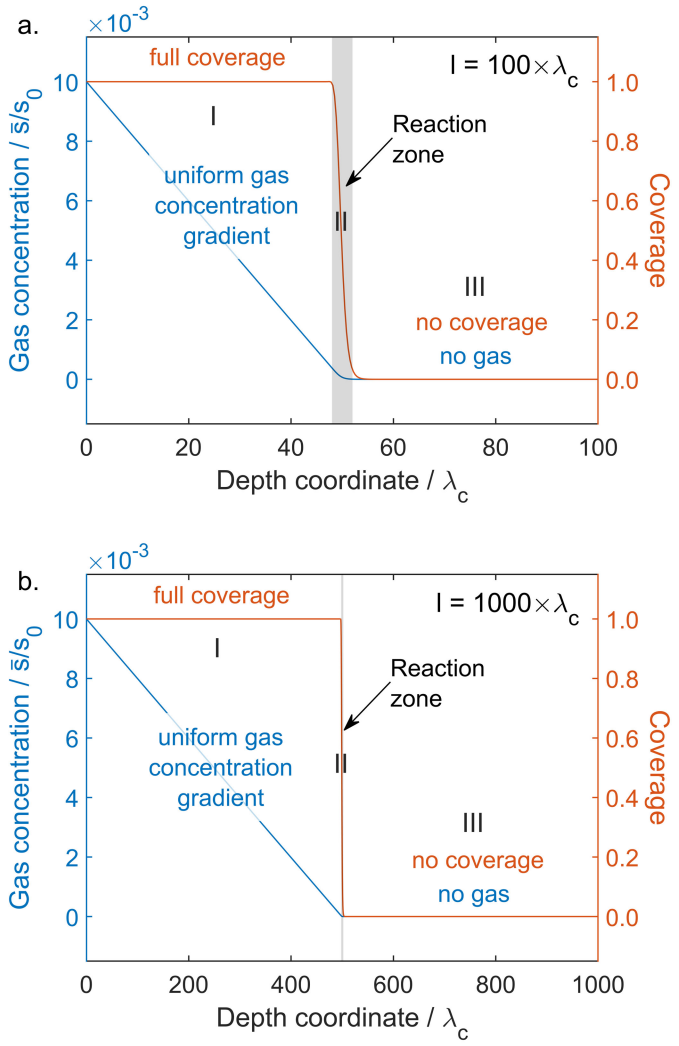

Figure 6.3. Two example solutions of the model (6.1) for the diffusion-limited regime: a) $l = 100\,\lambda_c$, b) l=1000 λ_c, for both n_R=0.01 $\bar{s}/s_0$. Gas concentration and coverage curves are plotted with respect to the depth coordinate. Three distinct zones are indicated with roman numerals: I - complete coverage zone; II - reaction zone and III - no-coverage zone.

In the solution one can distinguish three characteristic zones: I – complete coverage zone, II – reaction zone and III – no-coverage zone. In the zone I, the coverage is saturated, $\Theta = 1$, whereas the concentration exhibits a uniform gradient in this zone, bound by the left-sided condition $n(x = 0) = n_R$. The zone II follows deeper, where the coverage is not yet complete, $0 < \Theta < 1$, whereas the concentration n reaches zero, because the rapid chemisorption of molecules acts as a vacuum pump. The width of this zone is proportional to the length unit λ_c. In Figure 6.3 the reaction zone is marked with a grey overlay of width equal to 4 λ_c.

In the zone III, the $\Theta = 0$ and $n = 0$, while the precursor had no chance to reach it, getting consumed by chemisorption on a way within the reaction zone.

It is evident that in the diffusion-limited regime we observe that the coating proceeding into the structure can be approximated with a step-function, where the zone II determines the location of the step. The scaling law of coating depth in this regime is proposed as

$$z_c(\Phi_{wall}) = \sqrt{2D\tau_f s_0 \Phi_{wall}} = \lambda_c \sqrt{s_0 \beta_0 \Phi_{wall}}, \tag{6.30}$$

where z_c is the coating depth and Φ_{wall} is the gas exposure experienced by the topmost walls of the of the porous structure (close to $z = 0$). The derivation of (6.30) can be found in Appendix D.1. Scaling law (6.30) can be applied to any nanoporous structure, provided that its parameters are determined. In the context of diffusion-limited ALD regime, the of exposure unit $(s_0\beta_0)^{-1}$ represents an exposure, for which the porous nanostructure is coated down to the depth λ_c. If the gas concentration is constant throughout the pulsing and equal n_R, the scaling law (6.30) becomes

$$z_c(t) = \lambda_c \cdot \sqrt{\frac{n_R s_0}{\bar{s}} \frac{t}{\tau_c}}. \tag{6.31}$$

Taking into account, that λ_c is a measure of the mean path that molecule travels in the random walk until chemisorption, we take an educated guess, that it directly reflects the characteristic width of the reaction zone w_{II}. Namely we state that

$$w_{II} = \lambda_c. \tag{6.32}$$

The validity of (6.32) depends on the definition of w_{II}. Let us assume, that the blurred coverage step function, like the ones shown in Figure 6.3, can be described as a convolution of a Heaviside step function H and a smoothening filter function, f. Effectively, it means that the ideal sharp step-like coverage undergoes a low-pass filtering. Let us define w_{II} as the square root of variance of f. We perform a deconvolution and extract the z_c and w_{II} from the numerical solutions of the system (6.1) obtained for parameters fulfilling the condition of molecular gas transport regime (Kn$\gg$1) and diffusion-limited regime of ALD (6.29). The exact procedure is described in Appendix D.2. The results shown in Figure 6.4 confirm a remarkable agreement of the scaling laws (6.31) and (6.32) with the numerical solutions. The slight fluctuation of the numerical values of w_{II} is attributed to numerical errors. The drop of w_{II} at the end of the coating we attribute to the edge effect, which occurs when the coating depth z_c is approaching the total length of the system l.

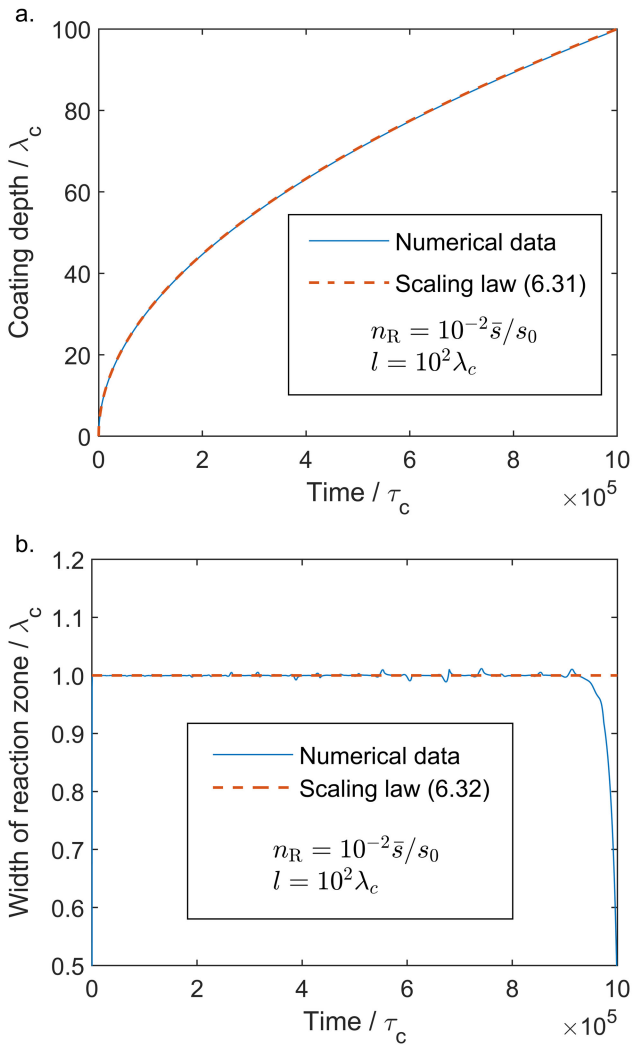

Figure 6.4. Numerical solutions of the system (6.1) compared to the respective scaling laws: a) the coating depth (6.31) and b) the width of the reaction zone (6.32).

6.1.5. Specifying the model parameters for the case of ALD on random fibrous media

In our previous work [252] we derived a novel theoretical framework for diffusion of gas in random fibrous materials. We are using a set of expressions from that work in the development of the ALD model presented here. For the truly randomly oriented fibres, which are allowed to intersect, the surface area to volume ratio α is expressed as

$$\alpha = \sigma\pi d \exp\left(-\sigma\frac{\pi d^2}{4}\right), \tag{6.33}$$

where d is the average fibre diameter and σ is the fibre length per volume. The expression for porosity ε is

$$\varepsilon = \exp\left(-\sigma\frac{\pi d^2}{4}\right). \tag{6.34}$$

The ratio of (6.33) and (6.34) gives the surface area to pore volume ratio $\bar{s}$,

$$\bar{s} = \frac{\alpha}{\varepsilon} = \sigma\pi d. \tag{6.35}$$

The mean flight time between the subsequent molecule-wall collisions τ_f is expressed as

$$\tau_\mathrm{f} = \frac{\pi^2}{2}\frac{1}{\bar{s}v}, \tag{6.36}$$

where v is the mean absolute velocity of gas molecules from the Maxwell-Boltzmann distribution. While we are assuming that the diffusion occurs in the molecular regime, we are using the equation for Knudsen diffusivity D,

$$D = \frac{\pi^2}{6}\frac{v}{\bar{s}}. \tag{6.37}$$

If a pure Knudsen gas diffusion regime cannot be assumed due to high pressures, one can implement the diffusivity equation accounting for the transition to the viscous regime presented in our previous work [252]. The Knudsen number for fibrous structures Kn is expressed as

$$\mathrm{Kn} = \frac{\sqrt{2}}{\pi^3}\frac{\bar{s}k_\mathrm{B}T}{pd_\mathrm{m}^2}, \tag{6.38}$$

where k_B is the Boltzmann constant, T is the gas temperature in K, p is the peak gas pressure, whereas d_m is the diameter of a precursor gas molecule. From the classical gas kinetics,

$$\frac{p}{k_\mathrm{B}T} = n_\mathrm{R}. \tag{6.39}$$

Moreover, we can assume that d_m^2 is approximately equal to the average area of an adsorbate surface site s_0. Hence,

$$\mathrm{Kn} \approx \frac{\sqrt{2}}{\pi^3}\frac{\bar{s}}{n_\mathrm{R}s_0} = \frac{\sqrt{2}}{\pi^3}\frac{1}{\bar{n}_\mathrm{R}}. \tag{6.40}$$

From equation (6.40) we can see, that for random fibrous membranes, the Kn is uniquely determined solely by the dimensionless gas concentration $\bar{n}_\mathrm{R}$, which further elucidates the physical relevance of the system of units defined. Clearly, for the assumption of the molecular regime of the gas transport, the $\bar{n}_\mathrm{R}$ needs to be much smaller than 1, so that the Kn is much greater than 1. Notably, Yanguas-Gil *et al*. [250,251] define an *excess number*, which is analogous to $\bar{n}_\mathrm{R}$. The excess number determines whether so-called *frozen surface approximation* of the system can be assumed, i.e. whether equilibration of the distribution of gas within the pores of the structure is much faster than the surface saturation. The relation (6.40) shown here elucidates that this property is intrinsically connected with the gas transport regime. This finding means that if the diffusion occurs in the Knudsen regime, utilisation of the frozen surface approximation is necessarily justified.

6.1.6. Coating profile of random fibrous nanostructures in a diffusion-limited ALD regime

While coating porous nanostructures with ALD in a diffusion-limited regime, the coating depth gradually decreases from cycle to cycle, see Figure 6.5. It happens so, because each cycle makes the structures tighter for the gas diffusion (decrease in ε), thus decreasing the Knudsen diffusivity. The other factor influencing the coating depth is a change in the surface area to volume ratio α from cycle to cycle. It affects both the Knudsen diffusivity and the amount of precursor required to saturate the given thickness of the porous structure as the surface area to be coated changes. Depending on the type of the structure, regular or inverse (as discussed in our previous work [252]), α gradually decreases or increases, respectively, as the film grows.

To mitigate the diffusion-limiting effect and achieve a consistently uniform coating in each cycle, one needs to adjust the gas exposure Φ_{wall} following the scaling law (6.31) according to the proceeding changes in surface area, porosity and diffusivity from one cycle to another. To examine the performance of the scaling law, we have performed an experiment of the diffusion-limited coating in an undersaturated mode, i.e. the coating depth z_{c} is less than the thickness of the porous mat to coat. The scaling law (6.30) allows to predict the ALD coating profile, which we perform here on the example of CNT mat as a model substrate.

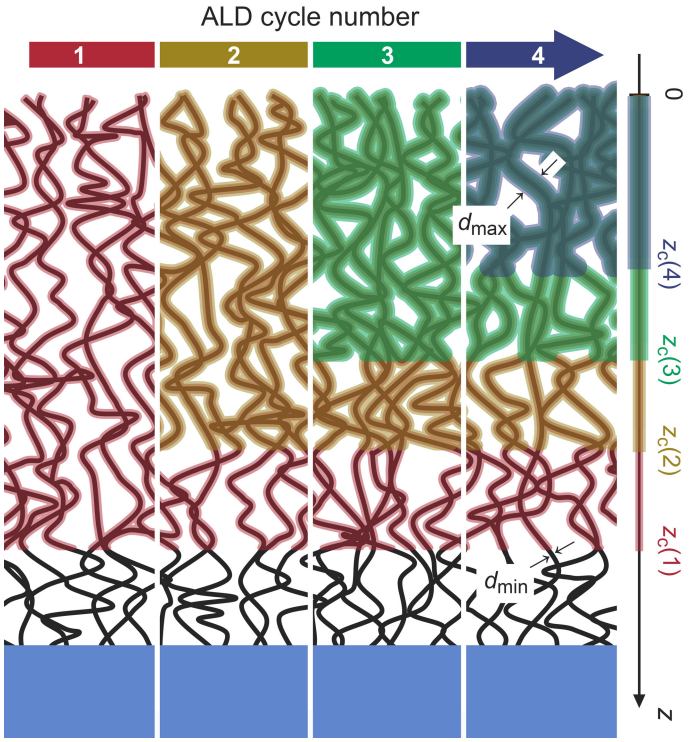

Figure 6.5. Schematic of ALD coating profile on a fibrous nanostructure on a flat support (not to scale) illustrating the decreasing coating depth z_{c} in subsequent ALD cycles; the numbers of the respective ALD cycles are given in brackets (1, 2, 3 and 4). Minimum and maximum fibre diameters are indicated as d_{min} and d_{max}, respectively.

Given the framework of expressions introduced in section 6.1.5, for the random fibre geometry the scaling law for the coating depth in the diffusion-limited regime (6.30), becomes

$$z_{\mathrm{c}}(\Phi_{\mathrm{wall}}) = \frac{\pi}{\sigma d}\sqrt{\frac{s_0}{6}\Phi_{\mathrm{wall}}}. \qquad (6.41)$$

Transformation of equation (6.41) gives the coating profile,

$$d(z) = \begin{cases} d_{\max} & \text{for} \quad d_{\text{aux}}(z) > d_{\max} \\ d_{\text{aux}}(z) & \text{for} \quad d_{\min} < d_{\text{aux}}(z) < d_{\max}, \\ d_{\min} & \text{for} \quad d_{\min} > d_{\text{aux}}(z) \end{cases} \tag{6.42}$$

Where $d(z)$ is the CNT diameter including the coating with respect to the depth in to the mat z, $d_{\min}$ is the initial fibre diameter, $d_{\max}$ is the diameter of the coated fibre measured at the top of the structure, where all the coating cycles are saturated. The $d_{\text{aux}}(z)$ is an auxiliary variable defined for convenience,

$$d_{\text{aux}}(z) := \frac{k}{z}, \qquad k = \frac{\pi}{\sigma}\sqrt{\frac{s_0}{6}\Phi_{\text{wall}}}. \tag{6.43}$$

Equations (6.42, 43) describe the diameter profile for a constant precursor exposure in each cycle for coating of fibrous substrates in a multicycle ALD process. We are using this profile in the further part of the work for interpretation of the experimentally measured diameters of the ALD-coated CNT array. The diameter profile (6.42,43) is schematically illustrated in Figure 6.6.

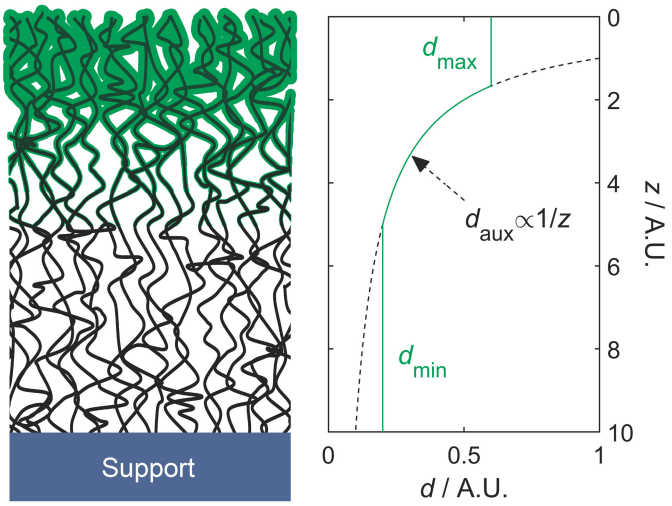

Figure 6.6. Schematic illustration of the diameter profile of CNTs coated with multicycle ALD in a diffusion-limited regime as described with equations (6.42,43); d – coated CNT diameter, z – depth coordinate, both shown in arbitrary units for illustrative purposes.

6.2. Experimental

The CNTs were synthesised on a silicon wafer by means of catalytic chemical vapour deposition, as described in more detail in Chapter 4. SEM imaging showed that the thickness of the CNT mat was ca. 300 ± 5 µm. In order to achieve and examine the diffusion-limited coating of the CNTs arrays, we performed ALD of Al_2O_3 on a CNT mat. The details of the ALD procedure are given in a following section. Subsequently, we carried out the SEM imaging of the coated CNT sample cross section in order to obtain the diameter profile data along the depth into the CNT mat. Subsequently, a theoretically expected diameter profile (6.42,43) and its confidence intervals are predicted based on the measured physical parameters of the model and their uncertainties. The predicted and measured coating profiles are compared to assess the performance of the model.

The parameters determining the profile are the average area of a surface site s_0, the axes length per volume of the CNTs σ, the precursor exposure Φ_{wall} and the mean CNT diameters prior to-

and after the ALD coating, $d_{\min}$ and $d_{\max}$, respectively. The s_0 can be realistically estimated from the growth per cycle h in terms of thickness increment in each ALD cycle [255],

$$s_0 = \frac{\mu_{Al_2O_3}}{2\varrho_{Al_2O_3} N_A h}, \tag{6.44}$$

where $\varrho_{Al_2O_3}$ is the density of the ALD-synthesised alumina being approximately 3.0 g/cm^3 [256,257], N_A – the Avogardo number, whereas $\mu_{Al_2O_3}$ – molar mass of the aluminum oxide. Division by 2 in equation (6.44) comes from the fact, that two TMA molecules are required to deposit one stoichiometric unit of Al_2O_3. For internal consistency, we are deriving the h from the diameters of the CNTs before and after the multicycle ALD, $d_{\min}$ and $d_{\max}$, respectively:

$$h = \frac{d_{\max} - d_{\min}}{2N_{cyc}}, \tag{6.45}$$

where N_{cyc} is the number of the ALD cycles. The $d_{\min}$ and $d_{\max}$ are determined by analysis of SEM images, as discussed in the further part of this work.

The absolute surface area of the coated CNTs is determined experimentally by Krypton adsorption, which allows to uniquely determine the CNT axes length per volume σ with equation (6.33) coupled with the given diameter profile. The procedure is explained in more detail in the further part of this work.

The exposure Φ_{wall} is determined by analysing the pressure curve recorded during the pulsing of TMA, which is elaborated on in the following sections.

Ultimately, when all the parameters and their uncertainties are set, the validity of the gas diffusion model introduced in this work is examined - the theoretically expected coating profile is evaluated and compared to the profile directly measured by SEM.

6.2.1. Atomic Layer Deposition procedure

The ALD process has been carried out in a commercial ALD reactor Savannah 100 (Cambridge Nanotech) in a viscous flow mode[5] –The temperature of the chamber was set to 225 °C, the high-purity nitrogen (99.9999 % purity) at 20 sccm was used as a carrier gas throughout the procedure with the vacuum pump always on. As precursors for Al_2O_3 coating, we used the TMA (Sigma-Aldrich, deposition-system grade) and ozone generated by an ozone generator (OL80F by Ozone Lab™).

It is known, that the CNTs surfaces are chemically inert [244], which may result in a spot-wise nucleation of ALD films . To increase the reactivity of the intrinsically inert CNTs, we first exposed them to ozone for 30 s in a pulsed manner: 100 ms long pulses separated by 1 s, afterwards letting the reactor get purged for 40 s. An analogous approach has been successfully applied in conformal coating of graphene [258] with alumina ALD.

Subsequently, in order to eliminate the influence of the differences in surface chemistry of ALD on carbon and on alumina in our experiments, we initially coated the CNTs with 5 cycles of seed layer,

[5] Within the range of pressures in our experiments, the mean free path of molecules is of the order of magnitude of micrometers ($\lambda_b \approx 20$ μm, see: section 6.3), which is much shorter than the characteristic dimensions of the ALD reactor. Therefore the Knudsen number in the reactor is much smaller than 1 and the viscous flow is justified.

ensuring a saturated coating by long pulsed exposures to the precursors. One cycle description: 10×150 ms TMA pulse separated by 1 s, 40 s waiting time; 10×100 ms ozone pulse separated by 1 s, 40 s waiting time.

Ultimately, the diffusion-limited coating has been carried out on such prepared substrate. 75 coating cycles have been carried out, each cycle was done as described: 1×100 ms TMA pulse, 40 s waiting time, 10×100 ms ozone pulse separated by 1 s, 40 s waiting time. Finishing the process, the reactor was cooled down to 80 °C and sample was extracted. The ALD processing is summarised in Table 6.1.

Table 6.1. Summary of the ALD processing protocol.

Repetitions		**Event**	**Duration**
1×	30×	O_3 pulse	100 ms
		wait	1s
	1×	wait	40 s
5×	10×	TMA pulse	150 ms
		wait	1s
	1×	wait	40 s
	10×	O_3 pulse	100 ms
		wait	1s
	1×	wait	40 s
75×	1×	TMA pulse	100 ms
		wait	40 s
	10×	O_3 pulse	100 ms
		wait	1s
	1×	wait	40 s

6.2.2. Establishing the precursor gas exposure from the pressure curves

The pressure curve recorded during TMA pulsing allows to determine the exposure Φ_{wall}. In principle, for an accurate estimate, one needs to carry out a complex simulation, involving fluid dynamics, modelling of the vacuum pump, precursor evaporation, etc. We are however suggesting a simplistic approach to the issue with several assumptions:

- One can treat the function of pressure versus time in the ALD reactor upon precursor pulsing as an "impulse response" to the delivered gas, in analogy to signal processing.
- The response is approximated as a decaying exponential, which reflects the vacuum pumping behaviour.
- A plug-flow of gas is assumed for simplicity.
- The flux of precursor gas during pulsing can be approximated as a temporal gaussian peak.

The decaying exponential function is a pressure response to the infinitesimally short precursor pulse (temporal Dirac delta). The time constant of the decaying exponential is subject to curve fitting. Effectively, while the precursor pulse is approximated as a gaussian, the pressure curve is predicted as a response to a gaussian-shaped precursor pulse, which is calculated as a convolution of the gaussian

and the decaying exponential. Such a curve is fit to the pressure datapoints and the gas exposure experienced by the sample is extracted. The example pressure graph and the calculation results are shown in Figure 6.7. The data analysis process is elaborated on in Appendix D.3. By integration of the resulting impinging rate over time, we obtain the exposure $\Phi_{wall}=(6.76\pm0.68)\times10^{19}$ cm^{-2}, where the confidence interval is 95% and comes from the analysis of 10 pulsing curves.

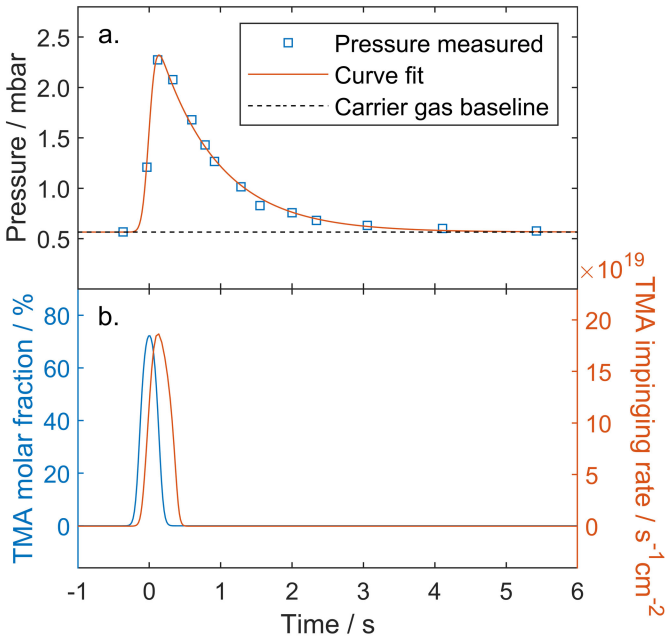

Figure 6.7. Evaluation of temporally-resolved impingement rate based on the analysis of the pressure recorded during TMA pulsing; a) a typical pressure curve as observed upon 100 ms TMA pulsing, with the correction for the base pressure and a model curve fit; b) TMA molar fraction at the inlet to the reactor and the impinging rate J_{wall} evaluated based on the model curve fitting result.

6.2.3. Scanning Electron Microscopy Imaging

In order to investigate the diameter profile of the alumina-coated CNT mat in the diffusion-limited ALD, we performed scanning electron microscopy (SEM) imaging. A fragment of CNT forest has been carefully removed with a razor, exposing the cross section of the coated mat. The imaging has been done with the Hitachi S4800 SEM at a 45° sample tilt. An overview image along with three example high-magnification images is shown in Figure 6.8. The imaging shows, that the top part of the CNT array is uniformly coated with the alumina giving a high contrast. Further deep into the structure, the structure appears gradually darker in the overview, which is linked to a declining coating thickness, as seen in the high-magnification images, and as expected from the coating in the diffusion-limited regime.

High-magnification images have been taken at 20 different depths into the structure. The images were analysed in the open-source ImageJ software; 10 diameters were measured by hand in each image for appreciable overall statistics. To avoid the human bias in the measurement, the images were first shuffled, and subsequently the measurements obtained were assigned to their respective original positions accordingly.

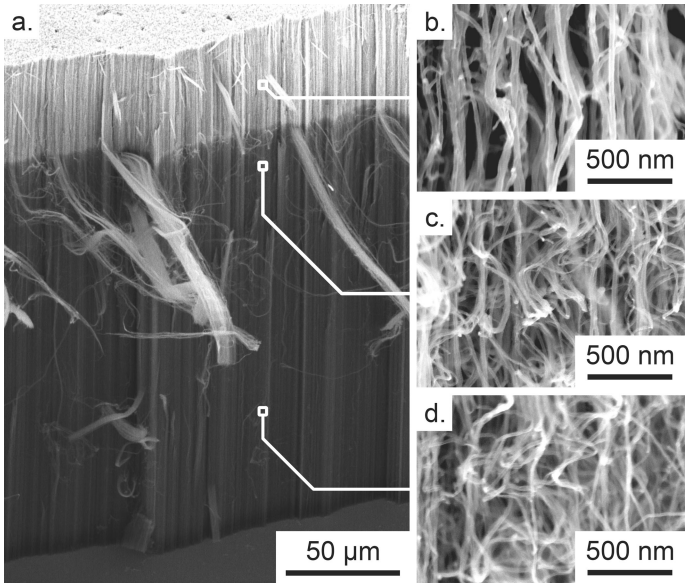

Figure 6.8. Scanning electron microscopy imaging of the alumina-coated CNTs; a. - overview of the CNT forest tilted by 45°; b., c., d. - high magnification images at depths of ca. 40 µm, 90 µm and 240 µm, respectively.

6.2.4. Measurement of surface area by Krypton adsorption-desorption isotherms

The absolute surface area of the coated CNTs was determined by the Brauner-Emmet-Teller method. Krypton adsorption-desorption isotherms of the silicon wafer with the alumina-coated CNTs were collected at 77 K using a Micromeritics 3Flex Surface area and Porosity Analyzer. Prior to the measurement, the sample was degassed for 20 h at 200 °C at a pressure of 1.3×10^{-2} mbar in order to remove water vapour and volatile organic compounds. Data points were recorded at a relative pressure (P/P_0) range between 0.02 to 0.62 and both adsorption and desorption branches were collected. In order to get reproducible results, the sample was measured 3 times. The resulting absolute surface area was measured as A=1182±63 cm^2, where the confidence interval is 95%, estimated as a double standard deviation. The surface area of the silicon wafer substrate is negligible compared to the total surface area measured. The value obtained by this method allows to uniquely determine the fibre axes length per volume σ, by equation (6.33) coupled with the diameter profile, as elaborated on in the next paragraph.

6.2.5. Analysis of the diffusion-limited coating profile

The diameter profile model of the multicycle ALD-coated CNT (6.42,43) was found to be highly sensitive to deviations of the model parameters. Therefore, in order to obtain a reliable estimate of the expected coating profile and its confidence intervals, we implemented a *bootstrap* approach. The bootstrapping relies on random data sampling with replacement carried out multiple times, calculating the estimators of interest in each randomisation and ultimately obtaining distributions of the estimators.

The profile model (6.42,43) has 3 independent parameters: $d_{\min}$, $d_{\max}$ and k. The $d_{\min}$ was determined in each bootstrap iteration as a mean value of randomly selected diameter measurements at depths higher than 110 µm, which we found to be deep enough, so that the diffusion-limited coating depth does not reach it at any cycle. If the number of measurements performed deeper than 110 µm was N_d, then N_d diameter measurements were drawn at random with returns, which follows the most common implementation of bootstrap. Analogously, the $d_{\max}$ was estimated in each bootstrap iteration for measurements taken at depths less than 50 µm. The parameter k requires information about the gas exposure Φ_{wall} and σ, therefore both of them need to be determined. To do so, in each bootstrap iteration, the exposure Φ_{wall} and the total surface area A are randomly drawn from their respective

gaussian distributions, taking the mean and standard deviations as the distribution parameters. By definition, A can be calculated as

$$A = S\int_0^l \alpha(x)\mathrm{d}x = S\int_0^l \sigma\pi d(x)\exp\left(-\sigma\frac{\pi d^2(x)}{4}\right)\mathrm{d}x, \tag{6.46}$$

where S is the surface area of the Si wafer substrate covered by the CNT mat. The parameter k is then obtained in each bootstrap iteration as a result of numerical solution of the system of equations (6.42,43,46). In the same procedure, σ is simultaneously obtained.

The number of bootstrap iterations in this work was set to 10^4. The results are presented in Figure 6.9 and the set of the relevant parameters is gathered in Table 6.2. The confidence intervals shown in the figure were calculated based on all the statistics obtained from the bootstrap.

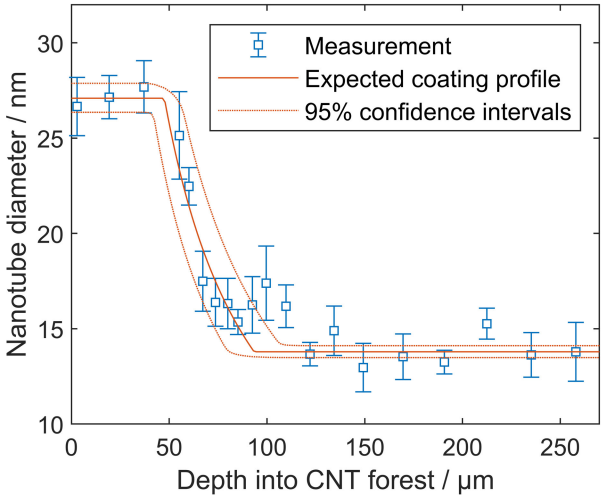

Figure 6.9. Measured diameters of the coated CNTs at a constant precursor exposure at each cycle together with the expected coating profile evaluated based on the measured parameters and the model presented in this work. The dotted lines indicate the 95% confidence interval of the expected coating profile resulting from uncertainties of the individual parameters determining the profile.

Table 6.2. The relevant parameters of the system and their confidence intervals resulting from measurements (a) and inferred from the bootstrap calculations (b).

Parameter	Value±Uncertainty	Unit
d_{min}[a]	13.79±0.31	nm
d_{max}[a]	27.10±0.76	nm
h[a]	0.888±0.055	Å
Φ_{wall}[a]	(6.76±0.68)×10^{19}	cm^{-2}
σ[b]	(4.63±0.65)×10^{10}	cm^{-2}

Figure 6.9 shows an excellent the agreement of the experimentally obtained coating profile and the theoretical prediction. The location and slope of the steep edge of the coating profile are predicted accurately, within the established confidence intervals, which constitutes validation

of the modelling provided in this work. The growth per cycle h is found to be consistent with the values reported typically in literature [259,260].

6.3. Discussion – the physical parameters of the system

The modelling introduced in this work and its fit to the experimental data allowed to evaluate a range of physical parameters of the system, as well as their evolution with the growing ALD film. We summarise the parameters in this section, for a straightforward comparison of the system of Al_2O_3 ALD on CNT mats in our experimental configuration to other related systems.

The evaluation of Knudsen number Kn requires additional discussion. While only the high values of Kn characterise the Knudsen diffusion regime, we made sure to not overestimate its value, to have the highest confidence, that the system is indeed governed by Knudsen diffusion. It means obtaining a realistically low estimate for the mean free path in the bulk gas. Equations for Kn (6.38-40) were introduced for a simplified case of only the precursor gas present. Neglecting the carrier gas might however lead to an overestimation of the mean free path λ_b and Kn, which, as mentioned above, is to be avoided. Therefore, the estimation about to be shown here accounts for the influence of the carrier gas (here: nitrogen) on the mean free path of TMA in the bulk gas λ_b and, consequently, Kn, following the definition (6.5). According to the classical molecular kinetic theory [261], the mean free path of a molecule in a binary mixture is expressed as

$$\lambda_\mathrm{b} = \frac{k_\mathrm{B} T}{\pi\sqrt{2} d_\mathrm{TMA}^2 p_\mathrm{TMA} + \pi \sqrt{1 + \frac{\mu_\mathrm{TMA}}{\mu_{\mathrm{N}_2}}} \left(\frac{d_\mathrm{TMA} + d_{\mathrm{N}_2}}{2}\right)^2 p_{\mathrm{N}_2}}, \tag{6.47}$$

where d_x is a is a kinetic diameter of a molecule, p_x – partial pressure, μ_x – molar mass. The subscripts x denote the gas mixture component. The kinetic diameter of nitrogen is established as 3.64 Å [262]. We estimate the kinetic diameter of TMA based on the average surface area of a reactive surface site s_0 assuming a close-packed arrangement of spherical molecules,

$$d_\mathrm{TMA}^2 = \frac{2}{\sqrt{3}} s_0, \tag{6.48}$$

which gives the value of d_TMA=6.06 ± 0.19 Å, consistent with literature [263].

The partial pressures of TMA and nitrogen over the sample with respect to time are evaluated for a typical precursor pulse curve, as described in Appendix D.3. The particular point in time is selected, for which the combination of partial pressures gives the smallest estimate of λ_b, which falls at the maximum of the partial pressure of TMA over sample.

The experiment carried out in this work does not allow to fit or evaluate the reactive sticking probability β_0, but it allows to estimate it from below. While in the experiment, the ALD coating was done in the diffusion-limited regime within the entire range of the diameter of the coated CNTs, we obtain a lower estimate of β_0 for the initial diameter d_min. From the condition (6.22) we obtain

$$\beta_0 \gg \frac{2D\tau_\mathrm{f}}{l^2}, \tag{6.49}$$

which results in the requirement for β_0 to be much greater than 5.7×10^{-7}. It means, that β_0 has to be at least an order of magnitude greater than this value, so that the ALD occurs in a diffusion-limited regime, as it did in the experiments presented. This is however a very conservative estimate. Precise investigation of sticking probability of ALD precursors, TMA particularly, is a topic currently widely pursued in the ALD community. So far, it has been best studied for the classical ALD of alumina with TMA as an aluminium precursor and water as an oxidiser (TMA+H_2O ALD). The recent work of Vandalon *et al.* [264] provided a precise measurement of sticking coefficient of TMA in TMA+H_2O ALD, obtaining a value of $\beta_0=(3.9\pm0.4)\times10^{-3}$, consistent also with other studies, such as another recent work of Gakis *et al.* [265]. In our process we used ozone as an oxidiser (TMA+O_3 ALD), therefore the surface termination prior to TMA exposure is of a different chemical character than in the TMA+H_2O ALD. However, it is safe to assume that the sticking probability is in this case of the same order of magnitude. Therefore in the evaluations of parameters which depend on β_0, we are using the value found by Vandalon *et al*.

The mean absolute velocity of TMA from Maxwell-Boltzmann distribution is given with

$$v = \sqrt{\frac{8N_\mathrm{A}k_\mathrm{B}T}{\pi\mu_\mathrm{TMA}}}, \tag{6.50}$$

where N_A is the Avogadro's constant. Equation (6.50) gives the value of v=392 m/s. The expected values and uncertainties of the parameters are evaluated by the following procedure. We generated 10^4 normally distributed instances of each of the quantities from Table 6.2, of β_0 obtained by Vandalon *et al.* and of CNT mat thickness l=300±5 µm. Subsequently, the value for each instance was evaluated based on an appropriate equation introduced in this work. Ultimately, the value and uncertainty of each parameter was calculated as average and 95% confidence range of the resultant, respectively. If a given parameter is affected by the CNT diameter, we show the values for both d_min and d_max, to elucidate how its value evolved with the proceeding ALD process. The gas impingement rate J_wall is estimated at the maximum TMA concentration. The evaluated parameters are gathered in Table 6.3.

Table 6.3. Physical system parameters determined as a result of the experiments and modelling carried out in this work. Abbreviations in the column headings: Sym. – symbol, Val. – mean value, Unc. – uncertainty determined as 95% confidence interval. Dashes in the Unit column reflect that the given quantity is dimensionless. If the given parameter is affected by the value of CNT diameter, the values for the diameter d_max and d_min are given in the first and second row, respectively. All values are shown up to 2 significant digits of the respective uncertainty. Parameters denoted with a superscript symbol † were determined assuming the sticking probability of TMA based on the results of Vandalon *et al.* [264]. The gas impingement rate is estimated at its expected maximum (at maximum TMA concentration in the reactor upon precursor pulsing).

Parameter name	Sym.	Val.	Unc.	Unit
Surface area to volume ratio	α	18.7	±2.4	$\frac{\mu m^2}{\mu m^3}$
		30.1	±3.0	
Knudsen diffusivity	D	0.32	±0.05	$\frac{cm^2}{s}$
		0.16	±0.03	
Porosity	ε	0.93	±0.01	-

		0.77	±0.04	
Thiele number	h_T	132	±23	-
		259	±45	
Gas impingement rate onto nanostructure walls	J_wall	1.67	±0.38	$\frac{10^{20}}{\mathrm{cm^2 s}}$
Knudsen number	Kn	79	±13	-
		156	±25	
Mean diffusion path until chemisorption†	λ_c	3.25	±0.57	µm
		1.65	±0.29	
Mean flight path confined by porous structure	λ_f	0.247	±0.035	µm
		0.126	±0.018	
Mean free path of TMA in bulk gas	λ_b	19.5	±1.4	µm
Reactive site surface area	s_0	31.8	±2.0	Å²
Pore wall surface area to pore volume ratio	$\bar{s}$	20.0	±2.8	$\frac{\mu m^2}{\mu m^3}$
		39.4	±5.5	
Mean diffusion time until chemisorption†	τ_c	168	±42	ns
		85	±21	
Mean flight time between subsequent molecule-wall collisions	τ_f	0.647	±0.091	ns
		0.329	±0.047	
Coating depth in the single cycle	z_c	94	±14	µm
		47.7	±7.4	

6.4. Summary and conclusions

In the present work we revisited continuum modelling of ALD on porous substrates. A new parametrisation of the model system has been introduced, based on the natural scales of the physical phenomena that govern the process, which are gas diffusion and chemisorption. The model expressed in its natural system of units returns entire classes of scalable solutions, which offers ease in determining the relevant scaling laws governing the described processes. This approach revealed a clear, direct and quantitative connection between the single-cycle ALD coating profile and the determination of the ALD regime (diffusion- or reaction limited). Moreover, we have shown, that the gas diffusion regime (determined by Knudsen number) and so-called excess number (ratio between gas equilibration rate and surface reaction rate) are two sides of the same coin, being determined by the same physical parameters and as such cannot be decoupled. We particularise the model for the case of diffusion-limited multicycle ALD coating of carbon nanotube forests, applying the theoretical framework of gas transport in random fibrous media developed in our previous work. We find a remarkable agreement between the theoretically predicted coating profile based on the determined process parameters and the directly measured coating profile from SEM imaging. The findings in this work constitute

a significant contribution to the understanding of ALD on porous structures in general and on random fibrous mats in particular.

Acknowledgements

The authors cordially thank the members of the Nanolino group at the Physics Department, University of Basel, Switzerland and members of the Swiss Nanoscience Institute for insightful comments and suggestions. Moreover, the authors also acknowledge Michel Calame (Transport at Nanoscale Interfaces, Empa, Switzerland) for providing access to infrastructure.

Chapter 7

Summary and outlook

"I begin with an idea and then it becomes something else."

Pablo Picasso

This short chapter contains the summary of the findings and outcomes of the studies described in this thesis, as well as their possible implications on the future developments of hierarchical composites.

In this thesis, we have tackled the concept of hierarchical composites based on carbon fibres (CFs) grafted with radially-aligned carbon nanotubes (CNTs) for nanoscale reinforcement of the fibre-matrix interface and enhancement of the off-axis performance of the fibre-reinforced epoxy composites. The issue of fibre degradation upon the harsh conditions of direct CNT growth by chemical vapour deposition (CVD) was tackled by application of a thin protective alumina coating by means of atomic layer deposition (ALD). The barrier coatings have been mostly avoided in the scientific community developing CNT-CF hierarchical composites, due to the potential downsides of this solution:

- The presence of the barrier coating increases the complexity of the composite system: it gives rise to additional interfaces, the mechanical stability of which needs to be ensured.
- The application of the barrier film increases the complexity of the composite manufacturing process.

There are however distinct advantages of this approach, considering in particular the alumina film applied by ALD:

- ALD is the method of choice for coating of geometrically complex substrates (such as CF fabrics of tows), allowing for an atomic precision in coating thickness over the entire substrate surface.
- ALD alumina is a very effective support for CNT synthesis due to the particular catalyst-substrate interaction, inherently allowing for a dense, uniform growth of high-quality CNTs.
- The film offers protection of the CF in the CNT growth process.

These advantages may outweigh the downsides, especially when pushing the limits of the composite performance is the priority. The application of the ALD alumina protective film offers a great promise of CNT-CF hierarchical composites, without compromises on the CF mechanical properties, nor on the grown CNT quality. Thus, the decision of applying the protective alumina film was motivated, spawning many research questions and challenges to pursue.

First of all, the protective effect of the alumina film needed to be confirmed. We acknowledge the work of Vogel *et al.* [90] carried out previously in our group. By means of micromechanical testing, Vogel *et al.* have demonstrated, that the alumina film indeed does allow to retain the CF mechanical properties upon the CNT growth conditions and found that the minimum film thickness for this purpose is 12 nm. The mechanisms which govern the protective effect could be at that point hypothesised, however the direct confirmation was clearly required.

The morphological changes that occur in the CFs upon the CVD of CNTs were investigated by means of nanotomography. Deterioration of the CF was found to be connected with the migration of iron catalyst nanoparticles into the subsurface regions of the CF, to about 100 nm in depth. Moreover, the mechanism of migration of iron into the CF has been evidenced: the iron was shown to remain in a localised form of nanoparticles throughout the migration process. This finding indicated, that the migration is driven by dissolution and diffusion of carbon through the nanoparticles, rather than by a simple dissolution of iron in the body of the CF. The 12 nm alumina film allowed to prevent the penetration of iron nanoparticles into the CF, which explained the protective effect.

Vogel *et al.* [90] had shown, that the adhesion of alumina to CF diminishes strongly under CNT growth conditions, posing a challenge in the development of hierarchical composites with the alumina barrier film. A modified ALD process was investigated, with an additional ozone pre-treatment of the CF surface, for enhancement of the covalent bonding between the fibre and the grown film. The retained interface shear strength of the alumina-CF interface was demonstrated by single-fibre pull-out testing.

Dense and vertically-aligned CNT arrays are readily wetted by epoxy, facilitated by the capillary action of the ultrahigh surface area of the CNTs. Moreover, this morphology allows reaching high CNT loadings in the matrix in order to harness the extraordinary mechanical properties of CNTs to the greatest extend, particularly in the out-of-plane direction. The CNT growth morphology is largely determined by the dispersion of the catalyst nanoparticles on the surfaces. This constitutes the motivation of the development of a coating method of alumina-finished complex structures, such as CF fabrics or tows, with the iron catalyst. We proposed an aminosilane treatment of the substrates and demonstrated its effectiveness in promoting a homogeneous coating with the iron catalyst precursor from an iron salt solution. The improvement of homogeneity of catalyst nanoparticle distribution was evidenced quantitatively by image analysis. The new catalyst coating strategy was shown to yield dense, homogeneous and aligned CNT growth, both on flat substrates, as well as on CF fabrics.

As the growth of CNTs by CVD occurs at a gas-solid interface, understanding of gas transport phenomena is crucial for an efficient manufacturing process development. For instance, considering a roll-to-roll process for CNT growth on CF tows, the carbon precursor gas needs to diffuse into the tow within the foreseen CVD treatment time. The diffusion limitation may become more pronounced as the CNT growth progresses, leading to an inhomogeneous CNT growth throughout the CF tows. We identified a knowledge gap in the fundamentals of gas transport in fibrous structures. To fill this gap, we introduced a theoretical framework of gas diffusion in fibrous membranes, encompassing the Knudsen diffusion occurring at low pressures, the molecular diffusion characteristic to relatively high pressures, as well as the transition between both the extremes. The model was derived from basic physical principles. Due to its generality and applicability at all scales, the progress in understanding of the gas transport provided in Chapter 5 has implications reaching far beyond the CNT growth on CFs.

The developed theory was then experimentally at the nanometre scale. The experiments were carried out on a model system of ALD on CNT mats, which is controlled by gas diffusion. This model system was chosen, because it allowed to isolate and quantify the effects of Knudsen diffusion. On top of the experimental validation of the theory, we provided a new approach to general description of ALD on arbitrary porous substrates, which led to multiple practical scaling laws describing the process and many enlightening physical insights into ALD on porous substrates in general.

The work carried out within the scope of this thesis opened the following paths of further study. The anchoring strength of CNTs on the ALD-alumina remains unknown and it might be subject to optimisation. Micromechanical testing methods such as single fibre pull-out testing can give an idea about the CNT-alumina interface. In this context, taking a step back towards the CNTs grown on flat substrates should be considered as well, for experimental simplicity. Moreover, with the electrical properties of the composite in mind, alumina may potentially be replaced with another material, which would not only adhere well to the fibre and provide an excellent support to the CNT growth, but would be a good electrical conductor as well. We used the alumina because of its wide availability in the ALD and because of its very well-understood ALD synthesis process. However, it would be certainly beneficial to find or develop a replacement coating material, with the electrical conductivity functionality. Furthermore, we developed an effective solvent-based iron catalyst coating method; however, an alternative approach may be beneficial in some applications. Namely, we suggest coating the CFs with the catalyst or catalyst precursor, also using ALD. One could consider a multistage gas phase processing furnace, with a range of temperatures and reactive gases, in which the CFs are coated, in sequence, with the protective film (ALD), with the catalyst (ALD) and ultimately grafted with the CNTs (CVD). Last, but not least, the development of a model of CNT growth throughout fibre tows or fabrics utilising the theoretical framework of gas transport introduced in the last chapters of this thesis should be taken into consideration, because it allows to increase the fundamental understanding of the process, and to straightforwardly establish the scaling laws governing the phenomena occurring

at the interface of gases and complex surfaces, thus facilitating the process development and optimisation.

This work has shown the viability of the strategy of manufacturing of CNT-CF hierarchical composites including a protective alumina film on CF. The adhesion of the alumina on CF has been ensured with an improved ALD coating process. Moreover, owing to the fact, that alumina is shown to function well not only as the CF protection, but also as an effective support for the CNT growth by CVD, the CNTs can be grown on the CFs without compromises on either CF strength, nor on the CNT density, homogeneity or alignment, which constitutes a significant improvement over many previous reports. Using the methods developed here, one can uniformly grow dense and aligned CNTs on substrates of geometries as complex as CF tows or fabrics, without catalyst deactivation by migration into the substrate subsurface regions. Furthermore, the theoretical work on gas diffusion in fibrous media presented here lays the foundation for understanding of complex gas-phase processing of the fibres and CNTs, as well as other fibrous substances, such as certain aerogels or electrospun nanofibre mats. Accounting for all the above, we believe that our work brings us a leap further in a journey of hierarchical composites, towards their use in extreme applications and ultimately, perhaps, their wide adoption, decreasing our environmental impact and improving our everyday lives.

Bibliography

[1] M. Holmes, Carbon fibre reinforced plastics market continues growth path, Reinf. Plast. 57 (2013) 24–29. https://doi.org/10.1016/S0034-3617(13)70186-3.

[2] M. Toozandehjani, Conventional and Advanced Composites in Aerospace Industry: Technologies Revisited, Am. J. Aerosp. Eng. 5 (2018) 9. https://doi.org/10.11648/j.ajae.20180501.12.

[3] K.E. Whitener, P.E. Sheehan, Graphene synthesis, Diam. Relat. Mater. 46 (2014) 25–34. https://doi.org/10.1016/j.diamond.2014.04.006.

[4] C.E. Baddour, C. Briens, Carbon Nanotube Synthesis: A Review, Int. J. Chem. React. Eng. 3 (2005). https://doi.org/10.2202/1542-6580.1279.

[5] T. Maiyalagan, B. Viswanathan, Template synthesis and characterization of well-aligned nitrogen containing carbon nanotubes, Mater. Chem. Phys. 93 (2005) 291–295. https://doi.org/10.1016/j.matchemphys.2005.03.039.

[6] S.A. Steiner, R. Li, B.L. Wardle, Circumventing the Mechanochemical Origins of Strength Loss in the Synthesis of Hierarchical Carbon Fibers, ACS Appl. Mater. Interfaces. 5 (2013) 4892–4903. https://doi.org/10.1021/am4006385.

[7] Production and properties of high modulus carbon fibres, Proc. R. Soc. Lond. Math. Phys. Sci. 319 (1970) 5–15. https://doi.org/10.1098/rspa.1970.0161.

[8] P.-X. Hou, J. Du, C. Liu, W. Ren, E.I. Kauppinen, H.-M. Cheng, Applications of carbon nanotubes and graphene produced by chemical vapor deposition, MRS Bull. 42 (2017) 825–833. https://doi.org/10.1557/mrs.2017.238.

[9] M. Yu, Strength and Breaking Mechanism of Multiwalled Carbon Nanotubes Under Tensile Load, Science. 287 (2000) 637–640. https://doi.org/10.1126/science.287.5453.637.

[10] C. Lee, X. Wei, J.W. Kysar, J. Hone, Measurement of the Elastic Properties and Intrinsic Strength of Monolayer Graphene, Science. 321 (2008) 385–388. https://doi.org/10.1126/science.1157996.

[11] E. Wang, Y. Dong, M.Z. Islam, L. Yu, F. Liu, S. Chen, X. Qi, Y. Zhu, Y. Fu, Z. Xu, N. Hu, Effect of graphene oxide-carbon nanotube hybrid filler on the mechanical property and thermal response speed of shape memory epoxy composites, Compos. Sci. Technol. 169 (2019) 209–216. https://doi.org/10.1016/j.compscitech.2018.11.022.

[12] V.P. Veedu, A. Cao, X. Li, K. Ma, C. Soldano, S. Kar, P.M. Ajayan, M.N. Ghasemi-Nejhad, Multifunctional composites using reinforced laminae with carbon-nanotube forests, Nat. Mater. 5 (2006) 457–462. https://doi.org/10.1038/nmat1650.

[13] H. Qian, A. Bismarck, E.S. Greenhalgh, M.S.P. Shaffer, Carbon nanotube grafted carbon fibres: A study of wetting and fibre fragmentation, Compos. Part Appl. Sci. Manuf. 41 (2010) 1107–1114. https://doi.org/10.1016/j.compositesa.2010.04.004.

[14] S.-B. Lee, O. Choi, W. Lee, J.-W. Yi, B.-S. Kim, J.-H. Byun, M.-K. Yoon, H. Fong, E.T. Thostenson, T.-W. Chou, Processing and characterization of multi-scale hybrid composites reinforced with nanoscale carbon reinforcements and carbon fibers, Compos. Part Appl. Sci. Manuf. 42 (2011) 337–344. https://doi.org/10.1016/j.compositesa.2010.10.016.

[15] E.H. Backes, F.R. Passador, C. Leopold, B. Fiedler, L.A. Pessan, Electrical, thermal and thermo-mechanical properties of epoxy/multi-wall carbon nanotubes/mineral fillers nanocomposites, J. Compos. Mater. 52 (2018) 3209–3217. https://doi.org/10.1177/0021998318763497.

[16] T.M. Herceg, M.S. Zainol Abidin, E.S. Greenhalgh, M.S.P. Shaffer, A. Bismarck, Thermosetting hierarchical composites with high carbon nanotube loadings: En route to high performance, Compos. Sci. Technol. 127 (2016) 134–141. https://doi.org/10.1016/j.compscitech.2016.02.015.

[17] Y. Wang, G.J. Weng, Electrical Conductivity of Carbon Nanotube- and Graphene-Based Nanocomposites, in: S.A. Meguid, G.J. Weng (Eds.), Micromechanics Nanomechanics Compos. Solids, Springer International Publishing, Cham, 2018: pp. 123–156. https://doi.org/10.1007/978-3-319-52794-9_4.

[18] J.K.W. Sandler, J.E. Kirk, I.A. Kinloch, M.S.P. Shaffer, A.H. Windle, Ultra-low electrical percolation threshold in carbon-nanotube-epoxy composites, Polymer. 44 (2003) 5893–5899. https://doi.org/10.1016/S0032-3861(03)00539-1.

[19] T. Augustin, J. Karsten, B. Kötter, B. Fiedler, Health monitoring of scarfed CFRP joints under cyclic loading via electrical resistance measurements using carbon nanotube modified adhesive films, Compos. Part Appl. Sci. Manuf. 105 (2018) 150–155. https://doi.org/10.1016/j.compositesa.2017.11.015.

[20] T. Augustin, J. Karsten, B. Fiedler, Detection and localization of impact damages in carbon nanotube–modified epoxy adhesive films with printed circuits, Struct. Health Monit. 17 (2018) 1166–1177. https://doi.org/10.1177/1475921717738140.

[21] X. Ma, F. Scarpa, H.-X. Peng, G. Allegri, J. Yuan, R. Ciobanu, Design of a hybrid carbon fibre/carbon nanotube composite for enhanced lightning strike resistance, Aerosp. Sci. Technol. 47 (2015) 367–377. https://doi.org/10.1016/j.ast.2015.10.002.

[22] H. Qian, H. Diao, M. Houllé, J. Amadou, N. Shirshova, E.S. Greenhalgh, M.S.P. Shaffer, A. Bismarck, Carbon fibre modifications for composite structural power devices, in: Proc. ECCM15 - 15th Eur. Conf. Compos. Mater., Venice, Italy, 2012. http://www.escm.eu.org/eccm15/data/assets/1884.pdf.

[23] P. Fratzl, R. Weinkamer, Nature's hierarchical materials, Prog. Mater. Sci. 52 (2007) 1263–1334. https://doi.org/10.1016/j.pmatsci.2007.06.001.

[24] D. Fengel, G. Wegener, Wood: chemistry, ultrastructure, reactions, 2011. https://doi.org/10.1515/9783110839654 (accessed July 25, 2020).

[25] F. Barthelat, R. Rabiei, Toughness amplification in natural composites, J. Mech. Phys. Solids. 59 (2011) 829–840. https://doi.org/10.1016/j.jmps.2011.01.001.

[26] A. Paipetis, C. Galiotis, Effect of fibre sizing on the stress transfer efficiency in carbon/epoxy model composites, Compos. Part Appl. Sci. Manuf. 27 (1996) 755–767. https://doi.org/10.1016/1359-835X(96)00054-1.

[27] Y.S. Song, J.R. Youn, Influence of dispersion states of carbon nanotubes on physical properties of epoxy nanocomposites, Carbon. 43 (2005) 1378–1385. https://doi.org/10.1016/j.carbon.2005.01.007.

[28] B. Fiedler, F.H. Gojny, M.H.G. Wichmann, M.C.M. Nolte, K. Schulte, Fundamental aspects of nano-reinforced composites, Compos. Sci. Technol. 66 (2006) 3115–3125. https://doi.org/10.1016/j.compscitech.2005.01.014.

[29] D. Quan, J.L. Urdániz, A. Ivanković, Enhancing mode-I and mode-II fracture toughness of epoxy and carbon fibre reinforced epoxy composites using multi-walled carbon nanotubes, Mater. Des. 143 (2018) 81–92. https://doi.org/10.1016/j.matdes.2018.01.051.

[30] I. Zaman, T.T. Phan, H.-C. Kuan, Q. Meng, L.T. Bao La, L. Luong, O. Youssf, J. Ma, Epoxy/graphene platelets nanocomposites with two levels of interface strength, Polymer. 52 (2011) 1603–1611. https://doi.org/10.1016/j.polymer.2011.02.003.

[31] Z. Jia, X. Feng, Y. Zou, An investigation on mode II fracture toughness enhancement of epoxy adhesive using graphene nanoplatelets, Compos. Part B Eng. 155 (2018) 452–456. https://doi.org/10.1016/j.compositesb.2018.09.094.

[32] D.R. Bortz, E.G. Heras, I. Martin-Gullon, Impressive Fatigue Life and Fracture Toughness Improvements in Graphene Oxide/Epoxy Composites, Macromolecules. 45 (2012) 238–245. https://doi.org/10.1021/ma201563k.

[33] B. Ahmadi-Moghadam, F. Taheri, Fracture and toughening mechanisms of GNP-based nanocomposites in modes I and II fracture, Eng. Fract. Mech. 131 (2014) 329–339. https://doi.org/10.1016/j.engfracmech.2014.08.008.

[34] H. Meeuw, J. Körbelin, V. Wisniewski, A. Nia, A. Vázquez, M. Lohe, X. Feng, B. Fiedler, Carbon Nanoparticles' Impact on Processability and Physical Properties of Epoxy Resins—A Comprehensive Study Covering Rheological, Electrical, Thermo-Mechanical, and Fracture Properties (Mode I and II), Polymers. 11 (2019) 231. https://doi.org/10.3390/polym11020231.

[35] C. Leopold, W.V. Liebig, H. Wittich, B. Fiedler, Size effect of graphene nanoparticle modified epoxy matrix, Compos. Sci. Technol. 134 (2016) 217–225. https://doi.org/10.1016/j.compscitech.2016.08.022.

[36] B.-C. Wang, X. Zhou, K.-M. Ma, Fabrication and properties of CNTs/carbon fabric hybrid multiscale composites processed via resin transfer molding technique, Compos. Part B Eng. 46 (2013) 123–129. https://doi.org/10.1016/j.compositesb.2012.10.022.

[37] S. Rahmanian, A.R. Suraya, M.A. Shazed, R. Zahari, E.S. Zainudin, Mechanical characterization of epoxy composite with multiscale reinforcements: Carbon nanotubes and short carbon fibers, Mater. Des. 60 (2014) 34–40. https://doi.org/10.1016/j.matdes.2014.03.039.

[38] V. Kostopoulos, A. Baltopoulos, P. Karapappas, A. Vavouliotis, A. Paipetis, Impact and after-impact properties of carbon fibre reinforced composites enhanced with multi-wall carbon nanotubes, Compos. Sci. Technol. 70 (2010) 553–563. https://doi.org/10.1016/j.compscitech.2009.11.023.

[39] B.-G. Cho, S.-H. Hwang, M. Park, J.K. Park, Y.-B. Park, H.G. Chae, The effects of plasma surface treatment on the mechanical properties of polycarbonate/carbon nanotube/carbon fiber composites, Compos. Part B Eng. 160 (2019) 436–445. https://doi.org/10.1016/j.compositesb.2018.12.062.

[40] R.M. Santos, D. Vale, J. Rocha, C. Martins, S.T. Mould, N. Rocha, Multiscale carbon fibre–reinforced polymer (CFRP) composites containing carbon nanotubes with tailored interfaces, Fatigue Fract. Eng. Mater. Struct. 42 (2019) 1521–1533. https://doi.org/10.1111/ffe.13006.

[41] V.K. Srivastava, T. Gries, D. Veit, T. Quadflieg, B. Mohr, M. Kolloch, Effect of nanomaterial on mode I and mode II interlaminar fracture toughness of woven carbon fabric reinforced polymer composites, Eng. Fract. Mech. 180 (2017) 73–86. https://doi.org/10.1016/j.engfracmech.2017.05.030.

[42] F.H. Gojny, M.H.G. Wichmann, U. Köpke, B. Fiedler, K. Schulte, Carbon nanotube-reinforced epoxy-composites: enhanced stiffness and fracture toughness at low nanotube content, Compos. Sci. Technol. 64 (2004) 2363–2371. https://doi.org/10.1016/j.compscitech.2004.04.002.

[43] R.B. Mathur, S. Chatterjee, B.P. Singh, Growth of carbon nanotubes on carbon fibre substrates to produce hybrid/phenolic composites with improved mechanical properties, Compos. Sci. Technol. 68 (2008) 1608–1615. https://doi.org/10.1016/j.compscitech.2008.02.020.

[44] E.J. García, A.J. Hart, B.L. Wardle, A.H. Slocum, Fabrication of composite microstructures by capillarity-driven wetting of aligned carbon nanotubes with polymers, Nanotechnology. 18 (2007) 165602. https://doi.org/10.1088/0957-4484/18/16/165602.

[45] E.J. García, A.J. Hart, B.L. Wardle, A.H. Slocum, Fabrication and Nanocompression Testing of Aligned Carbon-Nanotube–Polymer Nanocomposites, Adv. Mater. 19 (2007) 2151–2156. https://doi.org/10.1002/adma.200700237.

[46] B. Natarajan, N. Lachman, T. Lam, D. Jacobs, C. Long, M. Zhao, B.L. Wardle, R. Sharma, J.A. Liddle, The Evolution of Carbon Nanotube Network Structure in Unidirectional Nanocomposites Resolved by Quantitative Electron Tomography, ACS Nano. 9 (2015) 6050–6058. https://doi.org/10.1021/acsnano.5b01044.

[47] M. Bedewy, E.R. Meshot, H. Guo, E.A. Verploegen, W. Lu, A.J. Hart, Collective Mechanism for the Evolution and Self-Termination of Vertically Aligned Carbon Nanotube Growth, J. Phys. Chem. C. 113 (2009) 20576–20582. https://doi.org/10.1021/jp904152v.

[48] B.L. Wardle, D.S. Saito, E.J. García, A.J. Hart, R.G. de Villoria, E.A. Verploegen, Fabrication and Characterization of Ultrahigh-Volume- Fraction Aligned Carbon Nanotube-Polymer Composites, Adv. Mater. 20 (2008) 2707–2714. https://doi.org/10.1002/adma.200800295.

[49] J.N. Coleman, U. Khan, W.J. Blau, Y.K. Gun'ko, Small but strong: A review of the mechanical properties of carbon nanotube–polymer composites, Carbon. 44 (2006) 1624–1652. https://doi.org/10.1016/j.carbon.2006.02.038.

[50] P.D. Bradford, X. Wang, H. Zhao, J.-P. Maria, Q. Jia, Y.T. Zhu, A novel approach to fabricate high volume fraction nanocomposites with long aligned carbon nanotubes, Compos. Sci. Technol. 70 (2010) 1980–1985. https://doi.org/10.1016/j.compscitech.2010.07.020.

[51] S.S. Wicks, B.L. Wardle, Fracture Toughness of Aligned Carbon Nanotube Polymer Nanocomposites for the Reinforcement of Hierarchical Composite Materials, in: 55th AIAA ASME ASCE AHS ASC Struct. Struct. Dyn. Mater. Conf., American Institute of Aeronautics and Astronautics, National Harbor, Maryland, 2014. https://doi.org/10.2514/6.2014-0107.

[52] S.S. Wicks, A.S. Vazquez, B.L. Wardle, Fracture Toughness of Aligned Carbon Nanotube Polymer Nanocomposites, in: 56th AIAA ASCE AHS ASC Struct. Struct. Dyn. Mater. Conf., American Institute of Aeronautics and Astronautics, Kissimmee, Florida, 2015. https://doi.org/10.2514/6.2015-0125.

[53] V. Romanov, S.V. Lomov, I. Verpoest, L. Gorbatikh, Inter-fiber stresses in composites with carbon nanotube grafted and coated fibers, Compos. Sci. Technol. 114 (2015) 79–86. https://doi.org/10.1016/j.compscitech.2015.04.013.

[54] A. Puck, H. Schürmann, Failure analysis of FRP laminates by means of physically based phenomenological models, in: Fail. Criteria Fibre-Reinf.-Polym. Compos., Elsevier, 2004: pp. 832–876. https://doi.org/10.1016/B978-008044475-8/50028-7.

[55] P. Lv, Y. Feng, P. Zhang, H. Chen, N. Zhao, W. Feng, Increasing the interfacial strength in carbon fiber/epoxy composites by controlling the orientation and length of carbon nanotubes grown on the fibers, Carbon. 49 (2011) 4665–4673. https://doi.org/10.1016/j.carbon.2011.06.064.

[56] K. Ji, G. Meng, C. Yuan, E. Cui, Y. Li, J. Sun, Z. Dai, Synergistic effect of Fe and Al_2O_3 layers on the growth of vertically aligned carbon nanotubes for gecko-inspired adhesive applications, J. Manuf. Process. 33 (2018) 238–244. https://doi.org/10.1016/j.jmapro.2018.05.015.

[57] F. An, C. Lu, J. Guo, S. He, H. Lu, Y. Yang, Preparation of vertically aligned carbon nanotube arrays grown onto carbon fiber fabric and evaluating its wettability on effect of composite, Appl. Surf. Sci. 258 (2011) 1069–1076. https://doi.org/10.1016/j.apsusc.2011.09.003.

[58] A.Y. Boroujeni, M. Tehrani, A.J. Nelson, M. Al-Haik, Hybrid carbon nanotube–carbon fiber composites with improved in-plane mechanical properties, Compos. Part B Eng. 66 (2014) 475–483. https://doi.org/10.1016/j.compositesb.2014.06.010.

[59] S.P. Sharma, S.C. Lakkad, Effect of CNTs growth on carbon fibers on the tensile strength of CNTs grown carbon fiber-reinforced polymer matrix composites, Compos. Part Appl. Sci. Manuf. 42 (2011) 8–15. https://doi.org/10.1016/j.compositesa.2010.09.008.

[60] M.A. Shazed, A.R. Suraya, S. Rahmanian, M.A. Mohd Salleh, Effect of fibre coating and geometry on the tensile properties of hybrid carbon nanotube coated carbon fibre reinforced composite, Mater. Des. 1980-2015. 54 (2014) 660–669. https://doi.org/10.1016/j.matdes.2013.08.063.

[61] E. Garcia, B. Wardle, R. deVilloria, R. Guzman de Villoria, S. Wicks, K. Ishiguro, N. Yamamoto, A. Hart, Aligned Carbon Nanotube Reinforcement of Advanced Composite Ply Interfaces,

in: 49th AIAA ASME ASCE AHS ASC Struct. Struct. Dyn. Mater. Conf. Ltbrgt 16th AIAAASMEAHS Adapt. Struct. Conf. 10t, American Institute of Aeronautics and Astronautics, Schaumburg, IL, 2008. https://doi.org/10.2514/6.2008-1768.

[62] E. Garcia, B. Wardle, A. Johnhart, N. Yamamoto, Fabrication and multifunctional properties of a hybrid laminate with aligned carbon nanotubes grown In Situ, Compos. Sci. Technol. 68 (2008) 2034–2041. https://doi.org/10.1016/j.compscitech.2008.02.028.

[63] S.S. Wicks, W. Wang, M.R. Williams, B.L. Wardle, Multi-scale interlaminar fracture mechanisms in woven composite laminates reinforced with aligned carbon nanotubes, Compos. Sci. Technol. 100 (2014) 128–135. https://doi.org/10.1016/j.compscitech.2014.06.003.

[64] E.J. Garcia, B.L. Wardle, A. John Hart, Joining prepreg composite interfaces with aligned carbon nanotubes, Compos. Part Appl. Sci. Manuf. 39 (2008) 1065–1070. https://doi.org/10.1016/j.compositesa.2008.03.011.

[65] D.C. Davis, J.W. Wilkerson, J. Zhu, V.G. Hadjiev, A strategy for improving mechanical properties of a fiber reinforced epoxy composite using functionalized carbon nanotubes, Compos. Sci. Technol. 71 (2011) 1089–1097. https://doi.org/10.1016/j.compscitech.2011.03.014.

[66] D.C. Davis, B.D. Whelan, An experimental study of interlaminar shear fracture toughness of a nanotube reinforced composite, Compos. Part B Eng. 42 (2011) 105–116. https://doi.org/10.1016/j.compositesb.2010.06.001.

[67] W. Liu, S. Zhang, L. Hao, F. Yang, W. Jiao, X. Li, R. Wang, Fabrication of carbon nanotubes/carbon fiber hybrid fiber in industrial scale by sizing process, Appl. Surf. Sci. 284 (2013) 914–920. https://doi.org/10.1016/j.apsusc.2013.08.045.

[68] M.S. Zainol Abidin, T. Herceg, E.S. Greenhalgh, M. Shaffer, A. Bismarck, Enhanced fracture toughness of hierarchical carbon nanotube reinforced carbon fibre epoxy composites with engineered matrix microstructure, Compos. Sci. Technol. 170 (2019) 85–92. https://doi.org/10.1016/j.compscitech.2018.11.017.

[69] T.M. Herceg, S.-H. Yoon, M.S.Z. Abidin, E.S. Greenhalgh, A. Bismarck, M.S.P. Shaffer, Thermosetting nanocomposites with high carbon nanotube loadings processed by a scalable powder based method, Compos. Sci. Technol. 127 (2016) 62–70. https://doi.org/10.1016/j.compscitech.2016.01.017.

[70] J. Guo, C. Lu, Continuous preparation of multiscale reinforcement by electrophoretic deposition of carbon nanotubes onto carbon fiber tows, Carbon. 50 (2012) 3101–3103. https://doi.org/10.1016/j.carbon.2012.02.044.

[71] J.D. Schaefer, A.J. Rodriguez, M.E. Guzman, C.-S. Lim, B. Minaie, Effects of electrophoretically deposited carbon nanofibers on the interface of single carbon fibers embedded in epoxy matrix, Carbon. 49 (2011) 2750–2759. https://doi.org/10.1016/j.carbon.2011.02.070.

[72] Q. An, A.N. Rider, E.T. Thostenson, Electrophoretic deposition of carbon nanotubes onto carbon-fiber fabric for production of carbon/epoxy composites with improved mechanical properties, Carbon. 50 (2012) 4130–4143. https://doi.org/10.1016/j.carbon.2012.04.061.

[73] M.F.D. Riccardis, D. Carbone, Th.D. Makris, R. Giorgi, N. Lisi, E. Salernitano, Anchorage of carbon nanotubes grown on carbon fibres, Carbon. 44 (2006) 671–674. https://doi.org/10.1016/j.carbon.2005.09.024.

[74] R. Li, Hierarchical carbon fiber composites with radially aligned carbon nanotubes : preservation of in-plane tensile properties, Ph.D. Thesis, Massachusetts Institute of Technology, 2013. http://hdl.handle.net/1721.1/85806.

[75] R. Li, N. Lachman, P. Florin, H.D. Wagner, B.L. Wardle, Hierarchical carbon nanotube carbon fiber unidirectional composites with preserved tensile and interfacial properties, Compos. Sci. Technol. 117 (2015) 139–145. https://doi.org/10.1016/j.compscitech.2015.04.014.

[76] N. De Greef, L. Zhang, A. Magrez, L. Forró, J.-P. Locquet, I. Verpoest, J.W. Seo, Direct growth of carbon nanotubes on carbon fibers: Effect of the CVD parameters on the degradation of mechanical properties of carbon fibers, Diam. Relat. Mater. 51 (2015) 39–48. https://doi.org/10.1016/j.diamond.2014.11.002.

[77] C.C. Luhrs, D. Garcia, M. Tehrani, M. Al-Haik, M.R. Taha, J. Phillips, Generation of carbon nanofilaments on carbon fibers at 550°C, Carbon. 47 (2009) 3071–3078. https://doi.org/10.1016/j.carbon.2009.07.019.

[78] A.Y. Boroujeni, M. Al-Haik, Carbon nanotube – Carbon fiber reinforced polymer composites with extended fatigue life, Compos. Part B Eng. 164 (2019) 537–545. https://doi.org/10.1016/j.compositesb.2018.11.056.

[79] R. Cartwright, S. Esconjauregui, D. Hardeman, S. Bhardwaj, R. Weatherup, Y. Guo, L. D'Arsié, B. Bayer, P. Kidambi, S. Hofmann, E. Wright, J. Clarke, D. Oakes, C. Cepek, J. Robertson, Low temperature growth of carbon nanotubes on tetrahedral amorphous carbon using Fe–Cu catalyst, Carbon. 81 (2015) 639–649. https://doi.org/10.1016/j.carbon.2014.10.001.

[80] T.R. Pozegic, J.V. Anguita, I. Hamerton, K.D.G.I. Jayawardena, J.-S. Chen, V. Stolojan, P. Ballocchi, R. Walsh, S.R.P. Silva, Multi-Functional Carbon Fibre Composites using Carbon Nanotubes as an Alternative to Polymer Sizing, Sci. Rep. 6 (2016) 37334. https://doi.org/10.1038/srep37334.

[81] M. Escobar, G. Rubiolo, R. Candal, S. Goyanes, Effect of catalyst preparation on the yield of carbon nanotube growth, Phys. B Condens. Matter. 404 (2009) 2795–2798. https://doi.org/10.1016/j.physb.2009.06.088.

[82] G. Kaptay, J. Janczak-Rusch, G. Pigozzi, L.P.H. Jeurgens, Theoretical Analysis of Melting Point Depression of Pure Metals in Different Initial Configurations, J. Mater. Eng. Perform. 23 (2014) 1600–1607. https://doi.org/10.1007/s11665-014-0885-z.

[83] P.B. Amama, C.L. Pint, S.M. Kim, L. McJilton, K.G. Eyink, E.A. Stach, R.H. Hauge, B. Maruyama, Influence of Alumina Type on the Evolution and Activity of Alumina-Supported Fe Catalysts in Single-Walled Carbon Nanotube Carpet Growth, ACS Nano. 4 (2010) 895–904. https://doi.org/10.1021/nn901700u.

[84] T. Young, III. An essay on the cohesion of fluids, Philos. Trans. R. Soc. Lond. 95 (1805) 65–87. https://doi.org/10.1098/rstl.1805.0005.

[85] S. Sakurai, H. Nishino, D.N. Futaba, S. Yasuda, T. Yamada, A. Maigne, Y. Matsuo, E. Nakamura, M. Yumura, K. Hata, Role of Subsurface Diffusion and Ostwald Ripening in Catalyst

Formation for Single-Walled Carbon Nanotube Forest Growth, J. Am. Chem. Soc. 134 (2012) 2148–2153. https://doi.org/10.1021/ja208706c.

[86] S. Ratkovic, Dj. Vujicic, E. Kiss, G. Boskovic, O. Geszti, Different degrees of weak metal–support interaction in Fe–(Ni)/Al_2O_3 catalyst governing activity and selectivity in carbon nanotubes' production using ethylene, Mater. Chem. Phys. 129 (2011) 398–405. https://doi.org/10.1016/j.matchemphys.2011.04.036.

[87] S.M. Kim, C.L. Pint, P.B. Amama, D.N. Zakharov, R.H. Hauge, B. Maruyama, E.A. Stach, Evolution in Catalyst Morphology Leads to Carbon Nanotube Growth Termination, J. Phys. Chem. Lett. 1 (2010) 918–922. https://doi.org/10.1021/jz9004762.

[88] K. Nakashima, K. Takihira, K. Mori, N. Shinozaki, Wettability of Al_2O_3 Substrate by Liquid Iron - Effects of Oxygen in Liquid Iron and Purity of Al_2O_3 Substrate, Mater. Trans. JIM. 33 (1992) 918–926. https://doi.org/10.2320/matertrans1989.33.918.

[89] K. Ogino, K. Nogi, Y. Koshida, Effect of Oxygen on the Wettability of Solid Oxide with Molten Iron, Tetsu--Hagane. 59 (1973) 1380–1387. https://doi.org/10.2355/tetsutohagane1955.59.10_1380.

[90] S. Vogel, C. Dransfeld, B. Friedler, J. Gobrecht, Protective effect of thin alumina layer on carbon fibre to preserve tensile strength during CNT growth by CVD, in: Proc. ECCM16 - 16th Eur. Conf. Compos. Mater., Seville, Spain, 2014.

[91] L. Zhu, D.W. Hess, C.-P. Wong, Monitoring Carbon Nanotube Growth by Formation of Nanotube Stacks and Investigation of the Diffusion-Controlled Kinetics, J. Phys. Chem. B. 110 (2006) 5445–5449. https://doi.org/10.1021/jp060027q.

[92] M. Knudsen, Die Gesetze der Molekularströmung und der inneren Reibungsströmung der Gase durch Röhren, Ann. Phys. 333 (1909) 75–130. https://doi.org/10.1002/andp.19093330106.

[93] R. Menzel, M.Q. Tran, A. Menner, C.W.M. Kay, A. Bismarck, M.S.P. Shaffer, A versatile, solvent-free methodology for the functionalisation of carbon nanotubes, Chem. Sci. 1 (2010) 603. https://doi.org/10.1039/c0sc00287a.

[94] Q. Song, K. Li, H. Li, H. Li, C. Ren, Grafting straight carbon nanotubes radially onto carbon fibers and their effect on the mechanical properties of carbon/carbon composites, Carbon. 50 (2012) 3949–3952. https://doi.org/10.1016/j.carbon.2012.03.023.

[95] H. Qian, E.S. Greenhalgh, M.S.P. Shaffer, A. Bismarck, Carbon nanotube-based hierarchical composites: a review, J. Mater. Chem. 20 (2010) 4751. https://doi.org/10.1039/c000041h.

[96] J.W. Johnson, D.J. Thorne, Effect of internal polymer flaws on strength of carbon fibres prepared from an acrylic precursor, Carbon. 7 (1969) 659–661. https://doi.org/10.1016/0008-6223(69)90520-X.

[97] H. Qian, A. Bismarck, E.S. Greenhalgh, G. Kalinka, M.S.P. Shaffer, Hierarchical Composites Reinforced with Carbon Nanotube Grafted Fibers: The Potential Assessed at the Single Fiber Level, Chem. Mater. 20 (2008) 1862–1869. https://doi.org/10.1021/cm702782j.

[98] S. Zhu, C.-H. Su, S.L. Lehoczky, I. Muntele, D. Ila, Carbon nanotube growth on carbon fibers, Diam. Relat. Mater. 12 (2003) 1825–1828. https://doi.org/10.1016/S0925-9635(03)00205-X.

[99] N. Sonoyama, M. Ohshita, A. Nijubu, H. Nishikawa, H. Yanase, J. Hayashi, T. Chiba, Synthesis of carbon nanotubes on carbon fibers by means of two-step thermochemical vapor deposition, Carbon. 44 (2006) 1754–1761. https://doi.org/10.1016/j.carbon.2005.12.039.

[100] Q. Zhang, J. Liu, R. Sager, L. Dai, J. Baur, Hierarchical composites of carbon nanotubes on carbon fiber: Influence of growth condition on fiber tensile properties, Compos. Sci. Technol. 69 (2009) 594–601. https://doi.org/10.1016/j.compscitech.2008.12.002.

[101] R. Warren, C.H. Anderson, M. Carlsson, High-temperature compatibility of carbon fibres with nickel, J. Mater. Sci. 13 (1978) 178–188. https://doi.org/10.1007/BF00739289.

[102] W. Szmyt, S. Vogel, M. Holler, A. Diaz, J. Gobrecht, M. Calame, C. Dransfeld, Carbon fibre with and without a protective ultrathin alumina film grafted with carbon nanotubes for hierarchical composites observed by ptychographic X-ray computed tomography, in: Proc. ECCM17 - 17th Eur. Conf. Compos. Mater., Munich, Germany, 2016.

[103] M. Dierolf, A. Menzel, P. Thibault, P. Schneider, C.M. Kewish, R. Wepf, O. Bunk, F. Pfeiffer, Ptychographic X-ray computed tomography at the nanoscale, Nature. 467 (2010) 436–439. https://doi.org/10.1038/nature09419.

[104] A. Diaz, M. Guizar-Sicairos, A. Poeppel, A. Menzel, O. Bunk, Characterization of carbon fibers using X-ray phase nanotomography, Carbon. 67 (2014) 98–103. https://doi.org/10.1016/j.carbon.2013.09.066.

[105] M. Holler, A. Diaz, M. Guizar-Sicairos, P. Karvinen, E. Färm, E. Härkönen, M. Ritala, A. Menzel, J. Raabe, O. Bunk, X-ray ptychographic computed tomography at 16 nm isotropic 3D resolution, Sci. Rep. 4 (2014) 3857. https://doi.org/10.1038/srep03857.

[106] S.M. George, Atomic Layer Deposition: An Overview, Chem. Rev. 110 (2010) 111–131. https://doi.org/10.1021/cr900056b.

[107] M. Kumar, Y. Ando, Chemical Vapor Deposition of Carbon Nanotubes: A Review on Growth Mechanism and Mass Production, J. Nanosci. Nanotechnol. 10 (2010) 3739–3758. https://doi.org/10.1166/jnn.2010.2939.

[108] J.M. Rodenburg, A.C. Hurst, A.G. Cullis, B.R. Dobson, F. Pfeiffer, O. Bunk, C. David, K. Jefimovs, I. Johnson, Hard-X-Ray Lensless Imaging of Extended Objects, Phys. Rev. Lett. 98 (2007). https://doi.org/10.1103/PhysRevLett.98.034801.

[109] H.M.L. Faulkner, J.M. Rodenburg, Movable Aperture Lensless Transmission Microscopy: A Novel Phase Retrieval Algorithm, Phys. Rev. Lett. 93 (2004). https://doi.org/10.1103/PhysRevLett.93.023903.

[110] S. Gorelick, V.A. Guzenko, J. Vila-Comamala, C. David, Direct e-beam writing of dense and high aspect ratio nanostructures in thick layers of PMMA for electroplating, Nanotechnology. 21 (2010) 295303. https://doi.org/10.1088/0957-4484/21/29/295303.

[111] X. Huang, H. Yan, R. Harder, Y. Hwu, I.K. Robinson, Y.S. Chu, Optimization of overlap uniformness for ptychography, Opt. Express. 22 (2014) 12634. https://doi.org/10.1364/OE.22.012634.

[112] R. Dinapoli, A. Bergamaschi, B. Henrich, R. Horisberger, I. Johnson, A. Mozzanica, E. Schmid, B. Schmitt, A. Schreiber, X. Shi, G. Theidel, EIGER: Next generation single photon counting detector

for X-ray applications, Nucl. Instrum. Methods Phys. Res. Sect. Accel. Spectrometers Detect. Assoc. Equip. 650 (2011) 79–83. https://doi.org/10.1016/j.nima.2010.12.005.

[113] M. Dierolf, Ptychographic X-ray Microscopy and Tomography, Technical University Munich, 2015.

[114] P. Thibault, M. Dierolf, A. Menzel, O. Bunk, C. David, F. Pfeiffer, High-Resolution Scanning X-ray Diffraction Microscopy, Science. 321 (2008) 379–382. https://doi.org/10.1126/science.1158573.

[115] P. Thibault, M. Guizar-Sicairos, Maximum-likelihood refinement for coherent diffractive imaging, New J. Phys. 14 (2012) 063004. https://doi.org/10.1088/1367-2630/14/6/063004.

[116] M. Guizar-Sicairos, A. Diaz, M. Holler, M.S. Lucas, A. Menzel, R.A. Wepf, O. Bunk, Phase tomography from x-ray coherent diffractive imaging projections, Opt. Express. 19 (2011) 21345. https://doi.org/10.1364/OE.19.021345.

[117] M. Guizar-Sicairos, J.J. Boon, K. Mader, A. Diaz, A. Menzel, O. Bunk, Quantitative interior x-ray nanotomography by a hybrid imaging technique, Optica. 2 (2015) 259. https://doi.org/10.1364/OPTICA.2.000259.

[118] M. van Heel, M. Schatz, Fourier shell correlation threshold criteria, J. Struct. Biol. 151 (2005) 250–262. https://doi.org/10.1016/j.jsb.2005.05.009.

[119] M. Perezcabero, Characterization of carbon nanotubes and carbon nanofibers prepared by catalytic decomposition of acetylene in a fluidized bed reactor, J. Catal. 215 (2003) 305–316. https://doi.org/10.1016/S0021-9517(03)00026-5.

[120] A.K. Schaper, H. Hou, A. Greiner, F. Phillipp, The role of iron carbide in multiwalled carbon nanotube growth, J. Catal. 222 (2004) 250–254. https://doi.org/10.1016/j.jcat.2003.11.011.

[121] M.D. Groner, F.H. Fabreguette, J.W. Elam, S.M. George, Low-Temperature Al_2O_3 Atomic Layer Deposition, Chem. Mater. 16 (2004) 639–645. https://doi.org/10.1021/cm0304546.

[122] Hexcel©, HexTow® AS4 Carbon Fiber Product Data Sheet, (2016). www.hexcel.com/Resources/DataSheets/Carbon-Fiber-Data-Sheets/AS4.pdf.

[123] F.W. von Batchelder, R.F. Raeuchle, Re-examination of the symmetries of iron and nickel by the powder method, Acta Crystallogr. 7 (1954) 464–464. https://doi.org/10.1107/S0365110X54001466.

[124] I.G. Wood, L. Vočadlo, K.S. Knight, D.P. Dobson, W.G. Marshall, G.D. Price, J. Brodholt, Thermal expansion and crystal structure of cementite, Fe_3C, between 4 and 600 K determined by time-of-flight neutron powder diffraction, J. Appl. Crystallogr. 37 (2004) 82–90. https://doi.org/10.1107/S0021889803024695.

[125] J.C. Lagarias, J.A. Reeds, M.H. Wright, P.E. Wright, Convergence Properties of the Nelder--Mead Simplex Method in Low Dimensions, SIAM J. Optim. 9 (1998) 112–147. https://doi.org/10.1137/S1052623496303470.

[126] A.W. Bowman, A. Azzalini, Applied smoothing techniques for data analysis: the kernel approach with S-Plus illustrations, Clarendon Press ; Oxford University Press, Oxford : New York, 1997.

[127] W. Szmyt, S. Vogel, A. Diaz, M. Holler, J. Gobrecht, M. Calame, C. Dransfeld, Protective effect of ultrathin alumina film against diffusion of iron into carbon fiber during growth of carbon nanotubes for hierarchical composites investigated by ptychographic X-ray computed tomography, Carbon. 115 (2017) 347–362. https://doi.org/10.1016/j.carbon.2016.12.085.

[128] S. Zhandarov, E. Mäder, C. Scheffler, G. Kalinka, C. Poitzsch, S. Fliescher, Investigation of interfacial strength parameters in polymer matrix composites: Compatibility and reproducibility, Adv. Ind. Eng. Polym. Res. 1 (2018) 82–92. https://doi.org/10.1016/j.aiepr.2018.06.002.

[129] E. Mäder, C. Scheffler, A. Miene, S. Fliescher, U. Mörschel, C. Poitzsch, FIMATEST – A New Testing System to Determine the Fibre-Matrix Adhesion Strength by Means of Pull-Out Tests, in: Proc. 56th Dornbirn-MFC, Dornbirn, Austria, 2017. https://www.textechno.com/wp-content/uploads/2017/10/DornbirnMFC2017_FIMATEST.pdf.

[130] A. Gupta, P.A. Kelly, M. Ehrgott, S. Bickerton, A surrogate model based evolutionary game-theoretic approach for optimizing non-isothermal compression RTM processes, Compos. Sci. Technol. 84 (2013) 92–100. https://doi.org/10.1016/j.compscitech.2013.05.012.

[131] S.F. Zhandarov, E. Mäder, O.R. Yurkevich, Indirect estimation of fiber/polymer bond strength and interfacial friction from maximum load values recorded in the microbond and pull-out tests. Part I: local bond strength, J. Adhes. Sci. Technol. 16 (2002) 1171–1200. https://doi.org/10.1163/156856102320256837.

[132] S. Zhandarov, E. Mäder, Indirect estimation of fiber/polymer bond strength and interfacial friction from maximum load values recorded in the microbond and pull-out tests. Part II: Critical energy release rate, J. Adhes. Sci. Technol. 17 (2003) 967–980. https://doi.org/10.1163/156856103322112879.

[133] S. Zhandarov, Characterization of fiber/matrix interface strength: applicability of different tests, approaches and parameters, Compos. Sci. Technol. 65 (2005) 149–160. https://doi.org/10.1016/j.compscitech.2004.07.003.

[134] B. Efron, R. Tibshirani, An introduction to the bootstrap, Chapman & Hall, New York, 1993.

[135] H.J. Adèr, G.J. Mellenbergh, D.J. Hand, Advising on research methods: a consultant's companion, Johannes van Kessel, Huizen, 2008.

[136] E.G. Budylina, M.T. Azarova, A.K. Ievleva, T.K. Mikhailova, Thermooxidative stability of carbon fibres and methods of increasing it, Fibre Chem. 27 (1995) 95–97. https://doi.org/10.1007/BF00557667.

[137] P.D. Mangalgiri, Composite materials for aerospace applications, Bull. Mater. Sci. 22 (1999) 657–664. https://doi.org/10.1007/BF02749982.

[138] H. Adam, Carbon fibre in automotive applications, Mater. Des. 18 (1997) 349–355. https://doi.org/10.1016/S0261-3069(97)00076-9.

[139] R. Stewart, Carbon fibre composites poised for dramatic growth, Reinf. Plast. 53 (2009) 16–21. https://doi.org/10.1016/S0034-3617(09)70148-1.

[140] W. Yan, H.-Y. Liu, Y.-W. Mai, Mode II delamination toughness of z-pinned laminates, Compos. Sci. Technol. 64 (2004) 1937–1945. https://doi.org/10.1016/j.compscitech.2004.02.008.

[141] J. Brandt, K. Drechsler, F.-J. Arendts, Mechanical performance of composites based on various three-dimensional woven-fibre preforms, Compos. Sci. Technol. 56 (1996) 381–386. https://doi.org/10.1016/0266-3538(95)00135-2.

[142] Xiaogang Chen, L.W. Taylor, L.-J. Tsai, An overview on fabrication of three-dimensional woven textile preforms for composites, Text. Res. J. 81 (2011) 932–944. https://doi.org/10.1177/0040517510392471.

[143] L. Servinis, L.C. Henderson, T.R. Gengenbach, A.A. Kafi, M.G. Huson, B.L. Fox, Surface functionalization of unsized carbon fiber using nitrenes derived from organic azides, Carbon. 54 (2013) 378–388. https://doi.org/10.1016/j.carbon.2012.11.051.

[144] G.J. Ehlert, Y. Lin, H.A. Sodano, Carboxyl functionalization of carbon fibers through a grafting reaction that preserves fiber tensile strength, Carbon. 49 (2011) 4246–4255. https://doi.org/10.1016/j.carbon.2011.05.057.

[145] F. Zhao, Y. Huang, Improved interfacial properties of carbon fiber/epoxy composites through grafting polyhedral oligomeric silsesquioxane on carbon fiber surface, Mater. Lett. 64 (2010) 2742–2744. https://doi.org/10.1016/j.matlet.2010.08.074.

[146] P. Kainourgios, I.A. Kartsonakis, D.A. Dragatogiannis, E.P. Koumoulos, P. Goulis, C.A. Charitidis, Electrochemical surface functionalization of carbon fibers for chemical affinity improvement with epoxy resins, Appl. Surf. Sci. 416 (2017) 593–604. https://doi.org/10.1016/j.apsusc.2017.04.214.

[147] R.L. Zhang, B. Gao, Q.H. Ma, J. Zhang, H.Z. Cui, L. Liu, Directly grafting graphene oxide onto carbon fiber and the effect on the mechanical properties of carbon fiber composites, Mater. Des. 93 (2016) 364–369. https://doi.org/10.1016/j.matdes.2016.01.003.

[148] E.T. Thostenson, W.Z. Li, D.Z. Wang, Z.F. Ren, T.W. Chou, Carbon nanotube/carbon fiber hybrid multiscale composites, J. Appl. Phys. 91 (2002) 6034–6037. https://doi.org/10.1063/1.1466880.

[149] X. He, F. Zhang, R. Wang, W. Liu, Preparation of a carbon nanotube/carbon fiber multi-scale reinforcement by grafting multi-walled carbon nanotubes onto the fibers, Carbon. 45 (2007) 2559–2563. https://doi.org/10.1016/j.carbon.2007.08.018.

[150] A. Laachachi, A. Vivet, G. Nouet, B. Ben Doudou, C. Poilâne, J. Chen, J. Bo bai, M. Ayachi, A chemical method to graft carbon nanotubes onto a carbon fiber, Mater. Lett. 62 (2008) 394–397. https://doi.org/10.1016/j.matlet.2007.05.044.

[151] Y.-T. Liu, G.-P. Wu, C.-X. Lu, Grafting of carbon nanotubes onto carbon fiber surfaces by step-wise reduction of in-situ generated diazonium salts for enhancing carbon/epoxy interfaces, Mater. Lett. 134 (2014) 75–79. https://doi.org/10.1016/j.matlet.2014.07.053.

[152] E. Bekyarova, E.T. Thostenson, A. Yu, H. Kim, J. Gao, J. Tang, H.T. Hahn, T.-W. Chou, M.E. Itkis, R.C. Haddon, Multiscale Carbon Nanotube−Carbon Fiber Reinforcement for Advanced Epoxy Composites, Langmuir. 23 (2007) 3970–3974. https://doi.org/10.1021/la062743p.

[153] A. Battisti, D. Esqué-de los Ojos, R. Ghisleni, A.J. Brunner, Single fiber push-out characterization of interfacial properties of hierarchical CNT-carbon fiber composites prepared by electrophoretic deposition, Compos. Sci. Technol. 95 (2014) 121–127. https://doi.org/10.1016/j.compscitech.2014.02.017.

[154] N. De Greef, A. Magrez, E. Couteau, J.-P. Locquet, L. Forró, J.W. Seo, Growth of carbon nanotubes on carbon fibers without strength degradation, Phys. Status Solidi B. 249 (2012) 2420–2423. https://doi.org/10.1002/pssb.201200148.

[155] G. Lee, K.J. Kim, W.R. Yu, J.H. Youk, The effect of the surface roughness of carbon fibres on CNT growth by floating-catalyst chemical vapour deposition, Int. J. Nanotechnol. 10 (2013) 800. https://doi.org/10.1504/IJNT.2013.054219.

[156] D.B. Anthony, X. Sui, I. Kellersztein, H.G. De Luca, E.R. White, H.D. Wagner, E.S. Greenhalgh, A. Bismarck, M.S.P. Shaffer, Continuous carbon nanotube synthesis on charged carbon fibers, Compos. Part Appl. Sci. Manuf. 112 (2018) 525–538. https://doi.org/10.1016/j.compositesa.2018.05.027.

[157] C.J. Lee, D.W. Kim, T.J. Lee, Y.C. Choi, Y.S. Park, Y.H. Lee, W.B. Choi, N.S. Lee, G.-S. Park, J.M. Kim, Synthesis of aligned carbon nanotubes using thermal chemical vapor deposition, Chem. Phys. Lett. 312 (1999) 461–468. https://doi.org/10.1016/S0009-2614(99)01074-X.

[158] S. Fan, Self-Oriented Regular Arrays of Carbon Nanotubes and Their Field Emission Properties, Science. 283 (1999) 512–514. https://doi.org/10.1126/science.283.5401.512.

[159] W. Szmyt, M. Calame, C. Padeste, C. Dransfeld, Nanoengineering of fibre surface for carbon fibre-carbon nanotube hierarchical composites, in: Proc. ICCM22 - 22nd Int. Conf. Compos. Mater., Melbourne, Australia, 2019.

[160] R.F. Gibson, Principles of composite material mechanics, 2nd ed, CRC Press, Boca Raton, 2007.

[161] Ç. Öncel, Y. Yürüm, Carbon Nanotube Synthesis via the Catalytic CVD Method: A Review on the Effect of Reaction Parameters, Fuller. Nanotub. Carbon Nanostructures. 14 (2006) 17–37. https://doi.org/10.1080/15363830500538441.

[162] T. de los Arcos, M.G. Garnier, J.W. Seo, P. Oelhafen, V. Thommen, D. Mathys, The Influence of Catalyst Chemical State and Morphology on Carbon Nanotube Growth, J. Phys. Chem. B. 108 (2004) 7728–7734. https://doi.org/10.1021/jp049495v.

[163] L. Zhang, Z. Li, Y. Tan, G. Lolli, N. Sakulchaicharoen, F.G. Requejo, B.S. Mun, D.E. Resasco, Influence of a Top Crust of Entangled Nanotubes on the Structure of Vertically Aligned Forests of Single-Walled Carbon Nanotubes, Chem. Mater. 18 (2006) 5624–5629. https://doi.org/10.1021/cm061783b.

[164] H. Liu, Y. Zhang, D. Arato, R. Li, P. Mérel, X. Sun, Aligned multi-walled carbon nanotubes on different substrates by floating catalyst chemical vapor deposition: Critical effects of buffer layer, Surf. Coat. Technol. 202 (2008) 4114–4120. https://doi.org/10.1016/j.surfcoat.2008.02.025.

[165] S. Rahmanian, A.R. Suraya, R. Zahari, E.S. Zainudin, Synthesis of vertically aligned carbon nanotubes on carbon fiber, Appl. Surf. Sci. 271 (2013) 424–428. https://doi.org/10.1016/j.apsusc.2013.01.207.

[166] W.R. McGregor, F.J. Swinbourne, The reaction of iron chlorides with some aliphatic primary amines, J. Inorg. Nucl. Chem. 28 (1966) 1027–1030. https://doi.org/10.1016/0022-1902(66)80199-9.

[167] S. Gupta, P.C. Ramamurthy, G. Madras, Synthesis and characterization of flexible epoxy nanocomposites reinforced with amine functionalized alumina nanoparticles: a potential encapsulant for organic devices, Polym Chem. 2 (2011) 221–228. https://doi.org/10.1039/C0PY00270D.

[168] T. Lakshmikandhan, A. Chandramohan, K. Sethuraman, M. Alagar, Development and characterization of functionalized Al_2O_3 and TiO_2 -reinforced polybenzoxazine nanocomposites, Des. Monomers Polym. 19 (2016) 67–76. https://doi.org/10.1080/15685551.2015.1092014.

[169] D.J. Bray, S.G. Gilmour, F.J. Guild, A.C. Taylor, Quantifying nanoparticle dispersion by using the area disorder of Delaunay triangulation: Quantifying Nanoparticle Dispersion by using Area Disorder, J. R. Stat. Soc. Ser. C Appl. Stat. 61 (2012) 253–275. https://doi.org/10.1111/j.1467-9876.2011.01009.x.

[170] D.T. Lee, B.J. Schachter, Two algorithms for constructing a Delaunay triangulation, Int. J. Comput. Inf. Sci. 9 (1980) 219–242. https://doi.org/10.1007/BF00977785.

[171] S.N. Chiu, Spatial Point Pattern Analysis by using Voronoi Diagrams and Delaunay Tessellations – A Comparative Study, Biom. J. 45 (2003) 367–376. https://doi.org/10.1002/bimj.200390018.

[172] Image Processing Toolbox Documentation - MathWorks Switzerland, (n.d.). https://ch.mathworks.com/help/images/ (accessed May 7, 2020).

[173] M.F. Al-Kuhaili, M. Saleem, S.M.A. Durrani, Optical properties of iron oxide (α-Fe_2O_3) thin films deposited by the reactive evaporation of iron, J. Alloys Compd. 521 (2012) 178–182. https://doi.org/10.1016/j.jallcom.2012.01.115.

[174] S. Esconjauregui, M. Fouquet, B.C. Bayer, C. Ducati, R. Smajda, S. Hofmann, J. Robertson, Growth of Ultrahigh Density Vertically Aligned Carbon Nanotube Forests for Interconnects, ACS Nano. 4 (2010) 7431–7436. https://doi.org/10.1021/nn1025675.

[175] D.T. Danielson, D.K. Sparacin, J. Michel, L.C. Kimerling, Surface-energy-driven dewetting theory of silicon-on-insulator agglomeration, J. Appl. Phys. 100 (2006) 083507. https://doi.org/10.1063/1.2357345.

[176] D. Kim, A.L. Giermann, C.V. Thompson, Solid-state dewetting of patterned thin films, Appl. Phys. Lett. 95 (2009) 251903. https://doi.org/10.1063/1.3268477.

[177] Y.-W. Song, S. Yamashita, E. Einarsson, S. Maruyama, All-fiber pulsed lasers passively mode locked by transferable vertically aligned carbon nanotube film, Opt. Lett. 32 (2007) 1399. https://doi.org/10.1364/OL.32.001399.

[178] C. Chan, N. Zamel, X. Li, J. Shen, Experimental measurement of effective diffusion coefficient of gas diffusion layer/microporous layer in PEM fuel cells, Electrochimica Acta. 65 (2012) 13–21. https://doi.org/10.1016/j.electacta.2011.12.110.

[179] J.M. Cash, M. Jeschke, V.J. Wright, J.D.B. Sharman, Gas diffusion substrate, US10424795B2, 2019. https://patents.google.com/patent/US10424795B2/en (accessed November 10, 2019).

[180] E.S. Lee, D.H. Kim, E.C. Kim, J.Y. Jyoung, J.M. Gwak, S.J. Choi, T.N. Kim, J.K. Lee, Carbon Substrate For Gas Diffusion Layer, Gas Diffusion Layer Using The Same, And Electrode For Fuel Cell, Membrane-Electrode Assembly And Fuel Cell Comprising The Gas Diffusion Layer,

US20140011118A1, 2014. https://patents.google.com/patent/US20140011118A1/en (accessed November 10, 2019).

[181] J. Gilron, A. Soffer, Knudsen diffusion in microporous carbon membranes with molecular sieving character, J. Membr. Sci. 209 (2002) 339–352. https://doi.org/10.1016/S0376-7388(02)00074-1.

[182] J. Phattaranawik, Effect of pore size distribution and air flux on mass transport in direct contact membrane distillation, J. Membr. Sci. 215 (2003) 75–85. https://doi.org/10.1016/S0376-7388(02)00603-8.

[183] L. Li, K.K. Sirkar, Influence of microporous membrane properties on the desalination performance in direct contact membrane distillation, J. Membr. Sci. 513 (2016) 280–293. https://doi.org/10.1016/j.memsci.2016.04.015.

[184] A.S. Kim, H.-S. Lee, D.-S. Moon, H.-J. Kim, Self-adjusting, combined diffusion in direct contact and vacuum membrane distillation, J. Membr. Sci. 543 (2017) 255–268. https://doi.org/10.1016/j.memsci.2017.08.059.

[185] C.K. Ho, S.W. Webb, eds., Gas transport in porous media, Springer, Dordrecht, 2006.

[186] J.W. Elam, Coatings on High Aspect Ratio Structures, in: N. Pinna, M. Knez (Eds.), At. Layer Depos. Nanostructured Mater., Wiley-VCH Verlag GmbH & Co. KGaA, Weinheim, Germany, 2012: pp. 227–249. http://doi.wiley.com/10.1002/9783527639915.ch10 (accessed November 23, 2016).

[187] N. Yazdani, V. Chawla, E. Edwards, V. Wood, H.G. Park, I. Utke, Modeling and optimization of atomic layer deposition processes on vertically aligned carbon nanotubes, Beilstein J. Nanotechnol. 5 (2014) 234–244. https://doi.org/10.3762/bjnano.5.25.

[188] C. Guerra-Nuñez, Y. Zhang, M. Li, V. Chawla, R. Erni, J. Michler, H.G. Park, I. Utke, Morphology and crystallinity control of ultrathin TiO_2 layers deposited on carbon nanotubes by temperature-step atomic layer deposition, Nanoscale. 7 (2015) 10622–10633. https://doi.org/10.1039/C5NR02106E.

[189] C. Guerra-Nuñez, M. Döbeli, J. Michler, I. Utke, Reaction and Growth Mechanisms in Al_2O_3 deposited via Atomic Layer Deposition: Elucidating the Hydrogen Source, Chem. Mater. 29 (2017) 8690–8703. https://doi.org/10.1021/acs.chemmater.7b02759.

[190] J.W. Elam, D. Routkevitch, P.P. Mardilovich, S.M. George, Conformal Coating on Ultrahigh-Aspect-Ratio Nanopores of Anodic Alumina by Atomic Layer Deposition, Chem. Mater. 15 (2003) 3507–3517. https://doi.org/10.1021/cm0303080.

[191] R. g. Gordon, D. Hausmann, E. Kim, J. Shepard, A Kinetic Model for Step Coverage by Atomic Layer Deposition in Narrow Holes or Trenches, Chem. Vap. Depos. 9 (2003) 73–78. https://doi.org/10.1002/cvde.200390005.

[192] J. Dendooven, C. Detavernier, Basics of Atomic Layer Deposition: Growth Characteristics and Conformality, in: J. Bachmann (Ed.), At. Layer Depos. Energy Convers. Appl., Wiley-VCH Verlag GmbH & Co. KGaA, Weinheim, Germany, 2017: pp. 1–40. https://doi.org/10.1002/9783527694822.ch1.

[193] S.H. Baxamusa, K.K. Gleason, Thin Polymer Films with High Step Coverage in Microtrenches by Initiated CVD, Chem. Vap. Depos. 14 (2008) 313–318. https://doi.org/10.1002/cvde.200806713.

[194] H.-J. Li, X.-H. Hou, Y.-X. Chen, Densification of unidirectional carbon–carbon composites by isothermal chemical vapor infiltration, Carbon. 38 (2000) 423–427. https://doi.org/10.1016/S0008-6223(99)00122-0.

[195] H. Sun, J. Yao, D. Fan, C. Wang, Z. Sun, Gas transport mode criteria in ultra-tight porous media, Int. J. Heat Mass Transf. 83 (2015) 192–199. https://doi.org/10.1016/j.ijheatmasstransfer.2014.11.075.

[196] M. Knudsen, Die Molekularströmung der Gase durch Offnungen und die Effusion, Ann. Phys. 333 (1909) 999–1016. https://doi.org/10.1002/andp.19093330505.

[197] M. Knudsen, Das Cosinusgesetz in der kinetischen Gastheorie, Ann. Phys. 353 (1916) 1113–1121. https://doi.org/10.1002/andp.19163532409.

[198] K. Malek, M.-O. Coppens, Knudsen self- and Fickian diffusion in rough nanoporous media, J. Chem. Phys. 119 (2003) 2801–2811. https://doi.org/10.1063/1.1584652.

[199] J.A.H. Dreyer, N. Riefler, G.R. Pesch, M. Karamehmedović, U. Fritsching, W.Y. Teoh, L. Mädler, Simulation of gas diffusion in highly porous nanostructures by direct simulation Monte Carlo, Chem. Eng. Sci. 105 (2014) 69–76. https://doi.org/10.1016/j.ces.2013.10.038.

[200] Y. Shi, Y.T. Lee, A.S. Kim, Knudsen Diffusion Through Cylindrical Tubes of Varying Radii: Theory and Monte Carlo Simulations, Transp. Porous Media. 93 (2012) 517–541. https://doi.org/10.1007/s11242-012-9966-3.

[201] G.L. Vignoles, W. Ros, I. Szelengowicz, C. Germain, A Brownian motion algorithm for tow scale modeling of chemical vapor infiltration, Comput. Mater. Sci. 50 (2011) 1871–1878. https://doi.org/10.1016/j.commatsci.2011.01.031.

[202] R. Feres, G. Yablonsky, Knudsen's cosine law and random billiards, Chem. Eng. Sci. 59 (2004) 1541–1556. https://doi.org/10.1016/j.ces.2004.01.016.

[203] J.R. Welty, Fundamentals of momentum, heat and mass transfer, 6th edition, Wiley, Hoboken, NJ, 2015.

[204] M. Ylilammi, O.M.E. Ylivaara, R.L. Puurunen, Modeling growth kinetics of thin films made by atomic layer deposition in lateral high-aspect-ratio structures, J. Appl. Phys. 123 (2018) 205301. https://doi.org/10.1063/1.5028178.

[205] Q. Zheng, B. Yu, S. Wang, L. Luo, A diffusivity model for gas diffusion through fractal porous media, Chem. Eng. Sci. 68 (2012) 650–655. https://doi.org/10.1016/j.ces.2011.10.031.

[206] P. Levitz, Knudsen diffusion and excitation transfer in random porous media, J. Phys. Chem. 97 (1993) 3813–3818. https://doi.org/10.1021/j100117a030.

[207] W. Szmyt, C. Guerra, I. Utke, Diffusion of dilute gas in arrays of randomly distributed, vertically aligned, high-aspect-ratio cylinders, Beilstein J. Nanotechnol. 8 (2017) 64–73. https://doi.org/10.3762/bjnano.8.7.

[208] D. Shou, J. Fan, M. Mei, F. Ding, An analytical model for gas diffusion though nanoscale and microscale fibrous media, Microfluid. Nanofluidics. 16 (2014) 381–389. https://doi.org/10.1007/s10404-013-1215-8.

[209] M.M. Tomadakis, S.V. Sotirchos, Ordinary and transition regime diffusion in random fiber structures, AIChE J. 39 (1993) 397–412. https://doi.org/10.1002/aic.690390304.

[210] R.R. Melkote, K.F. Jensen, Gas diffusion in random-fiber substrates, AIChE J. 35 (1989) 1942–1952. https://doi.org/10.1002/aic.690351205.

[211] M.M. Tomadakis, S.V. Sotirchos, Effective Kundsen diffusivities in structures of randomly overlapping fibers, AIChE J. 37 (1991) 74–86. https://doi.org/10.1002/aic.690370107.

[212] P. Poodt, A. Mameli, J. Schulpen, W.M.M. (Erwin) Kessels, F. Roozeboom, Effect of reactor pressure on the conformal coating inside porous substrates by atomic layer deposition, J. Vac. Sci. Technol. Vac. Surf. Films. 35 (2017) 021502. https://doi.org/10.1116/1.4973350.

[213] J.F. O'Hanlon, A User's Guide to Vacuum Technology., John Wiley & Sons, Inc., Hoboken, 2005. http://www.123library.org/book_details/?id=15383 (accessed September 11, 2019).

[214] M. Cieplak, J. Koplik, J.R. Bavanar, Molecular dynamics of flows in the Knudsen regime, Phys. Stat. Mech. Its Appl. 287 (2000) 153–160. https://doi.org/10.1016/S0378-4371(00)00353-8.

[215] W. Steckelmacher, Knudsen flow 75 years on: the current state of the art for flow of rarefied gases in tubes and systems, Rep. Prog. Phys. 49 (1986) 1083–1107. https://doi.org/10.1088/0034-4885/49/10/001.

[216] A. Einstein, Über die von der molekularkinetischen Theorie der Wärme geforderte Bewegung von in ruhenden Flüssigkeiten suspendierten Teilchen, Ann. Phys. 322 (1905) 549–560. https://doi.org/10.1002/andp.19053220806.

[217] M. von Smoluchowski, Zur kinetischen Theorie der Brownschen Molekularbewegung und der Suspensionen, Ann. Phys. 326 (1906) 756–780. https://doi.org/10.1002/andp.19063261405.

[218] F. Colson, D.A. Barlow, Statistical method for modeling Knudsen diffusion in nanopores, Phys. Rev. E. 100 (2019) 062125. https://doi.org/10.1103/PhysRevE.100.062125.

[219] A.C. Jones, M.L. Hitchman, eds., Chemical vapour deposition: precursors, processes and applications, Royal Society of Chemistry, Cambridge, UK, 2009.

[220] G.S. Hwang, A.Z. Weber, Effective-Diffusivity Measurement of Partially-Saturated Fuel-Cell Gas-Diffusion Layers, J. Electrochem. Soc. 159 (2012) F683–F692. https://doi.org/10.1149/2.024211jes.

[221] V.N. Burganos, Gas diffusion in random binary media, J. Chem. Phys. 109 (1998) 6772–6779. https://doi.org/10.1063/1.477323.

[222] D. Mu, Z.-S. Liu, C. Huang, N. Djilali, Determination of the effective diffusion coefficient in porous media including Knudsen effects, Microfluid. Nanofluidics. 4 (2008) 257–260. https://doi.org/10.1007/s10404-007-0182-3.

[223] T.C. Zhang, P.L. Bishop, Evaluation of tortuosity factors and effective diffusivities in biofilms, Water Res. 28 (1994) 2279–2287. https://doi.org/10.1016/0043-1354(94)90043-4.

[224] H. Jin, Y. Nishiyama, M. Wada, S. Kuga, Nanofibrillar cellulose aerogels, Colloids Surf. Physicochem. Eng. Asp. 240 (2004) 63–67. https://doi.org/10.1016/j.colsurfa.2004.03.007.

[225] J. He, X. Li, D. Su, H. Ji, X. Wang, Ultra-low thermal conductivity and high strength of aerogels/fibrous ceramic composites, J. Eur. Ceram. Soc. 36 (2016) 1487–1493. https://doi.org/10.1016/j.jeurceramsoc.2015.11.021.

[226] M.B. Clennell, Tortuosity: a guide through the maze, Geol. Soc. Lond. Spec. Publ. 122 (1997) 299–344. https://doi.org/10.1144/GSL.SP.1997.122.01.18.

[227] R.L. Puurunen, Surface chemistry of atomic layer deposition: A case study for the trimethylaluminum/water process, J. Appl. Phys. 97 (2005) 121301. https://doi.org/10.1063/1.1940727.

[228] J.-O. Carlsson, Thermodynamics of the homogeneous and heterogeneous decomposition of trimethylaluminum, monomethylaluminum, and dimethylaluminumhydride: Effects of scavengers and ultraviolet-laser photolysis, J. Vac. Sci. Technol. B Microelectron. Nanometer Struct. 9 (1991) 2759. https://doi.org/10.1116/1.585642.

[229] E. Nagy, Membrane Gas Separation, in: Basic Equ. Mass Transp. Membr. Layer, Elsevier, 2019: pp. 457–481. https://doi.org/10.1016/B978-0-12-813722-2.00018-2.

[230] C. Detavernier, J. Dendooven, S. Pulinthanathu Sree, K.F. Ludwig, J.A. Martens, Tailoring nanoporous materials by atomic layer deposition, Chem. Soc. Rev. 40 (2011) 5242. https://doi.org/10.1039/c1cs15091j.

[231] T. Keuter, N.H. Menzler, G. Mauer, F. Vondahlen, R. Vaßen, H.P. Buchkremer, Modeling precursor diffusion and reaction of atomic layer deposition in porous structures, J. Vac. Sci. Technol. A. 33 (2015) 01A104. https://doi.org/10.1116/1.4892385.

[232] J.A. Libera, J.W. Elam, M.J. Pellin, Conformal ZnO coatings on high surface area silica gel using atomic layer deposition, Thin Solid Films. 516 (2008) 6158–6166. https://doi.org/10.1016/j.tsf.2007.11.044.

[233] S. Boukhalfa, K. Evanoff, G. Yushin, Atomic layer deposition of vanadium oxide on carbon nanotubes for high-power supercapacitor electrodes, Energy Environ. Sci. 5 (2012) 6872. https://doi.org/10.1039/c2ee21110f.

[234] R.A. Fisher, M.R. Watt, R. Konjeti, W.J. Ready, Atomic Layer Deposition of Titanium Oxide for Pseudocapacitive Functionalization of Vertically-Aligned Carbon Nanotube Supercapacitor Electrodes, ECS J. Solid State Sci. Technol. 4 (2015) M1–M5. https://doi.org/10.1149/2.0141502jss.

[235] J. Woo Kim, B. Kim, S. Won Park, W. Kim, J. Hyung Shim, Atomic layer deposition of ruthenium on plasma-treated vertically aligned carbon nanotubes for high-performance ultracapacitors, Nanotechnology. 25 (2014) 435404. https://doi.org/10.1088/0957-4484/25/43/435404.

[236] Y. Liang, Y. Li, H. Wang, H. Dai, Strongly Coupled Inorganic/Nanocarbon Hybrid Materials for Advanced Electrocatalysis, J. Am. Chem. Soc. 135 (2013) 2013–2036. https://doi.org/10.1021/ja3089923.

[237] D. Eder, Carbon Nanotube−Inorganic Hybrids, Chem. Rev. 110 (2010) 1348–1385. https://doi.org/10.1021/cr800433k.

[238] J.J. Vilatela, D. Eder, Nanocarbon Composites and Hybrids in Sustainability: A Review, ChemSusChem. 5 (2012) 456–478. https://doi.org/10.1002/cssc.201100536.

[239] S. Deng, S.W. Verbruggen, Z. He, D.J. Cott, P.M. Vereecken, J.A. Martens, S. Bals, S. Lenaerts, C. Detavernier, Atomic layer deposition-based synthesis of photoactive TiO_2 nanoparticle chains by using carbon nanotubes as sacrificial templates, RSC Adv. 4 (2014) 11648. https://doi.org/10.1039/c3ra42928h.

[240] T. Choi, S.H. Kim, C.W. Lee, H. Kim, S.-K. Choi, S.-H. Kim, E. Kim, J. Park, H. Kim, Synthesis of carbon nanotube–nickel nanocomposites using atomic layer deposition for high-performance non-enzymatic glucose sensing, Biosens. Bioelectron. 63 (2015) 325–330. https://doi.org/10.1016/j.bios.2014.07.059.

[241] Y. Nakashima, Y. Ohno, S. Kishimoto, M. Okochi, H. Honda, T. Mizutani, Fabrication Process of Carbon Nanotube Field Effect Transistors Using Atomic Layer Deposition Passivation for Biosensors, J. Nanosci. Nanotechnol. 10 (2010) 3805–3809. https://doi.org/10.1166/jnn.2010.1983.

[242] Y. Zhang, C. Guerra-Nuñez, I. Utke, J. Michler, M.D. Rossell, R. Erni, Understanding and Controlling Nucleation and Growth of TiO_2 Deposited on Multiwalled Carbon Nanotubes by Atomic Layer Deposition, J. Phys. Chem. C. 119 (2015) 3379–3387. https://doi.org/10.1021/jp511004h.

[243] L. Acauan, A.C. Dias, M.B. Pereira, F. Horowitz, C.P. Bergmann, Influence of Different Defects in Vertically Aligned Carbon Nanotubes on TiO_2 Nanoparticle Formation through Atomic Layer Deposition, ACS Appl. Mater. Interfaces. 8 (2016) 16444–16450. https://doi.org/10.1021/acsami.6b04001.

[244] K.L. Stano, M. Carroll, R. Padbury, M. McCord, J.S. Jur, P.D. Bradford, Conformal Atomic Layer Deposition of Alumina on Millimeter Tall, Vertically-Aligned Carbon Nanotube Arrays, ACS Appl. Mater. Interfaces. 6 (2014) 19135–19143. https://doi.org/10.1021/am505107s.

[245] D.S. Jensen, S.S. Kanyal, N. Madaan, A.J. Miles, R.C. Davis, R. Vanfleet, M.A. Vail, A.E. Dadson, M.R. Linford, Ozone priming of patterned carbon nanotube forests for subsequent atomic layer deposition-like deposition of SiO_2 for the preparation of microfabricated thin layer chromatography plates, J. Vac. Sci. Technol. B Nanotechnol. Microelectron. Mater. Process. Meas. Phenom. 31 (2013) 031803. https://doi.org/10.1116/1.4801834.

[246] A.S. Cavanagh, C.A. Wilson, A.W. Weimer, S.M. George, Atomic layer deposition on gram quantities of multi-walled carbon nanotubes, Nanotechnology. 20 (2009) 255602. https://doi.org/10.1088/0957-4484/20/25/255602.

[247] H. Wang, M. Wei, Z. Zhong, Y. Wang, Atomic-layer-deposition-enabled thin-film composite membranes of polyimide supported on nanoporous anodized alumina, J. Membr. Sci. 535 (2017) 56–62. https://doi.org/10.1016/j.memsci.2017.04.026.

[248] S. Ji, G.Y. Cho, W. Yu, P.-C. Su, M.H. Lee, S.W. Cha, Plasma-Enhanced Atomic Layer Deposition of Nanoscale Yttria-Stabilized Zirconia Electrolyte for Solid Oxide Fuel Cells with Porous Substrate, ACS Appl. Mater. Interfaces. 7 (2015) 2998–3002. https://doi.org/10.1021/am508710s.

[249] V. Cremers, R.L. Puurunen, J. Dendooven, Conformality in atomic layer deposition: Current status overview of analysis and modelling, Appl. Phys. Rev. 6 (2019) 021302. https://doi.org/10.1063/1.5060967.

[250] A. Yanguas-Gil, J.W. Elam, Self-Limited Reaction-Diffusion in Nanostructured Substrates: Surface Coverage Dynamics and Analytic Approximations to ALD Saturation Times, Chem. Vap. Depos. 18 (2012) 46–52. https://doi.org/10.1002/cvde.201106938.

[251] A. Yanguas-Gil, Thin Film Growth in Nanostructured Materials, in: Growth Transp. Nanostructured Mater., Springer International Publishing, Cham, 2017: pp. 69–99. https://doi.org/10.1007/978-3-319-24672-7_4.

[252] W. Szmyt, C. Guerra-Nunez, C. Dransfeld, I. Utke, Solving the inverse Knudsen problem: gas diffusion in random fibrous media, J. Membr. Sci (in press, 2020). https://doi.org/10.1016/j.memsci.2020.118728

[253] J. Dendooven, D. Deduytsche, J. Musschoot, R.L. Vanmeirhaeghe, C. Detavernier, Modeling the Conformality of Atomic Layer Deposition: The Effect of Sticking Probability, J. Electrochem. Soc. 156 (2009) P63. https://doi.org/10.1149/1.3072694.

[254] E.W. Thiele, Relation between Catalytic Activity and Size of Particle, Ind. Eng. Chem. 31 (1939) 916–920. https://doi.org/10.1021/ie50355a027.

[255] R.L. Puurunen, Growth Per Cycle in Atomic Layer Deposition: Real Application Examples of a Theoretical Model, Chem. Vap. Depos. 9 (2003) 327–332. https://doi.org/10.1002/cvde.200306266.

[256] B. Díaz, E. Härkönen, J. Światowska, V. Maurice, A. Seyeux, P. Marcus, M. Ritala, Low-temperature atomic layer deposition of Al_2O_3 thin coatings for corrosion protection of steel: Surface and electrochemical analysis, Corros. Sci. 53 (2011) 2168–2175. https://doi.org/10.1016/j.corsci.2011.02.036.

[257] A. Philip, S. Thomas, K.R. Kumar, Calculation of growth per cycle (GPC) of atomic layer deposited aluminium oxide nanolayers and dependence of GPC on surface OH concentration, Pramana. 82 (2014) 563–569. https://doi.org/10.1007/s12043-014-0715-8.

[258] B. Lee, S.-Y. Park, H.-C. Kim, K. Cho, E.M. Vogel, M.J. Kim, R.M. Wallace, J. Kim, Conformal Al_2O_3 dielectric layer deposited by atomic layer deposition for graphene-based nanoelectronics, Appl. Phys. Lett. 92 (2008) 203102. https://doi.org/10.1063/1.2928228.

[259] J. Kim, K. Chakrabarti, J. Lee, K.-Y. Oh, C. Lee, Effects of ozone as an oxygen source on the properties of the Al_2O_3 thin films prepared by atomic layer deposition, Mater. Chem. Phys. 78 (2003) 733–738. https://doi.org/10.1016/S0254-0584(02)00375-9.

[260] L. Cheng, X. Qin, A.T. Lucero, A. Azcatl, J. Huang, R.M. Wallace, K. Cho, J. Kim, Atomic Layer Deposition of a High-*k* Dielectric on MoS_2 Using Trimethylaluminum and Ozone, ACS Appl. Mater. Interfaces. 6 (2014) 11834–11838. https://doi.org/10.1021/am5032105.

[261] I. Bello, Vacuum and Ultravacuum: Physics and Technology, 1st ed., CRC Press, 2017. https://doi.org/10.1201/9781315155364.

[262] A.F. Ismail, K.C. Khulbe, T. Matsuura, Fundamentals of Gas Permeation Through Membranes, in: Gas Sep. Membr., Springer International Publishing, Cham, 2015: pp. 11–35. https://doi.org/10.1007/978-3-319-01095-3_2.

[263] M.R. Shaeri, T.-C. Jen, C.Y. Yuan, M. Behnia, Investigating atomic layer deposition characteristics in multi-outlet viscous flow reactors through reactor scale simulations, Int. J. Heat Mass Transf. 89 (2015) 468–481. https://doi.org/10.1016/j.ijheatmasstransfer.2015.05.079.

[264] V. Vandalon, W.M.M.E. Kessels, Initial Growth Study of Atomic-Layer Deposition of Al_2O_3 by Vibrational Sum-Frequency Generation, Langmuir. 35 (2019) 10374–10382. https://doi.org/10.1021/acs.langmuir.9b01600.

[265] G.P. Gakis, H. Vergnes, E. Scheid, C. Vahlas, A.G. Boudouvis, B. Caussat, Detailed investigation of the surface mechanisms and their interplay with transport phenomena in alumina atomic layer deposition from TMA and water, Chem. Eng. Sci. 195 (2019) 399–412. https://doi.org/10.1016/j.ces.2018.09.037.

[266] R.B. Bird, W.E. Stewart, E.N. Lightfoot, Transport phenomena, Wiley, New York, 1960.

[267] S. Chapman, T.G. Cowling, The mathematical theory of non-uniform gases: an account of the kinetic theory of viscosity, thermal conduction, and diffusion in gases, 3rd ed, Cambridge University Press, Cambridge ; New York, 1990.

[268] S. Matteucci, Y. Yampolskii, B.D. Freeman, I. Pinnau, Transport of Gases and Vapors in Glassy and Rubbery Polymers, in: Y. Yampolskii, I. Pinnau, B. Freeman (Eds.), Mater. Sci. Membr. Gas Vap. Sep., John Wiley & Sons, Ltd, Chichester, UK, 2006: pp. 1–47. https://doi.org/10.1002/047002903X.ch1.

[269] D.W. Breck, Zeolite molecular sieves: structure, chemistry, and use, R.E. Krieger, Malabar, Fla, 1984.

Appendices

Appendix A

Supplementary information to Chapter 2

This appendix contains additional experimental data of carbon fibre strength analysis, details of elemental characterisation process by EDX and its effect on the samples and numerical evaluation of the influence of the nanoparticle separation on the interpretation of the nanotomography data.

A.1. Single fibre tensile testing – the effect of alumina protection and fibre pre-tension

In this study we refer to the mechanical performance of the fibres examined in the previous work carried out in our group [90]. The influence of the thickness of the ALD alumina film necessary to apply prior to CVD processing in order to retain the tensile strength of a CF was studied. For the convenience of the reader we show these results here in a condensed form.

The influence of two factors on the fibre strength has been tested at varying thickness of the alumina film: fibre prestraining by 0.2% and CVD CNT growth process equivalent to the one carried out in this work. The results are summarised in Figure A.1.

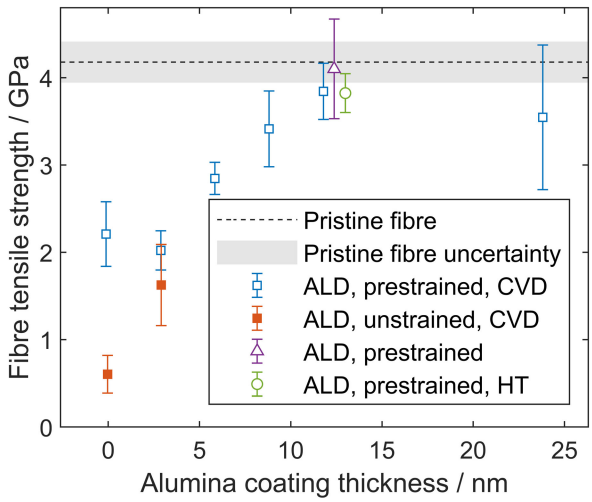

Figure A.1. Summary of the tensile test results carried out in our recent work [90]: dashed black line with grey bar represents the baseline strength of the AS4 fibre as received along with the error interval; closed red squares – loose (not prestrained) CF having undergone ALD and CVD processes; open blue squares – 0.2%-prestrained CF having undergone ALD and CVD processes, open purple triangle – CF after ALD with no further processing open green circle – CF having undergone 100 ALD cycles and thermal treatment at 750°C CVD temperature in argon, but with no presence of a catalyst or reactive gas. The latter two points are offset along the horizontal axis for clarity. Thickness of oxide layer equal 0 nm refers to no ALD processing for the given samples.

The results confirmed, that the prestrain is a crucial factor in retaining the CF strength in the process. Furthermore, we have concluded that the optimum alumina film thickness is about 12 nm and its further increase is not beneficial.

A.2. Influence of electron beam irradiation during EDX on secondary electron image

As mentioned in Chapter 2, the areas irradiated with electron beam during EDX have changed their appearance on secondary electron image. Within an irradiated ROI, the area of NP has increased intensity appearing brighter in the image, whereas the surrounding carbon has a decreased intensity, appearing darker, see Figure A.2.

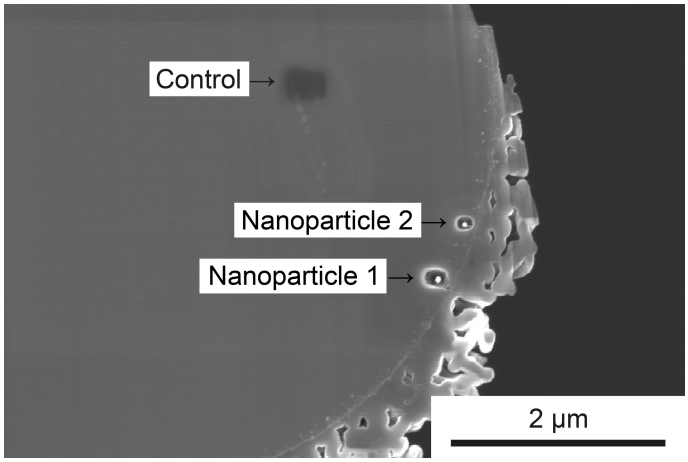

Figure A.2. SEM of the unprotected CF slice examined by EDX. Labels correspond to the spectra in Figure 2.15a.

The observations can be explained by the following phenomena. The well-known local deposition of amorphous carbon by electron beam from free hydrocarbons present in the non-perfect vacuum within the SEM chamber may have caused the local darkening of the secondary electron image of CF. The other phenomenon is the catalytic action of iron triggered by local heating by 3 keV electron beam. It could have resulted in diffusion of NP towards the surface and precipitation of carbon, causing the apparent brightening of the NP. The confirmation of the hypothesis however requires an additional study of the interaction of iron NPs with the surrounding carbon upon electron beam irradiation, which lies beyond the scope of this work.

A.3. Influence of small nanoparticle separation on the results of PXCT data analysis

In section 2.3.8 of this work, which is devoted to the verification of PXCT data analysis by means of FIB/STEM/EDX examination, we have pointed out that due to the high chance of NPs getting close together comparable to the spatial resolution obtained in PXCT, there is a possibility that multiple smaller NPs can be interpreted as a smaller number of larger NPs. However, we stated that it does not induce a significant error in the resulting estimate of iron content in a given region. In this section we support this statement by an example simulation of two NPs getting close together and its subsequent analysis employing an algorithm analogous to the one introduced in section 2.3.6. For the sake of simplicity, in the simulation we assumed an electron density for CF of ϱ_{CF}=0.5 Å^{-3} and an isotropic Gaussian PSF of σ=29 nm, which falls between the radial σ_r and the axial σ_z obtained from the analysis. We defined two NPs of 29 nm and 23 nm diameters, being not greater than σ. Blurring of NPs of diameter not greater than σ with PSF produces electron density images very well-described with a Gaussian

$$\varrho(\vec{r}) = \varrho_{\mathrm{CF}} + \frac{N_e}{\left(\sqrt{2\pi}\sigma\right)^3} \exp\left(-\frac{|\vec{r} - \vec{r}_0|^2}{2\sigma^2}\right), \tag{A.1}$$

where ϱ is the simulated electron density image, $\vec{r}$ is a position vector, $\vec{r}_0$ is the position of the center of the NP, N_e is the total number of electrons in the NP. N_e can be calculated as

$$N_e = \frac{Z_{\mathrm{Fe}} d_{\mathrm{Fe}} V_{\mathrm{NP}} N_{\mathrm{A}}}{\mu_{\mathrm{Fe}}}, \tag{A.2}$$

where V_{NP} is a volume of the NP, Z_{Fe}, is the atomic number of iron, d_{Fe} is iron mass density and μ_{Fe} is the molar mass of iron. This means that at this NP size all the information about any specific shape

is lost and the NPs can be defined as a 3D Dirac delta functions multiplied by the corresponding N_e. We took advantage of this fact to produce the simplified simulation. In the simulation, 40 evenly distributed values for distances between NPs were considered ranging from 0 nm, meaning a complete coalescence of the NPs, up to 116 nm. The cross sections of the produced images at 6 values for the NP separation are shown in Figure A.3. We can already see that at a distance of 46 nm it is no longer possible to identify the two NPs.

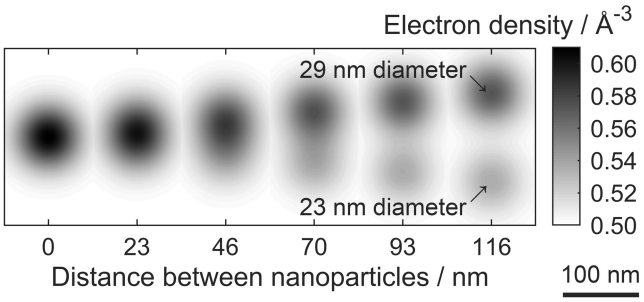

Figure A.3. Cross sections of simulated electron density images produced by two NPs of different diameters (indicated by arrows) at 6 distances.

The subsequent analysis has been carried out employing the methodology introduced in section 2.3.6 with minor changes. Instead of artificially adding Gaussian noise to the electron density maps, their histograms were numerically convolved with a Gaussian of rms=0.029 Å^{-3} being close to the experimental one. Such an operation is mathematically equivalent to adding noise, but it does not introduce noise at low histogram bins and the histograms remain smooth. Consequently, the fitting procedure does not have to account for the noise and the optimization function can be defined as

$$\mathrm{opt} = \frac{1}{N}\sum_{k=1}^{N} \log^2\left(\frac{H_\mathrm{e}(k)}{H_\mathrm{s}(k)}\right), \tag{A.3}$$

where H_e is the input histogram obtained from the simulated electron density map of the two NPs at proximity, whereas H_s is the histogram being a result of a linear combination of histograms of well-separated NPs of different volumes, in this version of the algorithm ranging from 0 to 2.1×10^4 nm. The optimisation function (A.3) represents a non-weighted mean square deviation at logarithmic scale. The usage of such an optimisation function is justified by the fact that the algorithm should be sensitive to the features of the histograms that become apparent at the logarithmic scale. The fitting termination criterion was set as opt$<5\times10^{-3}$ which has given excellent fitting results. A one-dimensional NP volume distribution $f(v)$ was set as a fitting parameter.

The resulting NP volume distribution is shown in Figure A.4. It is well-pronounced, that at distance greater than 100 nm being about 3.5σ, the NPs are well distinguished by the algorithm. However, as the distance decreases, the algorithm interprets the image as if the smaller NP was getting gradually larger, but its contribution to the final histogram was decreasing. On the other hand, the bigger NP contribution gradually intensifies. It continues until the distance of ~60 nm is reached, which corresponds to about 2σ. At this stage, the apparent contribution of the smaller NPs vanishes completely. With the further decrease of distance, the image is interpreted by the algorithm as if one NP was increasing in volume, but decreasing slightly in contribution to the histogram. Ultimately, at the distance equal 0 the output shows clearly one NP of a volume equal the sum of the two.

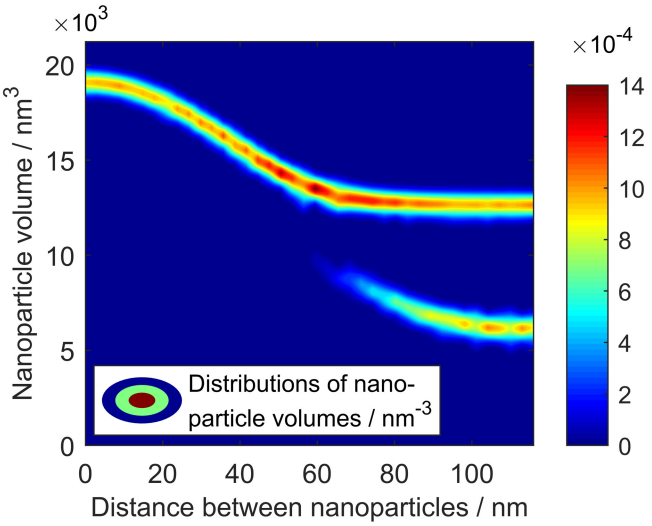

Figure A.4. Output NP volume distributions versus distance between the two NPs. An artefact of a peak at zero NP volume has been erased for clarity.

Using the output $f(v)$, the total iron volume V_{Fe} can be calculated as

$$V_{\mathrm{Fe}} = \int_0^{v_{\max}} v f(v) dv, \tag{A.4}$$

which can be compared with the expected total iron volume being the sum of the two NP volumes. The relative error of the evaluated total iron volume is presented in Figure A.5. We observe that the greatest error that is encountered is only about 6.5%, therefore we claim that it is not significant.

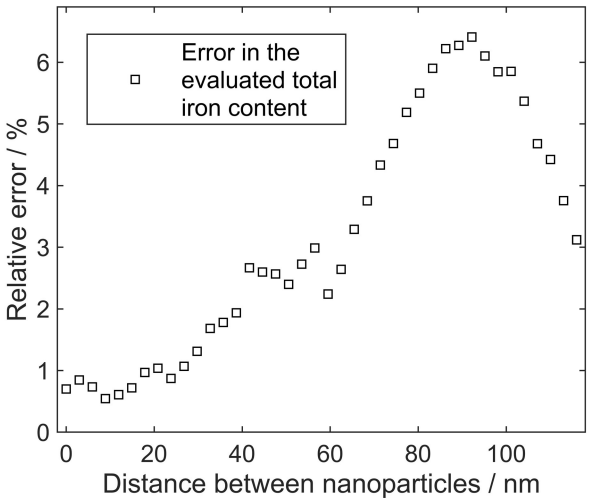

Figure A.5. Relative error in the total iron content evaluated using the methodology introduced in this work in the simulated case of two NPs separated by distances comparable to the PXCT resolution.

The results of this simulation constitute an example that, in case of close proximity between NPs, the introduced algorithm might mistake several NPs as one or misjudge the proportions of the NP sizes. Nonetheless, the simulation results exemplify that in such a case the algorithm does not introduce a significant error in the estimated total iron content.

Appendix B

Supplementary information to Chapter 4

This appendix contains modelling of the temperature distributions and gas glows in the CVD reactor and image analysis data of the surface nanoparticle coatings.

B.1. Temperature distribution and gas flow in the CVD reactor

In this appendix we present additional information about the temperature distribution and estimations of gas flow, which were not included in Chapter 4, but are nonetheless significant.

B.1.1. Temperature profile – measurement and modelling

As described in section 4.2.1, the temperature profile within the reactor along the reactor axis has been characterised using a thermocouple, see also: Figure 4.3. In order to verify our understanding of the temperature distribution, we prepared a heat flow finite element model simulation using COMSOL Multiphysics® 5.3a with a heat flow module. Several idealising assumptions were made in the model (refer also to Figure B.1):

i. The system exhibits an axial symmetry around the reactor tube axis.
ii. A mirror symmetry exists with respect to the midplane of the reactor.
iii. The heating zone in the middle of the reactor can be treated as a surface with the boundary condition of constant set temperature T_S.
iv. The remaining walls of the reactor tube act as an ideal insulation, i.e. a boundary condition

$$\dot{Q} = 0, \tag{B.1}$$

where $\dot{Q}$ denotes the heat flow through the surface in W/(m^{2}s).

v. The heat shields act as heat sinks with the heat flow proportional to the difference between the temperature at the boundary T_B and the ambient temperature T_A, which leads to the boundary condition

$$\dot{Q} = h(T_B - T_A), \tag{B.2}$$

where h is the proportionality constant in W/(Km^{2}s).

vi. The mass flow rate is negligible compared to the heat flow rate.
vii. Only argon at 1 bar is present in the chamber.

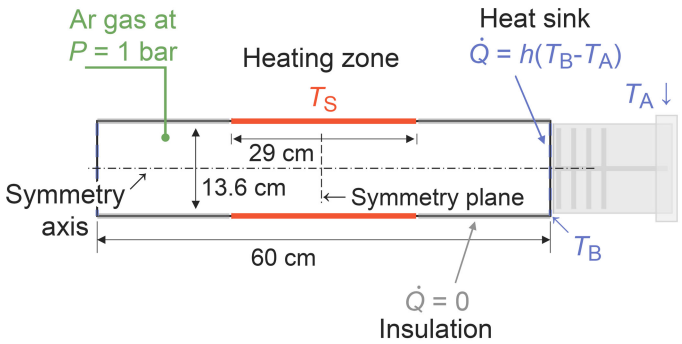

Figure B.1. The geometry and boundary conditions of the finite element heat flow model of the CVD reactor.

Some of the assumptions require discussion. The assumption ii. can be interpreted the following way. Let x describe the spatial coordinate along the reactor tube axis, with x=0 defined as in the middle of the heating zone. At at the midplane of the reactor tube – the plane perpendicular to the tube axis, crossing the axial coordinate x=0 – the temperature profile is locally symmetrical. In this case, the temperature gradient with respect to x vanishes. Hence, the heat flow across the symmetry plane necessarily equals 0 as well, as the temperature gradient is the driving force for the heat flow.

This assumption is consistent with our measurements of the temperature profile. Even though reality the reactor in is not symmetrical (see: Figure 4.3), the assumption remains valid, as long as the experimentally determined temperature profile peaks at x=0. We are simplifying the simulation by modelling only the region of interest, where the substrates for CNT growth are typically placed, which is to the right form x=0. In reality, the heat dissipation is most likely similar on both sides, but certainly not completely symmetrical. In the assumption v. a proportionality parameter of the heat sink effectiveness h was defined. It remains a free parameter of the simulation, adjusted to fit the simulation to the measurement data. The value of h fitting the experiment best was established as 0.11 W/(Km^{2}s). The ambient temperature was set as 25 °C in the simulations. In assumption vi., we state, that the mass flow rate is negligible compared to the heat flow rate. It means, that in the simulation we assume a quasi-static situation, where the gas is not flowing through the reactor, because the timescale of the gas flow is much longer than the timescale for equilibration of the temperature profile. We substantiate it by the following back-of-an-envelope calculation.

Let us consider the heat diffusion along the reactor tube, described with the equation

$$\frac{\partial T}{\partial t} = \frac{\partial}{\partial x}\left(\alpha \frac{\partial T}{\partial x}\right), \tag{B.3}$$

where t is time, T – temperature, α – heat diffusivity. In order to estimate the timescale of the diffusivity t_D, i.e. the characteristic time of equilibration of the temperature profile, let us equate the length of the reactor L = 90 nm to the diffusion length, which gives the expression

$$t_\alpha = \frac{L^2}{\alpha}, \tag{B.4}$$

which is analogous to the mass diffusivity; see also eq. (5.43). The assumption vi. holds if t_α is much smaller than the timescale of gas flow t_F, which is the time needed to deliver the amount of gas into the reactor equal to its capacity. We express t_F as

$$t_\mathrm{F} = \frac{N_\mathrm{C}}{r_\mathrm{Ar}}, \tag{B.5}$$

where r_Ar is the argon flow rate in moles per second, whereas N_C is the number of moles of gas in the reactor at atmospheric pressure and at the given temperature profile. In the following, we are establishing the estimates t_D and t_F.

The heat diffusivity of gas α is described with the equation

$$\alpha = \frac{k}{\rho c_\mathrm{p}}, \tag{B.6}$$

where k is heat conductivity in W(mK)$^{-1}$, ρ –density, c_p – heat capacity at constant pressure in terms of J(kgK)$^{-1}$ [266]. The heat conductivity of gas k is expressed as

$$k = 2\beta\rho\lambda_\mathrm{b}c_\mathrm{v}v, \tag{B.7}$$

where λ_b – mean free path of the gas molecule as given with eq. (5.1), v – mean thermal velocity of gas molecules, as given with eq. (5.3), whereas β is a constant factor of the order of 1, depending on the collision integral [267]. While the purpose of the calculations here is to compare the orders of magnitude, a precise measure of β is unnecessary, therefore we equate it to 1.

Combining together equations (B.6,7), (5.1,3) and the ideal gas law, we obtain the close-form expression for the heat diffusivity α,

$$\alpha = \frac{\left(\frac{k_B T}{\pi}\right)^{\frac{3}{2}}}{\sqrt{\frac{\mu}{N_A}} d_m^2 p \gamma}, \tag{B.8}$$

where k_B is the Boltzmann's constant, T – temperature in K, μ – molar mass of argon, N_A – Avogadro's constant, p – pressure, γ – ratio of c_p/c_v, for monoatomic gases, such as argon, equal 1.67. While in the reactor we measure a gradient of temperatures from the set temperature in the middle of the reactor T_S down to room temperature at its edge T_A, we consider both the extremes in the calculations, T_S=750 °C and T_A=25 °C, respectively. Consequently, equation (B.4) gives the values for t_α≈1.0 s and 6.1 s, for the higher and the lower temperature, respectively.

To estimate the timescale of gas flow t_F, we need a measure of the number of moles of gas in the reactor n_C, which requires the complete temperature profile within the reactor. The latter is unfortunately unavailable, due to technical obstacles. However, for these approximate estimations an educated guess of the temperature profile is sufficient. We assumed an approximately symmetric temperature profile in the heating zone of the reactor and a similar temperature drop across both heat shields, necessitating the transition to room temperature at both ends. The measured temperature profile, along with the inferred extension is shown in Figure B.2.

Following the ideal gas law, the total number of moles of gas in the chamber N_C is estimated as

$$N_C = \int_{x_1}^{x_2} \frac{p}{RT(x)} S \mathrm{d}x, \tag{B.9}$$

where $x_{1,2}$ are the coordinates of the reactor tube edges, $T(x)$ – the temperature profile, R – universal gas constant, S – the cross-section area of the reactor tube. Equation (B.9) returns the value of n_C≈0.28. Taking the flow rate of argon f_{Ar}, that we typically use in experiments, equal 2 L/min, we estimate the flow rate in terms of moles pes second,

$$r_{Ar} = f_{Ar} \frac{p}{RT_A}, \tag{B.10}$$

where p=1 bar, T_A=25 °C are the ambient conditions at which the volumetric gas flow f_{Ar} is measured,. We obtain the estimate of t_F≈200 s, which is clearly much greater than either of the values of t_α (1.0 s and 6.1 s). Therefore, the assumption vi. is valid and the mass transport in the reactor can be treated as quasi-static, and the temperature distribution can be accurately decoupled from the gas flow effects. The graph in Figure B.2 shows an excellent agreement of the measurement data with the simulated temperature profile.

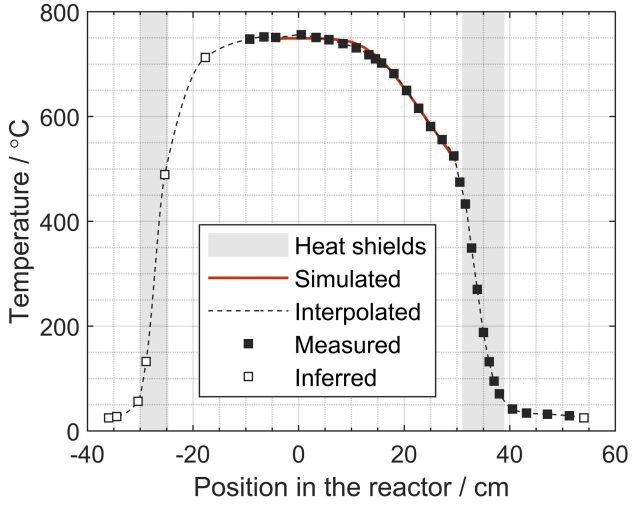

Figure B.2. Temperature profile measured at the 750 °C setting of the CVD reactor (closed squares), along with the estimated extension of the profile (open squares). The interpolation by a piecewise polynomial (dashed line) is used in the numerical calculations. The simulated temperature profile of the region of interest is shown (red solid line). Grey rectangles indicate the positions of the heat shields, for reference.

The simulations showed, that the temperature profile can be accurately scaled with the set temperature using the scaling law

$$T'(x) = (T(x) - T_\mathrm{A})\frac{T'_\mathrm{S} - T_\mathrm{A}}{T_\mathrm{S} - T_\mathrm{A}} + T_\mathrm{A}, \tag{B.11}$$

where $T(x)$ is the measured temperature profile at the temperature setting T_S, whereas the primes indicate the temperature profile and the setting to scale to. We use this knowledge in the further part of this appendix for estimations of precursor gas concentrations in the reactor at the lower temperature 725 °C.

B.1.2. Precursor concentration and exposure

In the calculations of the carbon precursor concentration and exposure we assume that the mass diffusion rate is much faster than the gas flow rate. It means, that the inhomogeneities in the gas concentrations in the reactor chamber are rapidly equilibrated at the timescales of the ethylene dosing time considered. This assumption is validated in a similar way, as the assumption vi. above – we compare the timescale of mass diffusion t_D with the timescale of the precursor dosing t_P. The shortest precursor dosing time in the experiments was 30 s, therefore we set it as the value of t_P.

The diffusion time is, analogously to equation (B.4),

$$t_\mathrm{D} = \frac{L^2}{D}, \tag{B.12}$$

where D is the diffusivity of the given component in the gas mixture. The D is expressed as

$$D = \frac{\lambda_\mathrm{b} v}{3}, \tag{B.13}$$

where λ_b is the mean free path of the given component in the bulk gas mixture. In equation (6.47) we described λ_b in a binary mixture of gases. Here, however, we need to consider the ternary mixture of ethylene, argon and hydrogen. The expression (6.47) is straightforwardly generalisable to N-component gas mixture [261],

$$\lambda_i = \left(\pi \sum_{j=1}^{N} \sqrt{1 + \frac{\mu_i}{\mu_j}} \left(\frac{d_i + d_j}{2} \right)^2 n_j \right)^{-1}, \tag{B.14}$$

where λ_i is the mean free path of the i-th component, $\mu_{i,j}$ – molar masses, $d_{i,j}$ – kinetic diameters, n_j – concentration of the j-th component in the mixture in terms of number of molecules per volume. Let us assign index 1 to ethylene, 2 to argon and 3 to hydrogen, therefore $\lambda_b \coloneqq \lambda_1$, λ_2 or λ_3, depending which component of the mixture is considered. While in the ideal gas law, the number of molecules at given pressure and temperature is proportional to volume and independent of the gas species, the gas concentration n_i is proportional to its respective volumetric flow rate f_i,

$$n_i = \frac{p}{k_B T} \frac{f_i}{\sum f_i}. \tag{B.15}$$

Parameters of the gases are summarised in Table B.1.

Table B.1. Parameters of gases considered in the gas flow calculations

	Ethylene	Argon	Hydrogen
Index i	1	2	3
Kinetic diameter d_i	3.9 Å[a]	3.4 Å[b]	2.9 Å[c]
Molar mass μ_i	28.05 g/mol	39.95 g/mol	2.02 g/mol
Volumetric flow rate f_i	0.4 L/min	2.0 L/min	0.6 L/min

[a] Matteucci *et al.*, 2006 [268],
[b] Breck, 1984 [269],
[c] Ismail *et al.*, 2015 [262].

Once again, let us consider both of the extreme temperatures in the reactor: the set temperature T=T_S=725 °C and the ambient temperature T=T_A=25 °C. The summary of the calculations is given in Table B.2.

Table B.2. Results of calculations for all the components of the gas mixture considered. The numbers are given up to 3 significant digits. Subscript i denotes the gas species: i=1 represents ethylene, i=2 – argon, i=3 – hydrogen.

Parameter	**Ethylene**		**Argon**		**Hydrogen**	
Temperature / °C	25 °C	725 °C	25 °C	725 °C	25 °C	725 °C
Concentration n_i / 10^{24} m^{-3}	3.28	0.980	16.4	4.90	4.92	1.47
Mean free path λ_i / nm	55.4	185	57.0	190	120	404
Diffusion time $t_{\mathrm{D},i}$ / s	2.93	0.478	3.39	0.554	0.360	0.0588

We find, that the diffusion time at any temperature and for any gas considered is indeed much shorter than the time of the ethylene dosing (always greater than 30 s). Therefore, the assumption of the assumption of rapid homogenisation of gas in the reactor tube is valid.

In this case, the amount of moles of the i-th component of the gas mixture in the reactor chamber N_i is described with a differential equation

$$\frac{\mathrm{d}N_i}{\mathrm{d}t} = r_i(t) - \frac{N_i}{N_\mathrm{C}} \sum_{j=1}^{3} r_j\,(t), \tag{B.16}$$

where r_i is the gas delivery rate in terms of moles per second, whereas N_C is the total amount of moles in the reactor introduced previously. The r_i, in principle, depends on time, because the gas flow can be controlled. In the case, when the temperature of the reactor changes in time, a more general form of the set of differential equations needs to be considered, namely,

$$\frac{\mathrm{d}N_i}{\mathrm{d}t} = r_i(t) + \frac{N_i}{N_\mathrm{C}(t)} \left(\frac{\mathrm{d}N_\mathrm{C}}{\mathrm{d}t} - \sum_{j=1}^{3} r_j\,(t) \right). \tag{B.17}$$

The N_C is dependent on temperature, following equation (B.9), and thus on time. Temperature profile $T(x)$ is evaluated at each point in time using the equation (B.11). This more complex approach was used to calculate the gas concentrations presented in Figure 4.4b,c. However, in the following considerations, we assume a constant temperature and use equation system (B.16), for simplicity.

At the beginning, ethylene is switched on for a given precursor dosing time t_P. Argon and hydrogen remain constant. Therefore, we set

$$r_1(t) = (H(t) - H(t - t_\mathrm{P}))\,\frac{f_1 p}{R T_\mathrm{A}}, \tag{B.18}$$

$$r_2(t) = \frac{f_2 p}{R T_\mathrm{A}} = \mathrm{const}, \tag{B.19}$$

$$r_3(t) = \frac{f_3 p}{R T_\mathrm{A}} = \mathrm{const}, \tag{B.20}$$

where p and T_A are the ambient pressure and temperature, respectively, H – Heaviside step function.

Initially, the chamber is completely flushed with a stable mixture of argon and hydrogen, therefore the initial conditions for N_i are

$$N_1(t=0) = 0, \tag{B.21}$$

$$N_2(t=0) = \frac{r_2}{r_2 + r_3} N_\mathrm{C}, \tag{B.22}$$

$$N_3(t=0) = \frac{r_3}{r_2 + r_3} N_\mathrm{C}, \tag{B.23}$$

for i=1, 2 and 3, respectively. Such defined problem is solvable analytically. The total amount of moles remains constant,

$$\sum_{i=1}^{3} N_i(t) = N_\mathrm{C} = \mathrm{const}, \tag{B.24}$$

as well as the ratio between argon and hydrogen, as they are both delivered at a constant rate into the reactor. Therefore, it is sufficient to solve for the ethylene N_1 and infer the other two components, $N_{2,3}$. N_1 is expressed as

$$N_1(t) = \begin{cases} N_\mathrm{C} \dfrac{r_1}{r_1 + r_2 + r_3} \left(1 - \exp\left(-t \dfrac{r_1 + r_2 + r_3}{N_\mathrm{C}}\right)\right) & \text{for} \quad 0 < t < t_\mathrm{P} \\ N_\mathrm{P} \exp\left(-(t - t_\mathrm{P}) \dfrac{r_2 + r_3}{N_\mathrm{C}}\right) & \text{for} \quad t_\mathrm{P} < t \end{cases}, \tag{B.25}$$

where N_p was implicitly defined for convenience,

$$N_\mathrm{p} \coloneqq N_\mathrm{C} \frac{r_1}{r_1 + r_2 + r_3} \left(1 - \exp\left(-t_\mathrm{P} \frac{r_1 + r_2 + r_3}{N_\mathrm{C}}\right)\right). \tag{B.26}$$

At each point in time, the $N_{2,3}$ are equal

$$N_2(t) = \left(N_\mathrm{C} - N_1(t)\right) \frac{r_2}{r_2 + r_3}, \tag{B.27}$$

$$N_3(t) = \left(N_\mathrm{C} - N_1(t)\right) \frac{r_3}{r_2 + r_3}, \tag{B.28}$$

respectively. Having the number of moles of each component in the chamber and the set temperature of T_S=725 °C, we calculate the respective gas concentrations experienced by the sample

$$n_i = \frac{N_i}{N_\mathrm{C}} \frac{p}{RT_\mathrm{S}}. \tag{B.29}$$

We evaluated the model for a set of different ethylene dosing times t_P from 0.5 min to 10 min, which is the range that we explored experimentally. The results are presented in Figure B.3.

Having the function of ethylene gas concentration with respect to time, we are able to evaluate the ethylene gas exposure Φ experienced by the samples. The exposure Φ is, by definition, a time integral from t=0 to infinity of impingement rate J, the latter being expressed by equation (6.2). The exact analytical solution for Φ is

$$\Phi(t_\mathrm{p}) = \frac{r_1}{r_1 + r_2 + r_3} \frac{pN_\mathrm{A}}{\sqrt{2\pi\mu_1 RT_\mathrm{s}}} \left(t_\mathrm{p} + \frac{N_\mathrm{C} r_1}{(r_2 + r_3)(r_1 + r_2 + r_3)} \left(1 - \exp\left(-t_\mathrm{p} \frac{r_1 + r_2 + r_3}{N_\mathrm{C}}\right)\right)\right), \tag{B.30}$$

which is very well approximated by the linear relationship

$$\Phi(t_\mathrm{p}) = \frac{r_1}{r_1 + r_2 + r_3} \frac{pN_\mathrm{A}}{\sqrt{2\pi\mu_1 RT_\mathrm{s}}}\, t_\mathrm{p}, \tag{B.31}$$

due to the fact, that the second additive term besides t_p in the major bracket in (B.30) is much smaller than t_p for the parameter range considered.

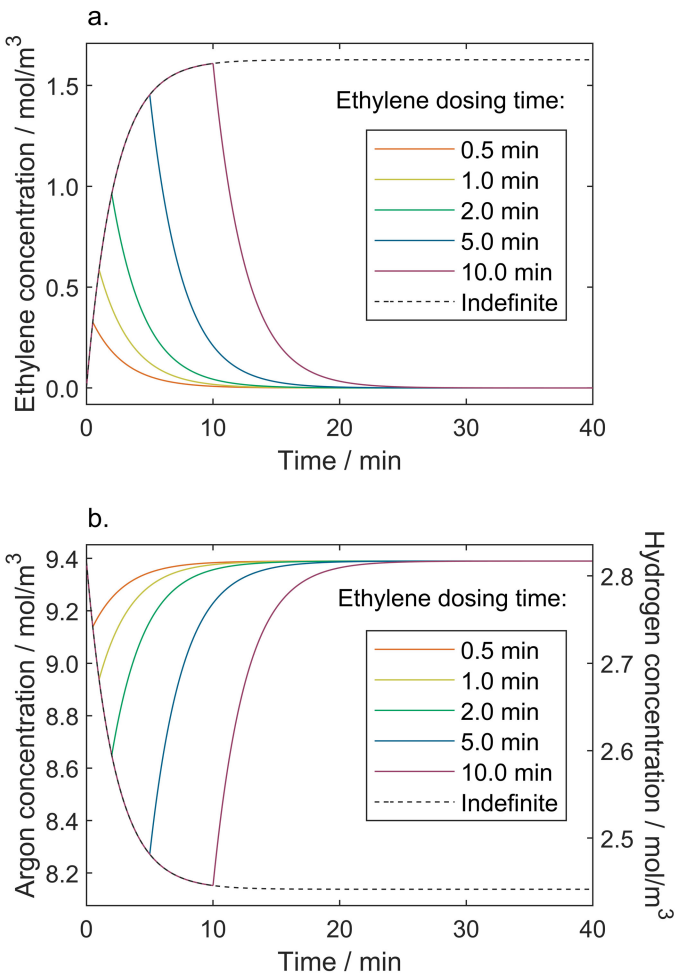

Figure B.3. Results of the calculations of the gas concentrations at a range of ethylene dosing times; a. ethylene concentration, b. concentration of argon and hydrogen. While argon and hydrogen remain at a constant ratio throughout the process, the data for them both is visualised once, with a double vertical axis.

B.2. Image analysis results and nanoparticle size histograms

In this appendix we present all the SEM images along with the essential subsequent image analysis steps, as described in detail in paragraph 4.3.2. The histograms were prepared in terms of nanoparticle diameters at logarithmic scale. The histograms indicate the number of nanoparticles which were neglected, below the threshold diameter of 4 nm. For completeness, in the histograms of each image we additionally indicate the total number of particles detected N, the area disorder of Delaunay triangulation $\mathrm{AD_{Del}}$ and the surface coverage with particles ϕ, in percent.

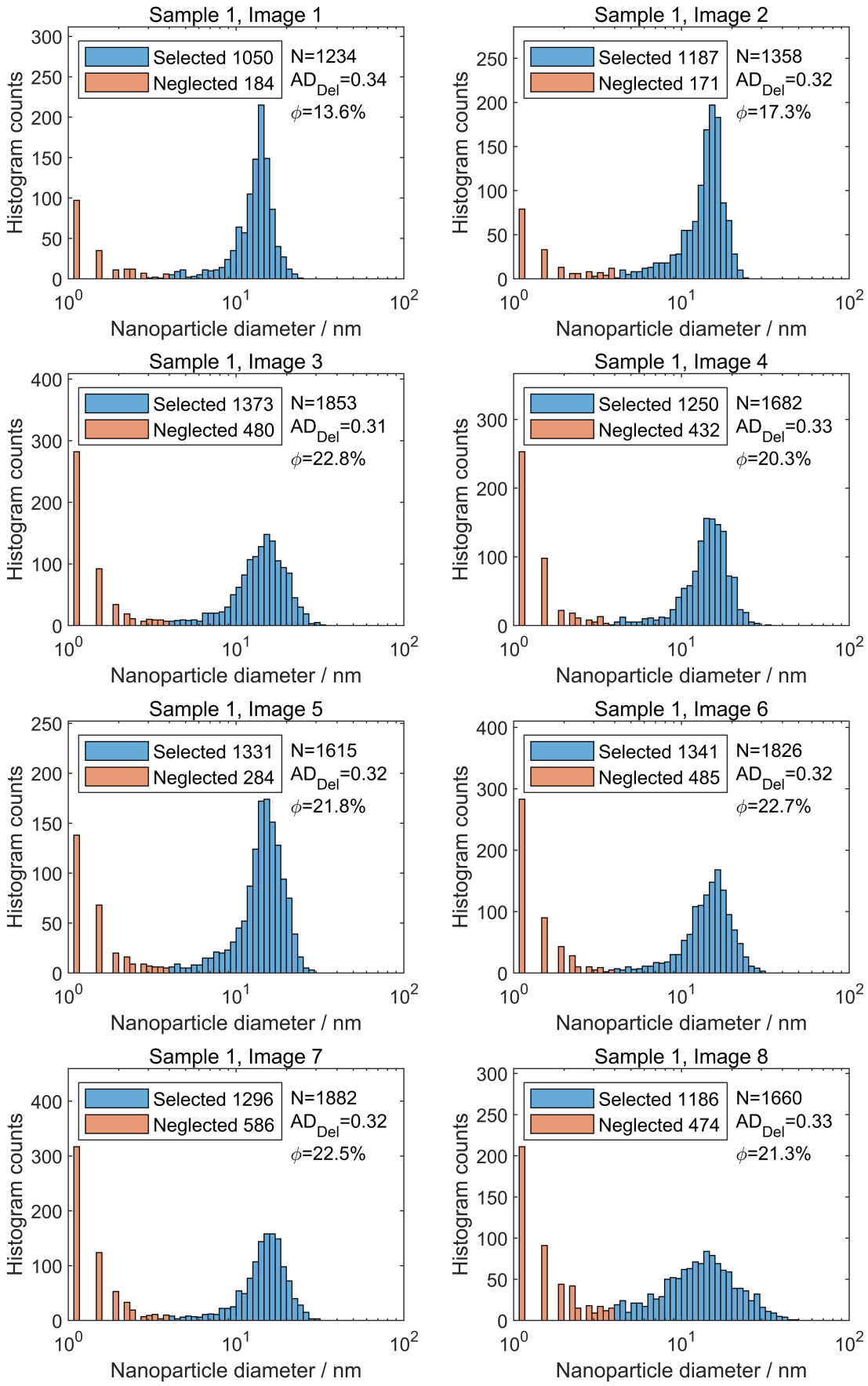

Figure B.4. Nanoparticle data extracted from SEM image analysis, Sample 1. For explanation of symbols, refer to the text in Appendix B.2.

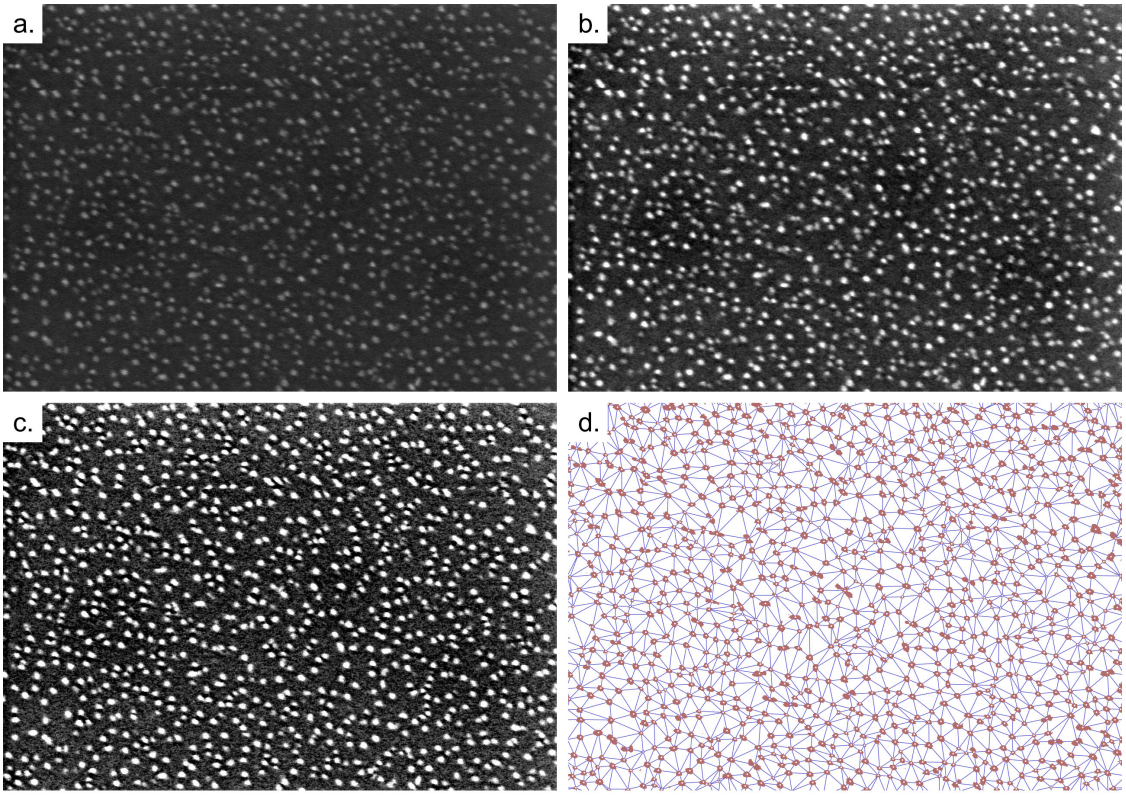
a.
b.
c.
d.
Sample 1, Image 1
500 nm

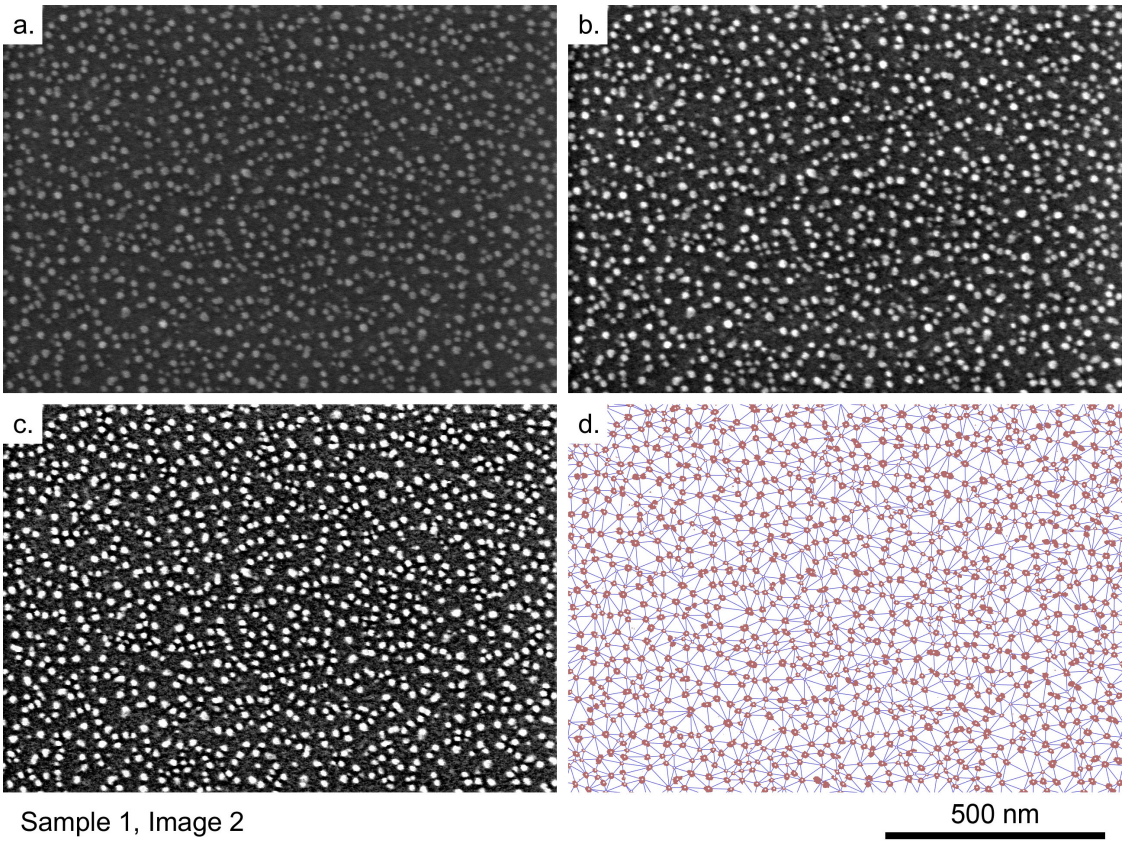
a.
b.
c.
d.
Sample 1, Image 2
500 nm

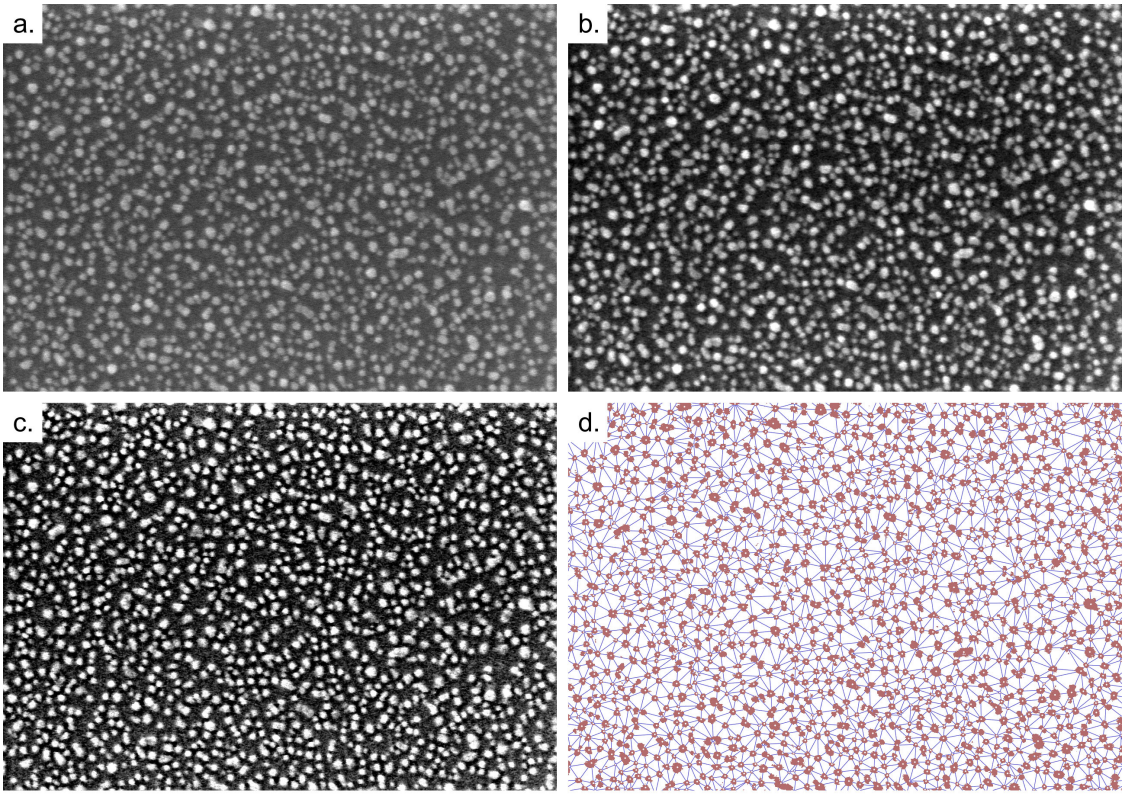
a.
b.
c.
d.
Sample 1, Image 3
500 nm

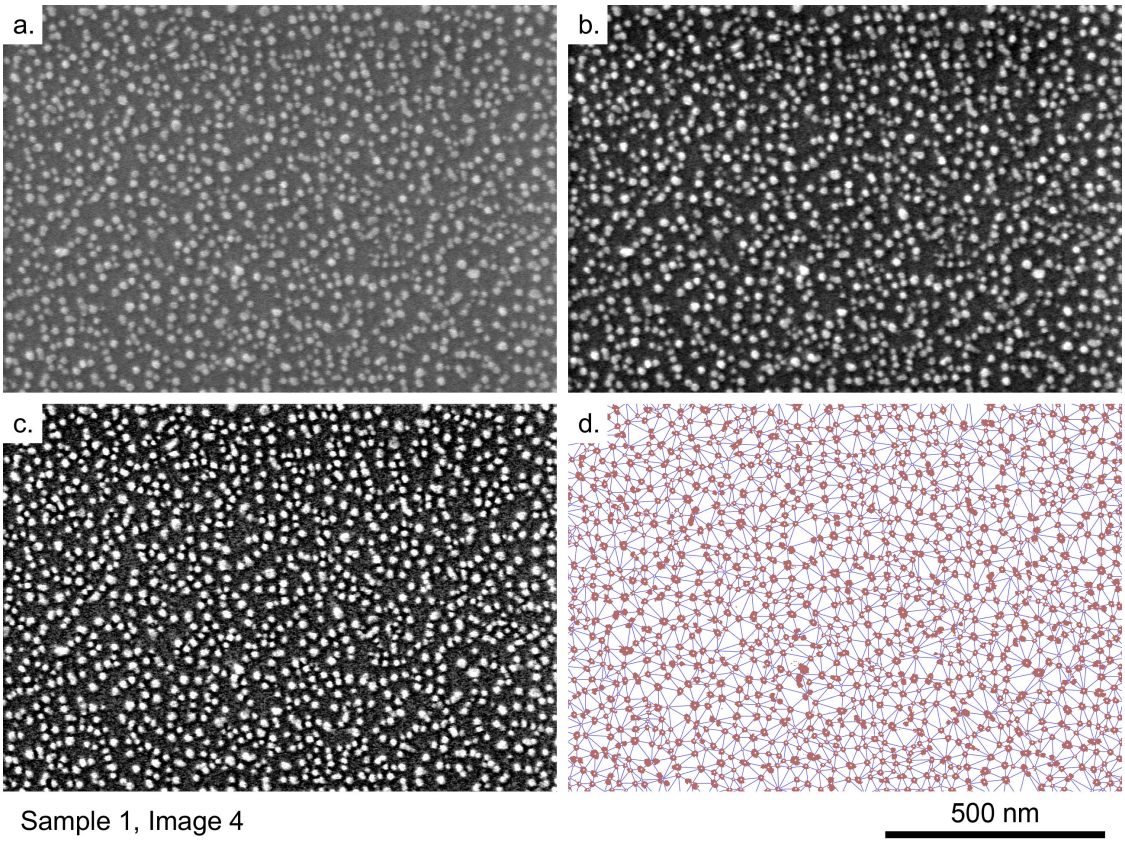
a.
b.
c.
d.
Sample 1, Image 4
500 nm

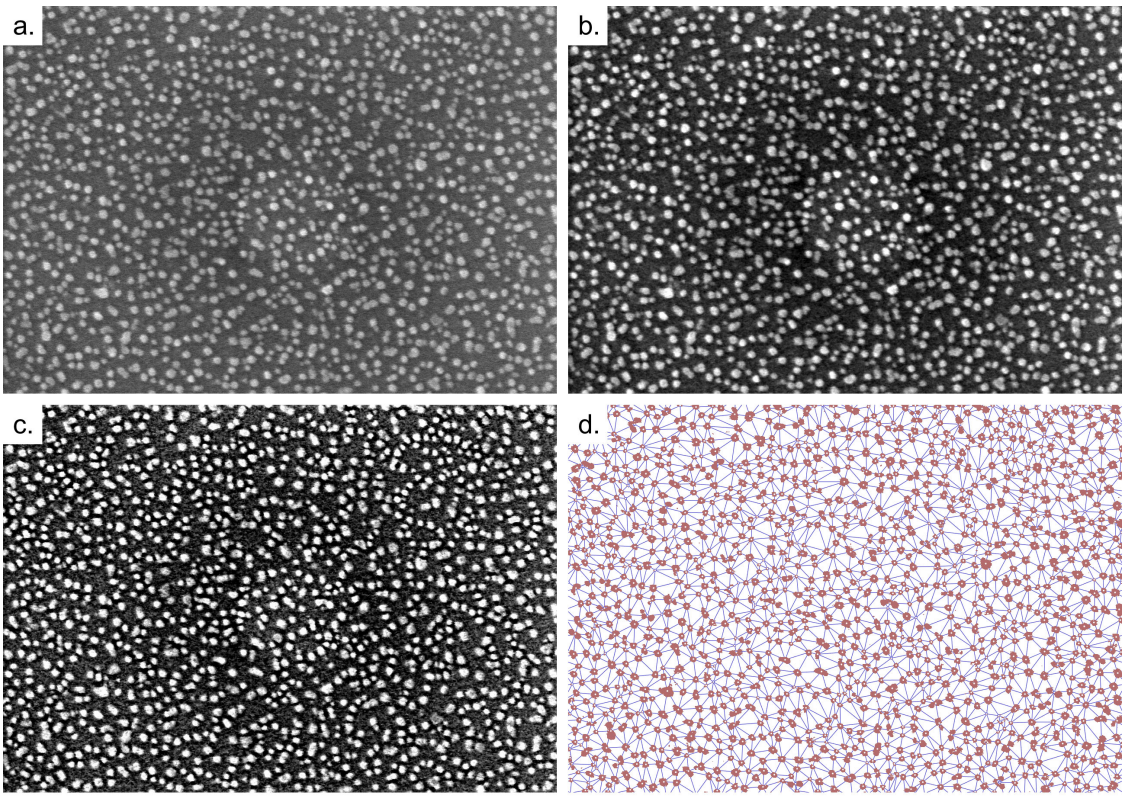
a.
b.
c.
d.
Sample 1, Image 5
500 nm

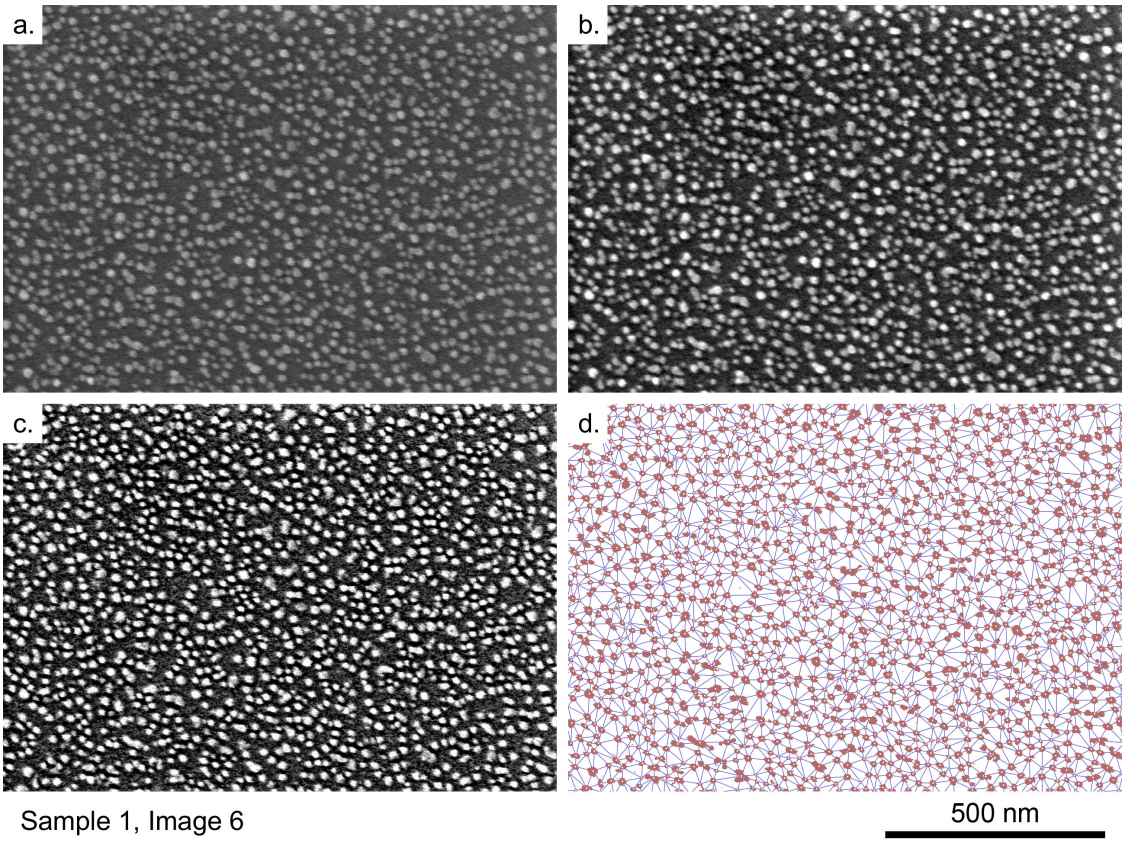
a.
b.
c.
d.
Sample 1, Image 6
500 nm

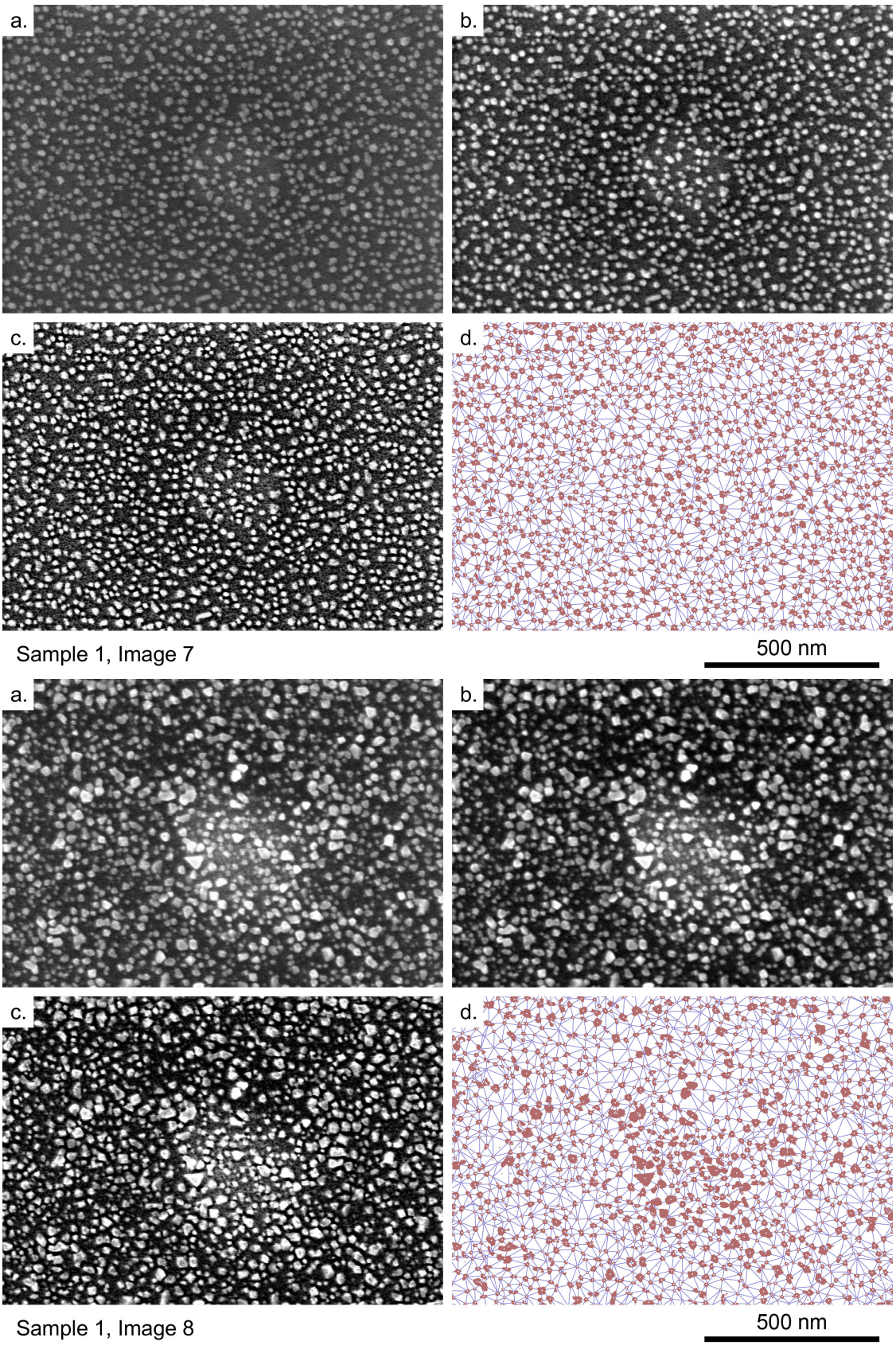

Figure B.5. Subsequent steps of image processing towards segmentation and triangulation of nanoparticles in SEM images of Sample 1; a) original image; b) linear normalisation of the image brightness and median filtering; c) local contrast enhancement; d) thresholding and Delaunay triangulation (red patches – NPs segmented, white dots – NP centroids, blue lines – triangulation result).

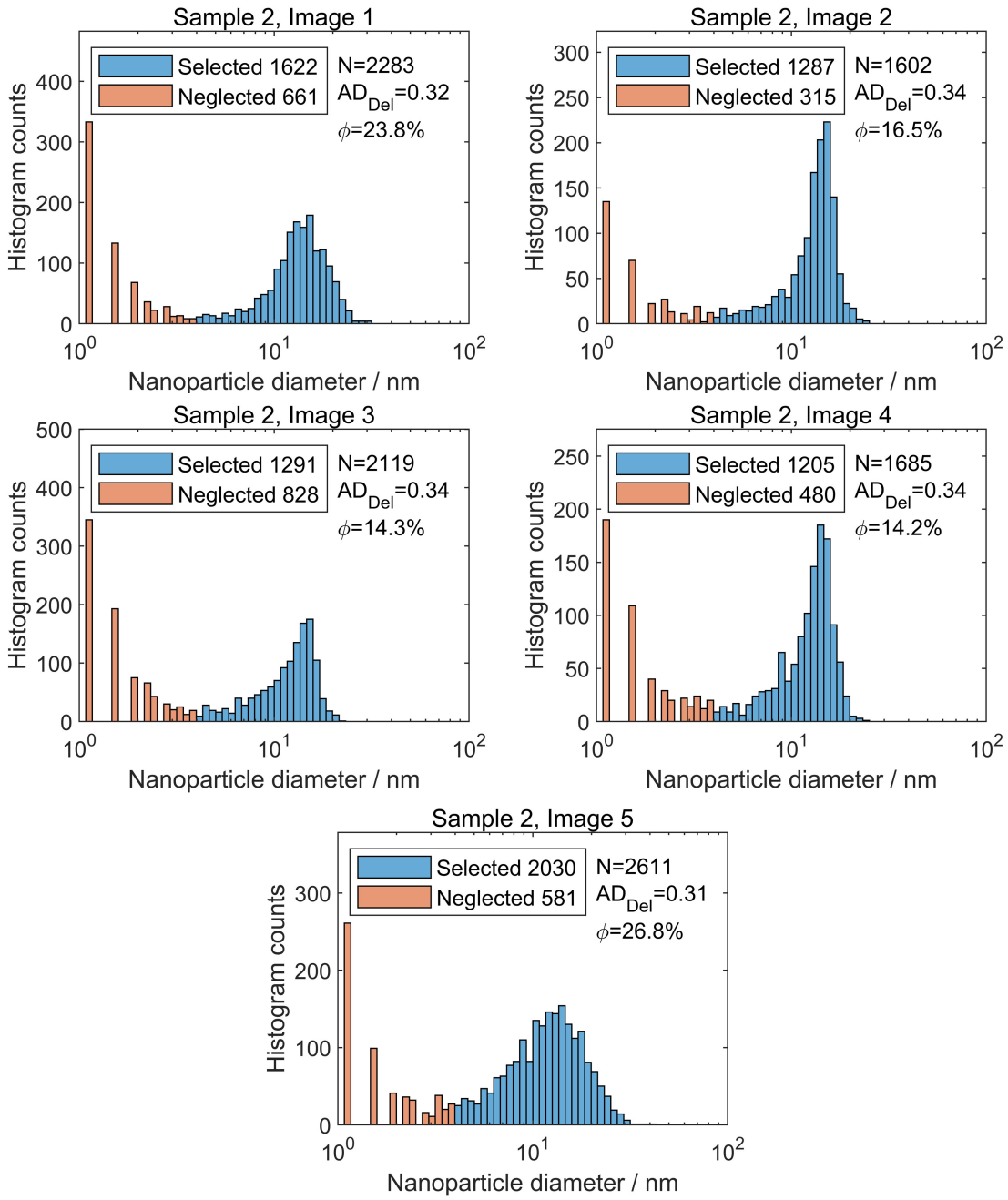

Figure B.6. Nanoparticle data extracted from SEM image analysis, Sample 2. For explanation of symbols, refer to the text in Appendix B.2.

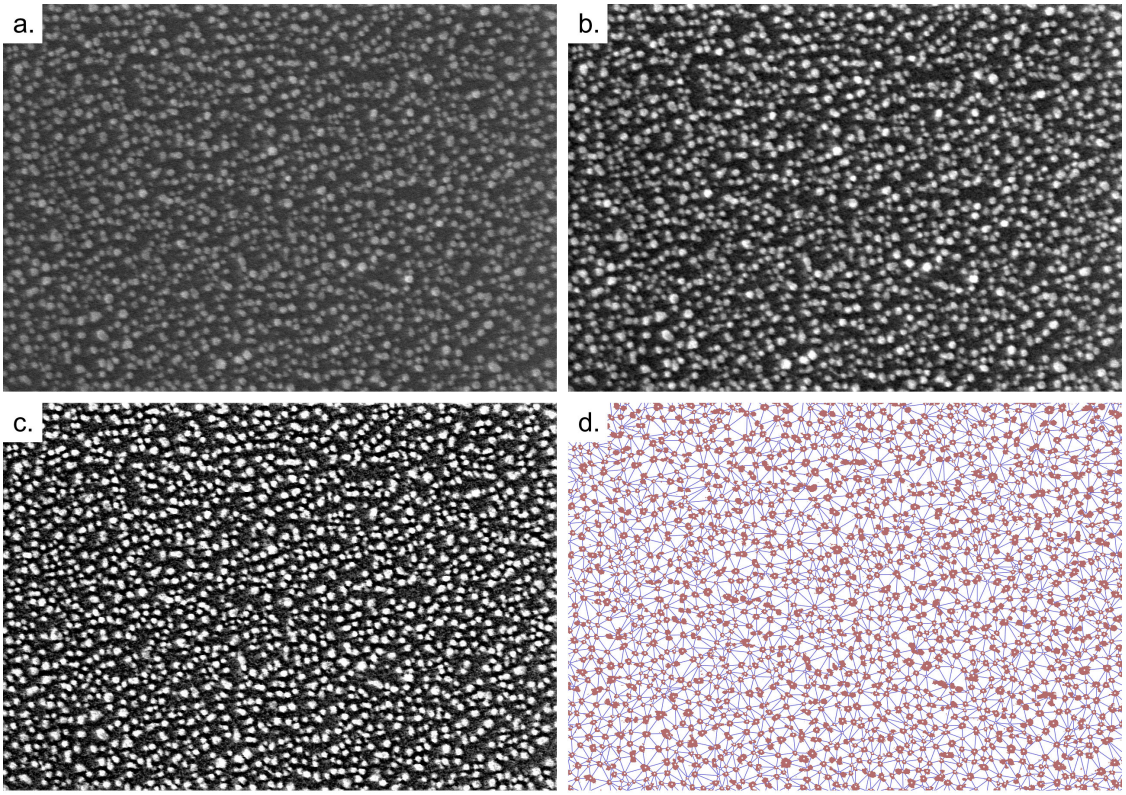
a.
b.
c.
d.
Sample 2, Image 1
500 nm

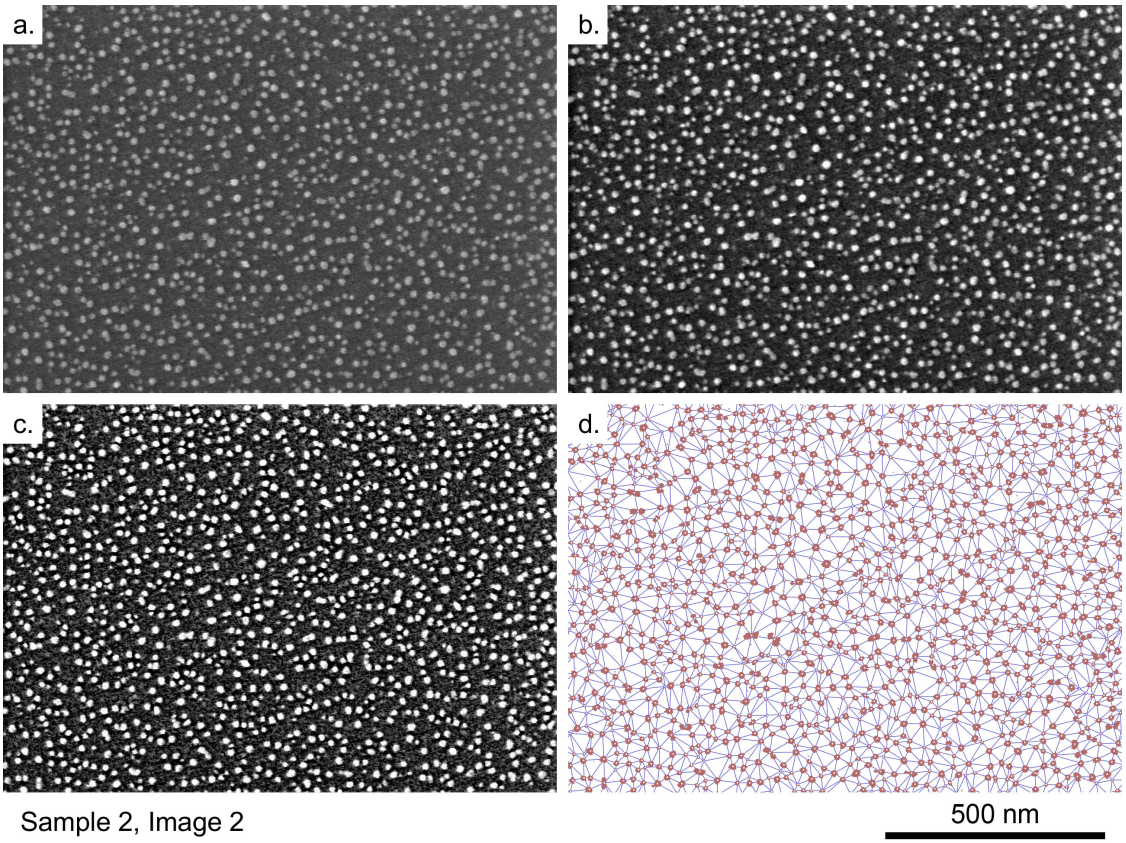
a.
b.
c.
d.
Sample 2, Image 2
500 nm

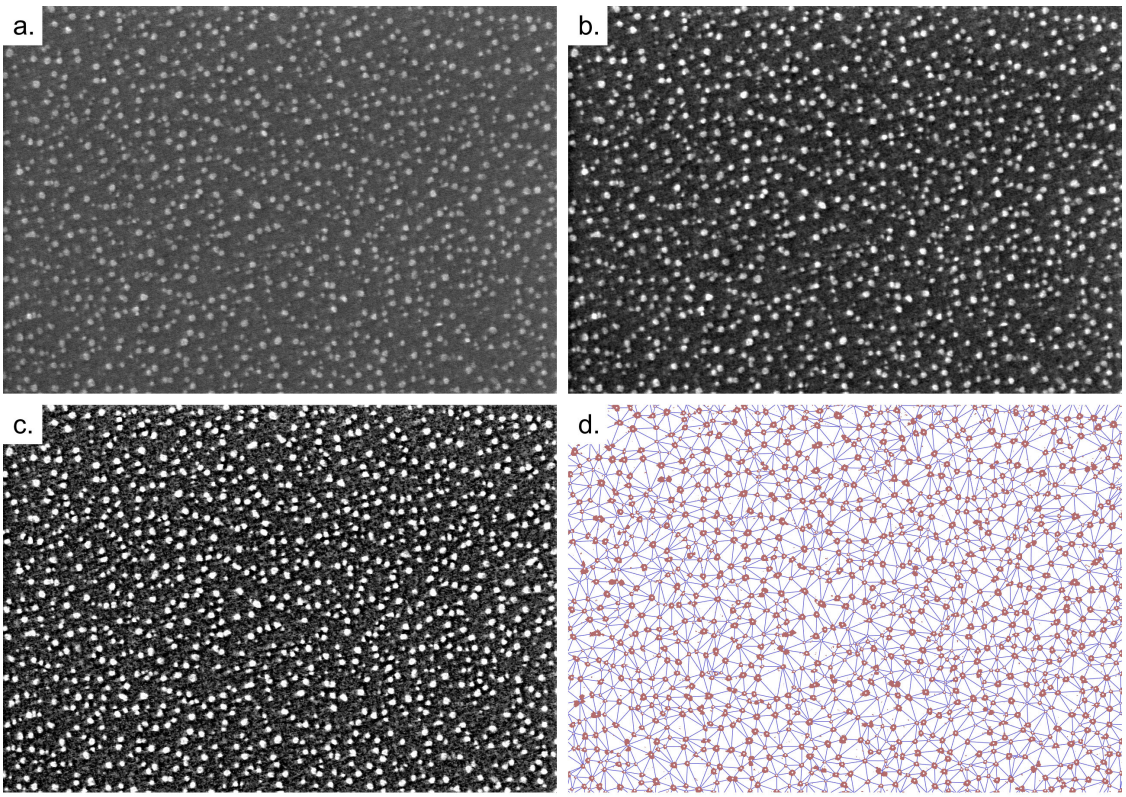
a.
b.
c.
d.
Sample 2, Image 3
500 nm

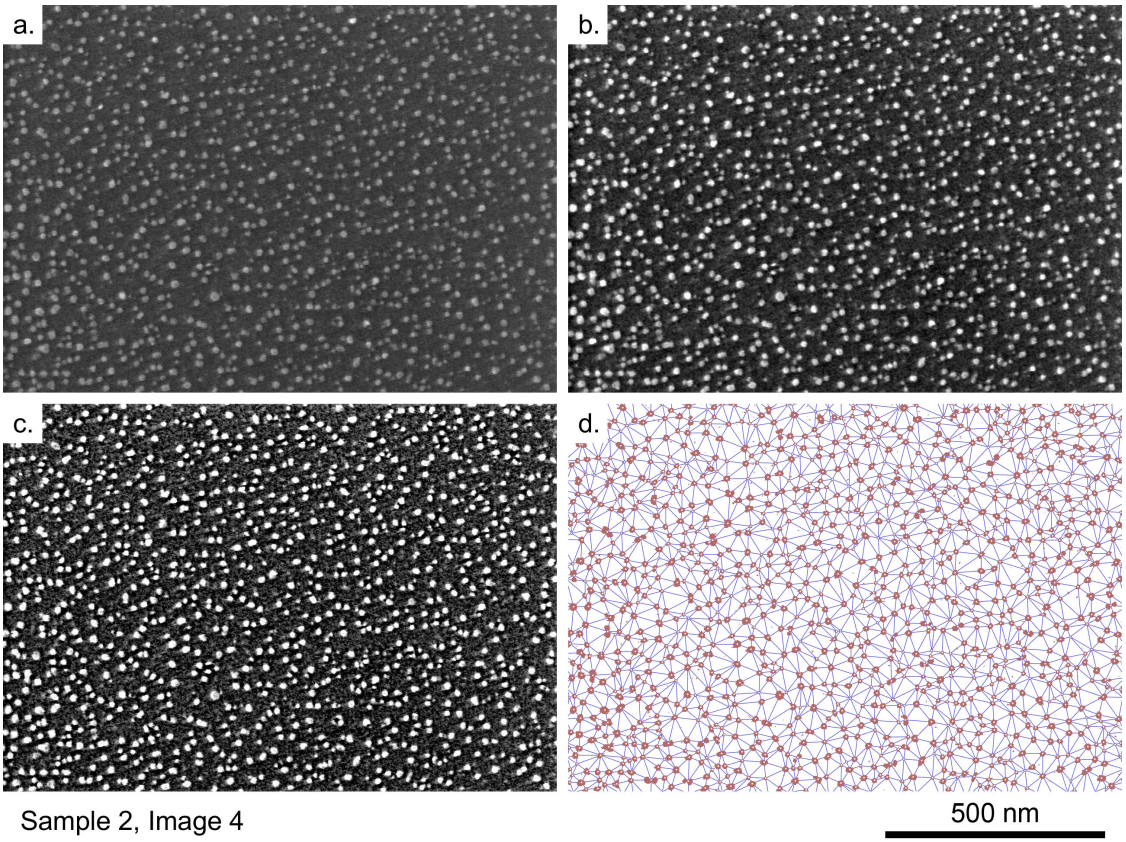
a.
b.
c.
d.
Sample 2, Image 4
500 nm

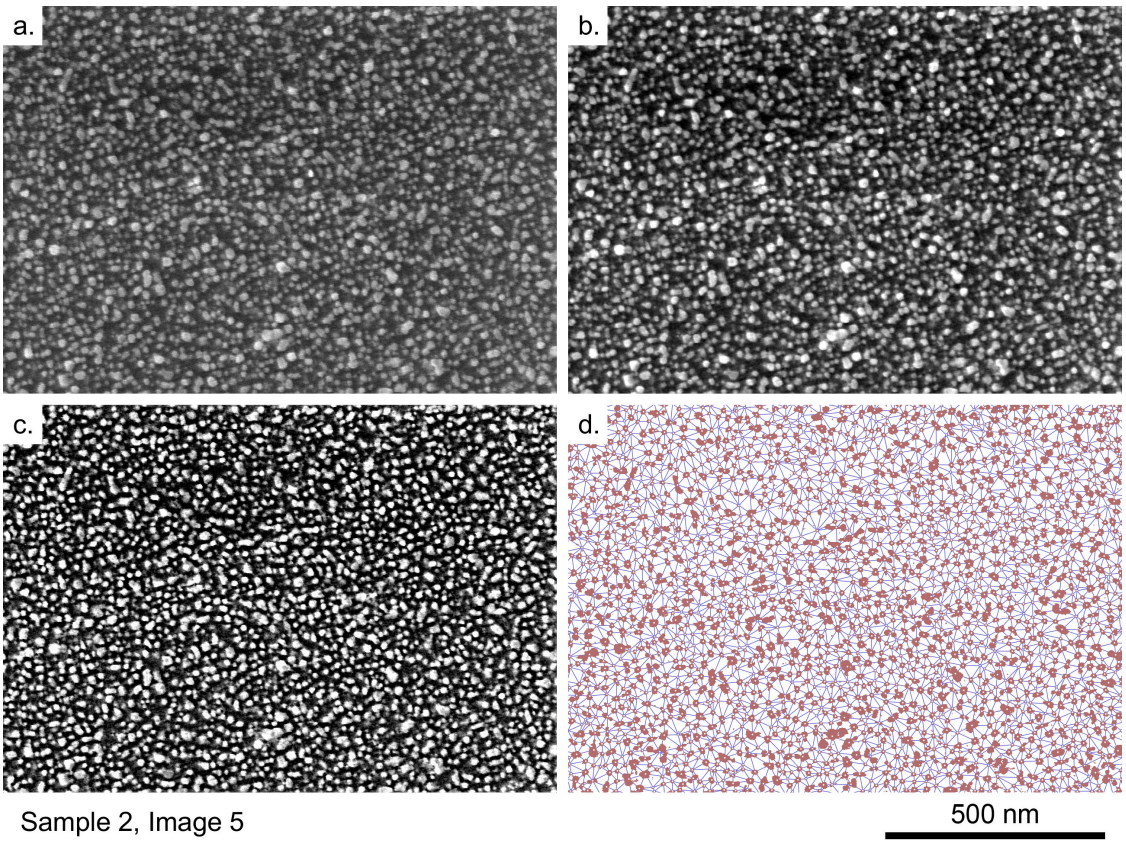

Figure B.7. Subsequent steps of image processing towards segmentation and triangulation of nanoparticles in SEM images of Sample 2; a) original image; b) linear normalisation of the image brightness and median filtering; c) local contrast enhancement; d) thresholding and Delaunay triangulation (red patches – NPs segmented, white dots – NP centroids, blue lines – triangulation result).

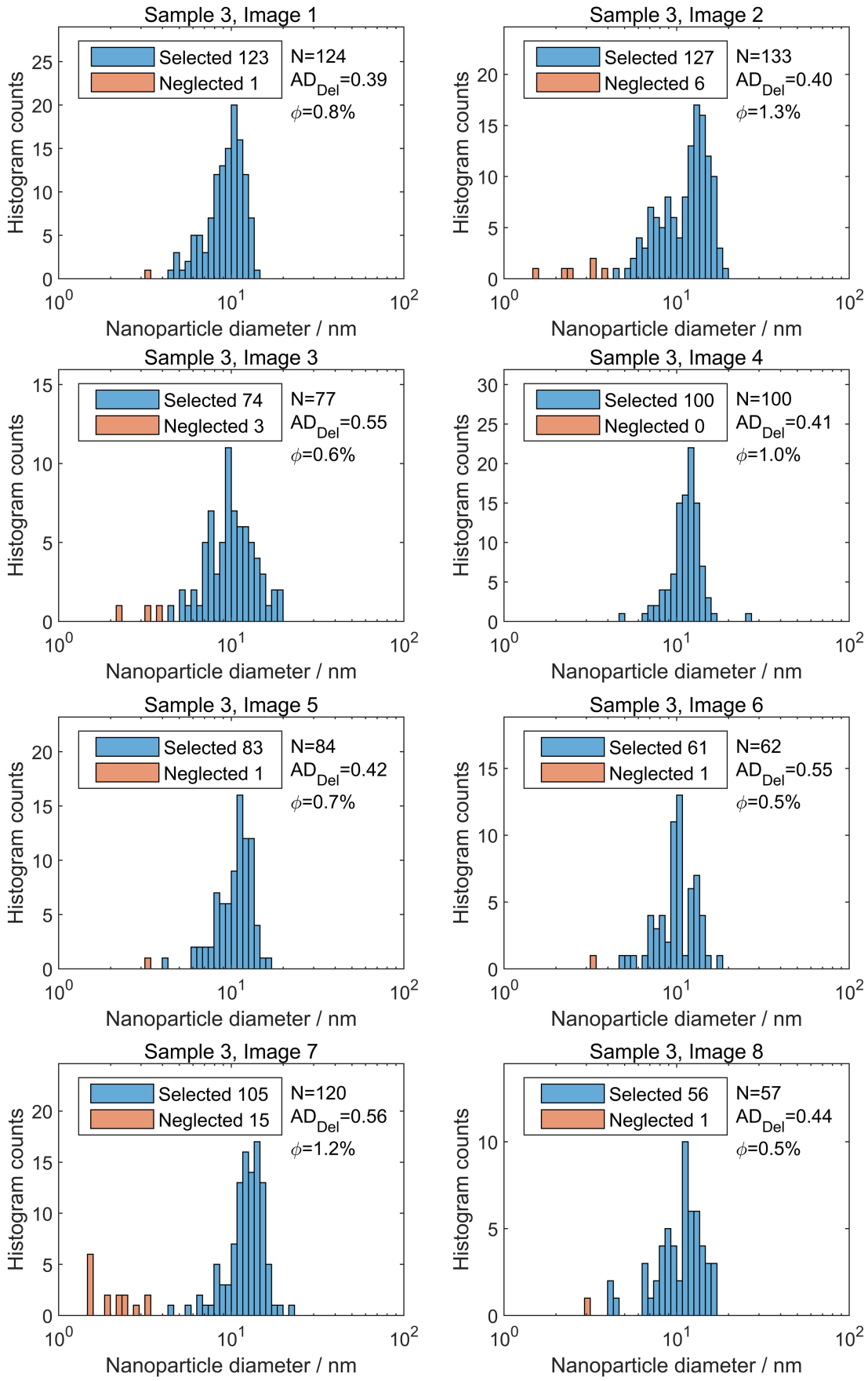

Figure B.8. Nanoparticle data extracted from SEM image analysis, Sample 3. For explanation of symbols, refer to the text in Appendix B.2.

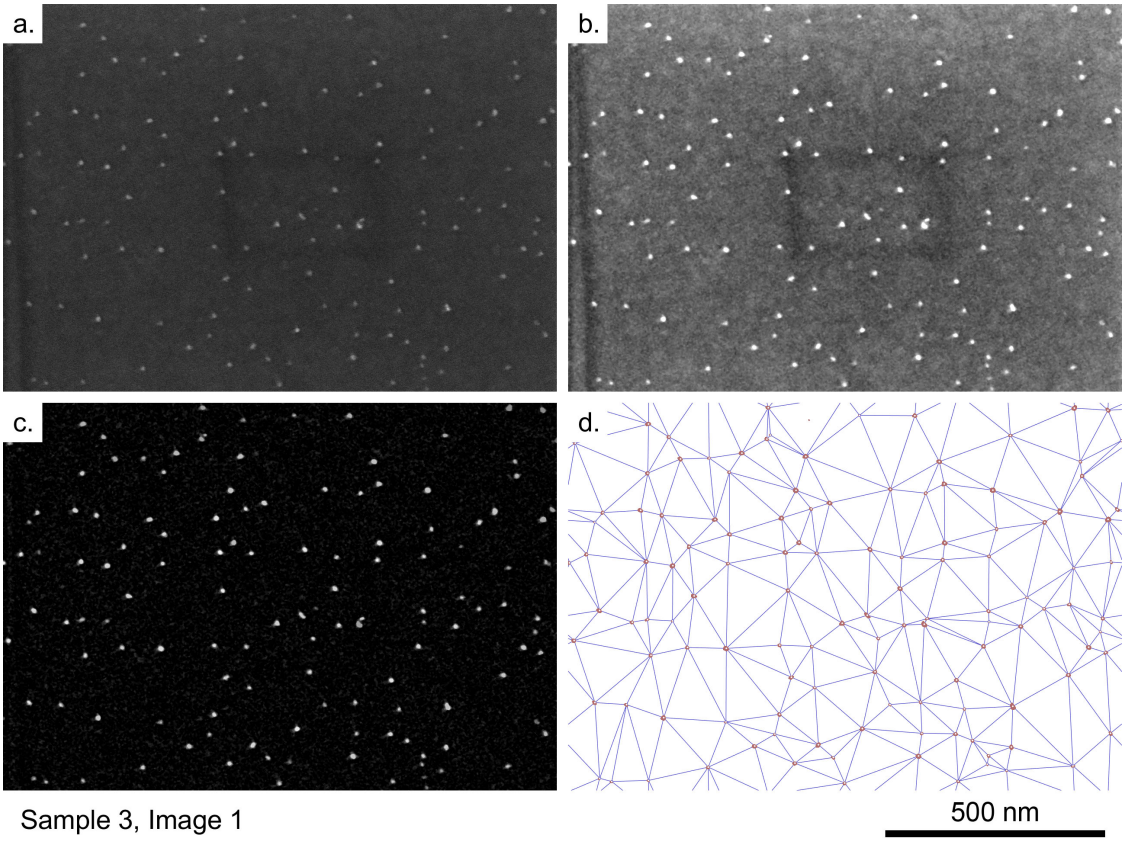
a.
b.
c.
d.
Sample 3, Image 1
500 nm

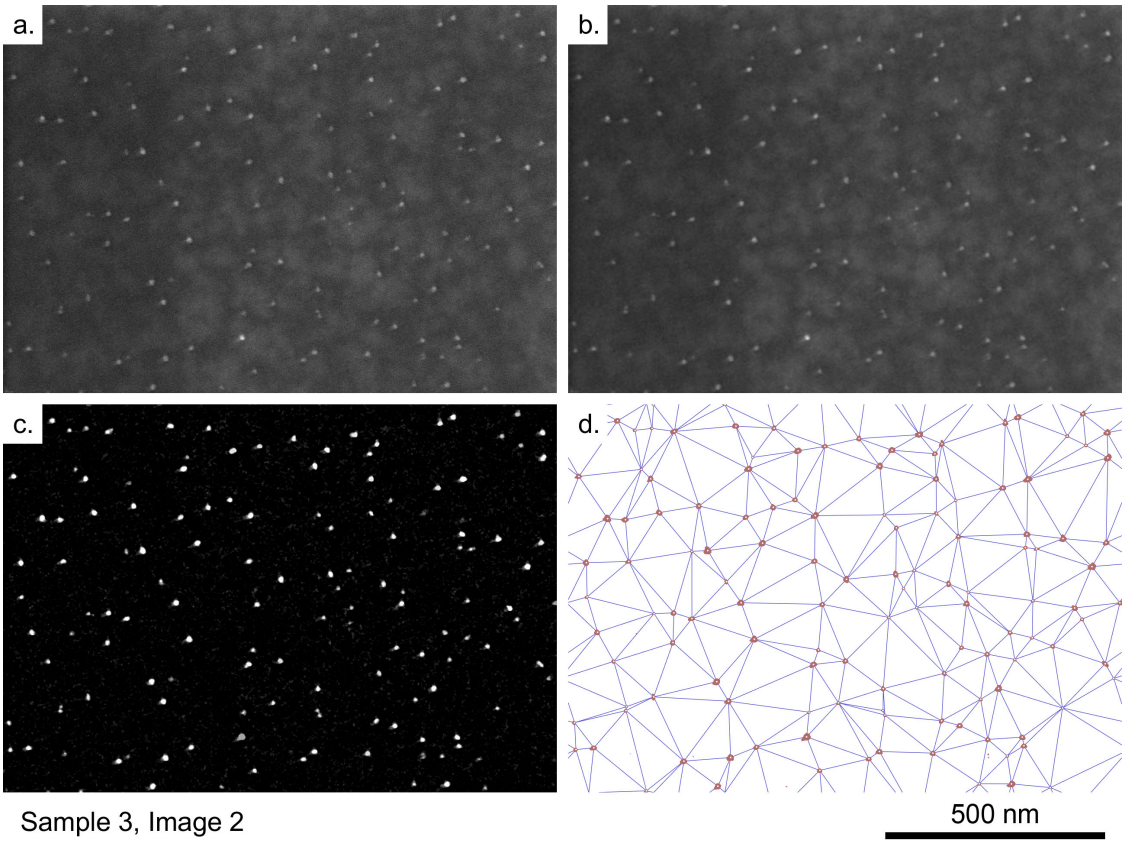
a.
b.
c.
d.
Sample 3, Image 2
500 nm

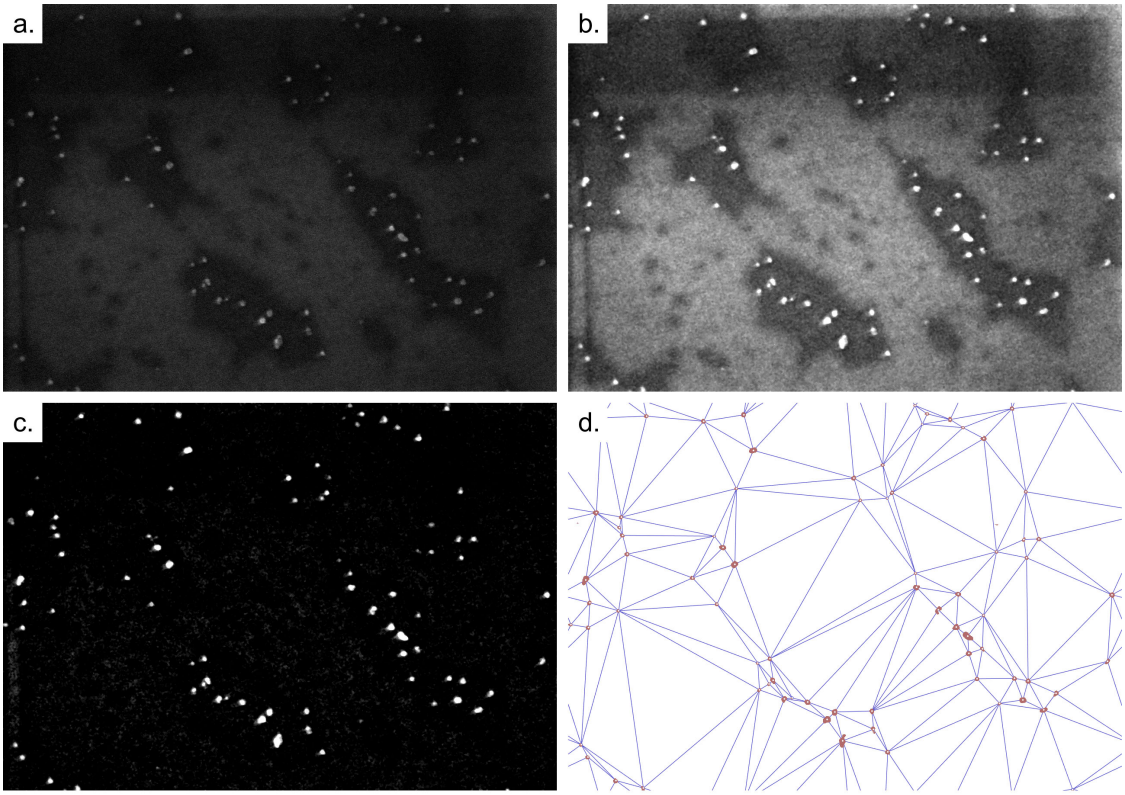

Sample 3, Image 3

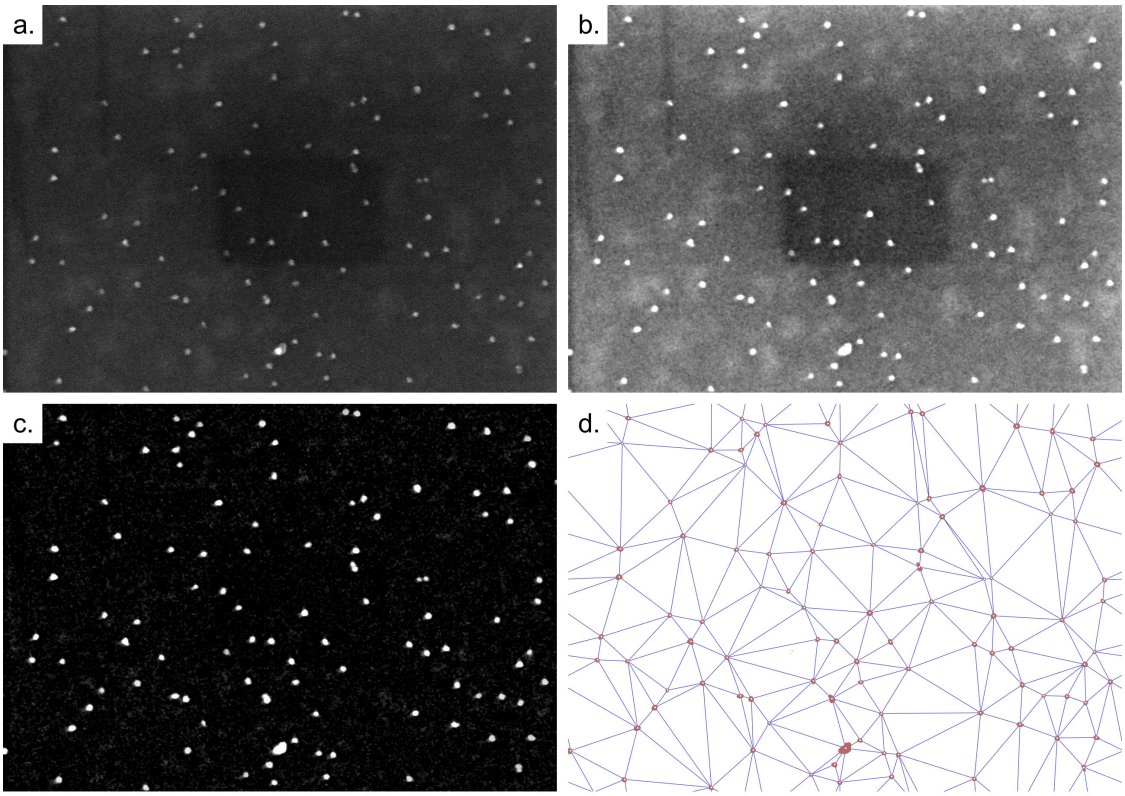

Sample 3, Image 4

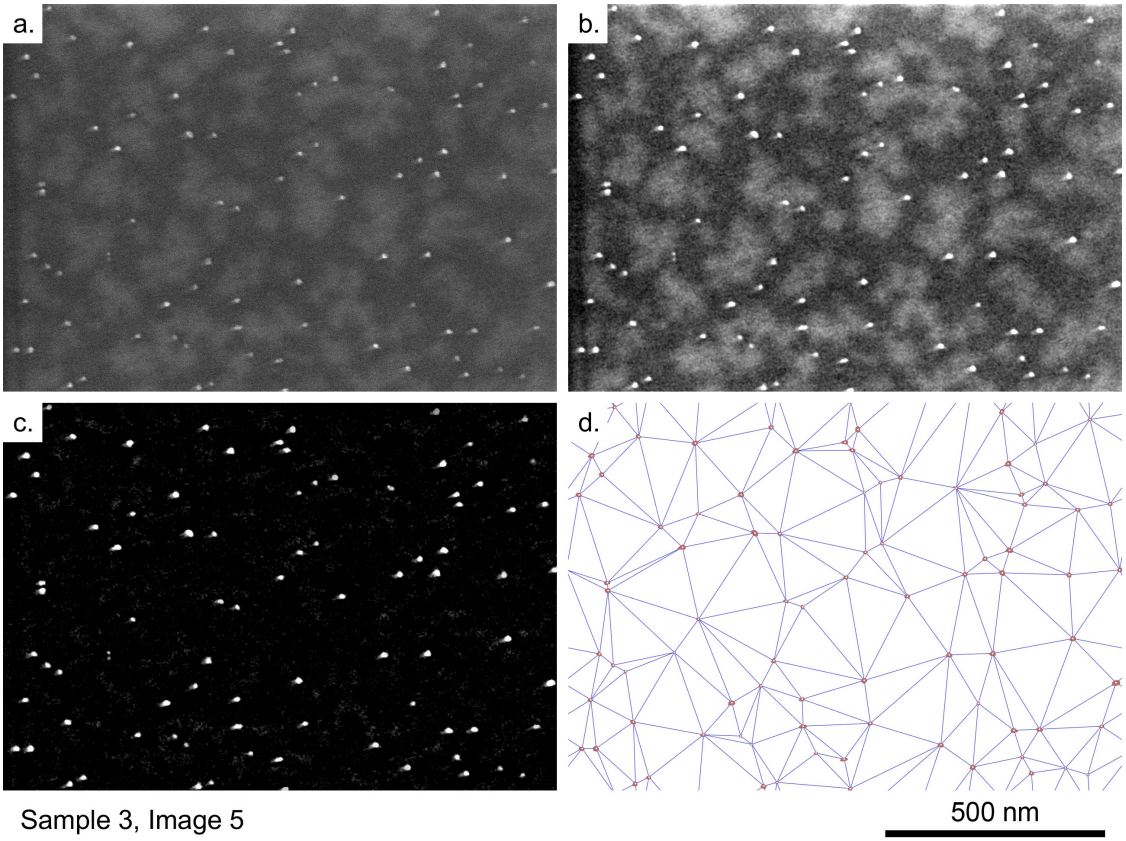
a.
b.
c.
d.
Sample 3, Image 5
500 nm

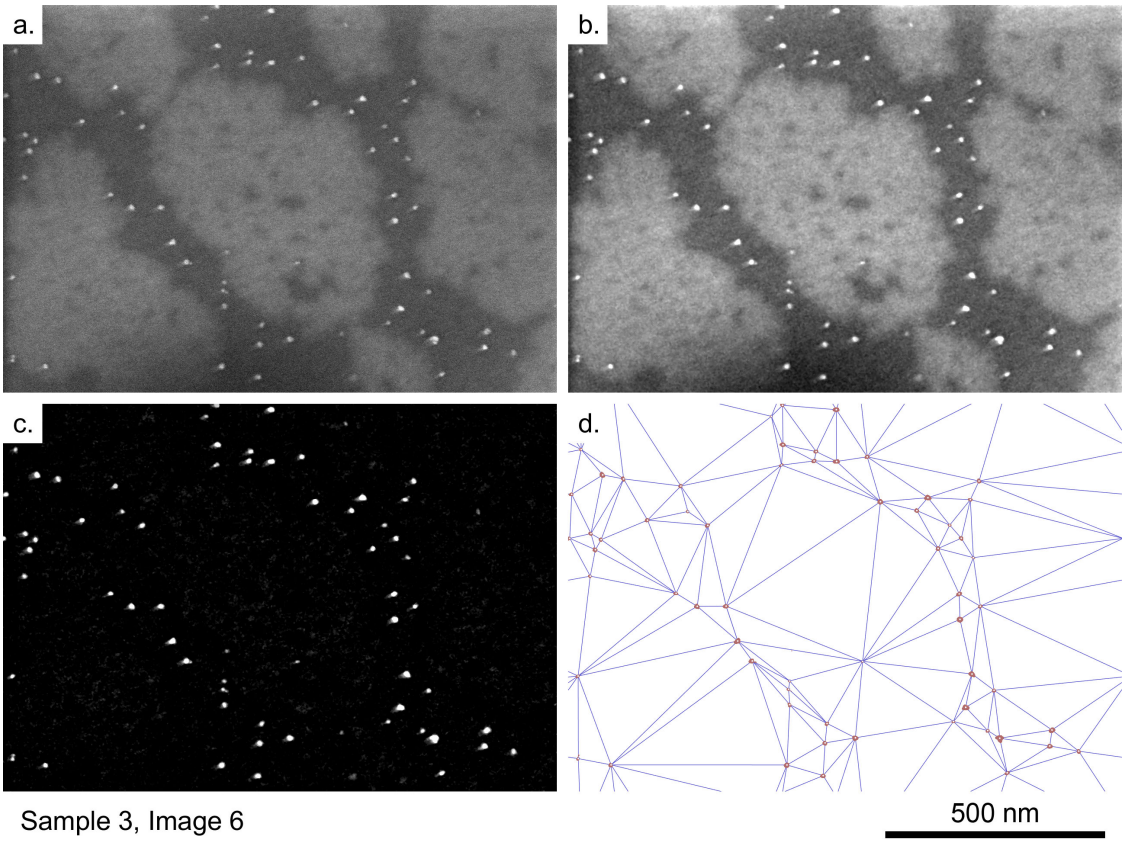
a.
b.
c.
d.
Sample 3, Image 6
500 nm

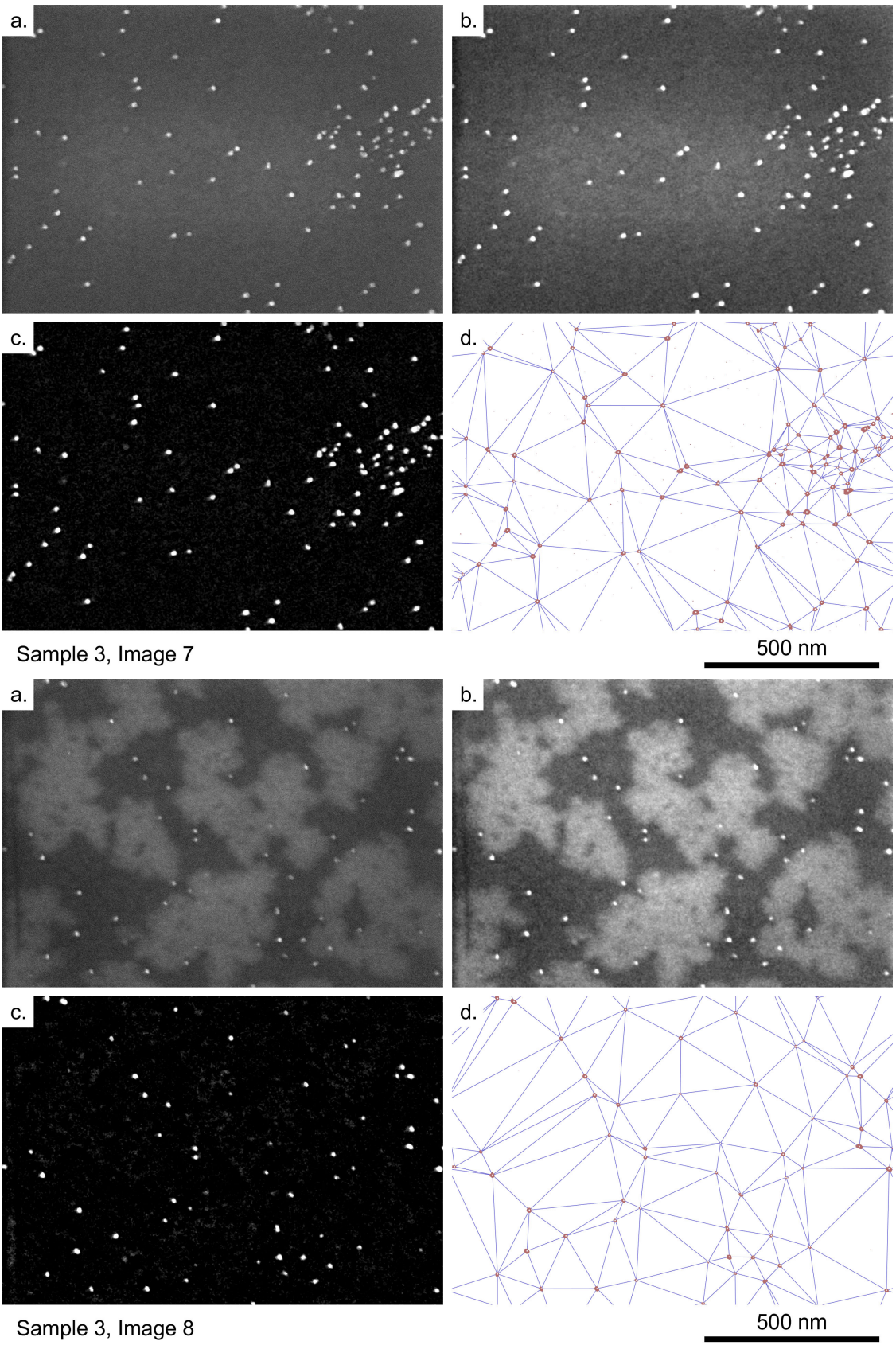

Figure B.9. Subsequent steps of image processing towards segmentation and triangulation of nanoparticles in SEM images of Sample 3; a) original image; b) linear normalisation of the image brightness and median filtering; c) local contrast enhancement; d) thresholding and Delaunay triangulation (red patches – NPs segmented, white dots – NP centroids, blue lines – triangulation result).

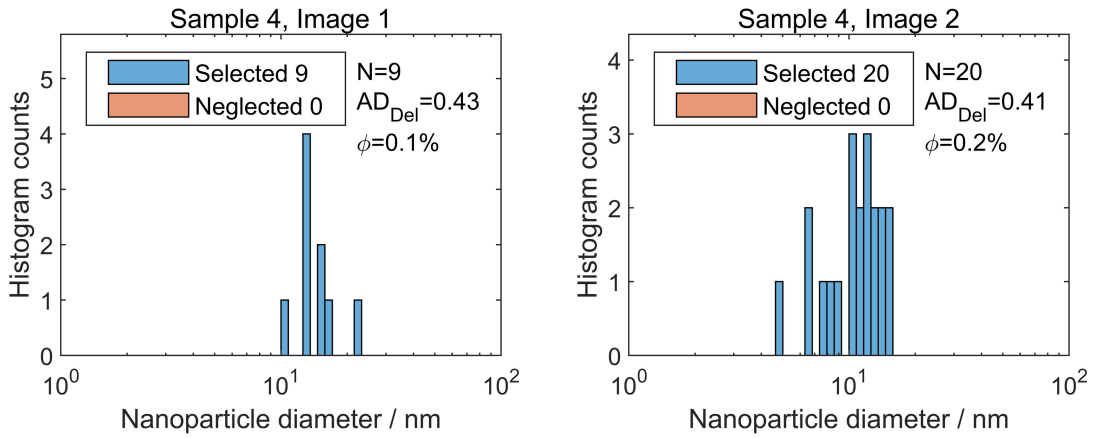

Figure B.10. Nanoparticle data extracted from SEM image analysis, Sample 4. For explanation of symbols, refer to the text in Appendix B.2.

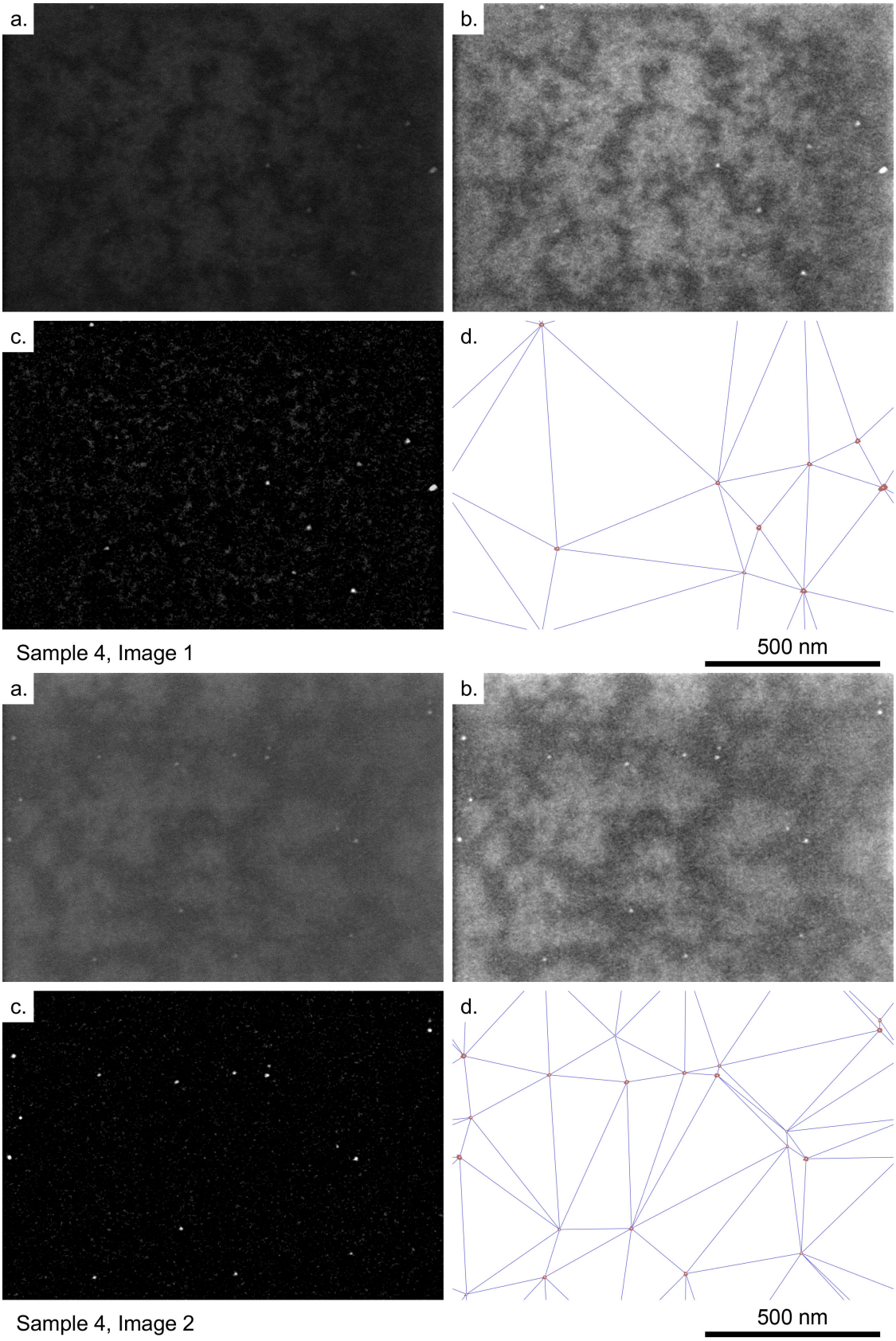

Figure B.11. Subsequent steps of image processing towards segmentation and triangulation of nanoparticles in SEM images of Sample 4; a) original image; b) linear normalisation of the image brightness and median filtering; c) local contrast enhancement; d) thresholding and Delaunay triangulation (red patches – NPs segmented, white dots – NP centroids, blue lines – triangulation result).

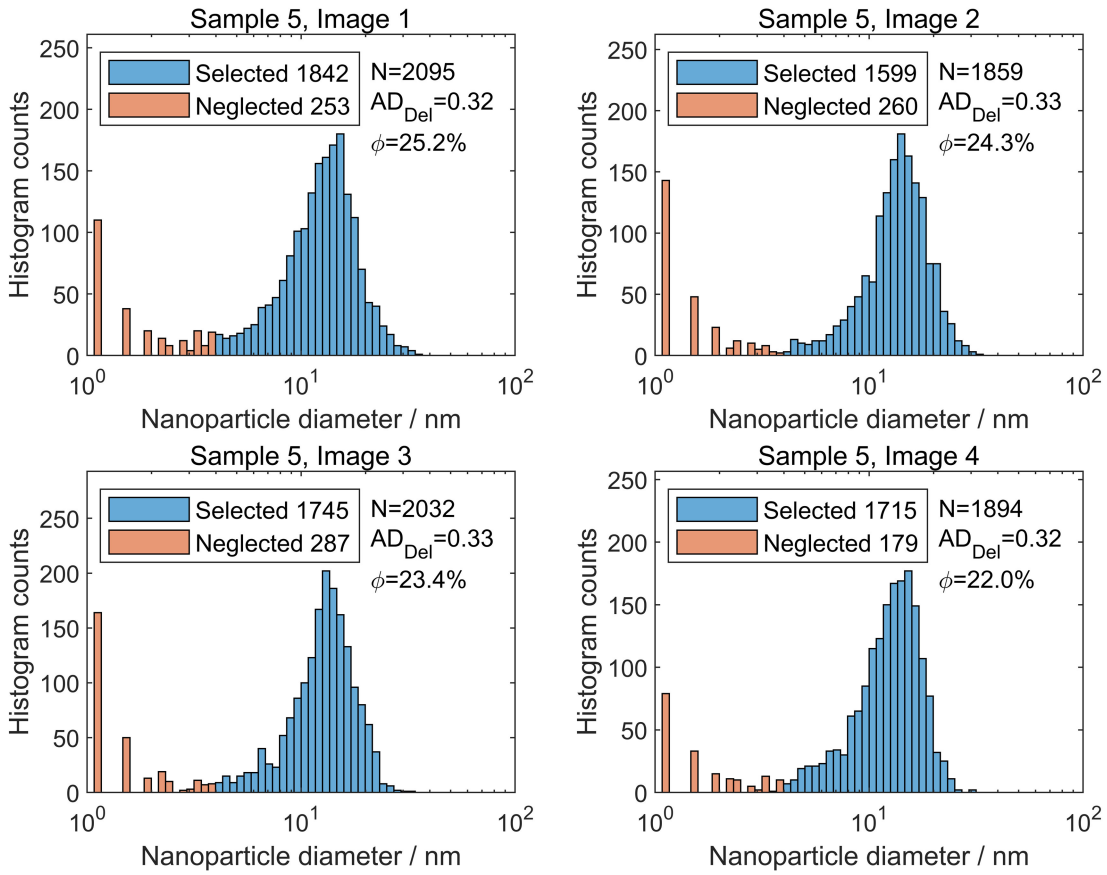

Figure B.12. Nanoparticle data extracted from SEM image analysis, Sample 5. For explanation of symbols, refer to the text in Appendix B.2.

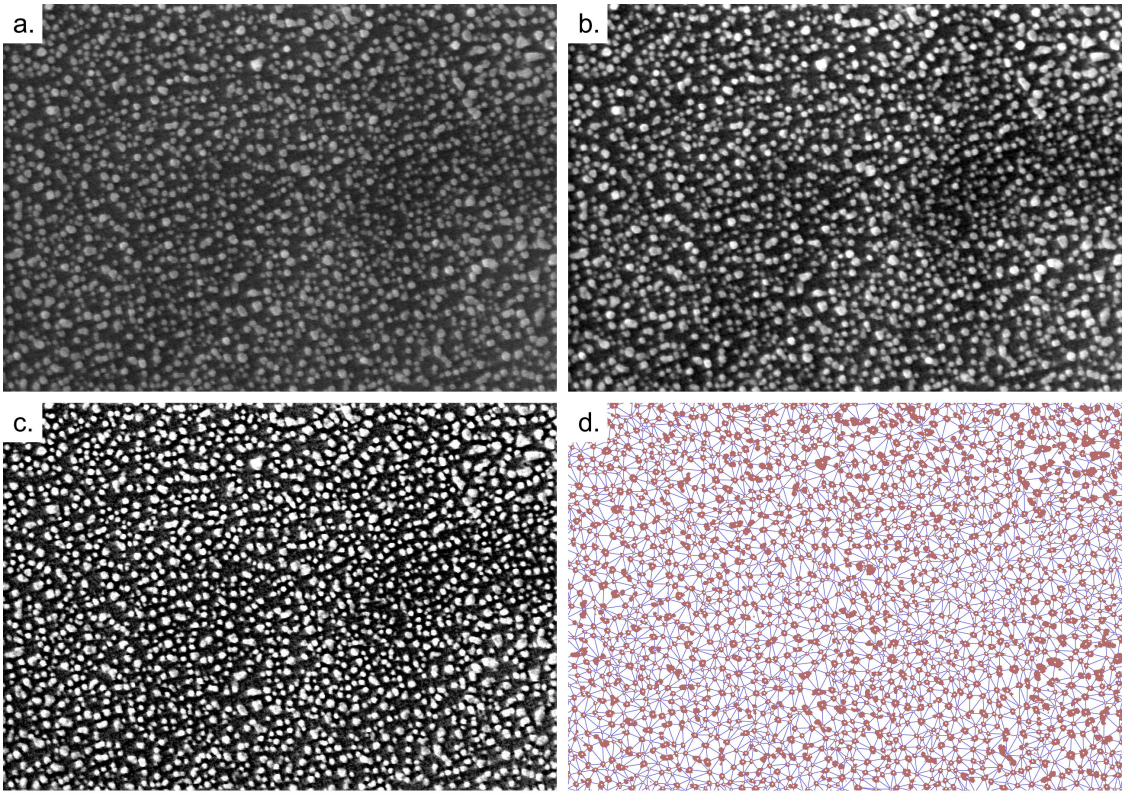
a.
b.
c.
d.
Sample 5, Image 1
500 nm

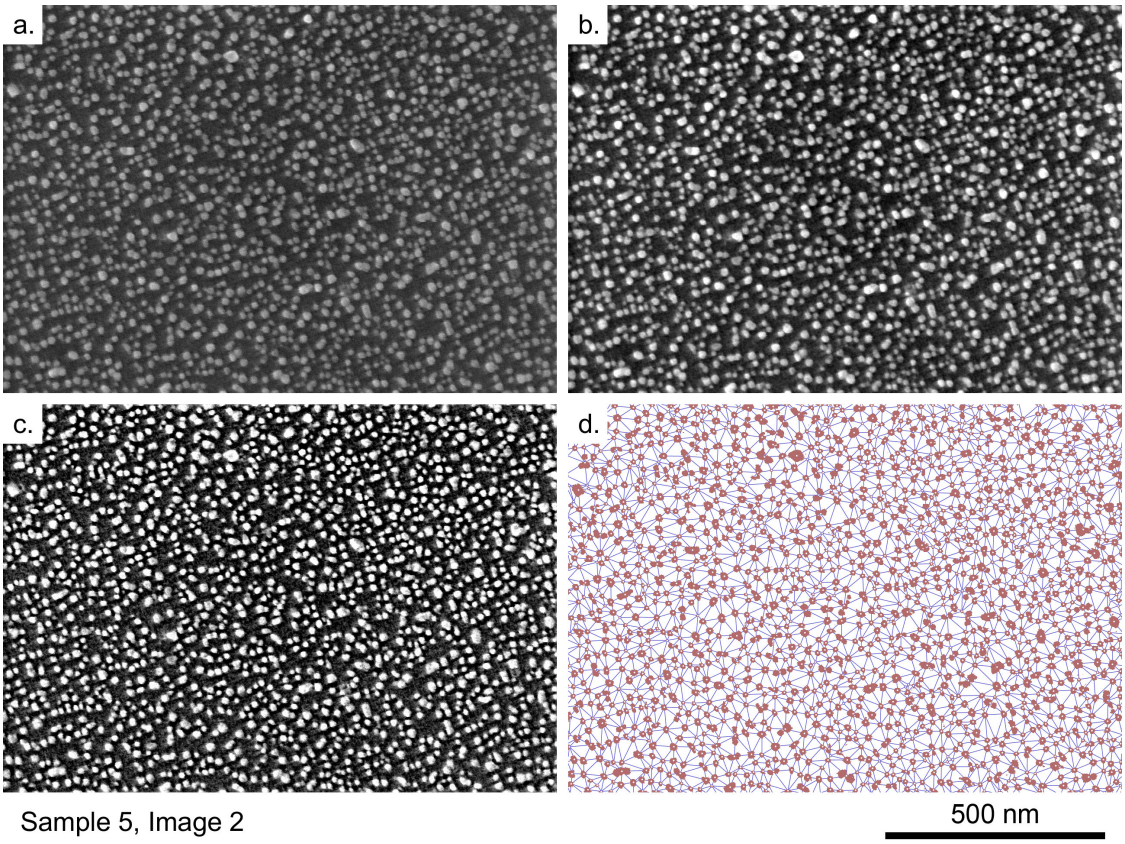
a.
b.
c.
d.
Sample 5, Image 2
500 nm

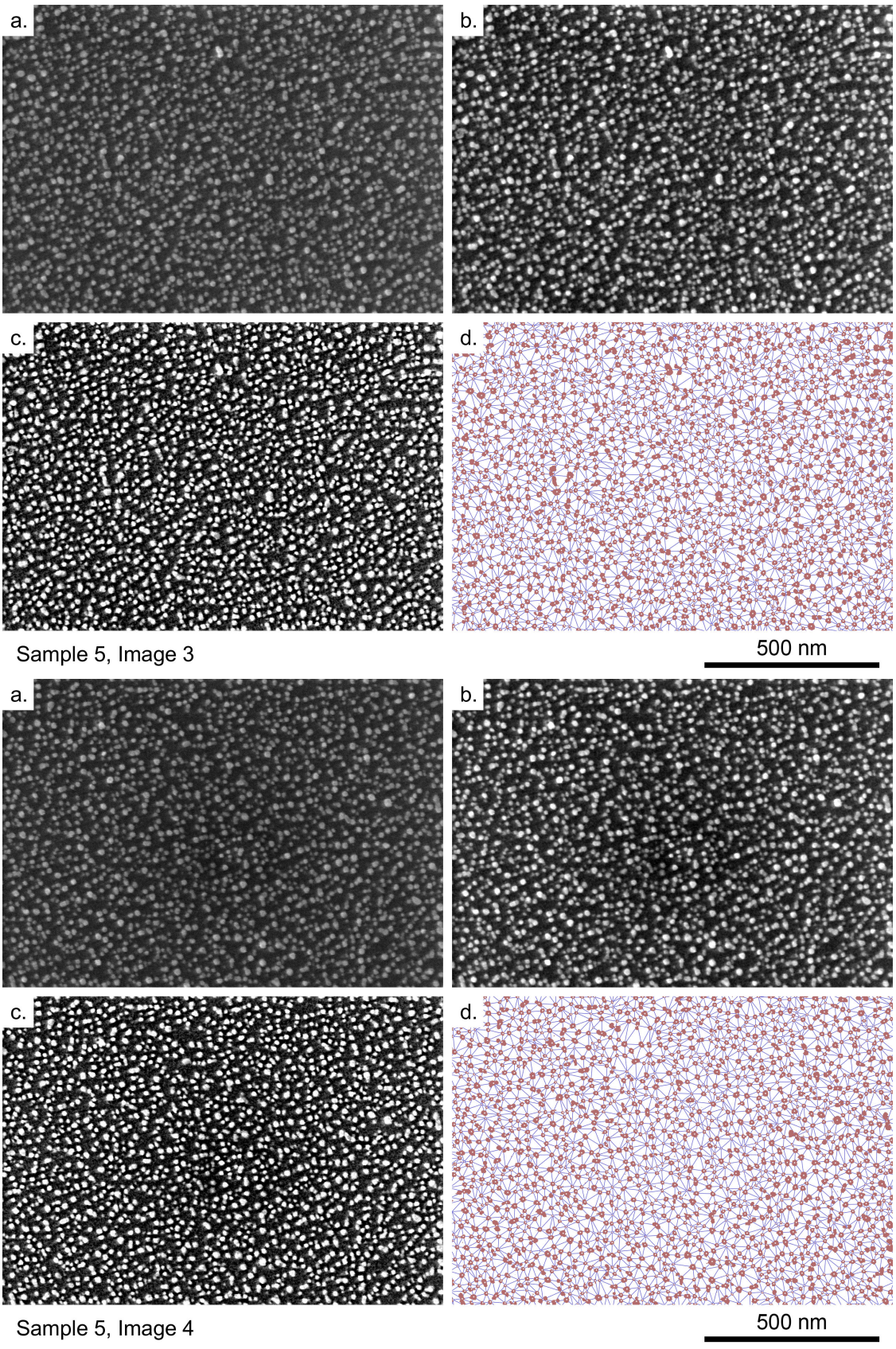

Figure B.13. Subsequent steps of image processing towards segmentation and triangulation of nanoparticles in SEM images of Sample 5; a) original image; b) linear normalisation of the image brightness and median filtering; c) local contrast enhancement; d) thresholding and Delaunay triangulation (red patches – NPs segmented, white dots – NP centroids, blue lines – triangulation result).

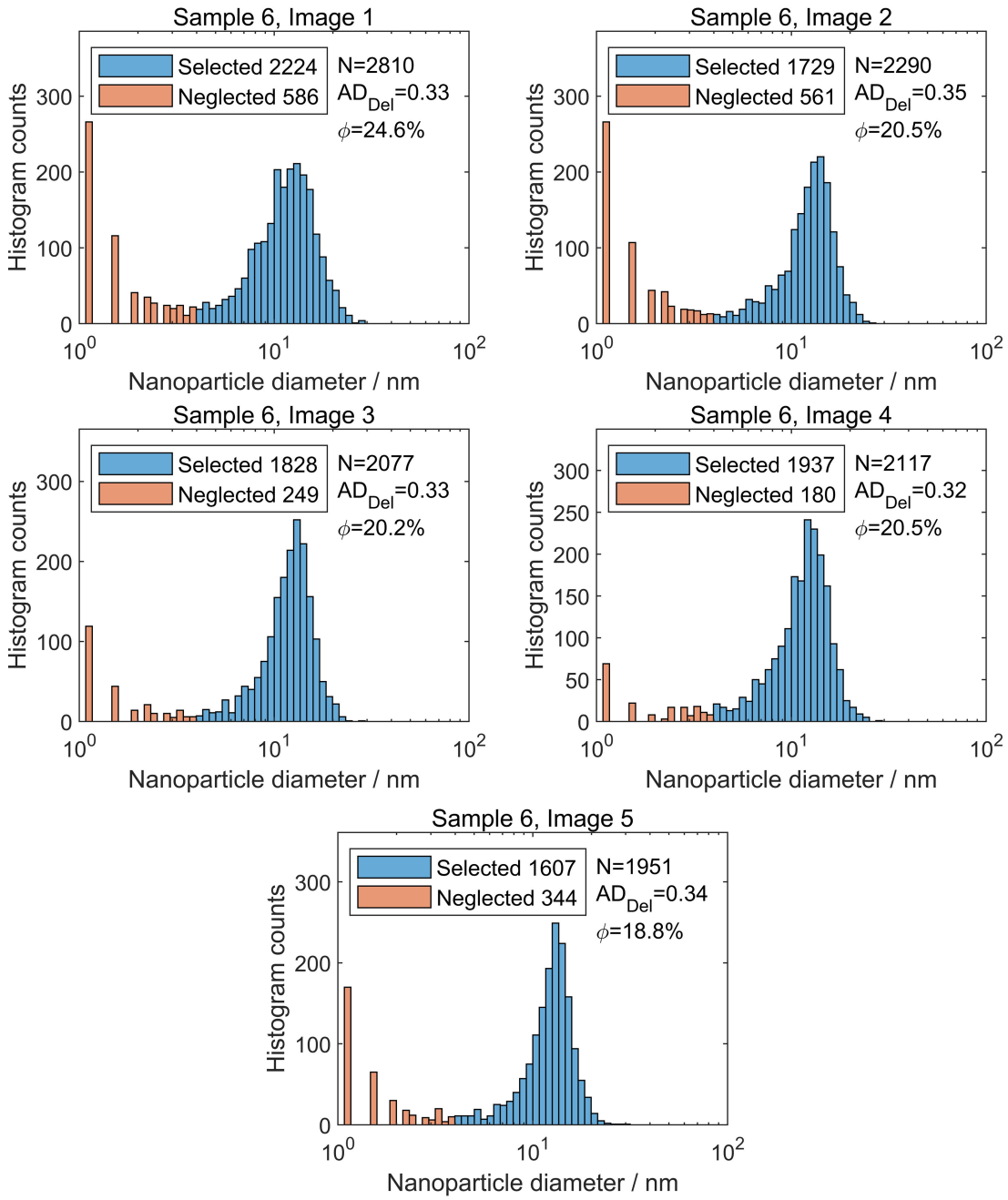

Figure B.14. Nanoparticle data extracted from SEM image analysis, Sample 6. For explanation of symbols, refer to the text in Appendix B.2.

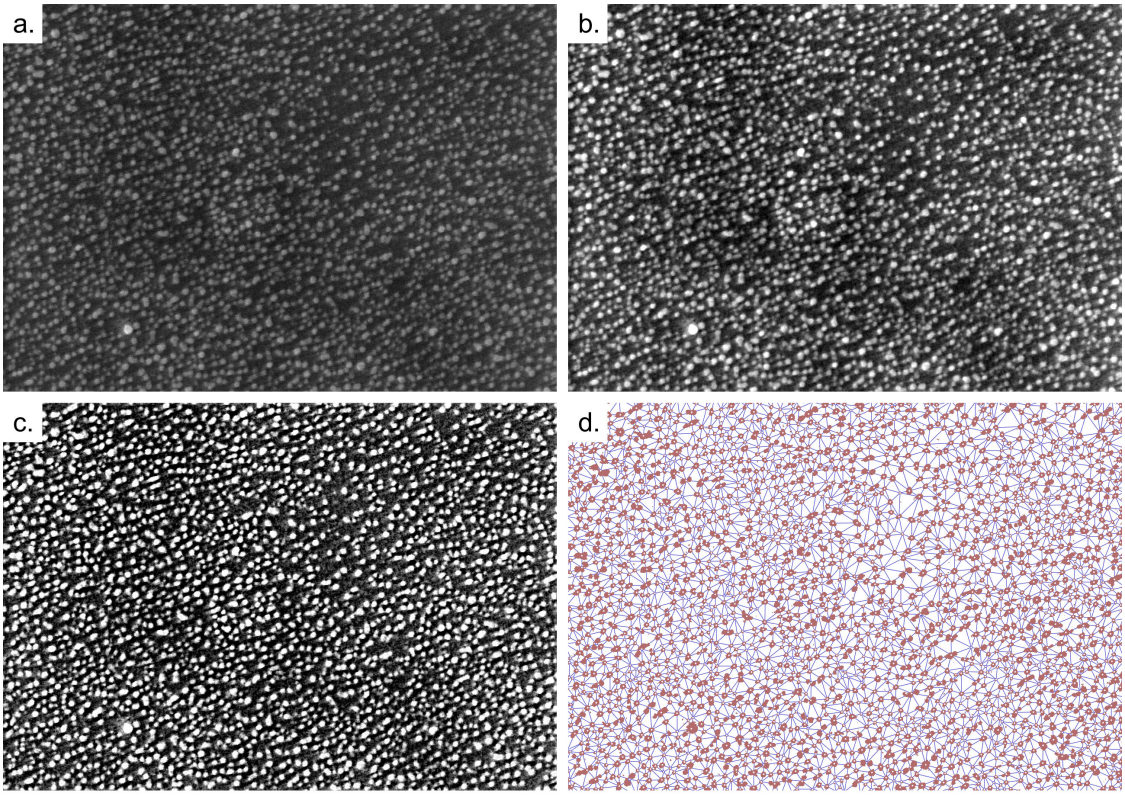
a.
b.
c.
d.
Sample 6, Image 1
500 nm

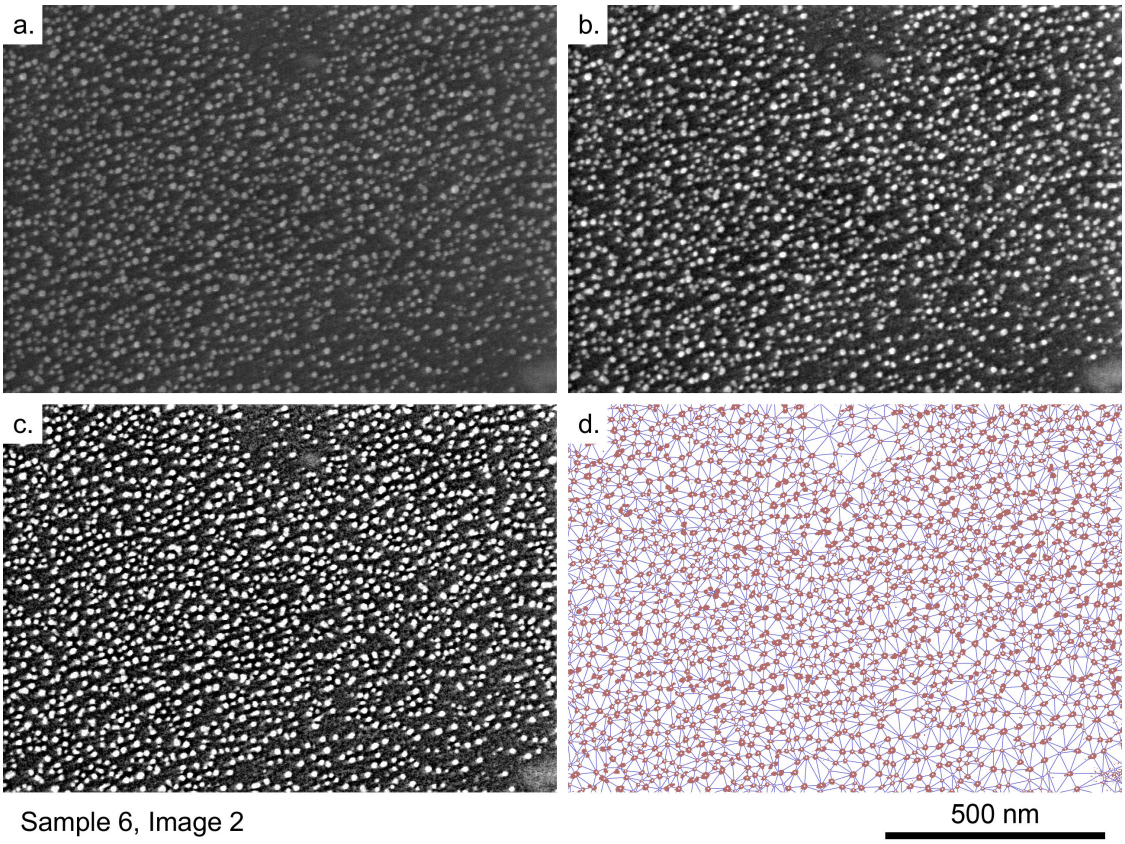
a.
b.
c.
d.
Sample 6, Image 2
500 nm

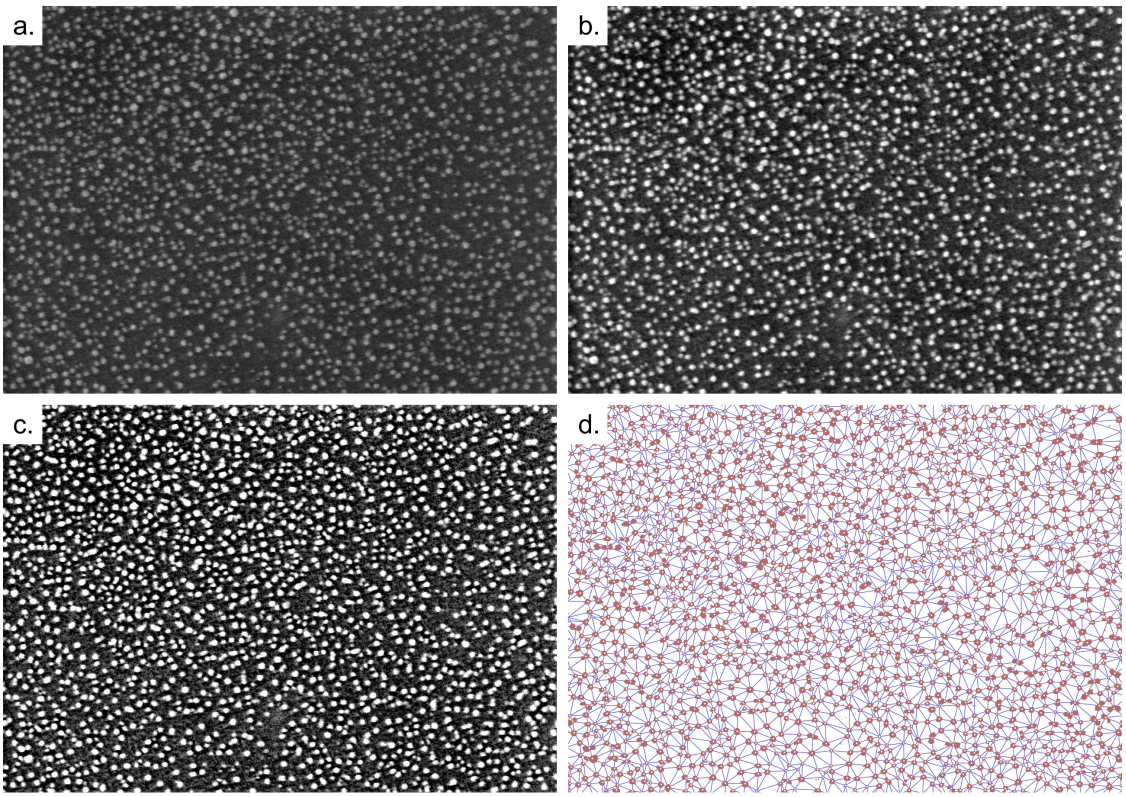
a.
b.
c.
d.
Sample 6, Image 3
500 nm

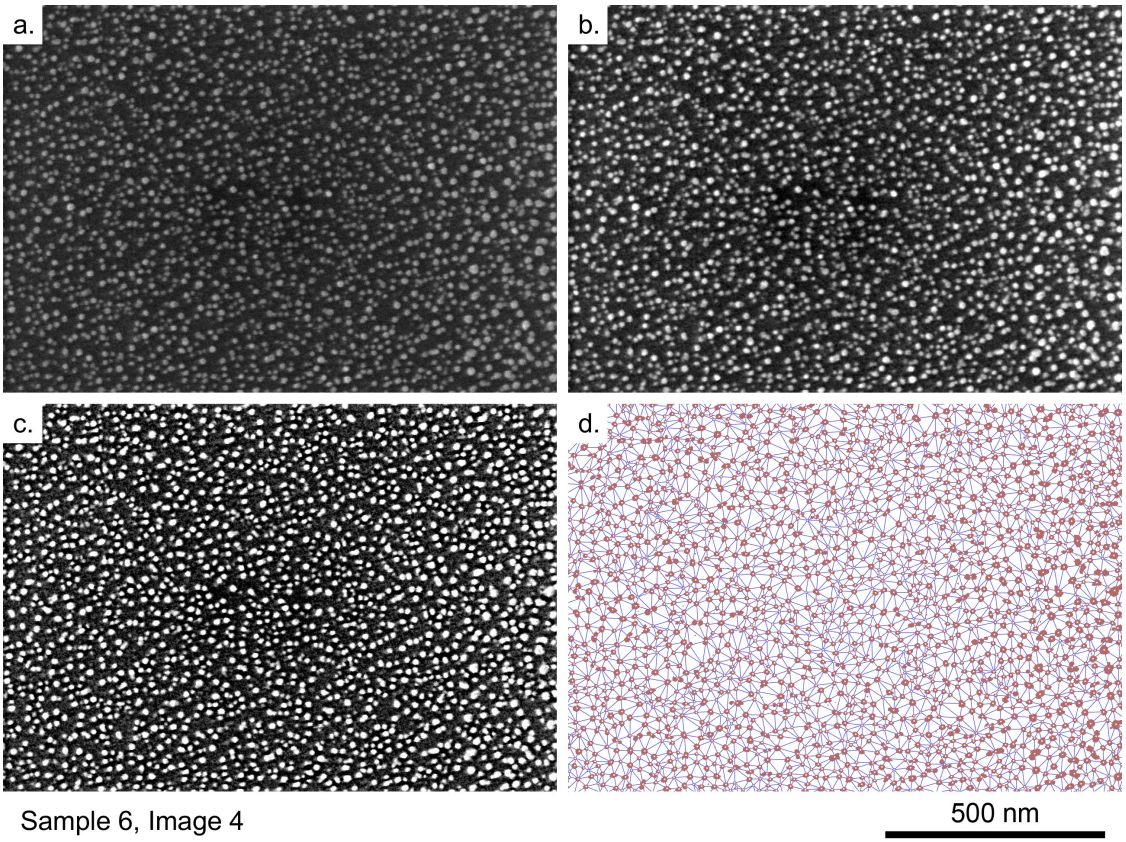
a.
b.
c.
d.
Sample 6, Image 4
500 nm

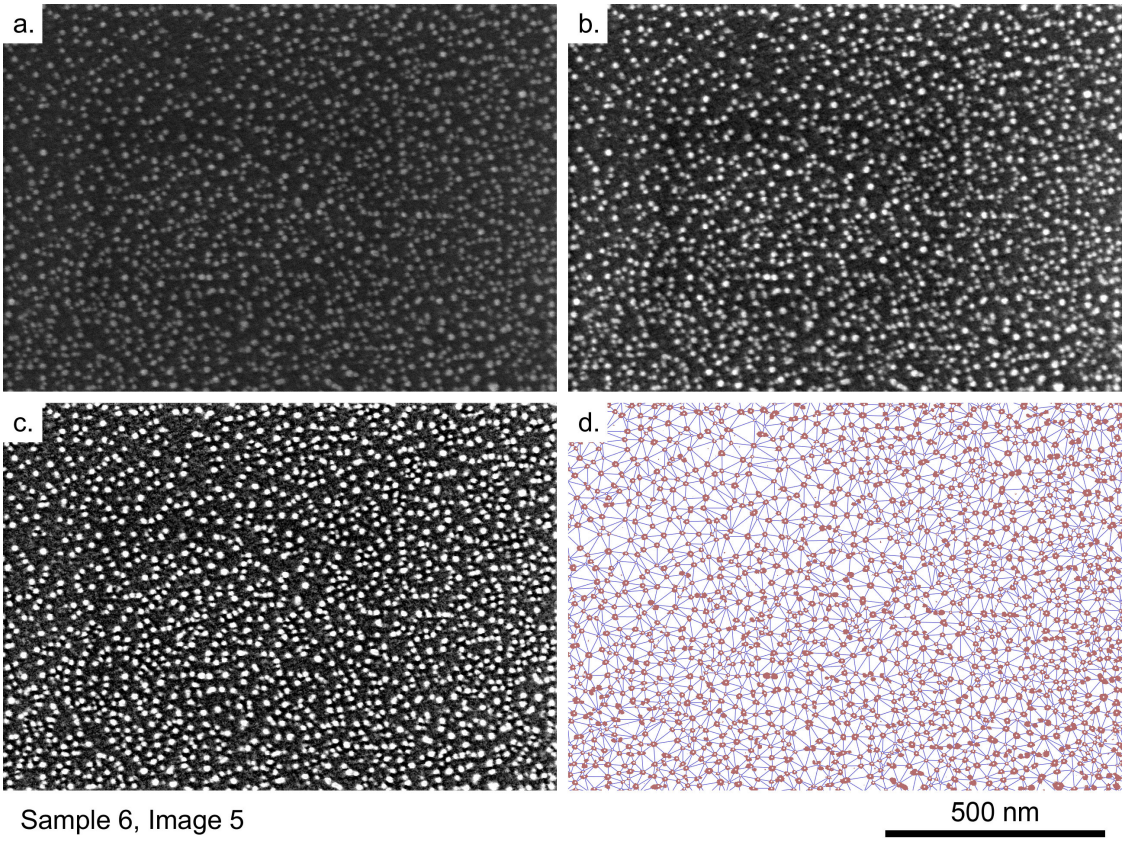

Figure B.15. Subsequent steps of image processing towards segmentation and triangulation of nanoparticles in SEM images of Sample 6; a) original image; b) linear normalisation of the image brightness and median filtering; c) local contrast enhancement; d) thresholding and Delaunay triangulation (red patches – NPs segmented, white dots – NP centroids, blue lines – triangulation result).

Appendix C

Supplementary information to Chapter 5

In this appendix we present additional derivations to the theory of gas diffusion in random fibrous media presented in Chapter 5.

C.1. Tortuosity factor of isotropically distributed cylinders

In section 5.4.1 we provided the expression for the tortuosity factor of isotropically-oriented cylinders τ=2. In this appendix, we are presenting the derivation that led to this value.

Consider a planar surface ΔS crossing the fibre carpet at the specific orientation, e.g. parallel to the substrate. The following derivation is based on establishing the number of fibres ΔN crossing the ΔS, which lets us find the expression for σ_0 in relation to σ, and consequently, the tortuosity factor, following the Eq. (5.14). The angle θ is measured with respect to the normal to ΔS. We are utilizing the rotational symmetry of the problem with respect to azimuthal rotation by the angle φ, which simplifies the calculations.

Consider the projection of the surface area ΔS onto the plane inclined at an angle θ, ΔS_θ (see: Figure C.1),

$$\Delta S_\theta = \Delta S \cos\theta. \tag{C.1}$$

The number of fibres that are approximately perpendicular to the ΔS_θ comprise of a fraction of all fibres corresponding to the $\mathrm{pdf}_\theta(\theta)$ (Eq. 5.21), namely

$$\mathrm{d}N(\theta)\mathrm{d}\theta = \sigma \Delta S_\theta \mathrm{pdf}_\theta(\theta)\mathrm{d}\theta = \sigma \Delta S \sin\theta \cos\theta \, \mathrm{d}\theta. \tag{C.2}$$

Upon integration over the domain of θ, we obtain

$$\sigma_0 = \frac{\Delta N}{\Delta S} = \sigma \int_0^{\pi/2} \sin\theta \cos\theta \, \mathrm{d}\theta = \frac{\sigma}{2}, \tag{C.3}$$

where the ΔN is the $\mathrm{d}N(\theta)\mathrm{d}\theta$ integrated over $\theta \in \left[0, \frac{\pi}{2}\right]$. Hence, the tortuosity factor indeed equals

$$\tau = \frac{\sigma}{\sigma_0} = 2. \tag{C.4}$$

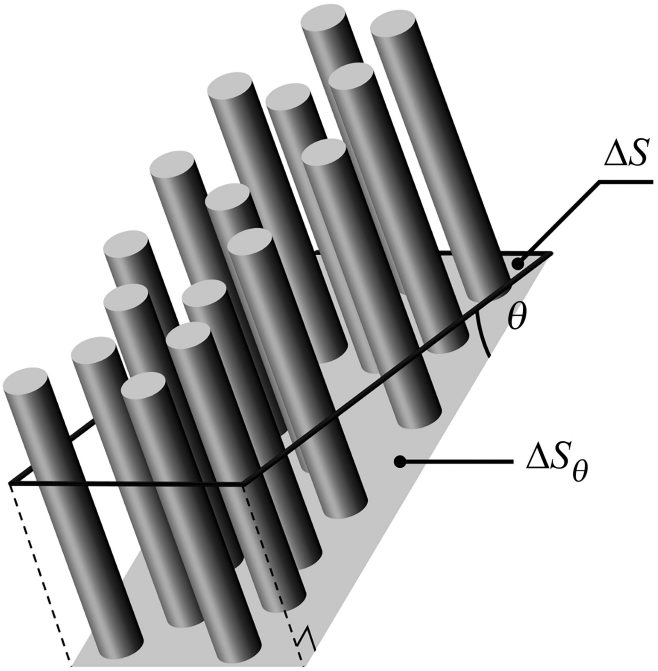

Figure C.1. Illustration of the geometry for the derivation of the tortuosity factor of the randomly oriented fibre carpets. For explanation of symbols, we refer to the main text. Porosity and surface area to volume ratio within intersecting fibre mats

C.2. Porosity and surface area of random fibre arrays

In the main part of the work we have presented the equations for α and ε (5.18,1919) for the case, when the fibres are allowed to intersect. The equations can be used in cases when $\sigma\pi d^2/4 \ll 1$, which means that the average fibre diameter is much smaller than the average spacing between the fibres (effectively: intersections can be neglected), or when films are grown on the fibres, and the film thicknesses are of the same order of magnitude as the fibre diameters or greater, e.g. as grown by means of ALD, CVD or CVI.

It is convenient to begin these derivations from the porosity ε. Consider the structure of fibres of average diameter d and axes length per volume σ. In the given volume ΔV there is a total length $\Delta l=\sigma\Delta V$, as per definition (5.14). The following derivation is constructed as a sequential addition of small fibre lengths $\mathrm{d}l$ into the structure, while examining the contribution to the void volume fraction (porosity) ε of each subsequent addition. The $l \in [0, \Delta l]$ is the independent variable.

If there were no intersections, a single fibre fragment $\mathrm{d}l$ would contribute $\mathrm{d}l{\cdot}\pi d^2/4$ to the total fibre volume. However, only the fraction of this contribution crosses the empty space, and this fraction is determined by the current porosity $\varepsilon(l)$. We write

$$\mathrm{d}\varepsilon = -\mathrm{d}l \cdot \frac{\pi d^2}{4\Delta V}\varepsilon(l) = -\mathrm{d}\sigma\frac{\pi d^2}{4}\varepsilon(\sigma), \tag{C.5}$$

where $\mathrm{d}\sigma \coloneqq \mathrm{d}l/\Delta V$ was defined for convenience. The integration of the above equation should be performed for σ from 0 up to its desired value, therefore the collision of symbols between the independent variable and the upper integration limit is not an issue. Given the initial condition

$$\varepsilon(\sigma = 0) = 1, \tag{C.6}$$

the solution of equation (C.5) is

$$\varepsilon = \exp\left(-\sigma\frac{\pi d^2}{4}\right), \tag{C.7}$$

as introduced in section 5.4.1. We treat the derivation of the α analogously. If there were no fibre intersections, each fibre element $\mathrm{d}l$ would contribute $\mathrm{d}l{\cdot}\pi d$ to the surface area, however only a fraction of the added fibre surface crosses the void and this fraction is determined by the already established ε. We write

$$\mathrm{d}A_1 \coloneqq \mathrm{d}l\pi d\varepsilon = \mathrm{d}\sigma\Delta V\pi d\exp\left(-\sigma\frac{\pi d^2}{4}\right), \tag{C.8}$$

Where $\mathrm{d}A_1$ is the first contribution of the fibre element to the surface area. There is however also a second - negative - contribution. As the fibre element crosses the existing structure, the already present surface area that is crossed by the fibre is excluded. The fraction of the excluded area is equal to the volume fraction occupied by the fibre element $\mathrm{d}l$. We write

$$\mathrm{d}A_2 \coloneqq -\frac{\mathrm{d}l\frac{\pi d^2}{4}}{\Delta V}A = -\mathrm{d}\sigma\frac{\pi d^2}{4}A, \tag{C.9}$$

where A is the current surface area. Setting $\mathrm{d}A = \mathrm{d}A_1 + \mathrm{d}A_2$, we obtain

$$\mathrm{d}A = \mathrm{d}\sigma\Delta V\pi d\exp\left(-\sigma\frac{\pi d^2}{4}\right) - \mathrm{d}\sigma\frac{\pi d^2}{4}A. \tag{C.10}$$

Dividing both sides of the equation by ΔV and rearranging terms, we transform equation (C.10) to

$$\frac{\mathrm{d}\alpha}{\mathrm{d}\sigma} = \pi d\exp\left(-\sigma\frac{\pi d^2}{4}\right) - \frac{\pi d^2}{4}\alpha. \tag{C.11}$$

Given the initial condition

$$\alpha(\sigma = 0) = 0, \tag{C.12}$$

we obtain the solution of (C.11),

$$\alpha = \pi\sigma d \exp\left(-\sigma\frac{\pi d^2}{4}\right), \tag{C.13}$$

as introduced in section 5.4.1. The above derivation is easily generalised to different shapes of randomly added intersecting objects, such as spherical particles, cubes and other irregular shapes, it is however beyond the scope of this work.

C.3. Physical meaning of the Knudsen tortuosity

In section 5.4.5 we derived the Knudsen diffusivity in arrays of random fibrous media. The expression for the Knudsen tortuosity (5.33) emerged and its physical meaning was outlined. In this appendix we elaborate on it. Let us consider a fibrous membrane of surface area ΔS, thickness l and surface area to volume ratio α. The dimensionless surface area enhancement of the membrane can be calculated as

$$\frac{\Delta A}{\Delta S} = \frac{\alpha \Delta V}{\Delta S} = \frac{\alpha \Delta S l}{\Delta S} = \alpha l. \tag{C.14}$$

Hence, α can be understood as a surface area enhancement per unit thickness. Consequently, given equation (5.33), it becomes clear that τ_K has a meaning of the surface area enhancement of the membrane of characteristic thickness equal to $2\lambda_b/\pi^2$.

C.4. Impingement rate onto a macroscopic object within a fibre carpet

As stated in section 5.4.7, we must differentiate between the macroscopic impingement rate Γ_c and the impingement rate in molecular regime Γ. Specifically, in this appendix we are showing that the impingement rate within the fibre carpet onto a macroscopic object, such as substrate, is in agreement with the classical gas kinetics. The following derivation is in principle no different than the derivation of the classical bulk gas impingement rate, however we find it necessary to substantiate that the presence of fibres does not change the impingement rate onto macroscopic object. It is of note, that for the simplicity and clarity of the calculations, we treated the molecule movement as if they were always at an average absolute velocity instead of invoking the Maxwell-Boltzmann distribution. It leads however to the same result, while in the following considerations the mean absolute velocity is the determining factor of the kinetics description and the specific profile of the velocity distribution is not relevant.

Consider a very thin slice of the structure adjacent to the macroscopic object surface, illustrated schematically in Figure C.2.

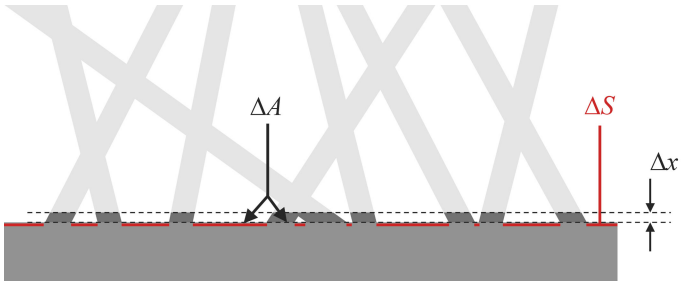

Figure C.2. Illustration supporting the derivation of macroscopic impingement rate.

The slice is so thin, that the molecules present within this slice inevitably either hit the underlying surface or drift away from it; the collision with fibre wall is negligibly likely.

Following the definition (5.35), we need to establish ΔN, Δt and ΔS in order to obtain Γ_c. The ΔN is

$$\Delta N = \frac{n}{2}\Delta V \varepsilon = \frac{n}{2}\Delta A \Delta x \varepsilon. \tag{C.15}$$

The division by 2 is present, because due to the isotropy of the gas flight directions, the movement of only half of all molecules nearby the plane ΔA is directed at the plane, whereas the other half is drifting away from it. The Δx is the thickness of the slice described above. Multiplication by ε reflects the volume fraction available to the gas molecules.

The surface area of the object available to be reached by the gas molecules is

$$\Delta S = \Delta A \varepsilon, \tag{C.16}$$

where ΔA is the element of the surface area of the object, including the parts obscured by the fibres. Taking only the gas molecules moving towards the object plane (v_x>0), their average drift velocity towards the object is

$$\langle v_x \rangle = \int_0^{\pi/2} v \cos\theta \, \mathrm{pdf}_\theta(\theta) d\theta = v \int_0^{\pi/2} \sin\theta \cos\theta \, d\theta = \frac{v}{2}, \tag{C.17}$$

which was calculated using the isotropic distribution of the angle θ, (5.21). For all the ΔN molecules within the slice Δx to hit the surface, it will take Δt time,

$$\Delta t = \frac{\Delta x}{\langle v_x \rangle} = \frac{2\Delta x}{v}. \tag{C.18}$$

Consequently, according to the definition (5.35), the Γ_c is

$$\Gamma_c = \frac{\Delta N}{\Delta S \Delta t} = \frac{\frac{n}{2}\Delta A \Delta x \varepsilon.}{\Delta A \varepsilon \frac{2\Delta x}{v}} = \frac{nv}{4}, \tag{C.19}$$

which does remain in agreement with the classical gas kinetics. Exactly the same expression for Γ_c holds at the bulk-to-fibres interface, which ensures that the gas concentration within the void of the fibrous structure is in equilibrium with the bulk gas.

C.5. Uniform distribution of distance of fibre axes from the flight path

In order to design the MC simulation in an optimal way, it is important to narrow the considered representative volume down to the necessary minimum while avoiding artefacts from boundary effects. In the considered case, the necessary minimum is the molecule path cylinder in which the collisions can occur, as discussed is section 5.4.4. To accurately simulate the isotropically random orientations and uniformly random positions of fibres in the narrow molecule path cylinder, we have identified two solutions:

a) generating the cylinders in a volume much greater than the volume of interest representing a big part of the porous structure and considering only the fibres that do cross the molecule flight path,
b) generating the cylinders directly in the molecule path cylinder with carefully chosen probability distribution of positions and orientations.

The option b) is much less computationally intensive than a). In order to implement the approach b), we validated the probability distribution of the fibre axis distance from the molecule flight path (5.24) with the approach a). For this purpose, we considered a molecule path cylinder of 70 nm in diameter and of 1 μm length and we generated straight lines corresponding to fibre axes within the cylinder of 10× larger diameter (700 nm) and of 20× larger length (20 μm), oriented co-axially with the molecule path cylinder. Each line was generated with an origin point uniformly distributed within the large cylinder volume and the orientation vector, following the isotropic distribution (5.20-21). The sequential line generation was continued until we obtained 10^7 axes crossing the small molecule path cylinder. Once the generation was complete, we evaluated the histogram of distances of the lines to the axis of the molecule path cylinder and normalised the histogram so that the histogram bar heights correspond to a probability density. Figure C.3 presents the result and a comparison to the distribution (5.24).

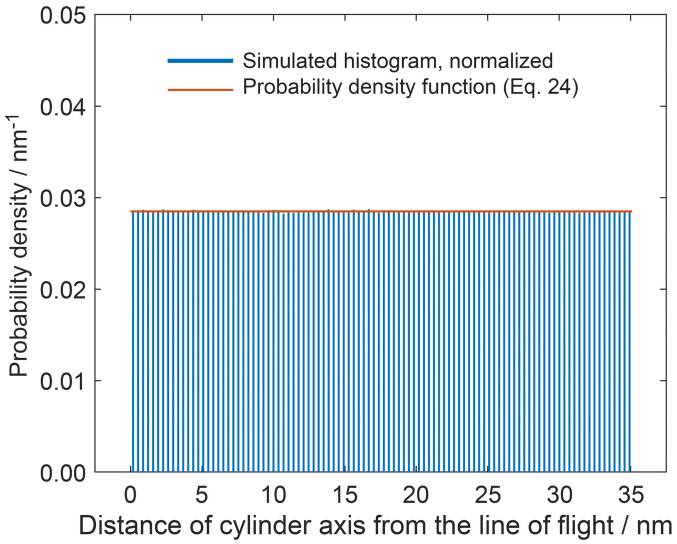

Figure C.3 Normalised histogram of the simulated distances of fibres from the molecule flight path compared to the uniform probability distribution (5.24).

As we can see in Figure C.3, the distance distribution indeed corresponds to the uniform probability distribution (5.24), which allows for the optimisation of the MC simulation algorithm.

C.6. Numerical evaluation of the molecule flight path

We define a 1D grid of 0.5 nm pitch along the flight path coincident with the axis z. Each element of the grid is assigned its distance to the closest fibre axis - distances to all lines are evaluated and a minimum value is chosen. We obtain dist_i, where i is a natural number indexing the discrete points of the grid and dist_i is the distance value for the given z_i. The z_r is identified as the first z, for which the distance crosses the value of $d/2$ and is increasing with z at this point, whereas the z_c is found as the first z greater than z_r, for which the distance crosses the value $d/2$ but is decreasing. A linear interpolation of the dist_i with respect to real values of z is implemented for an increase in accuracy, as exemplified in Figure C.4. The mean value of all collected values of Δz for given d and σ is the evaluated mean flight path λ_f.

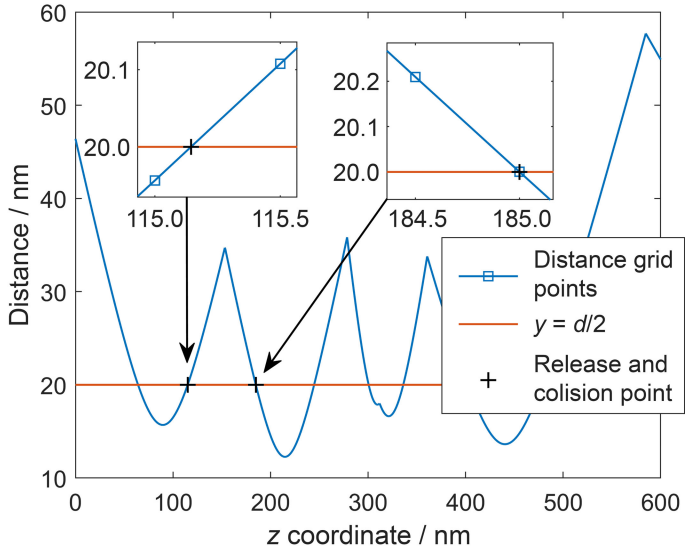

Figure C.4. Example evaluation of the release and collision point based on the linear interpolation of the grid of distance to the nearest fibre axis. For clarity, the square markers of distance grid points are shown only in the insets.

Appendix D

Supplementary information to Chapter 6

In this appendix we present additional derivations to the modelling of atomic layer deposition on porous substrates introduced in Chapter 6.

D.1. Diffusion-limited scaling law of coating depth

The condition for the diffusion-limited regime (6.29) is equivalent to setting the reaction zone width as negligible compared to the depth into the structure. We can see that clearly comparing Figure 6.3a and b – for the solution presented in Figure 6.3b, the total depth of the system l was set to be 10 times higher as for Figure 6.3a, rendering the reaction zone width comparatively smaller. From this, we can conclude, that for the diffusion-limited regime, the coverage profile approaches a step-function, and the gas concentration profile can be described with two linear sections. This lets us solve the system in a quasi-static manner, where the reaction zone is considered as a moving boundary with a boundary condition for concentration $n = 0$, and at every moment in time, the system is at an instantaneous equilibrium, i.e. the concentration gradient is constant in the zone I. The gradient can be expressed in this 1-dimentional case as a derivative

$$\frac{\mathrm{d}n}{\mathrm{d}z} = -\frac{n_\mathrm{R}}{z_\mathrm{c}}, \tag{D.1}$$

where z_c is the position of the reaction zone, i.e. coating depth and n_R is the gas concentration in the reactor, directly above the nanostructure. Of note is that in equation (D.1) the derivative is regular instead of partial, due to the quasi-static treatment of the problem. The concentration gradient is a driving force for the diffusion. The diffusion flux J_D is expressed as

$$J_\mathrm{D} = -D\frac{\mathrm{d}n}{\mathrm{d}z} = D\frac{n_\mathrm{R}}{z_\mathrm{c}}, \tag{D.2}$$

The flux delivers precursor particles to chemisorb in the zone II (at the moving boundary), by definition

$$J_\mathrm{D} = \frac{1}{S_\mathrm{v}}\frac{\mathrm{d}N}{\mathrm{d}t}, \tag{D.3}$$

where S_v is the surface area of a cross-section of void unoccupied by the solid elements of the nanostructure, whereas the $\mathrm{d}N/\mathrm{d}t$ is the number of precursor molecules delivered by the flux J_D in a unit of time. In order to advance the reaction zone position by $\mathrm{d}z_\mathrm{c}$, $\mathrm{d}N$ molecules need to be delivered,

$$\mathrm{d}N = \frac{\alpha S}{s_0}\mathrm{d}x_\mathrm{c}, \tag{D.4}$$

where α is the surface-area-to-volume ratio of the nanostructure, S - the surface area of the cross-section considered, s_0 – an average surface area of a chemisorption site. Combining equations (D.2-4) together, one obtains

$$\frac{DS_\mathrm{v}s_0}{\alpha S}n_\mathrm{R}(t)\mathrm{d}t = z_\mathrm{c}\mathrm{d}z_\mathrm{c}. \tag{D.5}$$

The $n_\mathrm{R} = n_\mathrm{R}(t)$ is set, while in principle it is a function of time. By definition, S_v/S equals porosity ε. The impingement rate J_wall is related to the n_R with equation (6.3), hence

$$\frac{\varepsilon}{\alpha} D s_0 \tau_f \bar{s} J_{\text{wall}}(t) \mathrm{d}t = z_c \mathrm{d}z_c. \tag{D.6}$$

By substituting equations (6.11), (6.12) and (6.35), we obtain

$$\frac{1}{2} \lambda_c^2 \beta_0 s_0 \cdot J_{\text{wall}}(t) \mathrm{d}t = z_c \mathrm{d}z_c, \tag{D.7}$$

which integrated and transformed gives the scaling law, that directly relates the coating depth z_c to the gas exposure Φ_{wall},

$$z_c(\Phi_{\text{wall}}) = \lambda_c \sqrt{\beta_0 s_0 \Phi_{\text{wall}}}. \tag{D.8}$$

D.2. Numerical extraction of coating depth and reaction zone width from simulation data

As mentioned in paragraph 6.1.4, in the diffusion-limited regime, the blurred coating profile can be expressed as a step-function convolved with a certain smoothening function f. Hence, we perform a deconvolution and extract the z_c as the location of the step and w_{II} as the square root of the variance of the smoothening function treated as a probability density function. For the simplicity of the analytical approximation, we perform the convolution in a domain of z from -∞ to ∞. This assumption is fulfilled if z_c is much further from the boundaries of the structure than λ_c.

Let us set

$$\Theta_i(z) = H(z_c - z), \tag{D.9}$$

$$f = f(z)\colon\ \mu_f = 0, \qquad V_f = w_{\text{II}}^2. \tag{D.10}$$

where $\Theta_i(z)$ is the idealised sharp coating profile, H - the Heaviside function, f – the considered filter function. The derivations do not assume any particular shape of the f, besides of requirement that its mean value μ_f is 0, that it has a finite variance V_f, implicitly set as w_{II}^2, and that it vanishes for $|z| \gg \lambda_c$. The convolution gives the actual coating profile Θ

$$\Theta(z) = (\Theta_i * f)(x) = \int_{-\infty}^{\infty} \Theta_i(z') f(z - z') \mathrm{d}z' = 1 - F(z - z_c), \tag{D.11}$$

where $*$ denotes a convolution operation, F is the cumulative distribution function of the f, namely

$$F(x) \coloneqq \int_{-\infty}^{z} f(z') \mathrm{d}z'. \tag{D.12}$$

To extract the z_c from the profile, we begin with the statement, that z_c can be calculated as an expected value of the f shifted by z_c and proceed with integration by parts, as follows:

$$z_c = \int_0^l z \cdot f(z - z_c)\mathrm{d}z = \left[z \cdot F(z - z_c) - \int F(z - z_c)\right]_0^l$$
$$= l - \int_0^l \big(1 - \Theta(z)\big)\mathrm{d}z = \int_0^l \Theta(z)\mathrm{d}z. \tag{D.13}$$

Analogously, we find the variance

$$w_{II}^2 = \int_0^l (z - z_c)^2 \cdot f(z - z_c)\mathrm{d}z$$
$$= [(z - z_c)^2 F(z - z_c)]_0^l - \int_0^l 2(z - z_c)F(z - z_c)\mathrm{d}z \tag{D.14}$$
$$= (l - z_c)^2 - \int_0^l 2(z - z_c)\big(1 - \Theta(z)\big)\mathrm{d}z = 2\int_0^l z\Theta(z)\mathrm{d}z - z_c^2.$$

Equations (D.13) and (D.14) allow for the numerical model-free extraction of the z_c and w_{II} directly from the coating profile $\Theta(z)$ resulting from the solution of the model (6.1).

D.3. Extraction of precursor exposure from recorded pressure in the ALD reactor

We developed a numerical procedure to estimate the precursor exposure experienced by the sample based on the analysis of the pressure recorded during the pulsing. For this purpose, simplifying assumptions were made, as enlisted in section 6.2.2.

The first step of the process is fitting of a model function to the pressure curve to estimate the amount of precursor pulsed over time. In our experimental setup, a nitrogen mass flow of v_{N_2}=20 sccm (standard cubic centimetres per minute) was constantly purging the reactor and the exhaust connected to the vacuum pump was always open, both also during the precursor pulsing. This led to a stable baseline purging pressure p_b. The nitrogen delivery rate r_{N_2} in terms of molecules per unit time can be calculated as

$$r_{N_2} = \frac{p_0 v_{N_2}}{k_B T_0} \times \frac{10^{-6}}{60}, \tag{D.15}$$

where p_0=1.01×10^5 Pa and T_0=273.15 K are standard conditions of pressure and temperature, respectively, referring to the definition of the unit of sccm, whereas k_B is the Boltzmann constant. The numerical factor is a conversion to SI units. We model the pressure response to the precursor impulse in an analogy to signal processing, where a defined temporal response of the system to a Dirac's delta convolved with the real shape of the impulse gives an actual response. If one molecule is instantaneously injected into the reactor chamber at time t=0, the impulse delivery rate of TMA $r_{i,TMA}$ can be described with a temporal Dirac's delta function δ,

$$r_{i,TMA}(t) = \delta(t). \tag{D.16}$$

We model the response of the pressure p_i to the gas pulse (D.16) as a decaying exponential with a time constant τ_{pump}, which reflects the pumping behaviour, multiplied by a Heaviside unit step function H,

$$p_{\mathrm{i}}(t) = p_{\mathrm{b}} + \frac{k_{\mathrm{B}}T}{V_{\mathrm{c}}} H(t) \exp\left(-t/\tau_{\mathrm{pump}}\right), \tag{D.17}$$

where V_{c}≈141 cm^3 is the reactor chamber volume, estimated based on the chamber dimensions (cylinder with 15 cm diameter and height of 0.8 cm; gas inlet and outlet are at far sides of one of the cylinder bases, see: specification of Savannah 100 ALD reactor). We approximate the real pulse of N_{TMA} molecules with a temporal gaussian centred at t=t_0 and of a duration parameter τ_{pulse}, therefore the model TMA delivery rate is

$$r_{\mathrm{TMA}}(t) = \frac{N_{\mathrm{TMA}}}{\sqrt{2\pi\tau_{\mathrm{pulse}}^2}} \exp\left(-\frac{1}{2}\left(\frac{t-t_0}{\tau_{\mathrm{pulse}}}\right)^2\right). \tag{D.18}$$

The model pressure curve is then a convolution of (D.17) and (D.18), based on the properties of response to an arbitrary impulse,

$$p(t) = (p_{\mathrm{i}} * r_{\mathrm{TMA}})(t), \tag{D.19}$$

where the symbol "$*$" represents the convolution operation. Equation (D.19) is evaluated numerically and is used as a model function to fit to the pressure data upon pulsing. The fitting parameters are N_{TMA}, τ_{pulse}, τ_{pump} and t_0.

The next step in the procedure is the estimation of the precursor exposure onto CNT walls. The total gas delivery rate r_{total} is

$$r_{\mathrm{total}}(t) = r_{\mathrm{N_2}} + r_{\mathrm{TMA}}(t). \tag{D.20}$$

The molar fraction of TMA at the inlet is

$$\varphi_{\mathrm{TMA}}(t) = \frac{r_{\mathrm{TMA}}(t)}{r_{\mathrm{total}}(t)} = \frac{1}{1 + \frac{r_{\mathrm{N_2}}}{r_{\mathrm{TMA}}(t)}}. \tag{D.21}$$

We account for the expansion of gas with the changing pressure. The gas mixture with the TMA fraction φ_{TMA} injected into the reactor at the time t flows over a sample with a certain delay, at a time t'. While the sample is in the middle of the reactor, we find the time t', for which the injected and expanded gas since the time t equals half of the reactor chamber volume V_{c}, based on the ideal gas law

$$\frac{k_{\mathrm{B}}T}{p(t')} \int_t^{t'} r_{\mathrm{total}}(t)\mathrm{d}t = \frac{V_{\mathrm{c}}}{2}. \tag{D.22}$$

Equation (D.22) is solved numerically, giving the function assigning uniquely the time of gas sweep over sample t' for each timepoint of injection t. The partial pressure of TMA over sample is calculated as

$$p_{\mathrm{TMA}}(t') = p(t')\varphi_{\mathrm{TMA}}(t). \tag{D.23}$$

Notice, that the time argument of φ_{TMA} in (D.23) is not primed – it is because the gas mixture of TMA fraction φ_{TMA} injected at time t reaches over the sample at time t'. The partial pressure of nitrogen $p_{\mathrm{N_2}}$ is then, naturally, the difference between p and p_{TMA}.

The gas impinging rate is then evaluated based on equation (6.3), substituting the time of flight τ_{f} specific to random fibrous geometry (6.36). We obtain

$$J_{\mathrm{wall}}(t') = \frac{2v}{\pi^2} n = \frac{2v}{\pi^2 k_{\mathrm{B}} T} p(t')\varphi_{\mathrm{TMA}}(t). \tag{D.24}$$

The gas exposure Φ_{wall} is then, by definition

$$\Phi_{\mathrm{wall}} = \int_{t_{\mathrm{start}}}^{t_{\mathrm{end}}} J_{\mathrm{wall}}(t')\mathrm{d}t', \tag{D.25}$$

where t_{start} and t_{end} are the time boundaries considered.

List of publications

[1] A. Szkudlarek, W. Szmyt, C. Kapusta, I. Utke, Lateral resolution in focused electron beam-induced deposition: scaling laws for pulsed and static exposure, Appl. Phys. A. 117 (2014) 1715–1726. https://doi.org/10.1007/s00339-014-8751-2.

[2] W. Szmyt, S. Vogel, M. Holler, A. Diaz, J. Gobrecht, M. Calame, C. Dransfeld, Carbon fibre with and without a protective ultrathin alumina film grafted with carbon nanotubes for hierarchical composites observed by ptychographic X-ray computed tomography, in: Proc. ECCM17 - 17th Eur. Conf. Compos. Mater., Munich, Germany, 2016.

[3] W. Szmyt, C. Guerra, I. Utke, Diffusion of dilute gas in arrays of randomly distributed, vertically aligned, high-aspect-ratio cylinders, Beilstein J. Nanotechnol. 8 (2017) 64–73. https://doi.org/10.3762/bjnano.8.7.

[4] W. Szmyt, S. Vogel, A. Diaz, M. Holler, J. Gobrecht, M. Calame, C. Dransfeld, Protective effect of ultrathin alumina film against diffusion of iron into carbon fiber during growth of carbon nanotubes for hierarchical composites investigated by ptychographic X-ray computed tomography, Carbon. 115 (2017) 347–362. https://doi.org/10.1016/j.carbon.2016.12.085.

[5] W. Szmyt, K. Kröning, B. Fiedler, C. Dransfeld, Carbon fiber-carbon nanotube multiscale composites – the key to multifunctionality, in: Proc. CAMX 2017 - Compos. Adv. Mater. Expo 2017, Orlando, Florida (US), 2017.

[6] W. Szmyt, L. Marot, M. Calame, C. Padeste, C. Dransfeld, Carbon fibre-carbon nanotube multiscale composites - nanoengineering of the fibre surface for protection in extreme processing conditions, in: Proc. ECCM18 - 18th Eur. Conf. Compos. Mater., Athens, Greece, 2018.

[7] W. Szmyt, M. Calame, C. Padeste, C. Dransfeld, Nanoengineering of fibre surface for carbon fibre-carbon nanotube hierarchical composites, in: Proc. ICCM22 - 22nd Int. Conf. Compos. Mater., Melbourne, Australia, 2019.

[8] W. Szmyt, C. Guerra-Nunez, C. Dransfeld, I. Utke, Solving the inverse Knudsen problem: gas diffusion in random fibrous media, J. Membr. Sci (in press, 2020). https://doi.org/10.1016/j.memsci.2020.118728

Curriculum Vitae

Personal data

Wojciech Szmyt, born on 12.08.1991 in Olsztyn, Poland

Current address:
Chemin du Rossignol 1
1110 Morges
Switzerland
Tel: +41764536272
E-mail: Wojciech.Szmyt@empa.ch

Education and distinctions

2015-19 PhD in Nanoscience at Department of Physics and Swiss Nanoscience Institute, University of Basel, Switzerland, in collaboration with Institute of Polymer Engineering, FHNW, Windisch, Switzerland; Laboratory for Micro- and Nanotechnology, PSI, Villigen, Switzerland; Transport at Nanoscale Interfaces Laboratory, EMPA Dübendorf, Switzerland; Aerospace Manufacturing Technologies, TU Delft, The Netherlands

2014-15 1.5 years MSc Applied Physics at the Faculty of Physics and Applied Computer Science, AGH University of Science and Technology, Cracow, Poland. Special focus: solid state physics and material science. Receiving EU-funded scholarship for top students throughout the time of studies. Additionally, receiving Rector's scholarship for extraordinary academic performance and achievements during the studies.

2010-14 3.5 years BSc in Applied Physics at the Faculty of Physics and Applied Computer Science, AGH University of Science and Technology, Cracow, Poland. Awarded guaranteed admission to the studies at the AGH becoming a laureate in the nationwide physics competition for the "Diamond Student Record AGH". Receiving EU-funded scholarship for top students throughout the time of studies.

Experience

2019-present: Scientific Assistant in Advanced Materials Processing Laboratory, Empa, Thun, Switzerland; located at Laboratory for Photonic Materials and Characterization LPMAT, EPFL, Lausanne, Switzerland.

2015-19: Employed by the Institute of Polymer Engineering, FHNW University of Applied Sciences and Arts Northwestern Switzerland – the Swiss Nanoscience Institute PhD project P1402 *Lightweight structures based on hierarchical composites*.

2015: 3-month internship at ABB Corporate Research Center in Cracow – *Simulations of copper diffusion in polymers*.

2014: Erasmus – 6-month internship in EMPA Thun – *ALD of TiO_2 on vertically-aligned CNTs. Modelling and experiments.*

2013: Erasmus – 3-month internship in EMPA Thun – *FEBID simulation and experiments*.

Skills

Analytical methods:

X-ray diffraction, Energy-dispersive X-ray spectroscopy, X-ray fluorescence, Ptychographic X-ray computed-tomography (synchrotron-based), Scanning electron microscopy (secondary- and backscatter electron imaging), Electron backscatter diffraction, Differential scanning calorimetry, Thermogravimetric analysis, Atomic force microscopy, Optical microscopy, Confocal laser scanning microscopy, Focused ion beam cross-sectioning, Ellipsometry.

Mechanical testing methods:

Instrumented nanoindentation, Single fiber fragmentation testing, Single fiber pullout test, Single-edge notch beam test, Double cantilever beam test.

Nano- and microfabrication methods:

Atomic layer deposition, Focused electron beam-induced deposition, Focused ion beam-induced deposition and milling, Chemical vapour deposition, high-vacuum chemical vapour deposition, Metal evaporation, Nanoparticle synthesis, Electron beam lithography, UV lithography.

Modelling, data analysis and experimental skills:

Monte-Carlo simulations, Continuum models, Finite element methods, Advanced data analysis (statistics, hypothesis testing); In general: ease in identifying and modelling of fundamental physical principles that govern particular phenomena; establishing efficient experimental routes to determine process parameters. Harvesting the maximum amount of information form the available data.

Selected software skills:

MATLAB – data analysis, simulation, problem solving, optimisation, preparation of graphs
Adobe Photoshop and Lightroom – preparing and enhancing of illustrations.
Autodesk Inventor – 3D CAD design.
LaTeX and MS Word – writing.
CASINO – Monte Carlo simulation of electron trajectories in solids.
COMSOL Multiphysics – finite element simulations.
LabView – custom interfacing with electronics.

Conferences

Szmyt, W.; Straczek, T.; Czajka, A.; Gaska, K.; Zajac, D.; Zukrowski, J.; Kapusta, C.; Reczynski, M.; Nowicka, B.; Sieklucka, B. *ISSRNS12 - 12th International School and Symposium on Synchrotron Radiation in Natural Science*, Warsaw, Poland, June 15-20, 2014.

Szmyt, W.; Vogel, S.; Diaz, A.; Holler, M.; Gobrecht, J.; Calame, M.; Dransfeld, C. *ECCM17 - 17th European Conference on Composite Materials*, Munich, Germany, June 26-30, 2016.

Szmyt, W.; Kröning, K.; Fiedler, B.; Dransfeld, C., *CAMX17 - Composites and Advanced Materials Expo 2017*, Orlando, Florida, USA, December 12-14, 2017.

Szmyt, W.; Marot, L.; Calame, M.; Padeste, C.; Dransfeld, C., *ECCM18 - 18th European Conference on Composite Materials*, Athens, Greece, June 24-28, 2018.

Szmyt, W.; Guerra, C.; Utke, I., HERALD 2018 - *Hooking together European research in Atomic Layer Deposition,* Braga, Portugal, September 25-28, 2018.

Szmyt, W.; Calame, M.; Padeste, C.; Dransfeld, C.; *Nano Today 2019 - 6th Nano Today Conference*, Lisbon, Portugal, June 16-20, 2019.

Szmyt, W.; Calame, M.; Padeste, C.; Dransfeld, C.; *ICCM22 – 22nd International Conference on composite Materials*, Melbourne (Australia), August 11-16, 2019.

Hobbies

Sports: Running, road cycling, mountain biking, roller-skating, hiking, bouldering, climbing.

Arts: Playing guitar, digital and analog photography, cooking.

Other: Following popular science (in particular, cosmology, astronomy, particle physics), watching good movies, travelling.